Optical Spectroscopy of Heavy Element Containing Molecules

In Support of Fundamental Physics

by

Duc Trung Nguyen

A Dissertation Presented in Partial Fulfillment
of the Requirements for the Degree
Doctor of Philosophy

Approved March 2019 by the
Graduate Supervisory Committee:

Timothy C Steimle, Chair
Ranko Richert
Andrew V.G. Chizmeshya

ARIZONA STATE UNIVERSITY

May 2019

ABSTRACT

Transient molecules are of great importance having proposed applications in quantum science and technology and tests of fundamental physics. In the present dissertation, the transient molecules studied are SrOH, ThF, ThCl, YbF and YbOH; each having been selected because of their proposed application. Specifically, SrOH is a candidate of constructing a molecular magneto-optical trap (MOT). The simple actinide molecules, ThF and ThCl, were selected as ligand bonding model systems to gain insight into chemical processing of Spent Nuclear Fuel. The lanthanides YbF and YbOH are venues for the determination of electron electric dipole moment (eEDM) and the studies in this dissertation provide the requisite properties for those experiments.

Intense supersonic molecular beams of these transient molecules were generated via laser ablation and spectroscopically characterized using a novel medium-resolution two-dimensional (2D) spectroscopic approach, as well as high-resolution laser induced fluorescence (LIF). The 2D medium resolution approach, which was used in the studies SrOH, ThF, ThCl and YbOH, uses a multiplexing method that simultaneously records dispersed fluorescence and excitation spectra. A significant advantage of 2D-LIF imaging is that all the electronics states can be targeted to determine the electronics states and associated vibrational spacing individually. Consequently, in the 2D spectra of ThF, ThCl and YbOH, several previously unobserved band systems have been detected in one single scan. For the DF spectra of SrOH and YbOH, the determined branching ratios show that the transitions of these molecules are diagonal (i.e. $\Delta v=0$), which is essential for the proposed potential for laser cooling. In the high-resolution of YbF, ThF, ThCl and SrOH

optical spectra were recorded to an accuracy of ±30 MHz, which represents an unprecedented precision of $1{:}10^{+8}$.

In addition to field free spectra, optical Stark and Zeeman studies were performed to determine the most fundamental magneto-and electro-static properties. Effective Hamiltonian operators were employed to analyze the recorded spectra and determine the spectroscopic parameters. This data set also establishes a contribution toward developing new computational methodologies for treating relativistic effects and electron correlation.

DEDICATION

This dissertation is dedicated to my family for their love, endless support and encouragement.

ACKNOWLEDGMENTS

First, I foremost thank my Ph.D. advisor Prof. Timothy C. Steimle for his insight and his belief in my capability to tackle research projects of a demanding nature. His optimistic attitude, competence and experience, combine with his thoughtfulness and constructive advising always give me confidence that I should not stay in my comfort zone but try to expose myself to various situations and push myself seeking for the solutions, even when the path forward was murky. Through working with him, I not only learned about physical sciences, but also acquired secondary skills such as computer programming, electronic circuitry capabilities, and metalworking. I have learned so many things as well, that I am very appreciative of, including a lot of practical skills. From learning how to work on various lasers and vacuum pumps to being able to troubleshoot issues with electronics and fixing leaks in plumbing, I will be leaving graduate school with a very large set of skills that I most certainly did not enter with.

I would like to thank my oral examination committee members (Prof. Ranko Richert, Prof. Andrew Chizmeshya, and Prof. Marcia Levitus) for enforcing diligence during my Ph.D. candidacy assessment. Special thanks to Prof. Chizmeshya for his insights in computational chemistry that helps us a lot in in the SrOH project. All your advices and comments make my research path complete. Additionally, I also would like to thank all former and present members in our research group for their help throughout the years.

Finally, I would like to thank my family. My parents never went beyond the border of my country, but they believe that an abroad higher education means better future. I could not go further like this in education without their endless love, supports and encouragements.

TABLE OF CONTENTS

CHAPTER Page

CHAPTER Page

LIST OF TABLES

Table Page

Table Page

Table Page

LIST OF FIGURES

Figure Page

Figure Page

Figure Page

CHAPTER 1

INTRODUCTION

Spectroscopy is to understand the interaction of radiated energy and matter. Generally, much of our knowledge about atomic and molecular energy levels, molecular geometries, chemical bonds, interactions of molecules, and related information are obtained from a spectroscopic investigation. Spectroscopy has been a field of research since 1814, when Fraunhofer made many subsequent contributions to optics and spectroscopy, including first observation of stellar spectra, discovery and construction of transmission diffraction gratings, etc. Later Kirchhoff established that each element and compound has its own unique spectrum, therefore by studying the spectrum of an unknown source it is feasible to determine its chemical composition and electronic structure. Many new techniques and instruments have been developed and proved their usefulness. One of the groundbreaking impetus to spectroscopic studies was the introduction of laser in the 1960s. These light sources have enhanced spectral resolution, momentously expand the amount of information delivered by various spectra. Lasers, with its advantages have boosted the field of high-resolution spectroscopy. Laser spectroscopic techniques that are common nowadays includes: laser-induced fluorescence spectroscopy (LIF), resonantly enhanced multiphoton ionization spectroscopy (REMPI), zero kinetic energy spectroscopy (ZEKE), etc. The pulsed and Continuous Wave (CW) lasers have been used extensively in the research conducted in our lab at ASU.

Over many years, various equipment, tools and methods (e.g., high resolution lasers, supersonic jets, double resonance techniques) have been developed to help simplify,

resolve, and interpret the electronic spectra of gas phase molecules. The reason is because those spectra are a rich source of information, however, often comprises of large numbers of peaks. Historically, there are several textbooks[1-4] devoted to systematize those extraction of knowledge from this aspect. From a fundamental scientific perspective, understanding the spectra of transient molecules, which is the focus here, reveals insights on the associated electronic, vibrational, rotational, fine, and hyperfine structure. All the molecules of interest that were studied in this dissertation are open-shell molecules containing a metal atom, especially a transition metal, a free radical is usually the result. Due to the presence of the unpaired electron(s), various electronic states are formed. Consequently, the molecular electron configurations exhibit multiple associated spin multiplicities and orbital angular momentum symmetries. Even small molecules may show unexpected behavior that remains challenging to study their spectra. For example, strong interaction with other electronic states can cause a generation of complex spectra. It is convenient to map out all those interactions in a single molecular orbital correlation diagram. Through the diagram, insight toward the bonding of the molecule's nuclei is illustrated. In the case of transition metal atoms, where s and d-electrons are important, additional mathematical descriptions are considered to accurately and precisely explain some of the spectroscopic observations.

Particular emphasis has been placed upon the effect of static electric and magnetic field. When a molecule having a permanent dipole moment is subjected to a static electric field, the interaction between the dipole moment and the electric field causes the spectral features to shift and/or split into several components. This is known as the Stark effect. Classically it could be explained as the electric field first polarizes the nuclei and electrons

and then interacts with the resulting electric dipole moment. Then the field generates torque on the molecule's dipole moment, consequently change the molecular rotational motion[5]. A more detailed explanation requires a quantum mechanical approach and will be focused on a later chapter. The electric dipole moment, $\overrightarrow{\mu_i}$, is one of fundamental electrostatic property of a molecule that is not only a major tool for molecular spectra but also can be involved in the description of numerous physical phenomena including light and matter interaction in resonant spectroscopy[6]. In terms of molecular spectroscopy, the most important of these is the electric dipole transition moment. The key advantage of utilizing the electric dipole moment is that the information of relative line strengths and transition selection rules can be related to the change of electric dipole moments between any two eigenfunctions of the molecular Hamiltonian[7-8]. It can also serve as a check on the assignment of spectral features. For theoreticians, the accuracy of a calculated dipole moment compared to an experimentally determined value becomes a great value to verify the reliability of the assumed wavefunction on their calculations. The calculated fundamental molecular properties (such as bond length, vibrational frequency, and dissociation energy) then may be directed and revised by experimental results as well. Specifically, magnitudes and signs of hyperfine interactions, when experimentally determined, also serve as a reliable benchmark to compare between theoretical methods.

If a molecule is subjected to a static magnetic field, the spectral features will also behave similarly to the Stark effect in that they shift and/or split into several components. This is called the Zeeman effect and it is a consequence of the interaction of the molecule's permanent magnetic moments with the magnetic field. The Zeeman effect can provide valuable information into not only about the orbital and spin angular momenta of a given

electronic state but also the nature of any perturbing electronic state. For the case of open shell molecules, the main contributor is the net electron spin, S and the total orbital angular momentum, Λ. It can serve as a check on the assignment of spectral features, specifically, the $^{2S+1}\Lambda$ term symbol for the linear molecules. This phenomenon is purely a quantum mechanical attribute of an electron with an assigned spin magnitude of 1/2 for each particle. Relative values are +1/2 and -1/2, and these two projections will split into different energy levels in the presence of a magnetic field. The proportionality constant relating the difference in energies of these spin projections with respect to the magnitude applied magnetic field is g_s. Known as the Lande g-factor, its value is taken as 2.0023[9] for a free electron. In case nonzero orbital angular momentum, the associated g-factor g_L of the electronic state will take on the values 1,2,3 etc. depending on the nature of the molecular orbital. The projection of L is Λ of the term symbol. With the knowledge of the electronic states, the Zeeman effect is predictable. Also, there are additional smaller terms including in the description of the Zeeman effect, anisotropic electron spin effects (g_l), and parity dependent effects (g_l'). These terms account for a reduction of symmetry and provide information as to interactions of the interested state with other nearby electronic states[1].

Recent progress has been made in our lab in ASU on those optical spectroscopy studies of ThF and ThCl. The development of new optical 2D techniques[10-12] for identifying new molecules and studying their associated electronic states have been utilized. Based on an earlier experiment by Schmidt and his co-workers[11], the experimental setup has been adapted and derives high sensitivity and signal-to-noise by exciting a sample with pulsed dye laser. An improved method for scanning and fluorescence detection on discovering new molecules is presented using the real-time tracking monochromator with

the charge-coupled device (CCD) camera. The optical system was used in conjunction with LabView program as the human-machine interface for control of laser-beam scanning and 2D spectrum processing. The combination allowed wide scanning, sensitive detecting and accurately addressing electronic states associated with new molecules**.** Identifying new molecules and accurate mapping their associated electronic states will enhance/boost the development of laser cooling experiments[13-18] as well as contribute to solving problems associated with treating, transmuting, and storage of spent nuclear fuel (SNF)[19-21].

The objective of the current researches is to discover new molecules and then experimentally determine the fundamental molecular properties of the open shell transient metal containing molecules:

i) Molecules relevant to laser cooling: SrOH

ii) Molecules relevant to Department of Energy project of processing the spent nuclear fuel: ThCl and ThF

iii) Molecules relevant to fundamental physics: YbF and YbOH

The focus of this dissertation is utilizing optical high-resolution coherent spectroscopy, 2D spectroscopy as an approach to identify new molecules and study complicated electronic spectra of those gas phase molecules. A number of optical spectroscopic studies on numerous molecular candidates were performed.

The first subsection of the dissertation will be devoted to molecular candidates toward the support for the construction of a Magneto-Optical trap and the measurement of eEDM experiments. The optical studies on laser-coolable polyatomic molecules SrOH, and Yb- containing molecules (YbF and YbOH) are involves in this subsection. The optical Stark and Zeeman study of those molecules is to support the laser cooling and trapping

technique which is one of the great cornerstones of modern atomic physics. The later chapters will be devoted to presenting the experimental study of the magnetic induced effect of the low rotational levels in the ground and excited electronic states of those molecules. A combination of high-resolution optical field-free, Stark spectroscopy, Zeeman spectroscopy of a cold molecular beam sample and a traditional effective Hamiltonian approach describing the interaction between the excited electronic states is involved in these studies. The determined magnetic *g*-factors for various electronic states will be presented. The measured fluorescence branching ratios obtained from the dispersed fluorescence resulting from laser excitation of rotationally resolved branch features of the dispersed fluorescence spectra are compared with Franck-Condon calculations. While optical study of SrOH is limited to support the MOT construction, the Yb- containing molecules research is to support particle physics for the determination of electron electric dipole moment (eEDM), *d*e, the existence of which indicates new physics beyond the Standard Model. The determination of the tiny eEDM ($< 1.0\times10^{-8}$ Debye) requires large electric fields applied to the electron which can be realized when the electron is in a s-orbital of a molecule having a heavy atom.

The second subsection is about experimentally and theoretically determined magnetic and electric dipole moments, bond distances and vibrational spacings in a comparative study of the bonding in ThF and ThCl. These two Thorium- containing molecules were selected because of existence of handful investigations[22-24] on those and they are good candidates to evaluate the sensitivity of the system. Through combining the medium resolution ($\Delta\nu\approx 0.1\text{cm}^{-1}$), two-dimensional (2D) spectroscopy and supersonically cooled molecular beam samples, several bands in the spectral range from 16400 cm^{-1} -

18800 cm^{-1} of ThF and ThCl were observed. Along with the medium- resolution spectroscopy, high resolution ($\Delta\nu$ < 20 MHz) field-free, Stark, and Zeeman spectroscopic experiments were also performed on the detected [18.6] Ω=3/2 – $X^2\Delta_{3/2}$ band of ThF near 538.4 nm and the [18.2] Ω=3/2 – $X^2\Delta_{3/2}$ band of ThCl near 551.0 nm. Following the detection of those bands are field-induced experiments. Stark and Zeeman splittings and shifts were analyzed to determine the permanent dipole moment and g-factor values associated with Thorium- containing molecules' electronic states. Specifically, those investigated states are $X^2\Delta_{3/2}$ and [18.6] Ω=3/2 states of ThF and the $X^2\Delta_{3/2}$ and [18.2] Ω=3/2 states of ThCl. The denotations, [18.2] and [18.6], indicate the energy levels of electronic states that these bands are near 18200 cm^{-1} and 18600cm^{-1}. Analysis of the dipole moments helps mapping the molecular orbital of the bonding between Th and F or Cl. A molecular orbital description of the ground states is used to understand the observed μ_{el} values for the ThX(X=F,Cl,O and S) series, and gather insight into the bonding mechanism. While on the other hand, g-factor values reflect the interaction of demonstrate that the $X^2\Delta_{3/2}$ and [18.6] Ω=3/2 states of ThF and the $X^2\Delta_{3/2}$ state of ThCl are predominately $^2\Delta_{3/2}$ spin-orbit components, whereas the [18.2] Ω=3/2 state of ThCl is an admixture of $^2\Delta_{3/2}$ and $^2\Pi_{3/2}$ spin- orbit components.

References

1. Brown, J. M.; Carrington, A., *Rotational spectroscopy of diatomic molecules*. Cambridge University Press: 2003.

2. Herzberg, G., Molecular spectra and molecular structure. Vol. 1: Spectra of diatomic molecules. *New York: Van Nostrand Reinhold, 1950, 2nd ed.* **1950**.

3. Kovács, I.; Nemes, L., *Rotational structure in the spectra of diatomic molecules*. Hilger London: 1969.

4. Lefebvre-Brion, H.; Field, R. W., *The Spectra and Dynamics of Diatomic Molecules: Revised and Enlarged Edition*. Elsevier: 2004.

5. Townes, C. H.; Schawlow, A. L., *Microwave spectroscopy*. Courier Corporation: 2013.

6. Steimle, T. C., Permanent electric dipole moments of metal containing molecules. *International Reviews in Physical Chemistry* **2000,** *19* (3), 455-477.

7. Bunker, P. R.; Jensen, P., *Molecular symmetry and spectroscopy*. NRC Research Press: 2006.

8. Hougen, J. T. *The calculation of rotational energy levels and rotational line intensities in diatomic molecules*; NATIONAL STANDARD REFERENCE DATA SYSTEM: 1970.

9. Mills, I.; Cvitas, T.; Homann, K.; Kallay, N.; Kuchitsu, K., Quantities, Units, and Symbols in Physical Chemistry. *Journal of the American Chemical Society* **1994,** *116* (19), 8861.

10. Steimle, T.; Kokkin, D. L.; Muscarella, S.; Ma, T., Detection of the Thorium Dimer via Two-Dimensional Fluorescence Spectroscopy. *The Journal of Physical Chemistry A* **2015,** *119* (35), 9281-9285.

11. Reilly, N. J.; Schmidt, T. W.; Kable, S. H., Two-Dimensional Fluorescence (Excitation/Emission) Spectroscopy as a Probe of Complex Chemical Environments. *The Journal of Physical Chemistry A* **2006,** *110* (45), 12355-12359.

12. Kokkin, D. L.; Steimle, T. C.; DeMille, D., Branching ratios and radiative lifetimes of the U, L, and I states of thorium oxide. *Physical Review A* **2014,** *90* (6), 062503.

13. Barry, J. F.; McCarron, D. J.; Norrgard, E. B.; Steinecker, M. H.; DeMille, D., Magneto-optical trapping of a diatomic molecule. *Nature* **2014,** *512*, 286.

14. McCarron, D. J.; Norrgard, E. B.; Steinecker, M. H.; DeMille, D., Improved magneto–optical trapping of a diatomic molecule. *New Journal of Physics* **2015,** *17* (3), 035014.

15. Julienne, P. S., Quo vadis now, cold molecules? *Nature Physics* **2018,** *14* (9), 873-874.

16. Klos, J.; Li, M.; Petrov, A.; Kotochigova, S., Chemistry of Laser-Coolable Polyatomic Molecules. *Bulletin of the American Physical Society* **2018**.

17. McCarron, D.; Steinecker, M.; Zhu, Y.; DeMille, D., Magnetic Trapping of an Ultracold Gas of Polar Molecules. *Physical review letters* **2018,** *121* (1), 013202.

18. Williams, H. J.; Caldwell, L.; Fitch, N. J.; Truppe, S.; Rodewald, J.; Hinds, E. A.; Sauer, B. E.; Tarbutt, M. R., Magnetic Trapping and Coherent Control of Laser-Cooled Molecules. *Physical Review Letters* **2018,** *120* (16), 163201.

19. Taylor, R., *Reprocessing and recycling of spent nuclear fuel*. Elsevier: 2015.

20. Veliscek-Carolan, J., Separation of actinides from spent nuclear fuel: A review. *Journal of hazardous materials* **2016,** *318*, 266-281.

21. Ewing, R. C., Long-term storage of spent nuclear fuel. *Nature Materials* **2015,** *14* (3), 252.

22. Barker, B. J.; Antonov, I. O.; Heaven, M. C.; Peterson, K. A., Spectroscopic investigations of ThF and ThF+. *The Journal of Chemical Physics* **2012,** *136* (10), 104305.

23. Heaven, M. C.; Barker, B. J.; Antonov, I. O., Spectroscopy and Structure of the Simplest Actinide Bonds. *The Journal of Physical Chemistry A* **2014,** *118* (46), 10867-10881.

24. VanGundy, R. A.; Bartlett, J. H.; Heaven, M. C.; Battey, S. R.; Peterson, K. A., Spectroscopic and theoretical studies of ThCl and ThCl+. *The Journal of Chemical Physics* **2017,** *146* (5), 054307.

CHAPTER 2

EXPERIMENTAL SETUP

The studied transient molecules, SrOH, ThF, ThCl, YbF, YbOH, have been generated using laser ablation production technique and detected by using the two-dimension spectroscopy and investigated further by high-resolution laser induced fluorescence technique. Laser induced fluorescence (LIF) excitation spectroscopy[1] is a relatively highly detailed, spectroscopic technique for investigations of optically excited states in both atoms and molecules. Combining supersonic jet technology with the LIF technique has not only made a profound effect on the quality and structure of molecular spectra, but also enhance the sensitivity of experimental optical spectroscopy. The other technique that is often used in conjunction with LIF excitation spectroscopy is dispersed fluorescence (DF) spectroscopy. Dispersed fluorescence usually yields not only the information relating to ground electronic states but can often also be used to investigate simultaneously various vibrational modes of numerous low- lying excited electronic states. This technique is invaluable in studying the complicated excitation spectra of new molecules.

Recently, a technique of combining the DF and LIF spectra in one big picture (a two-dimensional spectra) has been adapted and used to detect new molecules and their associated electronic states.[2-5] In contrast to traditional high-resolution spectra where peaks are recorded with respect to a single axis of energy, medium- resolution 2D spectra plot and illustrate informative patterns along two perpendicular frequency domains[5]. Hence The common signatures of both known and unknown species can be grouped together in

one single scan, and the correlation between electronic transition happening when molecules are excited to different higher energy states could be observed simultaneously. The advantage of this technique is that it can successfully produce patterns even when one-dimensional spectra appear patternless due to complexity and congestion associated with various electronic states. Also, due to the significantly increased number of laser shots that can be averaged while the fluorescence spectrum was being recorded the technique shows excellent sensitivity in compare scanning using a photomultiplier detection.

2.1. High-resolution spectroscopic setup

Our experiments employ the supersonic molecular beam technique to produce samples. Following the method of the previous study[6] the interested molecules are produced in a pulsed beam with a rotational temperature of approximately 20 Kelvin. A 700psi gas mixture of 95% Ar and 5% chemical agent is pushed through a solenoid valve. This valve opens every 50 ms to release gas pulses through a 20- micron hole into the vacuum chamber, where the pressure is kept below 10^{-6} mbar by the diffusion pump. Right outside the valve, a rod of metal (Sr, Yb or Th) is held perpendicular to a narrow hole through which the gas mixture flows pulse-to-pulse into the system. A pulse of 532 nm light, from a Nd:YAG laser, is focused onto the rod in order to ablate the metal. The ablated metal reacts with the chemical agent to form the resulting species containing the interested molecules in the supersonic expansion plasma. In order to maintain the efficiency of reactions, the metal rod is incessantly rotated and translated. Free jet expansion is probed and the expansion is skimmed to produce a molecular beam which is subsequently probed. In the latter case, approximately 100 cm downstream from the source, the beam is collimated by a skimmer and passes into a second vacuum chamber, where the pressure is

below 10^{-6} mbar. The experimental arrangement for the field free, optical Zeeman or Stark and measurements was identical to that used in the previous study of UF^{7}. Then fluorescence spectra were recorded when molecules entered electric or magnetic fields.

2.2. Two-dimensional spectroscopy

Being able to observe the DF spectrum at each laser wavelength means this technique is capable of readily assign the spectral features of the emitting species. Expanding on the work by Reilly, Schmidt, and Kable[5], we have developed the 2D fluorescence probe for application to diatomic and "large" polyatomic molecules. The technique has been used to detect by application to Thorium dimer[8] and multiple electronic states of ThO^{2}. The 2D imaging spectroscopy is a sensitive method capable of detecting weak spectral features, including those that are otherwise hidden beneath stronger bands.

Laser-induced fluorescence (LIF) was imaged on the variable width entrance slit of a 0.67 m monochromator equipped with a water-cooled, intensified, two-dimension (256 vertical ×1024 horizontal pixels) CCD array. An ~75 nm wide spectral window of the dispersed fluorescence (DF) was detected on the two-dimensional array at a given angle setting of the 300 lines/mm grating of the monochromator. The camera software summed down the 256 vertical pixel arrays of the CCD and returned a one-dimensional array of intensity versus dispersed fluorescence wavelength for a given laser excitation wavelength. The laser wavelength was then stepped, the grating angle was tuned, and the process was repeated to produce a 2D spectrum. The 2D spectrum was subsequently processed to produce excitation spectra by vertically summing the signal in a horizontal slice and to produce DF spectra by horizontally summing the signal in a vertical slice.

Wavelength calibration of the DF spectra was achieved by recording the emission lines from an argon pen lamp. The wavelength of the pulsed dye laser was determined using a commercial wavemeter. The radiative lifetimes were measured by tuning the excitation laser wavelength to be on-resonance with a particular feature and recording the DF spectrum at variable time delays from the pulsed laser. The resulting DF spectra were integrated over the appropriate wavelength region to give the relative fluorescence intensity at a given delay from the laser excitation pulse.

2.2.1. "2D" spectroscopy

The central idea of laser excitation spectroscopy using fluorescence detection is illustrated in Figure 1. The tunable laser puts molecules into a specific fine structure level of the excited state. These molecules then spontaneously relax to various levels in either the electronic ground or low-lying electronic states via fluorescence.

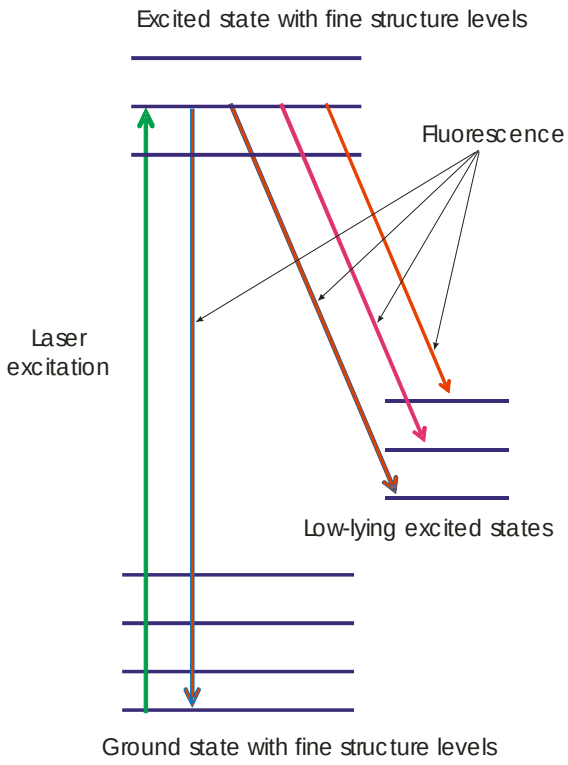

Figure 2.1. Laser excitation spectroscopy using fluorescence detection

There are two types of information in this process: the wavelength of the excitations (i.e. excitation spectra) and the wavelengths of the fluorescence (i.e. dispersed fluorescence (DF) spectra at any given wavelength of the exciting laser). Usually these two types of spectra were measured separately. In the past, the excitation spectra were recorded by monitoring wavelengths all of the fluorescence and the DF spectra were measured through fixing the excitation laser wavelength to a resonance and using a monochromator to disperse the fluorescence. Furthermore, in traditional DF spectroscopy, the detector on the monochromator was a photomultiplier tube as illustrated in Figure *2.2*.

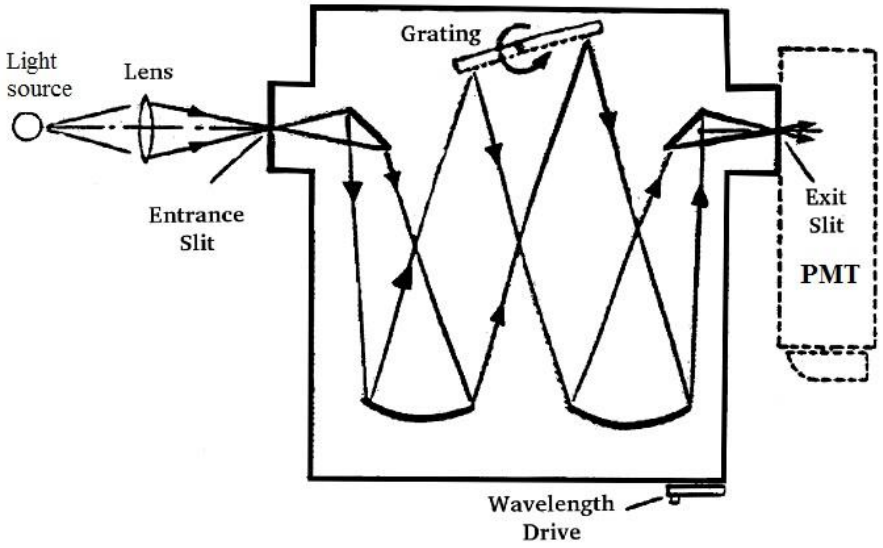

Figure 2.2. The monochromatic light resulting from the diffraction in the monochromator is directed to the photomultiplier tube

This approach in very inefficient because most of the disperse fluorescence does not hit the PMT at a given angle of the grating. A much more effective method is to replace the exit slits and PMT with a CCD detector as illustrated in Figure 2.3. Now an entire range of wavelengths are detected simultaneously, greatly improving the efficiencies of data collection. The monochromator in both the 2D and DF measurement was equipped with a 300 lines/mm grating, which corresponded to an approximately 75-nm-wide spectral window in the CCD ranged in visible dispersed fluorescence. For our gratings (300 lines/mm) the slits on the monochromator were approximately 1 mm for a resolution of approximately ±1.25 nm in the DF.

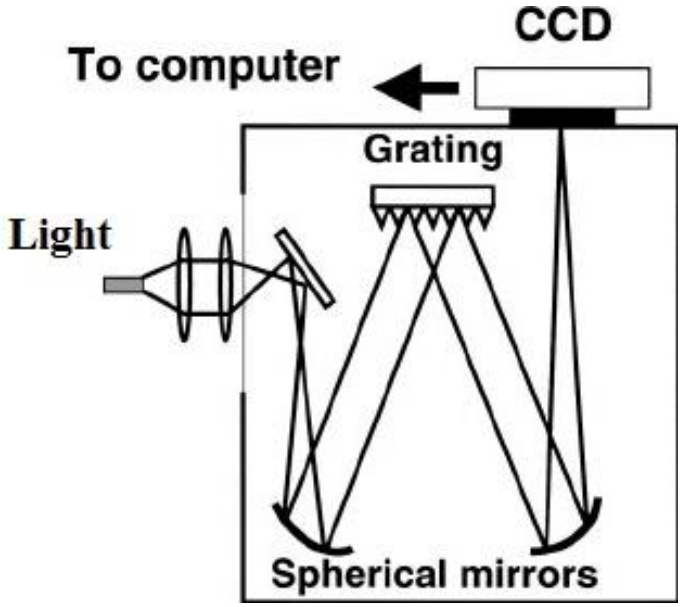

Figure 2.3. The CCD attached to the monochromator[9]

The "2D Spectroscopy" takes the advantage of the broad DF wavelength collection of the monochromator/CCD detector and couples it with excitation spectroscopy. Specifically, in our case, LIF excitation spectra were recorded using a two-dimensional (2D) spectroscopic technique as described in Refs[3, 5] The spectra were imaged on the variable width entrance slit of the monochromator equipped the CCD camera which is attached to the exit port of the monochromator. The camera software sums down the vertical arrays of the CCD and returns a one-dimensional array of intensity versus dispersed fluorescence wavelength at given laser excitation wavelength. The laser wavelength is then stepped in real-time by a commercial spectrometer, the whole process was conducted and checked by our LabView program using as the human-machine interface for control of laser-beam scanning and 2D spectrum processing, the grating angle was tuned, and the process was repeated, to produce a 2D spectrum with one of the dimensions being the laser excitation wavelength and the other dimension the DF. This produced a 3D surface of

fluorescence intensity versus the excitation laser wavenumber and the wavelength of the emitted and dispersed fluorescence, termed a 2D-LIF spectrum Due to the synchronization between the pulsed laser and the fluorescence spectrometer, in our scan, the laser remains at a fixed horizontal position at the detector, which is advantageous when scanning over a large excitation wavelength range. A 2D-LIF image from our ThF and ThCl paper[10] is shown in Figure 2.4 to illustrate the type of image obtained with this approach. Typically, 50 accumulations were collected at each step of the laser wavelength when recording 2D spectra. Unlike previous applications of this technique[3,5], here the 2D spectra were recorded by real-time tracking the transmission window of the monochromator relative to the laser wavelength. An ~75 nm wide spectral window of the dispersed fluorescence (DF) was detected on the two-dimensional array at a given angle setting of the 300 lines/mm grating of the monochromator. The window could be set to any wavelength relative to that of the laser (i.e. either "on-resonance" or "off-resonance") and tracked. The 2D spectrum is subsequently processed to produce excitation spectra by vertically summing the signal in a horizontal slice and to produce DF spectra by horizontally summing the signal in a vertical slice. Tracking the monochromator greatly facilitates the extraction of excitation and DF spectra from the 2D spectrum because the relevant information is in a vertical or horizontal slab (see below). The emission spectrum at specific excited laser's wavelength is then extracted from the obtained 2D spectrum. The wavelength resolved signal is detected by the CCD in vertical columns resulting in an intensity vs wavelength spectrum. In the below spectrum, it is a purple region.

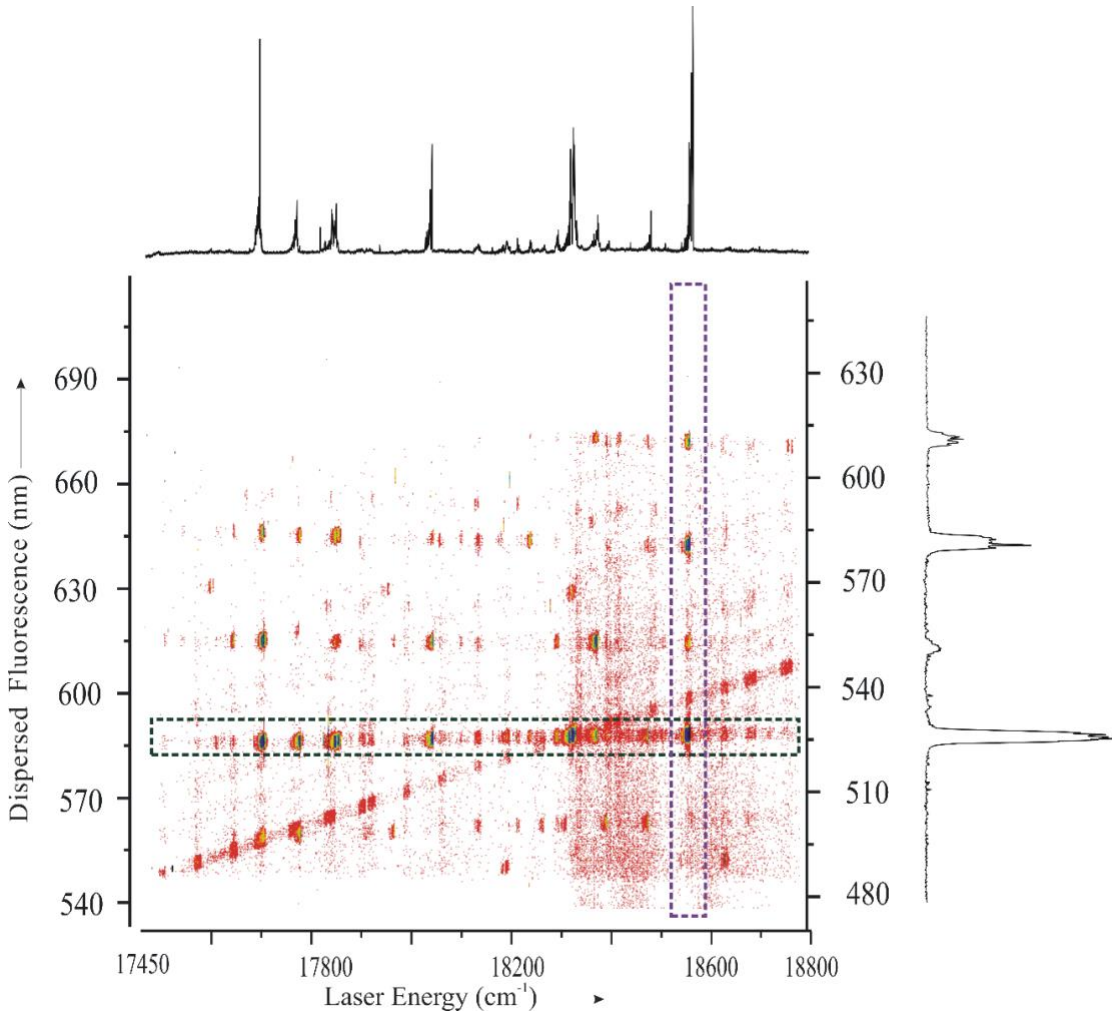

Figure 2.4. The 2D scan of ThF with the spectral from 17400 to 18800 cm^{-1}

The 2D spectrum was subsequently processed to produce excitation spectra by vertically summing the signal in a horizontal slice and to produce DF spectra by horizontally summing the signal in a vertical slice at that excitation wavenumber. Although the 2D spectrum contains a lot of information, for our purpose of detecting fluorescence signal from the molecules of interest, the horizonal integration and vertical slide task will be mainly focused. Vertical slices through the 2D images give a section of the DF spectrum, while complete vertical integration will give an LIF spectrum from the range of fluorescence collected. An argon pen lamp was used as a calibrated tool for the DF spectra.

The wavelength of the pulsed dye laser was determined using a commercial wavemeter. The resulting DF spectra were integrated over the appropriate wavelength region to give the relative fluorescence intensity at a given delay from the laser excitation pulse. The control programs for recording the 2D spectrum and the program for extraction of the excitation and DF spectra were developed as part of this experiment.

2.2.2. Dispersed fluorescence

We have also recorded separate DF spectra with higher averaging to get better signal to noise than simply taking a vertical slice through the 2D-LIF image. These DF spectra were recorded with the same spectrometer as for the 2D-LIF spectra and were recorded three times accumulating over 5000 shots each time, and an average taken. The image intensifier is gated to detect fluorescence in a time window come right after the laser pulse. The gate width is variable and typically depends on the fluorescence lifetime and the value was set several times of the lifetime. The signal from the fluorescence travels from the intensifier to the CCD and was processed after each accumulation. Similar to the 2D spectra, dispersed fluorescence spectra over the entire near-UV to NIR range were obtained using the commercial acquisition software provided with the iCCD. In this case the wavelength of the excitation laser was set to a specific value, which was usually the band head of typical interested transition determined from the 2D spectra., and an active 75-nm-wide segments of the DF spectra recorded. Typically, in this mode of accumulation operation ranging from 5000-10000 averages were taken at each monochromator transmission window. The multiple, 75-nm-wide, one-dimensional arrays of intensity versus dispersed fluorescence wavelength were plotted together and calibrated for absolute wavelength position and variation of sensitivity, to produce the DF spectra. The sensitivity

of the spectrometer as a function of wavelength was taken as the product of the quantum efficiency of the CCD, reflectivity of the monochromator mirrors, and efficiency of the grating. The CCD wavelength-response curve was fit to a fourth-order polynomial. Wavelength calibration of the DF spectra was achieved by recording the emission lines from an argon pen lamp. The wavelength of the pulsed dye laser was determined using a commercial wavemeter. The resulting DF spectra were integrated over the appropriate wavelength region to give the relative fluorescence intensity at a given delay from the laser excitation pulse.

2.3. References

1. Kinsey, J. L., Laser-induced fluorescence. *Annual Review of Physical Chemistry* **1977,** *28* (1), 349-372.

2. Kokkin, D. L.; Steimle, T. C.; DeMille, D., Branching ratios and radiative lifetimes of the U, L, and I states of thorium oxide. *Physical Review A* **2014,** *90* (6), 062503.

3. Gascooke, J. R.; Alexander, U. N.; Lawrance, W. D., Two dimensional laser induced fluorescence spectroscopy: A powerful technique for elucidating rovibronic structure in electronic transitions of polyatomic molecules. *The Journal of Chemical Physics* **2011,** *134* (18), 184301.

4. Chen, P. C., High Resolution Coherent 2D Spectroscopy. *The Journal of Physical Chemistry A* **2010,** *114* (43), 11365-11375.

5. Reilly, N. J.; Schmidt, T. W.; Kable, S. H., Two-Dimensional Fluorescence (Excitation/Emission) Spectroscopy as a Probe of Complex Chemical Environments. *The Journal of Physical Chemistry A* **2006,** *110* (45), 12355-12359.

6. Nguyen, D.-T.; Steimle, T. C.; Kozyryev, I.; Huang, M.; McCoy, A. B., Fluorescence branching ratios and magnetic tuning of the visible spectrum of SrOH. *Journal of Molecular Spectroscopy* **2018,** *347*, 7-18.

7. Linton, C.; Adam, A.; Steimle, T., Stark and Zeeman effect in the [18.6] 3.5–X (1) 4.5 transition of uranium monofluoride, UF. *The Journal of chemical physics* **2014,** *140* (21), 214305.

8. Steimle, T.; Kokkin, D. L.; Muscarella, S.; Ma, T., Detection of the Thorium Dimer via Two-Dimensional Fluorescence Spectroscopy. *The Journal of Physical Chemistry A* **2015,** *119* (35), 9281-9285.

9. Wang, H.-W.; Zhu, T. C.; Putt, M. E.; Solonenko, M.; Metz, J.; Dimofte, A.; Miles, J.; Fraker, D. L.; Glatstein, E.; Hahn, S. M.; Yodh, A. G., Broadband reflectance measurements of light penetration, blood oxygenation, hemoglobin concentration, and drug concentration in human intraperitoneal tissues before and after photodynamic therapy. *BIOMEDO* **2005,** *10* (1), 014004-01400413.

10. Nguyen, D.-T.; Steimle, T.; Linton, C.; Cheng, L., Optical Stark and Zeeman Spectroscopy of Thorium Fluoride (ThF) and Thorium Chloride (ThCl). *The Journal of Physical Chemistry A* **2019,** *123* (7), 1423-1433.

CHAPTER 3

MOLECULAR THEORY

The structure of a diatomic (or triatomic) molecule, when compared to something as complex as RNA or DNA, is relatively simple. In investigating the intricate details of the electronic structure of these simple molecules, however, turns out to be quite challenging even for the advanced *ab initio* methods, which still cannot account for all the experimental observations. This is particularly true for transient molecules containing an open shell transition metal with the contribution of d and s orbital to the molecular bonding. The core idea of these experiments presenting in this dissertation bases on the nature of the energy eigenstates associated with those molecules, SrOH, YbF, YbOH, ThF and ThCl. These molecular energy levels, which reflect the quantum mechanical nature of matter, dictate the molecular spectra, and the behavior of the spectra under external fields. When a photon with energy equal to the energy difference between the initial electronic state of the molecule and an excited electronic state is absorbed by the molecule, the molecule gets excited to the higher energy state. The molecule may then spontaneously relax to various lower energy states, releasing new photons with energy corresponding to the energy difference between the two states. A complex quantum mechanical approach is in need to studying these open-shell metal- containing molecules.

The quantum mechanical description of a diatomic molecule is even more complex in comparison with the atom's description. The quantum mechanical picture of a single atom involves a spherically symmetric potential, the electron motion relative to the nucleus and the relative electron positions. A quantum description of a molecule, in contrast, is

quite different. It involves axial symmetry (for diatomic and linear triatomic molecules), the relative motion of the two nuclei, the repulsive interaction between them and also the positions of the two nuclei themselves, etc. Consequently, the Hamiltonian operator needs to add the kinetic energy operators of the nuclei and the electrons, the potential energy operators between the nuclei, between the electrons, and between the nuclei and electrons. A complete picture of the molecular theory can be found in numerous molecular spectroscopy books[1-5]. However, the Hamiltonian operator corresponding to the total energy of any system is very complicated. Thus, instead of using the "complete" Hamiltonian operator, effective Hamiltonian method has been employed to process a small subset of molecular data (i.e experimental spectrum of one vibronic state) because it is more convenient and practical to use. This chapter only briefly describes the theory that will be used to analyze the observed spectra of diatomic molecules

3.1. Open-shell metal- containing molecules

3.2.1. Term symbol

An electronic state of an open-shell diatomic (or triatomic) molecule can be constructed from the molecular orbital description of the electrons. Obliviously when two or three atoms tie together to form a molecule, the spin and orbital angular momenta of each atom are combined, and therefore form a spin and angular momentum for the molecule. Note that the projection of the total orbital angular momentum of the atoms along the internuclear axis (usually denoted z) is often approximately conserved $[\hat{H},\hat{L}]=0 \rightarrow \hat{L}\Psi = \Lambda\Psi$. Thus, the z-axis projections of the net orbital angular momenta of all atoms sum produces the quantum number Λ. This quantum numbers only accept

integer values. $|\Lambda| = 0, 1, 2, 3, \ldots$ gives the corresponding $\Sigma, \Pi, \Delta, \Phi, \ldots$ states. The total sum of individual electronic spin angular momenta ($\boldsymbol{s}_i = 1/2$) of all atoms formed a total molecular spin denoted as S. The z-axis projection of spin which is also often approximately conversed, $[\hat{H}, \hat{S}_z] = 0 \rightarrow \hat{S}_z \Psi = \Sigma \Psi$, is given by the quantum number Σ, which is analogous to M_S, the z-component quantum number for total electron spin in atoms. Hence, the total angular momentum along the z-axis is given by $\Omega = \Lambda + \Sigma$ and ranges from $|\Lambda + S|$ to $|\Lambda - S|$ and is analogous to M_J in atoms. Generally, in a molecule, the total angular momentum (excluding nuclear spin), J, is the net vector resulting from orbital (L), spin (S), and nuclear rotation (R),

$$\vec{J} = \vec{L} + \vec{S} + \vec{R}$$

Table 3.1. Angular momenta labels for a diatomic molecule

Label	(z-axis) projection	Physical meaning
I	Ω_I	Nuclear spin
S	Σ	Total Electronic Spin
L	Λ	Total orbital angular momentum
R	0 ($\perp$ to z)	Rotation of the nuclear framework
$\vec{N} = \vec{L} + \vec{R}$	Λ	Total angular momentum w/o elec and nuc spins
$\vec{J} = \vec{L} + \vec{S} + \vec{R}$	Ω	Total ang. momentum w/o nucle spin
$\vec{F} = \vec{I} + \vec{L} + \vec{S} + \vec{R}$		Total angular momentum

The notation for various angular momenta and their projections on the internuclear z-axis are summarized in Table *3.1*. As we will see below, in the presence of strong spin-orbit

coupling Λ and Σ are not individually conserved, although Ω is. Λ is related with the projection of total orbital angular momentum, *L*, of the electron along the internuclear axis by the following expression:

$$\hat{L}_z \psi^{el} \cong \Lambda \psi^{el} . \tag{3.1}$$

We can now specify a molecular term as

$$^{2S+1}|\Lambda|^{(+/-)}_{(\Omega \text{ or } u/g)} . \tag{3.2}$$

In equation 3.2, 2*S*+1 is called the spin multiplicity. For example, if there is one unpaired electron, *S* = 1/2, resulting in a doublet state, if there are two unpaired electrons, S = 1, resulting in a triplet state. The lowest energy configuration of angular momentum of a molecule is determined based on the Hund's rule.

The total angular momentum J has a projection of Ωħ units of angular momentum along the internuclear axis. The relationship between J and Ω is expressed as following:

$$\hat{J}_z \psi^{el} \cong \Omega \psi^{el} . \tag{3.3}$$

The +/- superscript in equation 3.2 is only used in Σ states, which is related reflection symmetry. Consider $\hat{\sigma}$(x,z) is assumed as the reflection operator of electronic wavefunction through the xz-plane of molecular fixed coordinates where z-axis contains the nuclei. If the operator is applied on molecular with Λ > 0, it will result in two states, one state is symmetric with respect to this reflection and one state that is antisymmetric. However, for the Σ state (Λ = 0), this two-fold degeneracy disappears, and all Σ states are either symmetric under any plane containing the internuclear axis, or antisymmetric. The +/- superscripts are as following:

$$\hat{\sigma} \psi^{el} \cong \pm \psi^{el} \tag{3.4}$$

The g/u subscript is parity of the electronic states belonging to the term, and it is only relevant for the homonuclear molecule such that:

$$\hat{i}\,\psi^{el} \cong \pm\psi^{el} \tag{3.5}$$

where g and u represent + and -, respectively.

3.2.2. Hund' coupling cases

To describe rotational-vibrational electronic spectra, Hund has introduced definite momentum coupling cases for diatomic molecules, Hund's coupling case. Hund's coupling cases are idealized study cases describing the coupling of angular momenta which assists spectroscopists in studying the pattern of rotational levels and the consequential spectra. There are total five Hund's coupling cases which are described in details in a couple of textbooks[3, 6]. This section only describes in details the Hund's case that are used in analyzing of experimental spectra: Hund's case $a_{\beta J}$ and Hund's case $b_{\beta S}$.

Table 3.2. Hund's coupling cases and their requirements with A is a spin-orbit coupling constant, and B is a rotational constant.

Coupling case	Electrostatic	Spin-Orbit	Rotational	Good quantum numbers	Requirement
(a)	strong	intermediate	weak	$\eta, \Lambda, S, \Sigma, J, \Omega$	$A\Lambda >> BJ$
(b)	strong	weak	intermediate	η, Λ, N, S, J	$A\Lambda << BJ$
(c)	intermediate	strong	weak	$\eta, J_\alpha, J, \Omega$	$A\Lambda >> \Delta E_{el}$

Hund's coupling case offers which basis set should be used to obtain correct molecular eigenfunction. The angular momentum basis for Hund's case (a)-(e) derives are following:

Hund's case (a) $|nJS\Omega\Lambda\Sigma\rangle$, Hund's case (b) $|nJSN\Lambda(S_R)\rangle$, Hund's case (c) $|nJ[J_a]\Omega\rangle$. A summary of good quantum numbers and case's requirements is presented in Table 3.2

The textbook[3] written by Brown and Carrington describes in details of all cases. In the Hund's case (a), illustrated in Figure 3.1(A), **S** is coupled to **L** through spin-orbit coupling. Briefly, the **L** is strongly coupled to the inter-nuclear axis by electrostatic forces, while **S** is coupled with internal magnetic field along inter-nuclear axis, consequently they couple each other. The projections of **L** and **S** are well defined and denoted as Λ and Σ and their sum is Ω= Λ+Σ. The **R component** is coupled with a vector **J**. Therefore, the vector coupling can be written as:

$$\mathbf{\Omega} + \mathbf{R} = \mathbf{J} \quad (3.6)$$

which corresponds to the basis set $|\eta\Lambda\rangle|(S\Sigma|\Omega JM_J\rangle$.

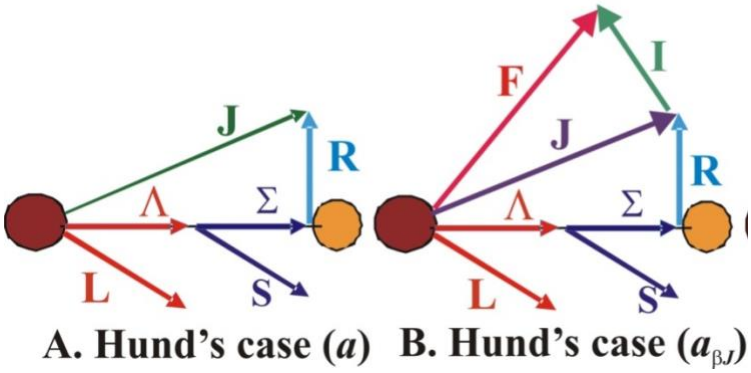

Figure 3.1. A. Hund's cases (a), B. Hund's cases ($a_{\beta J}$)

Hund's case ($a_{\beta J}$) is the extension of case (a) in which nuclear spin angular momentum, **I,** is coupled to **J** to form a grand total angular momentum, **F.** Hund's case ($a_{\beta J}$) limit, given in Table 3.2 with the approximately good intermediate quantum number, *J*, resulting from coupling the rotational angular momentum, **R**, with the electron spin

angular momentum, **S.** When nuclear spin, **I,** is strongly coupled with **J,** it produces total angular momentum, **F**. The resulting Hund's case ($a_{\beta J}$) vector coupling can be written as: $\mathbf{\Omega + R = J}$; $\mathbf{I + J = F}$ which corresponds to the basis set $|\eta\Lambda\rangle|(S\Sigma)\rangle(JI)\Omega, M_F\rangle$.

Specifically, consider YbF study that will be described in chapter 4, the energy level pattern for all the relevant rotational levels of the [18.6] and [18.7] states are those of the $|\Omega| = 1/2$ component of a $^2\Pi$ state near the Hund's case ($a_{\beta J}$) coupling scheme limit. The denotation of the two states, [18.6] and [18.7] states, indicate that those states are near 18600 cm^{-1} and 18700 cm^{-1}, respectively. The corresponding basis function according to Brown and Carrington[3] is $|\eta\Lambda>|S\Sigma>|J\Omega(JI)F>$. The $^{174}Yb^{19}F$ follows case $b_{\beta J}$ because of the small ^{19}F hyperfine then the $A^2\Pi - X^2\Sigma^+$ transition becomes case $a_{\beta J}$ – case $b_{\beta J,}$ that í why there is $^{\Delta N}\Delta J_{F',F''}$ (N") designation. In the other hand, in ^{171}YbF, there is a large hyperfine in $X^2\Sigma^+$ state so it turns out to be case $a_{\beta J}$ – case $b_{\beta S.}$ The Λ-doubling in the low-rotational levels of the [18.6] and [18.7] states are larger than the rotational spacin. showing that the magnetic hyperfine splitting is very small[7]. A conventional $^2\Pi$ (case $a_{\beta J}$) - $^2\Sigma^+$ (case $b_{\beta J}$) labeling scheme of $^{\Delta N}\Delta J_{Fi'Fi''}(N'')$ are used to characterizing the high-rotational levels, where *Fi"* and *Fi'* subscripts represent the spin components of the $X^2\Sigma^+$ and [18.6] or [18.7] states, respectively. All levels of a $^2\Pi_{1/2}$ state are assumed to have $Fi' = 1$. The Fi'' label is employed here only if the spin-rotation splitting in the $X^2\Sigma^+$ state is much larger than the hyperfine splitting. This happens when high-rotational branch features ($N > 20$) in the case of the [18.6]-$X^2\Sigma^+$ (v=0) band were considered. Specifically, where J in the $X^2\Sigma^+$ state is considered as a roughly good quantum number then Fi'' is set to equal 1 or 2 for $J=N+S$ or $N-S$, respectively. The term using for the a $^2\Pi_{1/2}$ (case $a_{\beta J}$) - $^2\Sigma^+$ (case $b_{\beta J}$) labeling

scheme, therefore, becomes the most appropriate terms to characterize the transition. They are P_1, Q_1, R_1, ${}^{P}Q_{12}$, ${}^{O}P_{12}$, and ${}^{Q}R_{12}$. It is expected in this labelling scheme to drop the superscript and the second subscript in the situation where $\Delta N=\Delta J$ and $Fi'' = Fi'$.

The intermediate quantum number J is not appropriate for the low rotational levels of the ground state $X^2\Sigma^+$, which follow a case ($b_{\beta S}$) vector coupling scheme, and hence neither does the Fi'' subscript of the conservative $^2\Pi$ (case $a_{\beta J}$) - $^2\Sigma^+$ (case $b_{\beta J}$) branch term. In these cases, the Fi'' label is replaced with the intermediate good quantum number G'' of the Hund's case ($b_{\beta S}$) coupling scheme. The six corresponding branches of the $^2\Pi_{1/2}$ (case $a_{\beta J}$) - $^2\Sigma^+$ (case $b_{\beta J}$) labeling scheme then rearrange into a group of eight branch features of the corresponding $^2\Pi$ (case $a_{\beta J}$) - $^2\Sigma^+$ (case $b_{\beta S}$) scheme. The corresponding branches for the $^2\Pi_{1/2}$ (case $a_{\beta J}$) - $^2\Sigma^+$ (case $b_{\beta S}$) sub-band are selected and denoted as ${}^{O}P_{1G}$, ${}^{P}P_{1G} + {}^{P}Q_{1G}$, ${}^{Q}Q_{1G} + {}^{Q}R_{1G}$, and ${}^{R}R_{1G}$ with $G = 0$ and 1. The abbreviation ${}^{P}P_{1G}$ and ${}^{Q}Q_{1G}$ for the ${}^{P}P_{1G} + {}^{P}Q_{1G}$ and ${}^{Q}Q_{1G} + {}^{Q}R_{1G}$ branches is used from now on.

In case (b), the spin-orbit coupling is weak or non-existent (if $\Lambda = 0$). In this case, N is defined as $N = \Lambda + R$ and $J = N + S$ with assumption that L processes around the internuclear axis. The good quantum numbers in case (b) are Λ, N, S, and J. the basis set $|\eta\Lambda>|(SI)G(GN)F>$ is suitable for characterizing those state following this case. For example, in the study case of YbF, the low-rotational energy levels of the $X^2\Sigma^+$ ($v = 0$) follow the case ($b_{\beta J}$) state because of the small spin-rotation interaction. In the wavefunction, $G = S + I$. In this case, $S = I = 1/2$, the intermediate quantum number G takes either value 0 or 1 (see Figure 4.2 of chapter 4 studying YbF). F is the total angular momentum resulting from coupling G and N. In the case with N=1, G=1 levels of the $X^2\Sigma^+$ ($v = 0$) state, $F = 0$, 1, and 2 levels go together as a closely spaced group while a single F=1

level arising from the coupling of G with N. It has been observed that the spin-rotation interaction in the $X^2\Sigma^+$ state quickly increases with vibrational excitation initiating the electron spin S to decouple from I and re-couple to N. Therefore, the energy level pattern for the N=1 levels of the $X^2\Sigma^+$ (v = 3) state follow that of a Hund's case ($b_{\beta J}$) limit pattern consisting the coupling of J = S + N with I cause the presence of a pair of F = 0 and 1 and a pair of F = 1 and 2 levels.

3.2. Effective Hamiltonian operator

The challenge of studying open-shell polyatomic molecules is that there exist many types of interactions, due to interaction of various nuclei with each other and with the electrons. In, (spin-orbit, spin-spin, etc.) that are present in the molecules. Furthermore, the density of states is much higher than the one of an atom. Thus, it is necessary to consider all effects together. According to the Born-Oppenheimer approximation, most of the interactions could be considered independent but there is possibly a significant interaction between states that could not be assumed to be non- eligible. The treatment of these open-shell molecules is only feasible by take in some level of approximations with careful consideration in each state.

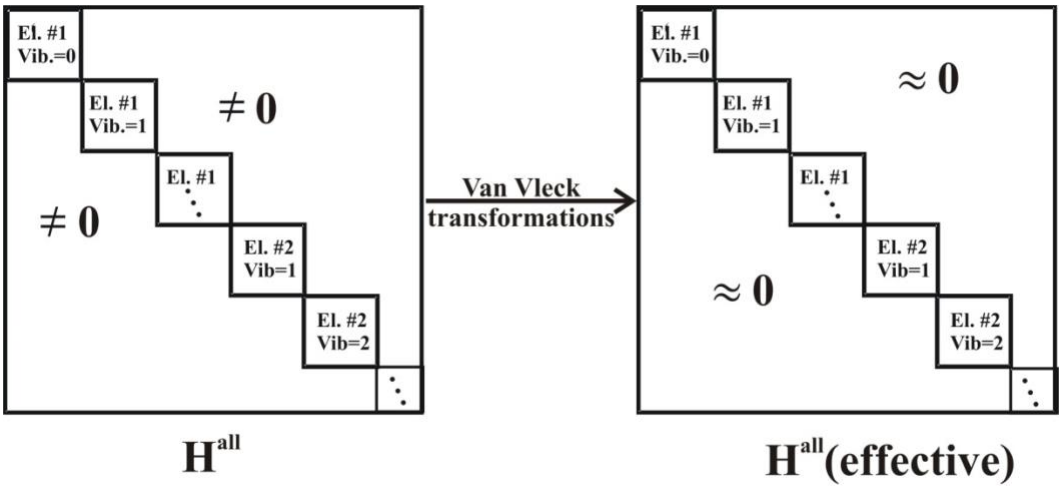

Figure 3.2. A schematic diagram of the transformation of the total Hamiltonian matrix representation (left) to the effective Hamiltonian (right).

3.2.1. $^2\Sigma$ state

The effective Hamiltonian operator for the $\tilde{X}\,^2\Sigma^+(0,0,0)$ and $\tilde{B}^2\Sigma^+(0,0,0)$ states included the origin, rotation, its centrifugal distortion, and spin-rotation terms[3]:

$$\mathbf{H}^{eff}(^2\Sigma) = T_v + B\mathbf{N}^2 - D\mathbf{N}^4 + \gamma\mathbf{N}\cdot\mathbf{S} \quad . \qquad 3.7)$$

Here N is the end-over-end rotational angular momentum operators, *B* is the rotational constant, associated centrifugal distortion correction (*D*) and S is the total electronic spin.

3.2.2. $^2\Pi$ state

To obtain the energy levels of the $\tilde{A}^2\Pi_r$ state of SrOH, the effective Hamiltonian operator for the $\tilde{A}^2\Pi_r(0,0,0)$ state including the origin, spin-orbit interaction and associated centrifugal distortion correction, rotation and associated centrifugal distortion correction, and the Δ-doubling interaction terms[3] is as following

$$\mathbf{H}^{\text{eff}}(\tilde{A}^2\Pi) = T_{\text{v}} + A\mathrm{L}_z\mathrm{S}_z + A_{\text{D}}\frac{1}{2}\left[\mathbf{N}^2, \mathrm{L}_z\mathrm{S}_z\right]^+ + B\mathbf{N}^2 - D\mathbf{N}^4 + \frac{1}{2}(p+2q)(\mathrm{e}^{2\mathrm{i}\varphi}\mathrm{S}_-\mathrm{J}_- + \mathrm{e}^{-2\mathrm{i}\varphi}\mathrm{S}_+\mathrm{J}_+) - \frac{1}{2}q(\mathrm{e}^{2\mathrm{i}\varphi}\mathrm{J}_-^2 + \mathrm{e}^{-2\mathrm{i}\varphi}\mathrm{J}_+^2) \quad (3.8)$$

In Eq. 3.8, A and A_D are spin-orbit terms, p and q are Λ-doubling terms, $J_{\pm}$ are the shift operators of the total angular momentum in the absence of the nuclear spin, **[ ]**$^+$ is the anti-commutator, and φ is the azimuthal angle of the electron.

In order to model the spectra of YbF molecule, the energies for the [18.2] and [18.7] states were modeled with the assumption that the states are the |Ω|=1/2 components of a $^2\Pi$ state. The model Hamiltonian includes the origin (T_{v}), spin-orbit interaction (A), rotation (B) and associated centrifugal distortion correction (D), the Λ-doubling (p+2q) and associated centrifugal distortion correction $(p+2q)_D$, and the effective magnetic hyperfine ($h_{1/2}$(^{19}F)) and parity-dependent magnetic hyperfine (d(^{19}F)) interaction terms:

$$\mathbf{H}^{eff}(^2\Sigma^+) = T_v + AL_zS_z + B\mathbf{N}^2 - D(\mathbf{N}^2)^2 + \frac{(p+2q)}{2}(\mathrm{e}^{-2i\phi}J^+S^+ + \mathrm{e}^{+2i\phi}J^-S^-)$$
$$+\frac{(p+2q)_D}{2}\left[(\mathrm{e}^{-2i\phi}J^+S^+ + \mathrm{e}^{+2i\phi}J^-S^-), \mathbf{N}^2\right]_+ \quad (3.9)$$
$$+h_{1/2}I_zL_z + \frac{d}{2}(\mathrm{e}^{-2i\phi}S^+I^+ + \mathrm{e}^{+2i\phi}S^-I^-).$$

The effective magnetic hyperfine parameter, $h_{1/2}$, for a $^2\Pi_{1/2}$ state is based on the Frosch and Foley a, b_{F} and c parameters by the given relationship $h_{1/2} = a - (b_F + 2c/3)/2$. In Eq. (3.9) $J^{\pm}$, $S^{\pm}$ and $I^{\pm}$ stand for the shift operators of the total angular momentum without the presence of nuclear spin, J, the total electron spin, S, and the ^{19}F nuclear spin, I, and ϕ stays as the azimuthal coordinate of the electrons. The [ ]$^+$ term stands as the anti-

commutator between the squared end-over-end angular momentum operator N^2 and the operator related to Λ-doubling.

3.2.3. $^2\Delta$ state

For the analysis performed in the later chapter studying [18.6] Ω=3/2 and [18.2] Ω=3/2 states of ThF and ThCl, respectively, it was assumed that the [18.6] Ω=3/2 and [18.2] Ω=3/2 states were both components of $^2\Delta$ states with identical spin-orbit splitting to the ground state counterparts. This Hund's case(a) picture assists in making a comparison with the *ab initio* predictions. The effective Hamiltonian operator used to model the energies and wave functions of these $^2\Delta$ states consisted of spin-orbit, rotational, and Ω-doubling terms[8]:

$$\hat{H}^{eff} = T_v + A\hat{L}_z\hat{S}_z + B(\hat{J}-\hat{L}-\hat{S})^2 - \frac{1}{2}(p_\Delta + 4q_\Delta)(\hat{S}_+\hat{J}_+^3 + \hat{S}_-\hat{J}_-^3) \qquad 3.10)$$

where the rotational term has been written in the $\boldsymbol{R}^2$ –form, $\hat{R} \equiv (\hat{J}-\hat{L}-\hat{S})$. The Ω-doubling term is written in terms of the raising and lowering operators.

3.2.4. Matrix elements Hamiltonian for diatomic molecule in a given electronic state

The eigenvalues and eigenvectors for a specific electronic state can be determined by constructing and diagonalizing a matrix representation of the total Hamiltonian operator with respect to a Hund's case basis set. The expression of the matrix elements have been provided in many textbook[19,33,41]. The matrix elements of an effective Hamiltonian operator using a Hund's case ($a_{\beta J}$) basis sets $\left|\eta\lambda; S\Sigma; J\Omega(JI_1)F_1(F_1I_2)F\right\rangle$ are taken from Ref. [1] listed in this subchapter.

Matrix elements for rotation, $\hat{\mathrm{H}}^{\mathrm{rot}}$:

$$\begin{aligned}&\left\langle \eta\Lambda; S\Sigma'; J\Omega'(JI_1)F_1'(F_1I_2)F' \left| \hat{H}^{rot} \right| \eta\Lambda; S\Sigma; J\Omega(JI_1)F_1(F_1I_2)F \right\rangle \\ &= B\left\{ \begin{array}{l} \delta_{\Sigma\Sigma'}\delta_{\Omega\Omega'} \times [J(J+1) - \Omega^2 + S(S+1) - \Sigma^2] \\ -2\sum_{q=\pm1} (-1)^{J-\Omega'+S-\Sigma'} \begin{pmatrix} J & 1 & J \\ -\Omega' & q & \Omega \end{pmatrix} \begin{pmatrix} S & 1 & S \\ -\Sigma' & q & \Sigma \end{pmatrix} \\ \times \sqrt{J(J+1)(2J+1)S(S+1)(2S+1)} \end{array} \right\}\end{aligned} \tag{3.11}$$

Matrix elements for centrifugal distortion, $\hat{\mathrm{H}}^{\mathrm{CD}}$:

$$\begin{aligned}&\left\langle \eta\Lambda; S\Sigma'; J\Omega'(JI_1)F_1(F_1I_2)F \left| \hat{H}^{CD} \right| \eta\Lambda; S\Sigma; J\Omega(JI_1)F_1(F_1I_2)F \right\rangle \\ &= -D\left\{ \begin{array}{l} \delta_{\Sigma'\Sigma}\delta_{\Omega'\Omega} \times \left\{ \begin{array}{l} [J(J+1) - \Omega^2 + S(S+1) - \Sigma^2]^2 \\ +4\sum_{q=\pm1}\sum_{\Omega''} \begin{pmatrix} J & 1 & J \\ -\Omega & q & \Omega'' \end{pmatrix}^2 \begin{pmatrix} S & 1 & S \\ -\Sigma & q & \Sigma'' \end{pmatrix}^2 \\ \times J(J+1)(2J+1)S(S+1)(2S+1) \end{array} \right\} \\ -2\sum_{q=\pm1} (-1)^{J-\Omega'+S-\Sigma'} \begin{pmatrix} J & 1 & J \\ -\Omega' & q & \Omega \end{pmatrix} \begin{pmatrix} S & 1 & S \\ -\Sigma' & q & \Sigma \end{pmatrix} \\ \times \sqrt{J(J+1)(2J+1)S(S+1)(2S+1)} \\ \times [2J(J+1) - (\Omega')^2 - \Omega^2 + S(2S+1) - (\Sigma')^2 - \Sigma^2] \end{array} \right\}\end{aligned} \tag{3.12}$$

Matrix elements for spin-orbit coupling interaction, $\hat{\mathrm{H}}^{\text{Spin-orbit}}$:

$$\left\langle \eta\Lambda; S\Sigma; J\Omega(JI_1)F_1(F_1I_2)F \left| \hat{\mathrm{H}}^{\text{Spin-orbit}} \right| \eta\Lambda; S\Sigma; J\Omega(JI_1)F_1(F_1I_2)F \right\rangle = A\Lambda\Sigma \tag{3.13}$$

Matrix elements for spin-spin interaction, $\hat{\mathrm{H}}^{\text{Spin-spin}}$:

$$\left\langle \eta\Lambda; S\Sigma; J\Omega(JI_1)F_1(F_1I_2)F \left| \hat{\mathrm{H}}^{\text{Spin-spin}} \right| \eta\Lambda; S\Sigma; J\Omega(JI_1)F_1(F_1I_2)F \right\rangle = \frac{2}{3}\lambda[3\Sigma^2 - S(S+1)]$$

(3.14)

Matrix elements for spin-rotation interaction, $\hat{\mathrm{H}}^{\text{Spin-rot}}$:

$$\left\langle \eta\lambda; S\Sigma'; J\Omega'(JI_1)F_1(F_1I_2)F \left| \hat{\mathrm{H}}^{\text{Spin-rot}} \right| \eta\Lambda; S\Sigma; J\Omega(JI_1)F_1(F_1I_2)F \right\rangle$$

$$= \gamma \left\{ \begin{array}{l} \delta_{\Sigma'\Sigma}\delta_{\Omega'\Omega} \times [\Sigma^2 - S(S+1) -] + \sum_{q=\pm 1} (-1)^{J-\Omega'+S-\Sigma'} \begin{pmatrix} J & 1 & J \\ -\Omega' & q & \Omega \end{pmatrix}^2 \begin{pmatrix} S & 1 & S \\ -\Sigma' & q & \Sigma \end{pmatrix}^2 \\ \times \sqrt{J(J+1)(2J+1)S(S+1)(2S+1)} \end{array} \right\} \tag{3.15}$$

Matrix elements for Λ-doubling, $\hat{\mathrm{H}}^{\mathrm{LD}}$:

$$\left\langle \eta\Lambda; S\Sigma'; J\Omega'(JI_1)F_1(F_1I_2)F \left| \hat{\mathrm{H}}^{\mathrm{LD}} \right| \eta\Lambda; S\Sigma; J\Omega(JI_1)F_1(F_1I_2)F \right\rangle$$

$$= \sum_{q=\pm 1} \delta_{\Lambda', \Lambda \mp 2} \left\{ \begin{array}{l} \delta_{\Omega'\Omega}(o+p+q) \sum_{\Sigma''} (-1)^{S-\Sigma'} \begin{pmatrix} S & 1 & S \\ -\Sigma' & q & \Sigma'' \end{pmatrix} \\ (-1)^{S-\Sigma''} \begin{pmatrix} S & 1 & S \\ -\Sigma'' & q & \Sigma \end{pmatrix} \times [(S(S+1)(2S+1)] \\ +(p+2q)(-1)^{J-\Omega'} \begin{pmatrix} J & 1 & J \\ -\Omega' & -q & \Omega \end{pmatrix} \\ (-1)^{S-\Sigma'} \begin{pmatrix} S & 1 & S \\ -\Sigma' & q & \Sigma \end{pmatrix} \times \sqrt{[(J(J+1)(2J+1)S(S+1)(2S+1)]} \\ \delta_{\Sigma'\Sigma} q \sum_{\Omega''} (-1)^{J-\Omega'} \begin{pmatrix} J & 1 & J \\ -\Omega' & -q & \Omega'' \end{pmatrix} (-1)^{J-\Omega''} \\ \times \begin{pmatrix} J & 1 & J \\ -\Omega'' & -q & \Omega \end{pmatrix} [J(J+1)(2J+1)] \end{array} \right\} \tag{3.16}$$

Matrix elements for magnetic hyperfine interaction, $\hat{\mathrm{H}}^{\mathrm{hfs}}$:

$$
\begin{aligned}
&\left\langle \eta\Lambda; S\Sigma'; J\Omega'(JI_1)F_1(F_1I_2)F \left| \hat{\mathrm{H}}^{\mathrm{hfs}} \right| \eta\Lambda; S\Sigma; J\Omega(JI_1)F_1(F_1I_2)F \right\rangle = \delta_{\Lambda'\Lambda} \\
&\left\{ \begin{array}{l}
(-1)^{J'+I_1+I_2+2F_1+F+1}\sqrt{I_2(I_2+1)(2I_2+1)(2F_2'+1)(2F_1+1)} \\
\times\sqrt{(2J'+1)(2J+1)} \begin{Bmatrix} F & I_2 & F_1 \\ 1 & F_1 & I_2 \end{Bmatrix} \begin{Bmatrix} I_1 & J' & F_1' \\ 1 & F_1 & J \end{Bmatrix} \sum_q (-1)^{J'-\Omega'} \begin{pmatrix} J' & 1 & J \\ -\Omega' & q & \Omega \end{pmatrix} \\
\times[a\Lambda\delta_{\Sigma\Sigma'}\delta_{\Omega\Omega'} + b_F(-1)^{S-\Sigma'} \begin{pmatrix} S & 1 & S \\ -\Sigma' & q & \Sigma \end{pmatrix} \times \sqrt{S(S+1)(2S+1)} \\
+ \dfrac{\sqrt{30}}{3} c(-1)^q (-1)^{S-\Sigma'} \begin{pmatrix} S & 1 & S \\ -\Sigma' & q & \Sigma \end{pmatrix} \begin{pmatrix} 1 & 2 & 1 \\ -q & 0 & q \end{pmatrix} \sqrt{(S(S+1)(2S+1)]}
\end{array} \right\} \\
&-d\sum_{q=\pm1} \delta_{\Lambda',\Lambda\mp2}(-1)^{J+I_1+I_2+2F_1+F+1}\sqrt{I_2(I_2+1)(2I_2+1)(2F_1'+1)(F_1+1)} \\
&\times\sqrt{(2J'+1)(2J+1)} \begin{Bmatrix} F & I_2 & F_1 \\ 1 & F_1 & I_2 \end{Bmatrix} \begin{Bmatrix} I_1 & J' & F_1' \\ 1 & F_1 & J \end{Bmatrix} (-1)^{J'-\Omega'} \\
&\times \begin{pmatrix} J' & 1 & J \\ -\Omega' & -q & \Omega \end{pmatrix} (-1)^{q+S-\Sigma'} \begin{pmatrix} S & 1 & S \\ -\Sigma' & q & \Sigma \end{pmatrix} \sqrt{(S(S+1)(2S+1)}
\end{aligned}
\tag{3.17}
$$

Matrix elements for quadrupole interaction, $\hat{\mathrm{H}}^{\mathrm{eq}}$:

$$
\begin{aligned}
&\left\langle \left\langle \eta\lambda; S\Sigma'; J\Omega'(JI_1)F_1'(F_1'I_2)F \right| \left| \hat{\mathrm{H}}^{\mathrm{eq}} \right| \eta\lambda; S\Sigma; J\Omega(JI_1)F_1(F_1I_2)F \right\rangle \\
&= \delta_{\Lambda\Lambda'}\delta_{\Omega'\Omega}(-1)^{J+I_1+I_2+2F_1'+F+1} \begin{Bmatrix} F & I_2 & F_1 \\ 2 & F_1 & I_2 \end{Bmatrix} \begin{Bmatrix} I_1 & J' & F_1' \\ 2 & F_1' & J \end{Bmatrix} \\
&\times\sqrt{(2J'+1)(2J+1)}\,\frac{eQq_0}{4}(-1)^{J'-\Omega} \begin{pmatrix} J' & 2 & J \\ -\Omega & 0 & \Omega \end{pmatrix} \begin{pmatrix} I_2 & 2 & I_2 \\ -I_2 & 0 & I_2 \end{pmatrix}^{-1}
\end{aligned}
$$

Matrix element for electric dipole transition moment

$$\left\langle \eta'\Lambda'S\Sigma'J'\Omega'IF'M_F'\left|T_p^1(\mu)\right|\eta\Lambda S\Sigma J\Omega IFM_F\right\rangle$$
$$=(-1)^{F'-M_F'}\begin{pmatrix} F' & 1 & F \\ M_F' & p & M_F \end{pmatrix}\left\langle \eta'\Lambda'S\Sigma'J'\Omega'IF'\left\|T^1(\mu)\right\|\eta\Lambda S\Sigma J\Omega IF\right\rangle$$
$$=(-1)^{F'-M_F'}\begin{pmatrix} F' & 1 & F \\ M_F' & p & M_F \end{pmatrix}$$
$$\times\delta_{\Sigma'\Sigma}(-1)^{J'+I+F+1}\begin{Bmatrix} I & J' & F' \\ 1 & F & J \end{Bmatrix}[(2F'+1)(2F+1)]^{1/2}$$
$$\times\sum_q(-1)^{J'-\Omega'}\begin{pmatrix} J' & 1 & J \\ -\Omega & q & \Omega \end{pmatrix}[(2J'+1)(2J+1)]^{1/2}\left\langle \eta'\Lambda'\left|T_p^1(\mu)\right|\eta\Lambda\right\rangle \quad (3.18)$$

3.3. Insights about the concepts of the strength, polarity of a chemical bond (Stark effect) and the number of unpaired electrons (Zeeman effect).

3.3.1. Stark effect

The Stark effect reflects the interaction of molecule when exposure to an external electric field. The Stark spectra shows the shifts and/or splittings of the spectral lines of atoms or molecules due to the molecular nature bonding. The interaction of the molecule with the static electric field can be modeled using the conventional Stark Hamiltonian:

$$\hat{H}^{Stark}=-\hat{\mu}\cdot\hat{E}$$

where $\hat{E}$ is the external electric field, and $\hat{\mu}$ is the electric dipole moment operator of the molecule. The expectation value of a dipole moment is a total sum of single electron operators $\mu_{el}=\sum_i e\vec{r}_i$

$$\mu_{el}=\left\langle \Phi\left|\sum_i e\vec{r}_i\right|\Phi\right\rangle$$

In the linear metal containing molecules, there is usually have spin- spin and spin- orbit interactions that are much larger than the spacing between the lowest rotational energies.

In this case the electronic spin angular momenta are quantized in the molecule fixed axis system and case $a_{\beta J}$ basis set was used. Following is the matrix elements for Stark shift, $\hat{H}^{Stark}$:

$$\begin{aligned}
&\left\langle \eta\Lambda';S\Sigma';J\Omega'(JI_1)F_1(F_1I_2)FM_F \left| \hat{H}^{Stark} \right| \eta\Lambda;S\Sigma;J\Omega(JI_1)F_1(F_1I_2)FM_F \right\rangle \\
&= \mu E_z \delta_{SS'}\delta_{\Sigma\Sigma'} \sum_{pq} (-1)^{F'-M_{F'}} \begin{pmatrix} F' & 1 & F \\ -M_F' & 0 & M_F \end{pmatrix} (-1)^p (-1)^{F+F_1'+1+I_2} \\
&\times \sqrt{(2F+1)(2F'+1)} \begin{Bmatrix} I_2 & F_1' & F \\ 1 & F & F_1 \end{Bmatrix} (-1)^{F_1+J'+1+I_1} \sqrt{(2F_1+1)(2F_1'+1)} \\
&\times \begin{Bmatrix} I_1 & J' & F_{11}' \\ 1 & F & J' \end{Bmatrix} (-1)^{J'-\Omega'} \sqrt{(2J+1)(2J'+1)} \begin{pmatrix} J' & 1 & J \\ -\Omega' & q & \Omega \end{pmatrix}
\end{aligned} \tag{3.19}$$

where q=0 for parallel polarization, and q=±1 for perpendicular polarization.

For open-shell metal-containing molecules, each rotational level often exists as a degenerate pair, which differs by the sign of Ω. Accordingly, the Stark shifts were modeled using the expression given by degenerate perturbation theory, following from the equation 3.19 with $|\Psi\rangle = |\Psi'\rangle$ then

$$\Delta E(\text{MHz}) = \frac{\mu(\text{D})\vec{E}(\text{V/cm})M_J\Omega}{J(J+1)}.50348 \tag{3.20}$$

3.3.2. Zeeman effect

The effective Zeeman Hamiltonian operator was taken as[3]:

$$\begin{aligned}
&H_{eff}^{Zee} = g_S \mu_B \hat{\mathbf{S}} \cdot \hat{\mathbf{B}} + g_L' \mu_B \hat{\mathbf{L}} \cdot \hat{\mathbf{B}} + \\
&g_l \mu_B (\hat{S}_x \hat{B}_x + \hat{S}_y \hat{B}_y) + g_l' \mu_B (e^{-2i\phi} \hat{S}_+ \hat{B}_+ + e^{+2i\phi} \hat{S}_- \hat{B}_-)
\end{aligned} \tag{3.21}$$

where $\hat{S}_x$ and $\hat{B}_x$ refer to the x-axis molecule-fixed components of the electronic spin angular momentum and magnetic field, respectively, and ϕ is the azimuthal angle of the electronic coordinates. Analysis of the Zeeman high-resolution spectra were performed by fitting the measured transition wavenumbers to those predicted by determine the energy

levels and the appropriate difference in energies for the electronic states. The small contributions from the rotational and nuclear spin magnetic moments have been ignored. Modeling the Zeeman effect in a $^2\Sigma^+$ state requires varying g_l, and possibly g_S (i.e. $A_2\Pi$), while modeling the Zeeman effect in a state with non-zero orbital angular momentum requires varying g'_L, g_l, g'_l, and possibly g_S. The four electronic spin g-factor, g_S, and the orbital g-factor, g'_L, of the effective Hamiltonian are variables accounting for the interaction between the ground and excited states, $\tilde{X}^{\,2}\Sigma^+$, $\tilde{A}^{\,2}\Pi_r$ and $\tilde{B}^{\,2}\Sigma^+$ states. In the case of a "free" electron, $g_S \approx 2.0023$ and $g'_L \approx 1.00$.

Matrix elements for Zeeman shift, $\hat{H}^{\text{Zeeman}}$:

$$\begin{aligned}
&\left\langle \eta\lambda; S\Sigma'; J\Omega'(JI_1)F_1'(F_1I_2)F'M_{F'} \middle| \hat{H}^{\text{Zeeman}} \middle| \eta\lambda; S\Sigma; J\Omega(JI_1)F_1(F_1I_2)FM_F \right\rangle \\
&= \delta_{\eta\eta'}\mu_B B_z (-1)^{F'-M_{F'}} \times \begin{pmatrix} F' & 1 & F \\ -M_F' & 0 & M_F \end{pmatrix} (-1)^{F+F_1'+1+I_2} \sqrt{(2F+1)(2F'+1)} \\
&\begin{Bmatrix} F_1 & F & I_2 \\ -F' & F_1' & 1 \end{Bmatrix} (-1)^{F_1+J'+1+I_1} \sqrt{(2F_1+1)(2F_1'+1)} \begin{Bmatrix} J & F_1 & I_1 \\ F_1' & J' & 1 \end{Bmatrix} \sum_q (-1)^{J'-\Omega'} \begin{pmatrix} J' & 1 & J \\ \Omega' & q & \Omega \end{pmatrix} \\
&\times \sqrt{(2J'+1)(2J+1)} \begin{bmatrix} \delta_{\Lambda,\Lambda'} g_s (-1)^{S-\Sigma'} \begin{pmatrix} S & 1 & S \\ -\Sigma' & q & \Sigma \end{pmatrix} \sqrt{S(S+1)(2S+1)} - \\ \delta_{\Lambda,\Lambda'} g_l \Sigma + \delta_{\Sigma,\Sigma'} g_l (-1)^{L-\Lambda'} \begin{pmatrix} L & 1 & L \\ -\Lambda' & q & \Lambda \end{pmatrix} \sqrt{L(L+1)(2L+1)} \end{bmatrix}
\end{aligned} \tag{3.22}$$

3.4. The Franck-Condon factor of the triatomic molecules

The Franck–Condon principle plays an important role in understanding the nature of optical transitions in molecules and optical spectroscopic processes that take place when a molecule absorbs or emits photons. The principle narrates the interaction between the electronic and vibrational motions assuming that, like the Born–Oppenheimer

approximation, the nuclear masses are much larger than the electronic mass. There is a statement[9-10] that the electronic transitions happen instantaneous, and their timescale is so significantly short as compared with the nuclear motion, so the probability of the transition can be determined with respect to fixed nuclear positions correspond to the electronic states that a molecule populates. The charge redistribution in a molecule after the photon – molecule interaction reflects a change in Coulombic forces on the nuclei and hence makes deviations in the vibrational state of the molecule. While analyzing the vibrational structure of electronic spectra, the picture of intensity distributions has been observed in the spectra of molecules like SrOH and YbOH. In the case of SrOH, first, the (0,0,0–0,0,0) band corresponding to a stretching vibrational transition $v'' = (0,0,0) \rightarrow v' = (0,0,0)$ is found to be most intense and the intensity sharply decreases on moving along the v'−progression ($v'' = 0$, $v' = 0, 1, 2,\ldots$). For instance, ν_1= Sr-OH (stretching), ν_2=Sr-O-H (bending) While on the other hand, the intensity corresponding to the bending vibrational transition ν_2, along the v'−progression ($v'' = 0$, $v' = 1$ was not allowed. These intensity distributions can be explained in terms of the Franck–Condon principle by referring to the shapes of the potential energy curves of the two electronic states and the position of their potential energy minima.

By definition, the Franck- Condon factor is the square of the overlap integral between two electronic states. The method for calculating the FCFs for one dimensional harmonic oscillator is well understood. Still, for polyatomic molecules, the multidimensional oscillators involving Duschinsky effects (which will be described in Chapter 6) makes the FCFs calculations much more difficult in comparison with those for the one-dimensional problem. In case of SrOH molecule, the FCFs problem separates into

two problems: a two dimension bending modes and a 1-dimensional problem for the stretching vibrational mode:

$$\mathrm{FCF} = \left|\left\langle \upsilon_1' \upsilon_3' \middle| 00 \right\rangle\right|^2 \left|\left\langle \upsilon_2' \middle| 0 \right\rangle\right|^2 . \quad (3.23)$$

The vibrational overlap integral between vibronic levels $|00\rangle$ and $|\upsilon_1'\upsilon_1'\rangle$ given by:

$$\left\langle \upsilon_1' \upsilon_1' \middle| 00 \right\rangle = \mathrm{N}' \int_{-\infty}^{\infty}\int_{-\infty}^{\infty} \mathrm{H}_{\upsilon_1(\tilde{A}^1B_2)} \sqrt{\alpha_1(\tilde{A}^1B_2)} Q_1(\tilde{A}^1B_2) \mathrm{H}_{\upsilon_2(\tilde{A}^1B_2)} \sqrt{\alpha_2(\tilde{A}^1B_2)} Q_2(\tilde{A}^1B_2)$$
$$\exp(-\frac{1}{2}\alpha_1(\tilde{A}^1B_2)Q_1(\tilde{A}^1B_2) - \frac{1}{2}\alpha_2(\tilde{A}^1B_2)Q_2(\tilde{A}^1B_2)$$
$$-\frac{1}{2}\alpha_1(\tilde{X}^1A)Q_1(\tilde{X}^1A)^2 - \frac{1}{2}\alpha_2(\tilde{X}^1A)Q_2(\tilde{X}^1A)^2) dQ_1(\tilde{A}^1B_2) dQ_2(\tilde{A}^1B_2) \quad ,(3.24)$$

where $N' = \frac{1}{\pi} \frac{\sqrt{\alpha_1(\tilde{A}^1B_2)\alpha_2(\tilde{A}^1B_2)\alpha_1'(\tilde{X}^1A)\alpha_2'(\tilde{X}^1A)}}{2^{\upsilon_1(\tilde{A}^1B_2)+\upsilon_2(\tilde{A}^1B_2)}\upsilon_1(\tilde{A}^1B_2)!\upsilon_2(\tilde{A}^1B_2)!}$ (3.19) and $\alpha_i = \frac{\omega_i}{\hbar}$ (3.25)

In equation 3.24, H_{υ_i} is the Hermite polynomial, **Q1** and **Q2** are the normal coordinates. Equation 3.24 shows that the vibrational overlap integral are related to the normal coordinates of the interested excited state **Q**($\tilde{A}^1B_2$) and the normal coordinates of ground state **Q**($\tilde{X}^1A_1$).

3.5. References

1. Herzberg, G., Molecular spectra and molecular structure. Vol. 1: Spectra of diatomic molecules. *New York: Van Nostrand Reinhold, 1950, 2nd ed.* **1950**.

2. Kovács, I.; Nemes, L., *Rotational structure in the spectra of diatomic molecules*. Hilger London: 1969.

3. Brown, J. M.; Carrington, A., *Rotational spectroscopy of diatomic molecules*. Cambridge University Press: 2003.

4. Lefebvre-Brion, H.; Field, R. W., *The Spectra and Dynamics of Diatomic Molecules: Revised and Enlarged Edition*. Elsevier: 2004.

5. Bunker, P. R.; Jensen, P., *Molecular symmetry and spectroscopy*. NRC Research Press: 2006.

6. Townes, C. H.; Schawlow, A. L., *Microwave spectroscopy*. Courier Corporation: 2013.

7. Sauer, B. E.; Cahn, S. B.; Kozlov, M. G.; Redgrave, G. D.; Hinds, E. A., Perturbed hyperfine doubling in the A2Π1/2 and [18.6]0.5 states of YbF. *The Journal of Chemical Physics* **1999,** *110* (17), 8424-8428.

8. Brown, J. M.; Cheung, A. S. C.; Merer, A. J., Λ-Type doubling parameters for molecules in Δ electronic states. *J. Mol. Spectrosc.* **1987,** *124* (2), 464-75.

9. Condon, E. U., Nuclear Motions Associated with Electron Transitions in Diatomic Molecules. *Physical Review* **1928,** *32* (6), 858-872.

10. Franck, J.; Dymond, E. G., Elementary processes of photochemical reactions. *Transactions of the Faraday Society* **1926,** *21* (February), 536-542.

CHAPTER 4

THE [18.6]-$X^2\Sigma^+$ AND [18.7]- $X^2\Sigma^+$ BANDS OF EVEN ISOTOPE YTTERBIUM FLUORIDE,^{174}YBF

4.1. Introduction

The ytterbium fluoride, YbF, is important and attracts particular interests for fundamental physics since it is used to measure the electron's electric dipole moment (eEDM)[1-2]. These experiments do not only explore the probe of high energy scales via eEDM, test the Standard Model of particle physics, such as supersymmetric theories, but also provide a probe for new sources of the violation of charge conjugation parity symmetry that could explain the observed matter-antimatter asymmetry in the Universe[1]. The precision of the eEDM measurement could be greatly enhanced by producing a slow and cooled molecule beam and temperatures under micro-kelvin levels, and that seems achievable using laser cooling which has recently been successfully performed on several diatomic species[3-6] and even to polyatomic molecules[7]. For instance, SrF and CaF diatomic molecules have been kept in magneto-optical traps[8-10] and temperatures as low as 50 micro-kelvin[10]. Because the electronic structure of YbF resembles that of SrF and CaF, it is proposed as a candidate for laser cooling. A recent studying of ^{174}YbF[11] measuring the lifetime and Franck-Condon factor of $A^2\Pi_{1/2} - X^2\Sigma^+$ transition has proved the possibility of making the Magneto- Optical Trap (MOT) from this molecule. Also, an experiment to measure the eEDM using laser-cooled YbF molecules has been proposed[12] and is now being built at Imperial college with our collaborators.

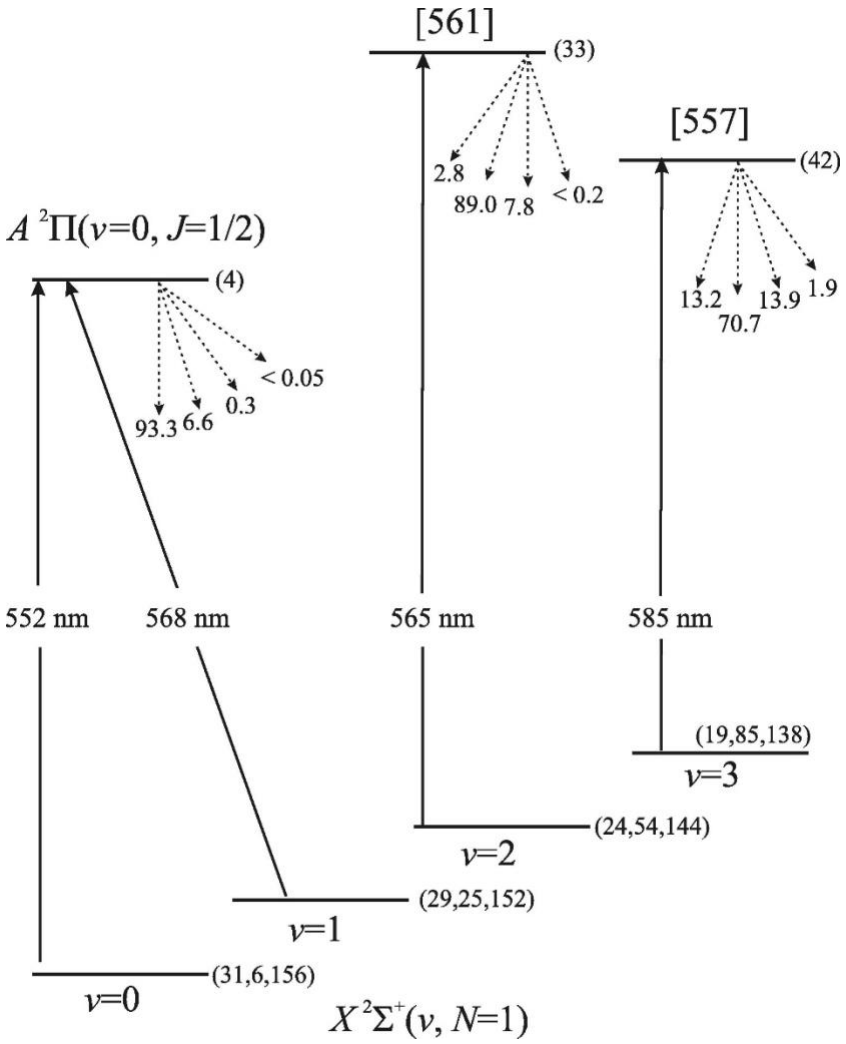

Figure 4.1. The transitions involved in the proposed laser cooling scheme. The relevant branching ratios for the decays of the excited states to v=0,1,2,3 are shown (from left to right).

In Figure 4.1, those branching ratios are taken from references[13] and [11], and they sum to 100% within their quoted uncertainties. The main cooling transition is the $A^2\Pi_{1/2}$(v=0, J=1/2) – $X^2\Sigma^+$(v=0, N=1) transition at 552 nm. Additional lasers are used to "repump" population that decays to the $X^2\Sigma^+$(v=1,2,3) states back into the cooling cycle. Each laser must address the four hyperfine components of the lower level. The numbers in

parentheses are the separations in MHz between the closely spaced hyperfine levels (see Figure 4.2).

Figure 4.1 shows the transitions involved in the interested laser cooling experiment. This experiment is done in collaboration with Imperial College, UK. The corresponding branching ratios for the decays of the excited states have been measured previously and annotated in the above figure[13]. The focal cooling transition is the $A^2\Pi_{1/2}(v=0, J=1/2) - X^2\Sigma^+(v=0, N=1)$ transition at 552 nm. Additional lasers are used to "repump" molecules that relaxed to the various vibrational levels (v=1,2,3) of the ground state $X^2\Sigma^+$ back into the cooling cycle. The two states labelled [18.6] and [18.7], which are admixtures of the $A^2\Pi_{1/2}(v=1)$ state and a perturbing state with $|\Omega| = 1/2$, are the targets to repump YbF molecules from v=2 and v=3 levels ; they could be referred to as the [18.6]0.5 and [18.7]0.5 states[14-15] . These levels from the two states reside at 474 cm^{-1} and 599 cm^{-1} above the $A^2\Pi_{1/2}$ (v=0) state[15]. Those two states are corresponding to the energies of 18574 cm^{-1} (557 THz) and 18699 cm^{-1} (561 THz). The repump transitions lie in congested regions of the spectrum of YbF. Three required tasks to perform laser cooling are (i) locating these repump transitions, (ii) knowing precisely the transition frequencies, and (iii) determining the hyperfine structure of the transition so that appropriate sidebands can be added to the lasers to address each hyperfine component. Because of both the importance of knowing spectroscopic parameters of the two states, the [18.6] and [18.7] excited states and lacking knowledge about the $X^2\Sigma^+(v=2,3)$ ground states or, none of these tasks have been precisely performed. Optical studies the [18.6] – $X^2\Sigma^+(v = 0,1,2,3)$ and [18.7] – $X^2\Sigma^+$ (v =2) bands of ^{174}YbF were studied as a contribution toward the laser cooling work.

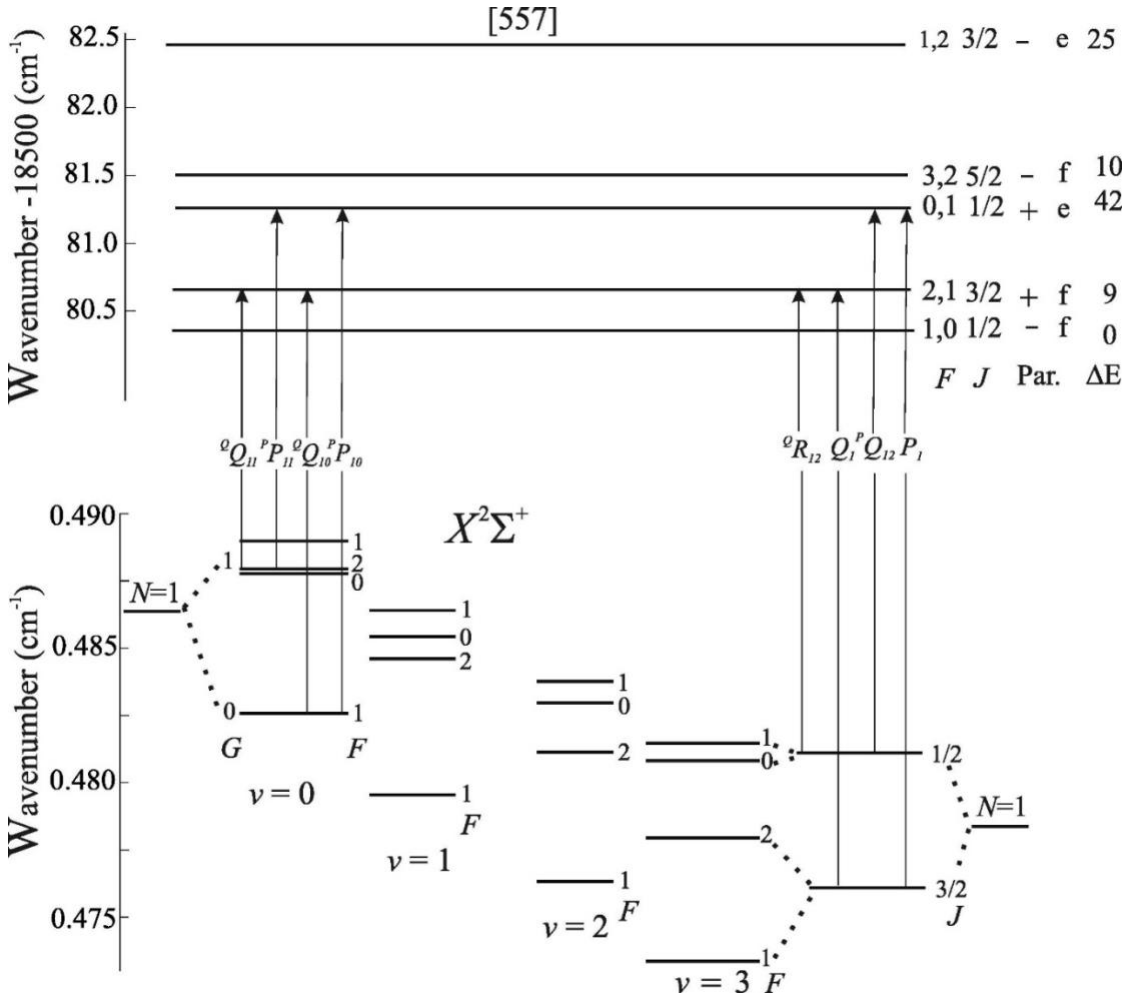

Figure 4.2. The energy level pattern for the N=1 level of the $X^2\Sigma^+$ (v = 0, 1, 2, and 3) states and the low J levels of the [18.7] state.

In Figure 4.2, the energies of the $X^2\Sigma^+$ (v = 1, 2, and 3) levels have been shifted such that the lowest levels (i.e., the N=0, G=0, F=0 levels) coincide. ΔE is the predicted magnetic hyperfine splitting in the [18.6] state, the unit is in MHz. The hyperfine splittings in the $X^2\Sigma^+$ levels are (in MHz): (v = 0)→31,6,156. (v = 1)→29,25,152, (v = 2)→24,54,144, (v = 3)→19,85,138.

Relevant spectroscopic studies of YbF prior to 2009 are summarized in the previous study performed in our lab focusing on the optical Zeeman tuning of the (0,0) $A^2\Pi_{1/2} - X^2\Sigma^+$ band[16] and in the more recent microwave and optical spectroscopic study of

the ^{171}YbF isotopologue[17]. Because of the importance of YbF as a venue for fundamental physics, there have been three recent papers devoted to study high-level, relativistic, electronic structure of the $X^2\Sigma^+$ state[18-20]. Although the (0,0) $A^2\Pi_{1/2} - X^2\Sigma^+$ (ν~18100 cm^{-1}) band has been well investigated, the two [18.6] – $X^2\Sigma^+(v=2)$ and [18.7] – $X^2\Sigma^+(v=2)$ bands are much less studied. Dunflield and coworkers[14] have studied the [18.6] and [18.7] states by the Doppler-limited excitation spectroscopy employing laser induced fluorescence (LIF) detection of a high temperature source and the fine structure parameters were determined. This data is not particularly useful for the project from Imperial University because it did not probe the low rotational levels. The LIF spectroscopy of a well collimated molecular beam from a high-temperature Broida oven with a mixture of Yb metal and AlF_3 was analyzed to produce magnetic hyperfine parameters for the ^{174}YbF isotopologue[15]. The assignment of the very complicated LIF spectrum of the high temperature source was done by taking advantage of the previously measured laser–radio frequency double resonance (LRDR) spectrum[21]. The values of $A_{||}$ and $A_{\perp}$ ^{19}F-magnetic hyperfine parameters the [18.6] and [18.7] states were determined, they were 63.3±3 MHz and -31.9±1 MHz, 48.8 ±3 MHz and -24.7±1 MHz, correspondingly. The ground state $X^2\Sigma^+(v=0$ and 1) of ^{174}YbF have been well studied from the investigation of Sauer et al.[21] and more recently through the Fourier transform microwave (FTMW) spectrum[22]. Additionally, there is no previous spectroscopic studies focusing on vibrational levels of the $X^2\Sigma^+$ state beyond v=2.

4.2. Observation

Yb atom has numerous isotopes: ^{170}Yb, ^{171}Yb, ^{172}Yb, ^{173}Yb, ^{174}Yb, and ^{176}Yb with a relative abundance of 0.035, 0.143, 0.219, 0.161, 0.318 and 0.127, respectively, thus the observed optical spectra are complicated because of the overlap of transitions from all isotopes. Furthermore, the odd Yb isotopologue spectra reveal a very large magnetic hyperfine splitting. This chapter focuses on assigning and analyzing spectral features from transitions of the ^{174}YbF spectra. The previous works[11, 13-16, 21-25] has devoted on describing to some extent the energy levels and resulting optical spectra, for both the [18.6]-$X^2\Sigma^+$(v=0-3) and [18.7]-$X^2\Sigma^+$(v=2) bands. The energy level pattern for the N=1 levels of the $X^2\Sigma^+$ (v = 0, 1, 2, and 3) states and the J=1/2-5/2 levels of the [18.6] state are presented in Figure 4.2. Also indicated are the allowed transitions and branch terms. The energies of the $X^2\Sigma^+$ (v = 1, 2, and 3) levels presented in Figure 4.2 have been shifted such that the lowest levels in these vibronic states (i.e. the N=0, G=0, F=0 level) agree with the lowest level of the $X^2\Sigma^+$ (v = 0) state. The predicted hyperfine intervals in the [18.6] state was also given in the same figure.

As Dunfield has pointed out in the analysis of the [18.6]-$X^2\Sigma^+$(v=0,1) and [18.7]-$X^2\Sigma^+$(v=0,1) bands[14], the branch ordering is uncommon since the observed Λ-doubling parameters, p+2q, in the [18.7] and [18.6] states are larger than two times of the rotational parameter, 2B. This makes the $^{Q}Q_{1G}$ + $^{Q}R_{1G}$ (in case $b_{\beta S}$ scheme) or Q_1 and $^{Q}R_{12}$ (in case $b_{\beta J}$ scheme) features to be at lower transition wavenumbers than the corresponding $^{P}P_{1G}$ + $^{P}Q_{1G}$ (case $b_{\beta S}$ scheme) or P_1 and $^{P}Q_{12}$ (case $b_{\beta J}$ scheme) branch features. Therefore, the correct wavenumber ordering of the branch features is $^{O}P_{1G}$ < $^{Q}Q_{1G}$ + $^{Q}R_{1G}$ < $^{P}P_{1G}$ + $^{P}Q_{1G}$

$< {}^{R}R_{1G}$ (based on case $b_{\beta S}$ scheme) or ${}^{O}P_{12} < Q_1$ and ${}^{Q}R_{12} < P_1$ and ${}^{P}Q_{12} < R_1$ (based on case $b_{\beta J}$ scheme). The more usual way is P < Q < R.

A portion of ${}^{Q}Q_{1G} + {}^{Q}R_{1G}$ near the [18.6]-$X^2\Sigma^+(v=0)$ band head and the Q_1 and ${}^{Q}R_{12}$ band near the [18.6]-$X^2\Sigma^+(v=3)$ band head is presented in Figure 4.3 and Figure 4.4, respectively. The observed spectra of both bands are complicated. However, the assignments can be made. It is noteworthy that the prediction of both Figure 4.3 and Figure 4.4 using the line intensities proportional to the magnitude of the transition moment, $I \propto \left|\langle \psi_i | \hat{\mu} | \psi_f \rangle\right|$, gives better agreement with the experimental data then the usual assumption of $I \propto \left|\langle \psi_i | \hat{\mu} | \psi_f \rangle\right|^2$. A FWHM of approximately 20 MHz, which is slightly smaller than the observed linewidth, is used to demonstrate the combined spectral features.

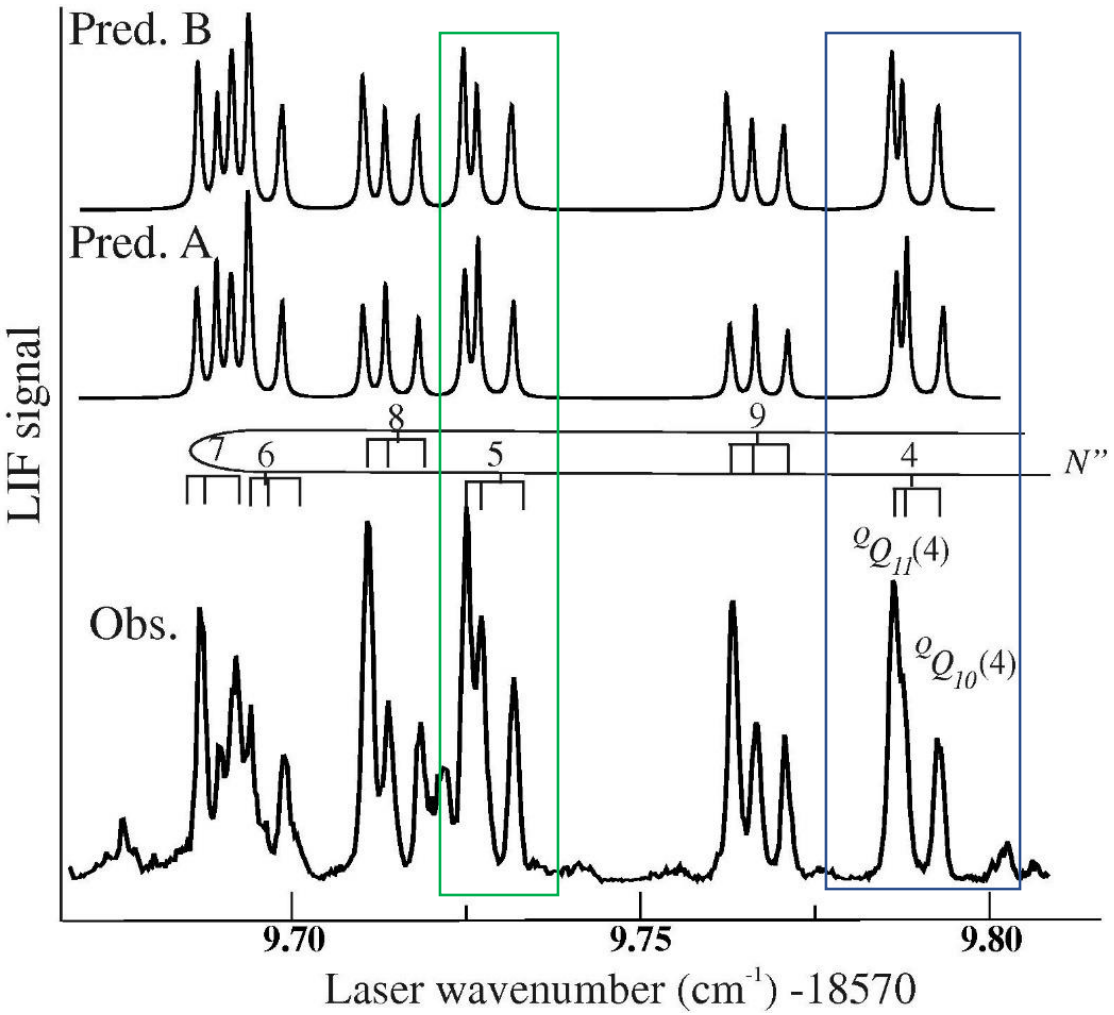

Figure 4.3. A portion of the [18.6]-$X^2\Sigma^+$(v=0) LIF spectrum near the $^{Q}Q_{1G}$ + $^{Q}R_{1G}$ band head.

In the Figure 4.3, the predicted spectra were obtained using the optimized parameters of Table 4.1 and Table 4.2. Prediction A was obtained assuming a square dependence on the transition moment. Prediction B used the magnitude of the transition moment and more closely reproduces the observation because it partially accounts for saturation.

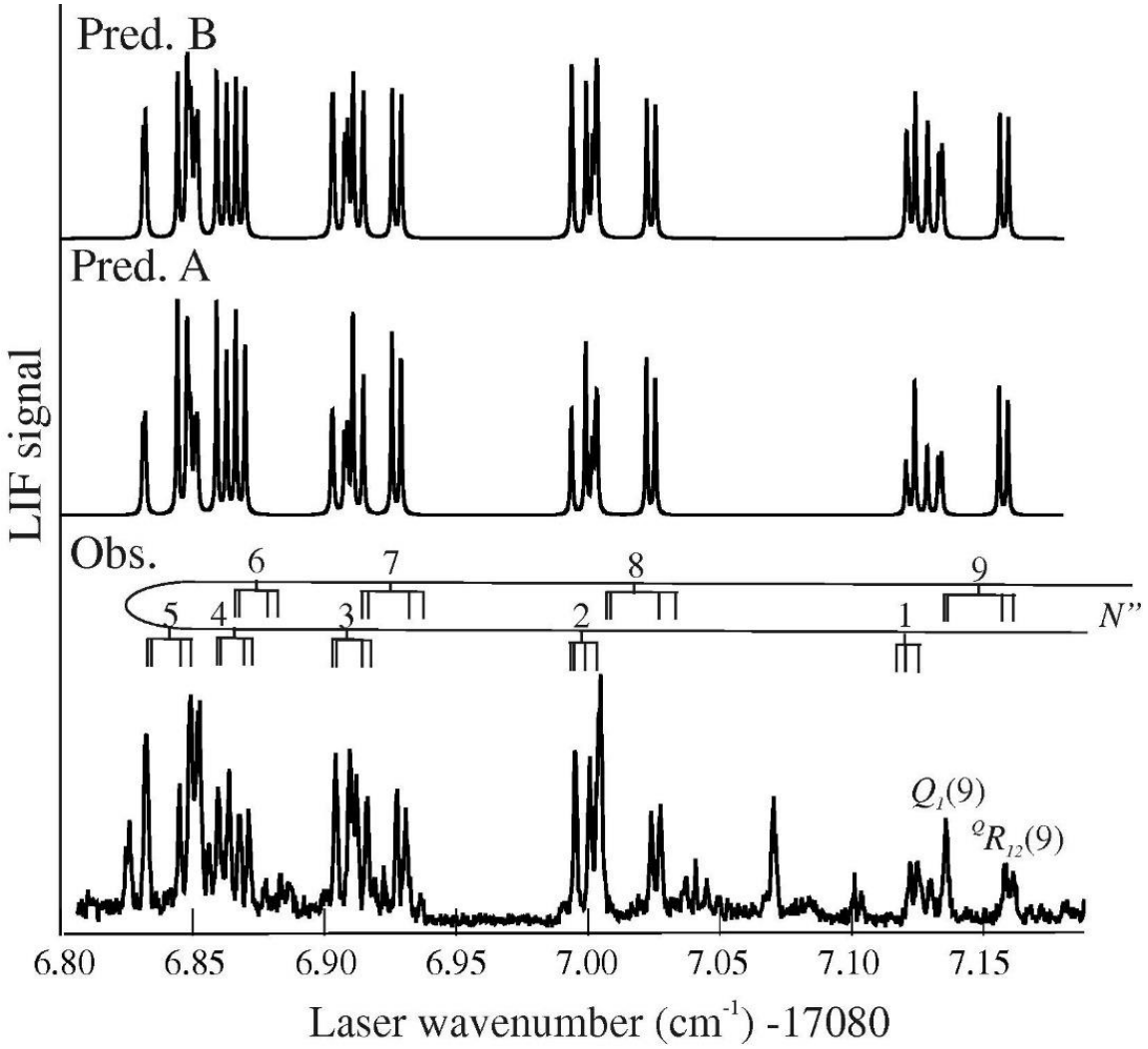

Figure 4.4. A portion of the [18.6]-$X^2\Sigma^+$(v=3) LIF spectrum near the Q_1 and $^{Q}R_{12}$ band head.

In Figure 4.4, the Q_1 and $^{Q}R_{12}$ branch features are to the lower transition wavenumber than the P_1 and $^{P}Q_{12}$ features because of the unusually large Λ-doubling in the [18.6] state. The predicted spectra were obtained using the optimized parameters of Table 4.1and Table 4.2. Prediction A was obtained assuming the expected square dependence on the transition moment. Prediction B used the magnitude of the transition moment and more closely reproduces the observation because it partially accounts for saturation.

One of the objectives of the current study was to model the hyperfine interaction in the [18.6] and [18.7] states. There are two hyperfine parameters, $h_{1/2}$ and d which effect this splitting. Figure 4.3 presents the ${}^{Q}Q_{1G} + {}^{Q}R_{1G}$ (4) branch feature of the [18.6]-$X^2\Sigma^+(v=0)$ band. This branch feature is composed of partially resolved lines for the ${}^{Q}Q_{11} + {}^{Q}R_{11}$ (4) transitions and a single feature to higher wavenumber for the ${}^{Q}Q_{10} + {}^{Q}R_{10}$ (4) transition. A long with N'' increases, the ${}^{Q}Q_{11} + {}^{Q}R_{11}$ (N) group of lines tear apart and separate into two features. At the same time, the $X^2\Sigma^+(v=0)$ state energy level pattern begins to change from the case $b_{\beta S}$ limit to a case $b_{\beta J}$ limit. The splitting between the ${}^{Q}Q_{11} + {}^{Q}R_{11}$ (N) and ${}^{Q}Q_{10} + {}^{Q}R_{10}$ (N) features stay almost constant (estimated $\Delta\nu \sim 170$ MHz = b_F), as expected for a $\Pi_{1/2}$ (case $a_{\beta J}$) - $^2\Sigma^+$ (case $b_{\beta S}$) band. However in the experimental spectrum of the [18.6]-$X^2\Sigma^+(v=3)$ bands, in Figure 4.4, shows that the pair of closed spacings in the Q_1(N") features at low N'' the separation of which increases approximately linearly with increasing N'', as it agrees with the assumption of a $^2\Pi_{1/2}$ (case $a_{\beta J}$) - $^2\Sigma^+$ (case $b_{\beta J}$) band. The weaker lines of this pair of features are members of the satellite ${}^{Q}R_{12}$ branch and the stronger features belong to the main Q_1 branch.

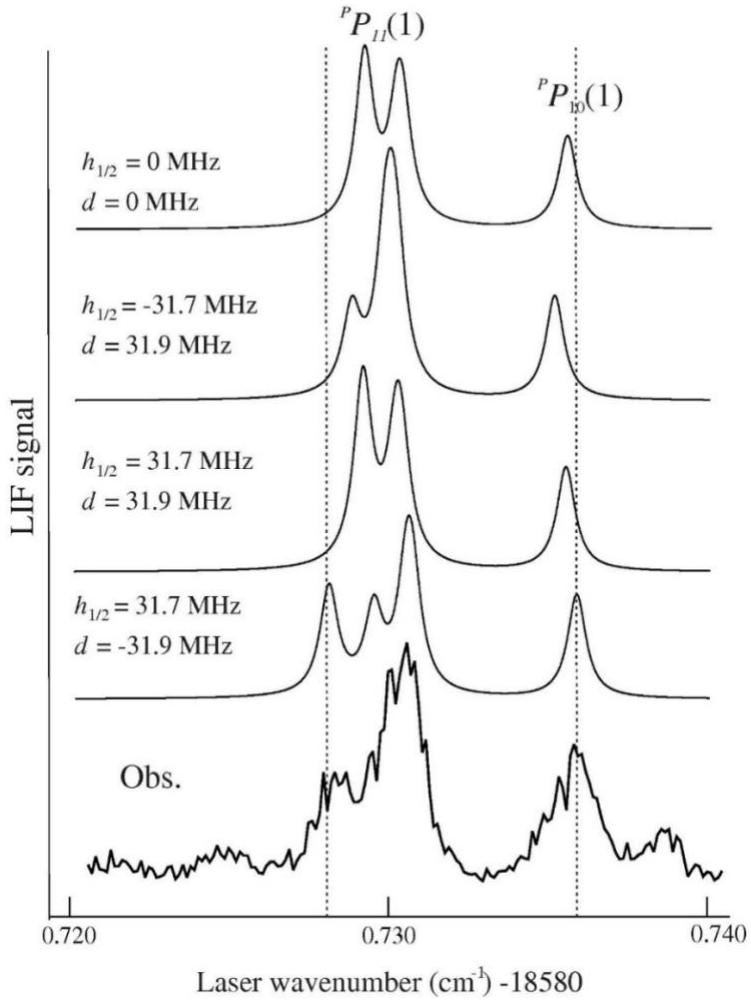

Figure 4.5. High resolution scan of the LIF spectrum in the region of the $^{P}P_{11} + {}^{P}Q_{11}(1)$(ν= 18581.732 cm^{-1}) and $^{P}P_{10} + {}^{P}Q_{10}$ (1) (ν= 18581.737 cm^{-1}) transitions of the [18.6]-$X^2\Sigma^+$(v=0) band along with predicted spectra obtained using the optimized spectroscopic parameters of Table 4.1 and Table 4.2 and various values of the magnetic hyperfine parameters for the [18.6] state. Best agreement is obtained with $h_{1/2}$ = 31.7 MHz and d = -31.9 MHz

The high resolution scans including the $^{P}P_{11} + {}^{P}Q_{11}$ (1) (at ν=18580.732 cm^{-1}) and $^{P}P_{10} + {}^{P}Q_{10}$ (1) (at ν= 18580.737 cm^{-1}) lines of the $X^2\Sigma^+(v=0)$-[18.6] band are presented in Figure 4.5. The upper energy levels of these spectral features correspond to the F = 0 and 1 hyperfine components of the J=1/2, e-component, plus-parity level (as being presented in Figure 4.2). The four upper panels of Figure 4.5 are predicted spectra employing

numerous different values for the excited state magnetic hyperfine parameters. The magnetic hyperfine interaction in the [18.6] state causes a small, moderately resolved, splitting of the ${}^{P}P_{11} + {}^{P}Q_{11}$ (1) transition. The effect can be reproduced using the previously determined magnetic hyperfine parameters of Sauer et al[14] but with the opposite sign of d (=-$A_{\perp}$).

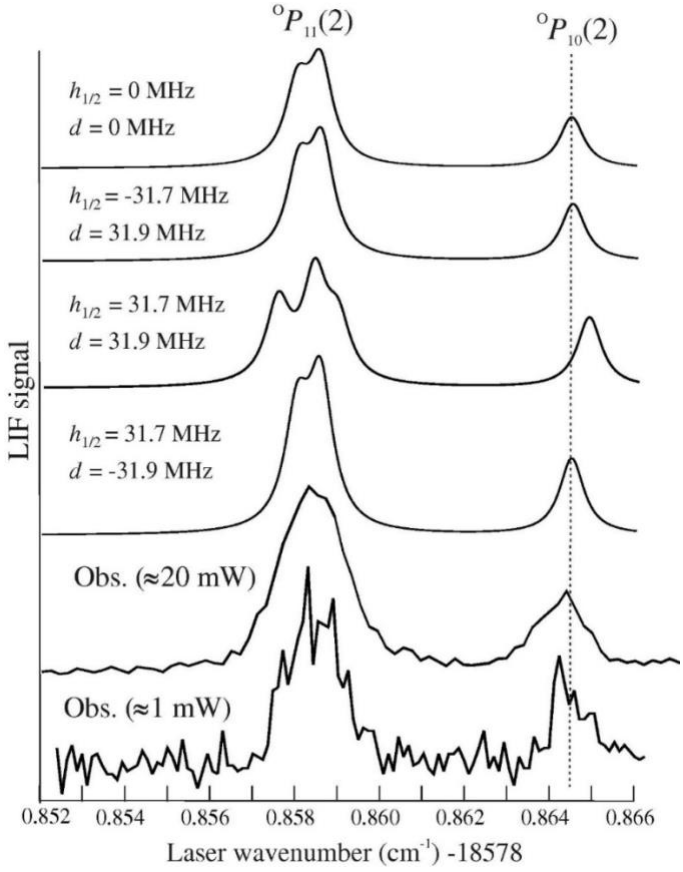

Figure 4.6. The ${}^{O}P_{11}(2)$ (ν= 18578.858 cm^{-1}) and ${}^{O}P_{10}(2)$ (ν= 18578.864 cm^{-1}) transitions of the [18.6]-$X^2\Sigma^+(v=0)$ band recorded at high (~ 20 mW) and low (~ 1 mW) laser power. Also shown are the predicted spectra obtained using the optimized spectroscopic parameters of Table 4.1 and Table 4.2 and various values of the magnetic hyperfine parameters for the [18.6] state.

The high-resolution spectrum of the ${}^{O}P_{11}(2)$ (ν=18578.858 cm^{-1}) and ${}^{O}P_{10}(2)$ (ν= 18578.864 cm^{-1}) lines of the [18.6]-$X^2\Sigma^+(v=0)$ band along with the prediction are presented in Figure 4.6. There is no evidence of the splitting, broadening, or shift due to the magnetic

hyperfine interaction from the interested [18.6] state. The upper energy boundaries of these spectral features belong to the F= 0 and 1 hyperfine components of the J=1/2, f-component, minus-parity level (see Figure 4.2). Similarly, a better match between the observation and the prediction is resulted from applying the value of $A_\perp$ opposite sign. The prediction and high-resolution spectra involving the $R_{11}(0)$ (ν=18582.4214 cm^{-1}) and $R_{10}(0)$ (ν= 18582.434 cm^{-1}) lines of the [18.6]-$X^2\Sigma^+(v=0)$ band are presented in Figure 7. The upper energy levels of these spectral features belong to the F = 1 and 2 hyperfine components of the J=3/2, e-component, minus-parity level (presented in Figure 2). The spectrum is modelled using the earlier determined magnetic hyperfine parameters from Sauer's investigation[15] and agrees well with our observation only if the sign of $A_\perp$ is reversed. In our experimental spectrum, this transition is overlapped by features of the other Yb-isotopologues. While small splittings and shifts for spectral features involving e-levels were observed, there is no evidence of observing the splitting for spectral features involving f-levels of the [18.6] state through our high-resolution scans of various low-rotational branch features of the [18.6]-$X^2\Sigma^+(v=0,1,2,3)$ bands in the condition that the molecules are generated from supersonic expansion sources.

4.3. Analysis

A fit involving total of 78, 53, 57, 71, and 76 precisely assigned and measured transition wavenumbers which were obtained through 92, 57, 67, 85, and 91 transitions for the [18.6]-$X^2\Sigma^+(v=0\text{-}3)$ and [18.7]-$X^2\Sigma^+(v=2)$ bands, respectively, has been performed. Various assignments to a single transition frequency were made in order to make sure that the predicted overlapping features have comparable transition intensities. The assignments

of observed transition wavenumbers, and the difference between the observed and predicted transition wavenumbers for the [18.6]-$X^2\,\Sigma^+(v=0\text{-}3)$ and [18.7]-$X^2\Sigma^+(v=2)$ bands are given in Tables 4.1-4.4.

The five band systems were fit all together. The total input of 392 measured transition wavenumbers attained from Tables 4.1-4 were input to a non-weighted, non-linear, least squares fitting program that output the optimized parameters including the five band origins, B and γ parameters for $X^2\,\Sigma^+$ (v = 2 and 3) states, and B, $(p+2q)$, $(p+2q)_D$, and D for the [18.6] and [18.7] states. The standard deviation of the fit is 16 MHz, which is adequate with the estimated uncertainties. No systematic trends in the residuals are observed. Modeling the spectra significantly based on the assignment of quantum numbers, mostly in the case of the exceedingly overlapped ${}^{Q}Q_{1G}$ and ${}^{P}P_{1G}$ branch features.

Table 4.1. ^{174}YbF spectroscopic parameters (MHz) for the $X^2\Sigma^+$ state determined from the [18.6] – $X^2\Sigma^+(v)$ spectra.

Parameter	$X^2\Sigma^+(v=0)$[a]	$X^2\Sigma^+(v=1)$ [a]	$X^2\Sigma^+(v=2)$	$X^2\Sigma^+(v=3)$
B	7233.8271	7188.8919	7144.20(13) [b]	7099.63 (16)
$10^3\times D$	7.159 [c]	6.904 [c]	6.649[c]	6.394 [c]
γ	-13.41679	-33.81036	-53.89(73)	-74.5(13)
b_F(F)	170.26374(20)	168.770	167.28[d]	165.78 [d]
c(F)	85.4208	86.7120	88.02 [d]	89.33 [d]

[a] All but D constrained to the FTMW values of Ref [22].

[b] The numbers in parentheses represents a 1σ error estimate.

[c] v=0 and v=1 values constrained to the previously values[15] v=2 and 3 values are linear extrapolations.

[d] v=2 and v=3 values constrained to linear extrapolated values of v=0 and 1.

Table 4.2. Determined ^{174}YbF spectroscopic parameters (cm^{-1}) for the [18.6] and [18.7] states.

Parameter	[18.6]		[18.7]	
	Present	Ref. 13	Present	Ref. 13
A^a	1365.2908		1365.2908	
B	0.2547177(76)[b]	0.255305(27)	0.2569399(78)	0.256964(23)
$10^6 \times D$	1.19(7)	0.9670(45)	-0.70(8)	-0.5934(58)
$(p+2q)$	-0.905939(44)	-0.89614(25)	-1.002931(84)	-0.74895(42)[e]
$10^5 \times (p+2q)_D$	9.419(85)	8.265(14)	-9.36(17)	-9.910(30)
$h_{1/2}$(F)[c]	0.001057		0.000814	
d(F)[c]	-0.001064		-0.000824	
$T(v"=0)$[d]	19263.02419(14)		-	
$T(v"=1)$[d]	18760.87329(16)		-	
$T(v"=2)$[d]	18263.21129(14)		-	
$T(v"=3)$[d]	17770.00267(15)		-	
$T(v"=2)$[d]			18387.63723(14)	
	Std. of fit= 0.00054 cm^{-1} =16 MHz			

[a] Spin-orbit parameter, A, held fixed to previously determined (Ref. [13]) value of 1365.2908 cm^{-1}.

[b] The numbers in parentheses represents a 1σ error estimate.

[c] The magnetic hyperfine parameters for the [18.6] and [18.7] states constrained to values from Ref[15] but sign of d altered (see text).

[d] Value of T for the excited state relative to the lowest energy level of $X^2\Sigma^+(v)$ vibronic state.

[e] This value has now been corrected to -1.00964(48) cm^{-1} [33].

Table 4.3 Energies for the $X^2\Sigma^+$ state.

N,*G*,*F*	$X^2\Sigma^+(v=0)$	$X^2\Sigma^+(v=1)$	$X^2\Sigma^+(v=2)$	$X^2\Sigma^+(v=3)$
0,0, 0	0.00000	502.15093	999.81290	1493.02152
0,1, 1	0.00568	502.15653	999.81848	1493.02705
1,0, 1	0.48257	502.63040	1000.28928	1493.49475
1,1, 0	0.48777	502.63628	1000.29590	1493.50217
1,1, 2	0.48795	502.63546	1000.29409	1493.49934
1,1, 1	0.48898	502.63726	1000.29670	1493.50282
2,0, 2	1.44771	503.58939	1001.24207	1494.44130
2,1, 3	1.45285	503.59403	1001.24635	1494.44531
2,1, 1	1.45363	503.59650	1001.25050	1494.45117
2,1, 2	1.45418	503.59661	1001.25032	1494.45078
3,0, 3	2.89541	505.02788	1002.67132	1495.86129
3,1, 4	2.90035	505.03219	1002.67523	1495.86129
3,1, 2	2.90169	505.03591	1002.68129	1495.87255
3,1, 3	2.90197	505.03562	1002.68066	1495.86492
4,0, 4	4.82564	506.94587	1004.57704	1495.87339
4,1, 5	4.83041	506.94992	1004.58068	1497.75475
4,1, 3	4.83225	506.95482	1004.58860	1497.76803
4,1, 4	4.83233	506.95424	1004.58768	1497.75814
5,0, 5	7.23839	509.34335	1006.95925	1497.76915
5,1, 6	7.24300	509.34718	1006.96269	1500.12174
5,1, 5	7.24523	509.35245	1006.97131	1500.12494
5,1, 4	7.24533	509.35325	1006.97244	1500.13716
6,0, 6	10.13363	512.22030	1009.81794	1500.13847
6,1, 7	10.13809	512.22396	1009.82123	1502.96223
6,1, 6	10.14064	512.23020	1009.83152	1502.96530
6,1, 5	10.14089	512.23118	1009.83280	1502.97989
7,0, 7	13.51133	515.57669	1013.15309	1502.98134
7,1, 8	13.51566	515.58021	1013.15627	1506.27621
7,1, 7	13.51853	515.58745	1013.16824	1506.27919
7,1, 6	13.51892	515.58857	1013.16965	1506.29618

Table 4.4. Energies for the [18.6] and [18.7] states.

J, F, par., e/f	[18.6][a]	[18.7] [a]
1/2, 1, –, *e*	580.31219	704.69699
1/2, 0, –, *e*	580.31219	704.69699
3/2, 2, +, *e*	580.62344	704.96580
3/2, 1, +, *e*	580.62372	704.96602
1/2, 0, +, *f*	581.21698	705.69919
1/2, 1, +, *f*	581.21840	705.70029
5/2, 3, –, *e*	581.44460	705.74792
5/2, 2, –, *e*	581.44596	705.74821
3/2, 1, –, *f*	582.43413	706.97209
3/2, 2, –, *f*	582.43498	706.97274
7/2, 4, +, *e*	582.77584	707.04308
7/2, 3, +, *e*	582.77625	707.04340
5/2, 2, +, *f*	584.15955	708.75903
5/2, 3, +, *f*	584.16028	708.75959
9/2, 5, –, *e*	584.61737	708.85105
9/2, 4, –, *e*	584.61780	708.85138
7/2, 3, –, *f*	586.39325	711.06063
7/2, 4, –, *f*	586.39393	711.06116
11/2, 6, +, *e*	586.96931	711.17161
11/2, 5, +, *e*	586.96976	711.17196
9/2, 4, +, *f*	589.13489	713.87727
9/2, 5, +, *f*	589.13552	713.87776
13/2, 7, –, *e*	589.83182	714.00458
13/2, 6, –, *e*	589.83228	714.00494
11/2, 5, –, *f*	592.38402	717.20929
11/2, 6, –, *f*	592.38465	717.20977
15/2, 8, +, *e*	593.20499	717.34979
15/2, 7, +, *e*	593.20545	717.35015
13/2,6, +, *f*	596.14025	721.05708
13/2, 7, +, *f*	596.14086	721.05755
17/2, 9, –, *e*	597.08888	721.20708
17/2, 8, –, *e*	597.08936	721.20745
15/2, 7, –, *f*	600.40308	725.42103
15/2,8, –, *f*	600.40368	725.42150

Energy -18000.00000 cm^{-1}.

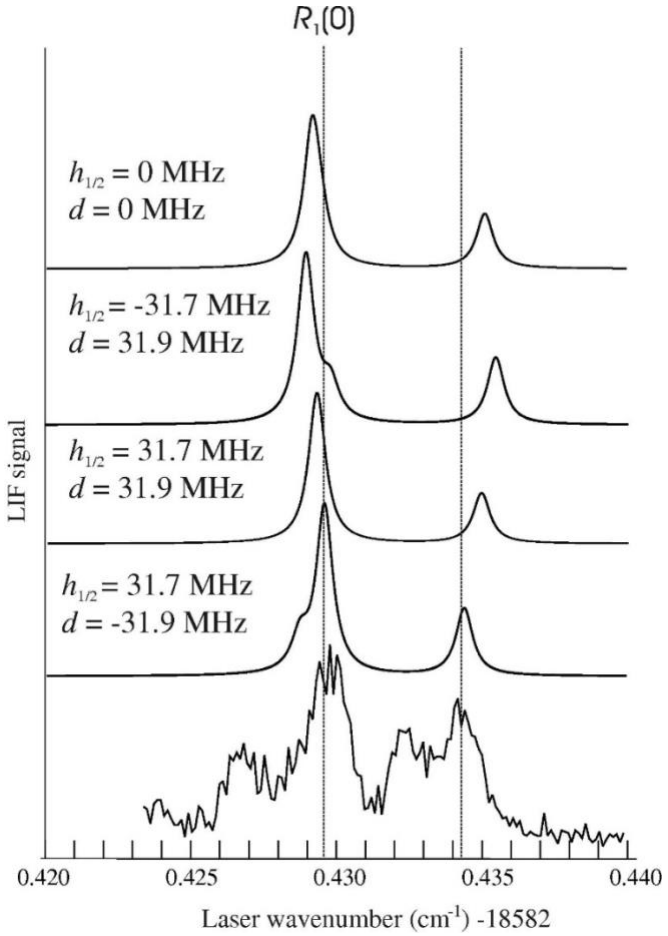

Figure 4.7. The $R_{11}(0)$(ν=18582.429 cm^{-1}) and $R_{10}(0)$ (ν= 18582.434 cm^{-1}) lines of the [18.6]-$X^2\Sigma^+(v=0)$ band. Also shown are the predicted spectra obtained using the optimized spectroscopic parameters of Tables 1 and 2 and various values of the magnetic hyperfine parameters for the [18.6] state. Best agreement is obtained with $h_{1/2}$ = 31.7 MHz and d = -31.9 MHz.

4.4. Discussion

The observed and predicted spectra come to an agreement when reversing the sign of previously determined hyperfine parameter d (= $-A_{\perp}$) has been made. The explanation for such a contradict is most likely related to the choice of phase. The present analysis, it has been assumed as following

$$\left\langle \Lambda = \pm 1 \left| e^{\pm 2i\phi} \right| \Lambda = \mp 1 \right\rangle = -1, \tag{4.3}$$

The assumption bases on the standard spherical harmonic phase choice[26]. Whereas in the previous analysis, the phase choice is not specified. A similar situation was noted in making the comparison of d and $A_{\perp}$ for the Lead Fluoride, PbF molecule by Mawhorter et al[27]. A negative d is consistent with a simple molecular orbital description which is discussed more below.

This is essential data for proper laser cooling. The energies of low-lying levels of the $X^2\Sigma^+$ (v = 0- 3), [18.6] and [18.7] states are given in Table 4.3 and Table 4.4, respectively. For using other certain field-free transitions, their frequencies and relative intensities can be predicted by applying the newly determined parameters of Table 4.1 and Table 4.2. Grouping the band origins yields the spacing between the $X^2\Sigma^+$ (with v = 0-3) levels of 502.15090 cm^{-1}, 497.66200 cm^{-1}, and 493.20862 cm^{-1}, based on that, the determined parameters are $\omega_e = 506.616 \pm 0.026$ cm^{-1} and $\omega_e x_e = 2.235 \pm 0.007$ cm^{-1}. These parameters are suitable for picturing the potential energy curve which turns out to be a criterion for predicting fluorescence branching ratios.

The spin-rotation interaction in the $X^2\Sigma^+$ state should be dominated by the second-order contribution[26]:

$$\gamma^{(2)} = 2\sum_{^2\Pi} \frac{\left\langle {}^2\Sigma_{-1/2} \left| BL^- \right| {}^2\Pi_{1/2} \right\rangle \left\langle {}^2\Pi_{1/2} \left| \sum_i a_i l_i^+ s_i^- \right| {}^2\Sigma_{1/2} \right\rangle}{T({}^2\Pi) - T({}^2\Sigma)} \tag{4.4}$$

where the microscopic form of the spin-orbit operator has been used and the summation includes all $^2\Pi$ states. The study by Sauer and coworkers[23] concludes that more than one state enters into the summation of Eq. 4.4 which implies through their interpretation of γ for the $X^2\Sigma^+$ (v=0). A strong vibrational dependence of γ has been observed in Table 4.1. Recall that the primary configuration for the $X^2\Sigma^+$ state has a sole unpaired electron in an Yb^+-centered 6*s*/6*p* hybrid orbital:

$$X\,{}^2\Sigma^+ : \left([\mathrm{Xe}]4f^{14}\right)_{\mathrm{Yb}} [\mathrm{He}]_{\mathrm{F}}\, \sigma^2_{\mathrm{F}(2s)} \sigma^2_{\mathrm{F}(2p)} \pi^4_{\mathrm{F}(2p)} \sigma^1_{\mathrm{Yb}(6s6p)} \tag{4.5}$$

The analysis of the hyperfine structure by Sauer et al[15] specified that the [18.6] and [18.7] states were approximately equal mixtures of the two configurations as following:

$$\psi^{el}([557],[561]) \approx \mathrm{c}_1 \psi_A^{el} + \mathrm{c}_2 \psi_B^{el}, \tag{4.6}$$

where $\mathrm{c}_1 \approx \mathrm{c}_2 \approx (2)^{-1/2}$ and ψ_A^{el}, ψ_A^{el} are as following

$$\psi_A^{el} : \left([\mathrm{Xe}]4f^{13}\right)_{\mathrm{Yb}} [\mathrm{He}]_{\mathrm{F}}\, \sigma^2_{\mathrm{F}(2s)} \sigma^2_{\mathrm{F}(2p)} \pi^4_{\mathrm{F}(2p)} \sigma^2_{\mathrm{Yb}(6s6p)} \rightarrow {}^2\Pi_i, {}^2\Phi_i, {}^2\Delta_i, \text{and } {}^2\Sigma^+ \tag{4.7}$$

$$\psi_B^{el} : \left([\mathrm{Xe}]4f^{14}\right)_{\mathrm{Yb}} [\mathrm{He}]_{\mathrm{F}}\, \sigma^2_{\mathrm{F}(2s)} \sigma^2_{\mathrm{F}(2p)} \pi^4_{\mathrm{F}(2p)} \pi^1_{\mathrm{Yb}(6p5d)} \rightarrow {}^2\Pi_r \quad . \tag{4.8}$$

Then

$$\gamma^{(2)} \approx \sum_{v'} \left|\langle v' | v'' \rangle\right|^2 \times$$

$$\left[-c_1^2 \frac{\left\langle \sigma_{\mathrm{Yb}(6s6p)} \left| Bl^- \right| \pi_{\mathrm{Yb}(4f)} \right\rangle \left\langle \pi_{\mathrm{Yb}(4f)} \left| al_i^+ \right| \sigma_{\mathrm{Yb}(6s6p)} \right\rangle}{T_{v'} - T(X\,^2\Sigma^+)} + c_2^2 \frac{\left\langle \sigma_{\mathrm{Yb}(6s6p)} \left| Bl^- \right| \pi_{\mathrm{Yb}(6p5d)} \right\rangle \left\langle \pi_{\mathrm{Yb}(6p5d)} \left| al_i^+ \right| \sigma_{\mathrm{Yb}(6s6p)} \right\rangle}{T_{v'} - T(X\,^2\Sigma^+)} \right]$$

(4.9)

where $\left|\langle v' | v'' \rangle\right|^2$ are the Franck-Condon factors (FCFs) and the summation goes over all vibrational levels of the excited $^2\Pi$ states. Recall that the two contributions to $\gamma^{(2)}$ have opposite sign because the ψ_A^{el} configuration has a hole while ψ_B^{el} configuration has a single unpaired electron according to Simard et al[28]. Sauer et al[23] states if the $A^2\Pi_{1/2}$ (v=0) state is assumed to be the sole perturbing state, it should have a dominant ψ_B^{el} configuration (i.e. c_1=0 and c_2=1), and the $\pi_{\mathrm{Yb}(6p5d)}$ orbital is a close 50/50 hybrid mixture. Eq. 4.9 then turns out to be able to give out a calculated $\gamma(v'=0)$ value that is roughly 20 times larger than observed values. In fact, the values of γ for the $X^2\Sigma^+(v=0)$ state is actually small since both terms in Eq. 4.9 nearly cancel each other. The configuration of Eq. 4.7 characterizes an excitation of an electron from the compact 4*f*-orbital to the valence Yb-centered 6*s*6*p*, σ-type, hybrid orbital that is polarized away from the electrophilic F-center. The configuration of Eq. 4.8 shows the excitation of an electron from the Yb-centered, back polarized, 6*s*6*p*, σ-type, hybrid orbital to a 6*p*5*d*, π-type orbital that reduced amount of polarizing effect. Excited states that have a dominant ψ_A^{el} configuration will behave remarkedly different which signify in their bond distances and potentials compared to those that have a dominant ψ_B^{el} configuration. Therefore, it is expected that $\gamma^{(2)}$ will be a

complicated function that are admixtures of ψ_A^{el} and ψ_B^{el} configurations from various excited states. This is the explanation for the strong vibrational dependence of γ parameter of ^{174}YbF.

The newly determined spectroscopic parameters for the [18.7] state show a significantly different from the previous values determined by Dunfield[14]. Specifically, the value for the Λ-doubling parameter $p+2q$ are different by roughly 25% from ours. Therefore, the predicted spectrum and the previous constants show a slight disagreement with to our measured spectrum. This inconsistency encouraged to perform a reanalysis of the earlier spectroscopic data which exposed a mistake in the previous analysis and gives an improved $p+2q$ value of -1.00964(48) cm^{-1} from Linton et al[29], which is 0.7% different from our value

The hyperfine splitting from the excited state of ^{19}F is small because of the localization of the unpaired electron density on Yb-centered. If we assume that only that unpaired electron occupied the $\sigma_{F(2p)}$ orbital then based one Fitzpatricket al [34], b_F=0 then $h_{1/2} = a - c/3 = d$ ≈ 1700 MHz which is two orders of magnitude. This value is significantly larger than what is observed for the $A^2\Pi_{1/2}$ (v=0), [18.6], and [18.7] states. In $A^2\Pi_{1/2}$ (v=0) state, the hyperfine interaction is much larger than the interaction at [18.6] and [18.7] states while the value of $h_{1/2} \approx -d$ for all three $A^2\Pi_{1/2}$ (v=0), [18.6], and [18.7] states. The small ^{19}F hyperfine interaction in these three states comes from the spin polarization effects[30-33]. Precisely, the α-spin unpaired, Yb-centered, electron interacts with the α- and β-spin electrons in the filled F-centered $\sigma_{F(2p)}$ orbital. The result of this

interaction then produces an over-all β-spin density. The observed negligible ^{19}F hyperfine splitting for the $A^2\Pi_{1/2}$ (v=0) state implies that either the spin-polarization effects are less than that in the [18.6] and [18.7] states or there are other undetermined contributions.

4.5. Conclusion

A high-resolution spectra of the [557]-$X^2\Sigma^+$(v = 0–3) and [561]-$X^2\Sigma^+$(v = 2) bands of ^{174}YbF have been recorded and analyzed. The resulting precisely determined parameters will contribute to model the energies and transition intensities relevant to proposed laser cooling experiments. The new parameters for the [561] state disagree with previous determined values[13] especially for the Λ-doubling parameter, but a reanalysis of the previous data has resolved this discrepancy[33]. All the spectroscopic information required for implementing a laser cooling scheme that addresses vibrational levels up to $v'' = 3$ is now available.

4.6. References

1. Hudson, J. J.; Kara, D. M.; Smallman, I. J.; Sauer, B. E.; Tarbutt, M. R.; Hinds, E. A., Improved measurement of the shape of the electron. *Nature* **2011,** *473*, 493.

2. Kara, D. M.; Smallman, I. J.; Hudson, J. J.; Sauer, B. E.; Tarbutt, M. R.; Hinds, E. A., Measurement of the electron's electric dipole moment using YbF molecules: methods and data analysis. *New Journal of Physics* **2012,** *14* (10), 103051.

3. Shuman, E. S.; Barry, J. F.; DeMille, D., Laser cooling of a diatomic molecule. *Nature* **2010,** *467*, 820.

4. Hummon, M. T.; Yeo, M.; Stuhl, B. K.; Collopy, A. L.; Xia, Y.; Ye, J., 2D magneto-optical trapping of diatomic molecules. *Physical Review Letters* **2013,** *110* (14), 143001.

5. Zhelyazkova, V.; Cournol, A.; Wall, T. E.; Matsushima, A.; Hudson, J. J.; Hinds, E.; Tarbutt, M.; Sauer, B., Laser cooling and slowing of CaF molecules. *Physical Review A* **2014,** *89* (5), 053416.

6. Truppe, S.; Williams, H. J.; Fitch, N. J.; Hambach, M.; Wall, T. E.; Hinds, E. A.; Sauer, B. E.; Tarbutt, M. R., An intense, cold, velocity-controlled molecular beam by frequency-chirped laser slowing. *New Journal of Physics* **2017,** *19* (2), 022001.

7. Kozyryev, I.; Baum, L.; Matsuda, K.; Augenbraun, B. L.; Anderegg, L.; Sedlack, A. P.; Doyle, J. M., Sisyphus Laser Cooling of a Polyatomic Molecule. *Physical Review Letters* **2017,** *118* (17), 173201.

8. Barry, J. F.; McCarron, D. J.; Norrgard, E. B.; Steinecker, M. H.; DeMille, D., Magneto-optical trapping of a diatomic molecule. *Nature* **2014,** *512*, 286.

9. Norrgard, E.; McCarron, D.; Steinecker, M.; Tarbutt, M.; DeMille, D., Submillikelvin dipolar molecules in a radio-frequency magneto-optical trap. *Physical review letters* **2016,** *116* (6), 063004.

10. Truppe, S.; Williams, H.; Hambach, M.; Caldwell, L.; Fitch, N.; Hinds, E.; Sauer, B.; Tarbutt, M., Molecules cooled below the Doppler limit. *Nature Physics* **2017,** *13* (12), 1173.

11. Zhuang, X.; Le, A.; Steimle, T. C.; Bulleid, N. E.; Smallman, I. J.; Hendricks, R. J.; Skoff, S. M.; Hudson, J. J.; Sauer, B. E.; Hinds, E. A.; Tarbutt, M. R., Franck–Condon factors and radiative lifetime of the A2Π1/2–X2Σ+ transition of ytterbium monofluoride, YbF. *Physical Chemistry Chemical Physics* **2011,** *13* (42), 19013-19017.

12. Tarbutt, M.; Sauer, B.; Hudson, J.; Hinds, E., Design for a fountain of YbF molecules to measure the electron's electric dipole moment. *New Journal of Physics* **2013,** *15* (5), 053034.

13. Smallman, I. J.; Wang, F.; Steimle, T. C.; Tarbutt, M. R.; Hinds, E. A., Radiative branching ratios for excited states of 174YbF: Application to laser cooling. *Journal of Molecular Spectroscopy* **2014,** *300*, 3-6.

14. Dunfield, K. L.; Linton, C.; Clarke, T. E.; McBride, J.; Adam, A. G.; Peers, J. R. D., Laser Spectroscopy of the Lanthanide Monofluorides: Analysis of theA2Π–X2Σ+Transition of Ytterbium Monofluoride. *Journal of Molecular Spectroscopy* **1995,** *174* (2), 433-445.

15. Sauer, B. E.; Cahn, S. B.; Kozlov, M. G.; Redgrave, G. D.; Hinds, E. A., Perturbed hyperfine doubling in the A2Π1/2 and [18.6]0.5 states of YbF. *The Journal of Chemical Physics* **1999,** *110* (17), 8424-8428.

16. Ma, T.; Butler, C.; Brown, J. M.; Linton, C.; Steimle, T. C., Optical Zeeman Spectroscopy of Ytterbium Monofluoride, YbF. *The Journal of Physical Chemistry A* **2009,** *113* (28), 8038-8044.

17. Glassman, Z.; Mawhorter, R.; Grabow, J.-U.; Le, A.; Steimle, T. C., The hyperfine interaction in the odd isotope of ytterbium fluoride, 171YbF. *Journal of Molecular Spectroscopy* **2014,** *300*, 7-11.

18. Fukuda, M.; Soga, K.; Senami, M.; Tachibana, A., Local spin dynamics with the electron electric dipole moment. *Physical Review A* **2016,** *93* (1), 012518.

19. Pašteka, L. F.; Mawhorter, R. J.; Schwerdtfeger, P., Relativistic coupled-cluster calculations of the 173Yb nuclear quadrupole coupling constant for the YbF molecule. *Molecular Physics* **2016,** *114* (7-8), 1110-1117.

20. Sunaga, A.; Abe, M.; Hada, M.; Das, B. P., Relativistic coupled-cluster calculation of the electron-nucleus scalar-pseudoscalar interaction constant W s in YbF. *Physical Review A* **2016,** *93* (4), 042507.

21. Sauer, B. E.; Wang, J.; Hinds, E. A., Laser-rf double resonance spectroscopy of 174YbF in the X 2Σ+ state: Spin-rotation, hyperfine interactions, and the electric dipole moment. *The Journal of Chemical Physics* **1996,** *105* (17), 7412-7420.

22. Dickinson, C. S.; Coxon, J. A.; Walker, N. R.; Gerry, M. C. L., Fourier transform microwave spectroscopy of the 2Σ+ ground states of YbX (X=F, Cl, Br): Characterization of hyperfine effects and determination of the molecular geometries. *The Journal of Chemical Physics* **2001,** *115* (15), 6979-6989.

23. Sauer, B. E.; Wang, J.; Hinds, E. A., Anomalous Spin-Rotation Coupling in the ${X}^{2}{\ensuremath{\Sigma}}^{+}$ State of YbF. *Physical Review Letters* **1995,** *74* (9), 1554-1557.

24. Condylis, P.; Hudson, J.; Tarbutt, M.; Sauer, B.; Hinds, E., Stark shift of the A 2 Π 1⁄2 state in YbF 174. AIP: 2005.

25. Steimle, T. C.; Ma, T.; Linton, C., The hyperfine interaction in the A (2) Pi (1/2) and X (2) Sigma (+) states of ytterbium monofluoride (vol 127, art no 234316, 2007). *JOURNAL OF CHEMICAL PHYSICS* **2008,** *128* (20).

26. Brown, J. M.; Carrington, A., *Rotational spectroscopy of diatomic molecules*. Cambridge University Press: 2003.

27. Mawhorter, R. J.; Murphy, B. S.; Baum, A. L.; Sears, T. J.; Yang, T.; Rupasinghe, P.; McRaven, C.; Shafer-Ray, N.; Alphei, L. D.; Grabow, J.-U., Characterization of the ground X 1 state of 204 Pb 19 F, 206 Pb 19 F, 207 Pb 19 F, and 208 Pb 19 F. *Physical Review A* **2011,** *84* (2), 022508.

28. Simard, B.; Watson, J. K. G.; Merer, A. J.; Steimle, T. C., Comment on "Fine and magnetic hyperfine structure in the A2Π and X2Σ+ states of yttrium monoxide" [J. Chem. Phys. 88, 598 (1988)]. *The Journal of Chemical Physics* **1999,** *111* (13), 6148-6149.

29. Linton, C., Private communication. **2017**.

30. Amano, T., Interpretation of magnetic hyperfine coupling constants. *Journal of Molecular Spectroscopy* **1990,** *144* (2), 454-457.

31. Chipman, D. M., The spin polarization model for hyperfine coupling constants. *Theoretica chimica acta* **1992,** *82* (1), 93-115.

32. Munzarová, M.; Kaupp, M., A Critical Validation of Density Functional and Coupled-Cluster Approaches for the Calculation of EPR Hyperfine Coupling Constants in Transition Metal Complexes. *The Journal of Physical Chemistry A* **1999,** *103* (48), 9966-9983.

33. Munzarová, M. L.; Kubáček, P.; Kaupp, M., Mechanisms of EPR Hyperfine Coupling in Transition Metal Complexes. *Journal of the American Chemical Society* **2000,** *122* (48), 11900-11913.

CHAPTER 5

OPTICAL STARK AND ZEEMAN SPECTROSCOPY OF THORIUM FLUORIDE, THF, THORIUM CHLORIDE, THCL

5.1. Introduction

The development of new, environmentally safe technologies of nuclear waste processing and (long-term) disposal has attracted a lot of researchers and engineers working in many countries. The purpose is to provide freshly recycled fuel for nuclear plants through recovering fissile and fusional materials. Over five decades, the central idea of processing used fuel is to recover unused plutonium and uranium from the Spent Nuclear Fuel (SNF) thereby complete the fuel cycle with expectations of obtaining some 25% more energy from the original uranium in the process. In the last decade, the idea of recovering all long-lived actinides together (i.e. with plutonium) then recycling them in fast breeder reactors where they will be then converted into short-lived fission products. The advantage of this procedure is reducing the long-term radioactivity in high-level wastes and preventing the possibility of leaking wasted plutonium to civil use. Therefore, discovering new element-specific ligands for the separation of the minor actinides from the lanthanides present in the plutonium and uranium extraction (PUREX) process is needed to improve the treatment of spent nuclear fuel [1-5].

Primarily, the separation of actinides and lanthanides in processing the nuclear wastes and the separation of lanthanides and actinides within each group of compounds point back to classical problems in molecular recognition of chemical systems with similar structures and properties. These problems are the challenges in both experimental and theoretical

aspects. Both two aspects are employed to study general laws and tendencies that effect the relationships between the recognition structure and the target property. For a long time, the discovering of new lanthanides or actinides compounds was based on the synthesis of multiple series of compounds chosen from the previous experience and qualitative intuitive considerations and then test the trial structures experimentally. The cycle keeps going until the desired results are achieved. The early experience obviously indicates that further improvement in solving these problems needs a deep insight into the nature of metal – ligand bonding in the complexes of lanthanides and actinides compounds. However, for an improved chemical understanding of actinide elements that are not easy to study experimentally, it critically relies on the advance of computational methodologies for modeling molecular properties and transformations. One of the most effective means of evaluating computational methodologies is by making a comparison between experimental results and predicted properties for simple Th and U containing gas-phase molecules[6-7], which can be obtained by employing high-resolution spectroscopy.

Of particular interest in studying the bonding of actinides employing the high-resolution spectroscopy, permanent electric dipole moment and magnetic g- factor are the most effective gauge of bond properties. The electric dipole moment, $\overrightarrow{\mu_{el}}$, is the fundamental electrostatic property of a neutral molecule, a characteristic tool for understanding the electronic configuration. It is not only essential for studying the ionic character of a chemical bond but also useful in constructing molecular orbital-based models. As a matter of fact, electric dipole moments can be predicted *ab initio*, becoming a good candidate to approve the agreement between theory and experiment. While in the other end, the magnetic dipole moment, μ_m, also appears to be a valuable tool for

understanding the electronic structures of metal- containing compounds. It provides additional useful information for inferring the molecular configuration associating with specific electronic states. $\overrightarrow{\mu_m}$ also can be predicted *a priori* employing the theoretically predicted spin-orbit coupled eigenstate compositions by ligand field theory[8-9] or *ab initio*[10-12]. Given the molecular configurations of a particular electronic state, a given electronic state must have an μ_m being consistent with the experimentally determined μ_m. For instance, in Hund's case (a) coupling basis, Λ and Σ are well defined and the effective g-factor $g_e = \Lambda + 2.002\Sigma$ could be predicted if the ΛS state composition of a specific observed Ω-state is known [13-15]. In addition to providing benchmark properties, from a computational point of view, energies and wave functions from electronic structure calculations are further combined in terms of ab initio ligand field theory (AILFT), these studies on this approach has focused on the fundamental question concerning the extent and nature of 5*f* and 6*d* participation in actinide metal−ligand covalency[16] trends along the series, which contributes to the actinide/lanthanide separation chemistry.

This work presents the optical medium and high-resolution spectroscopic study on thorium fluoride, ThF, and thorium chloride, ThCl in the 16400 cm^{-1}-18800 cm^{-1} range. The studies involve the determination of $|\vec{\mu}_{el}|$ values, magnetic g-factors, vibrational spacings, and bond distances from the analysis of electronic spectra recorded. The expected ground state of these molecule is $^2\Delta_{3/2}$ by deducing the ligand-field interaction of the $Th^+(7s^2 6d^1)$ and $Th^+(7s^1 6d^2)$ configurations according Morse et al.[17] In thorium ion, Th^+, the energy of 5*f*, 6*d*, and 7*s* orbitals are close to each other. When the bond is formed the energies of the 5s, 6d, 7s orbitals shift. As a result, the final orbitals' reordering generates

numerous corresponding states whose relative energies depend upon oxidation state, bond distance and bond polarity. For instance, the $Th^+(7s^26d^1)$ forms the $X^2\Delta_{3/2}$, $X^2\Delta_{5/2}$, $A^2\Pi_{1/2}$, $A^2\Pi_{3/2}$ and $B^2\Sigma^+$ states, or the low-lying excited $Th^+(7s^16d^2)$ configuration ligand-field splits into 90 additional strongly interacting states (45 Ω-doublets) of slightly higher energy. ThF has the expected ground $|\Omega| = 3/2$ state belong to the $^2\Delta_r$ state (i.e. $X^2\Delta_{3/2}$) arising from the $Th^+(7s^26d^1)$ configuration. One of the goals of the current work is to verify qualitatively the usefulness of applying a ligand-field interaction in studying the experimental properties of ThF and ThCl.

The current work is the extension of the previous experimental and theoretical studies performed by Heaven's group on the ThF/ThF^+[10] and ThCl/$ThCl^+$ system[12]. The earlier study focused on analyzing the electronic spectrum of ThF in the 19,500–21,300 cm^{-1} spectral range and then performing electronic structure calculations [10]. Specifically, the observed spectrum was obtained by utilizing the mass-selected resonance enhanced multi-photon ionization (REMPI) spectrometry. In addition, the Heaven group recorded and analyzed three bands labeled ({19.92}, {20.44}, {20.95}) using medium-resolution LIF detection. The spectra were assigned, and the fine structure was then processed to obtain the rotational constant, B_0 (=0.237(5) cm^{-1}) for the $X^2\Delta_{3/2}$ ground state. From the DF spectra, the ground state vibrational spacing, $\Delta G_{1/2}$, of 605(15) cm^{-1} and the energy for the $X^2\Delta_{3/2}$ spin-orbit component of 2575 cm^{-1} were determined. Multi-reference configuration interaction (MRCI) and couple cluster calculations were performed. Those calculation predicted B_0 and $\Delta G_{1/2}$ values for the $X^2\Delta_{3/2}$ state of 0.2264 cm^{-1} and 574 cm^{-1}, respectively. The ground state $^2\Delta_r$ of ThF is predicted to have a $Th^+(7s^26d^1)F^-(2p^6)$ configuration. The $Th^+(7s^26d^1)$ configuration also gives arises the two low-lying states, the $A^2\Pi_{1/2}$ and $A^2\Pi_{3/2}$

states which were predicted their term energies at 4253 and 6134 cm^{-1}, respectively. About ThCl, another study[12] by Heaven's group devotes on studying the ThCl/$ThCl^+$ system using laser induced fluorescence and two-photon ionization techniques. In that study, ThCl was done by recording the low resolution LIF spectrum in the 18,100 - 25,000 cm^{-1} range was recorded and then later identifying observed bands associated with ThCl using mass-selected REMPI spectroscopy. The two bands at 21,977.6 and 23,507.9 cm^{-1} were studied at moderate resolution using LIF excitation and dispersed fluorescence spectroscopy to study both ThCl isotopes, $Th^{35}Cl$ and $Th^{37}Cl$. The data processing of those spectra provides determined constants associated with the the $X^2\Delta_{3/2}$ state including B_0 and $\Delta G_{1/2}$ values of 0.08899(18) cm^{-1} and 341(14) cm^{-1}, and also term energies of the assigned low-lying excited states $X^2\Delta_{5/2}$, $^4\Phi_{3/2}$ and $^2\Pi_{3/2}$, of 3498, 4075, and 4361 cm^{-1} ,respectively. Following the experiments, the theoretical calculations have been done by employing a complete active space self-consistent field (CASSCF) which was followed by second-order perturbation theory calculations to predict the low-lying $\Lambda\Sigma$ excited electronic states of ThCl and $ThCl^+$ through apply corresponded basis sets, scc-pV*n*Z-PP (*n* = D,T,Q) for Th and aug-cc-pV(*n*+d)Z for Cl. The results output the term energies and nature of those Ω-states. However, the values of $\vec{\mu}_{el}$ and g-factors were not reported for either of these combined theoretical and experimental studies of ThF and ThCl.

5.2. Observation

The 2D spectrum of the products generated via ablation of thorium with the CF_4/Argon (ratio 5:95) mixture covers the spectral range from 17,400 cm^{-1} to 18,800 cm^{-1} playing as the initial search for Th- containing molecules. Figure 5.1 presents a 2D scan

results from the reaction of Th and CF_4/Ar mixture. At the beginning of the scan (i.e. 17,400 cm^{-1}) the central DLIF wavelength is approximately 590 nm and at the end of the scan (i.e. 18,800cm^{-1}) it is approximately 545 nm.

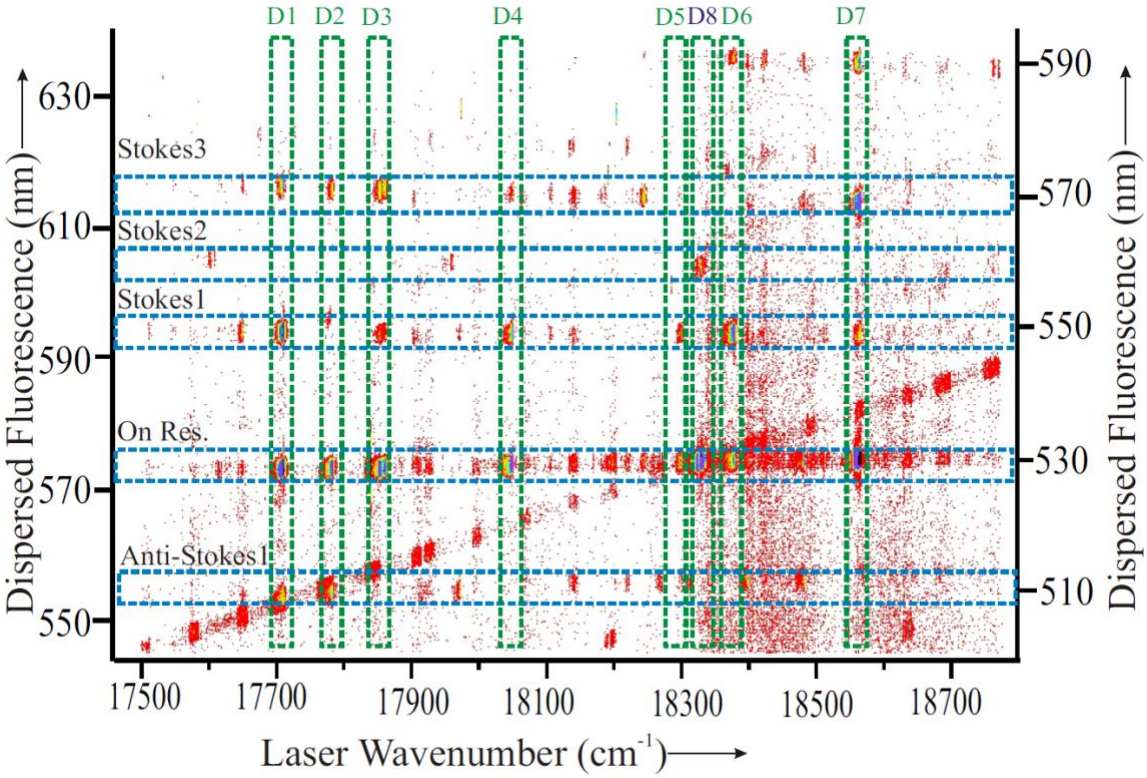

Figure 5.1. The 2D spectrum of the molecules produced in the ablation of thorium with the CF_4/argon mixture within spectral range.

In Figure 5.1, the horizontal bands of fluorescence are the excitation spectra monitored either on resonance, to higher frequency (Stokes1-3), or to lower frequency (Anti-Stokes) than that of the laser. The bands at 17700, 17790, 17865, 18030, 18295, 18360 and 18575 cm^{-1} have DLIF spectra (D1-D7) characteristic of ThF. The band at systems 18327 has a DLIF spectrum (D8) characteristic of ThO and is the $F\,^1\Sigma^+ - X\,^1\Sigma^+(0,0)$ transition. High-resolution spectroscopy was performed on the intense band at 18575 cm^{-1} which is assigned as the [18.6] $\mathbf{\Omega}$=3/2 – X $^2\Delta_{3/2}$(v',0) transition.

In Figure 5.1, the horizontal bands of fluorescence are the excitation spectra. Those spectra are classified into on resonance, Stokes (fluorescence to higher frequency in comparison to the laser), or anti-Stokes (fluorescence to lower frequency than that of the laser). The on resonances band represents the net fluorescence of all species generated from the supersonic expansion source with respect to the shift of the excitation laser's energy. There is a diagonal streak crossing over the spectrum. This diagonal stripe of fluorescence, which appears at 546.1 nm in the DLIF, is an artifact originating from the emission of the very intense ThO $F^1\Sigma^+ - X^1\Sigma^+(0,0)$ band excited by amplified stimulated emission (ASE) of our pulsed dye laser. In Figure 5.1, the diagonal stripe of fluorescence crosses the on-resonance excitation signal at 18,313 cm^{-1}. It is also worth to note that this band fluoresces predominantly on resonance. There are also eight band systems being identified from the DLIF spectrum and they are highlighted by the green vertical slices labeled D1 to D8 in Figure 5.1. Using the known vibrational spacing[18] of 895 cm^{-1} (Stokes 2) shifting from the excitation laser, the D8 band was assigned to the $F^1\Sigma^+ - X^1\Sigma^+(0,0)$ (ν=18313 cm^{-1}) transition of ThO. There are similar observed patterns repeating from band D1 to D7. They show features shifted by approximately 600 cm^{-1} (Stokes 1) and 1200 cm^{-1} (Stokes 3) toward the red of the excitation spectrum and are assigned to ThF excited state emission down to either v" =1 and v" =2 of the $X^2\Delta_{3/2}$ state. With the exception of D1 and D2, which exhibit an anti-Stokes component, the transitions are excitation from the $X^2\Delta_{3/2}$(v=0) level to multiple excited electronic states. Hence the bands at 17712, 17790, 17864, 18030, 18295, 18360 and 18575 cm^{-1} are assigned to ThF. In a similar approach, additional bands of ThF at 16335, 16364, 16527 and 16564 cm^{-1} were identified and assigned in the 16400 cm^{-1}-18800 cm^{-1} spectral range. Higher resolution DFLIF spectra

resulting from pulsed laser excitation of the band heads at 17712, 17865 and 18575 cm^{-1} are presented in

Figure 5.2. It is evident that the band at 17712 cm^{-1} is an excitation from the $X^2\Delta_{3/2}$ (v" =1) state due to presence of an anti-Stokes feature. The relaxation of ThF to the $X^2\Delta_{5/2}$ state were also observed and the heretofore unobserved $A^2\Pi_{1/2}$ state are observed. The measured $X^2\Delta_{3/2}$ state $\Delta G_{v+1/2}$ spacings were determined to be 595.6, 594.4, 591.5 and 589.1 cm^{-1} for v=0, 1, 2 and 3 of the $X^2\Delta_{3/2}$ state, respectively. A linear least squares fit of these values to the standard expression for vibrational spacing outputs the better values of ω_e (600.6±4 cm^{-1}) and $\omega_e x_e$ (1.2 ± 1/2 cm^{-1}) for the $X^2\Delta_{3/2}$ state, which is in an agreement with the previously determined[10] ω_e value of 605(15) cm^{-1}. Later the high-resolution field-free, Stark and Zeeman spectroscopy was performed focusing on the intense 18575 cm^{-1} band

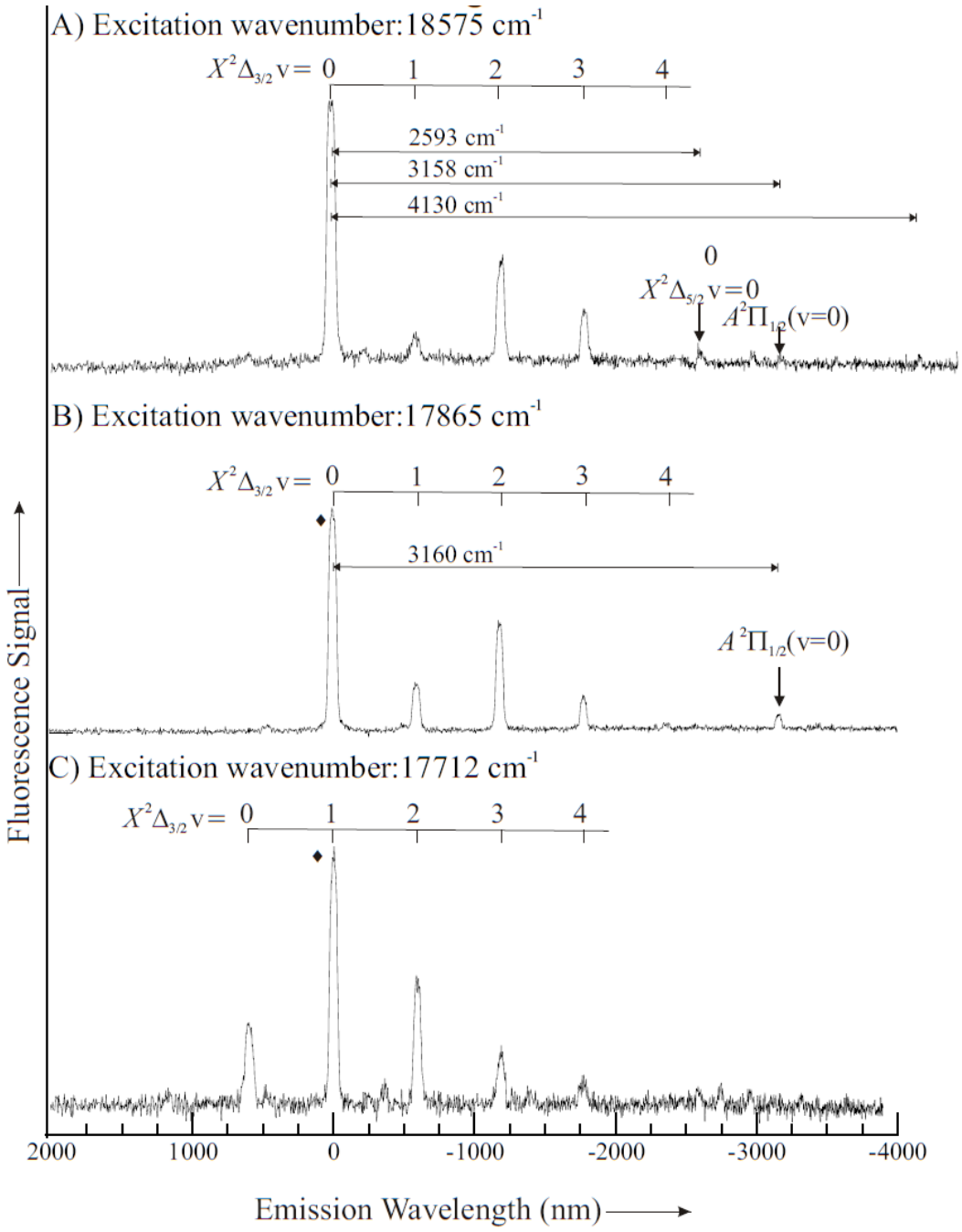

Figure 5.2. Higher resolution DFLIF spectra resulting from pulsed dye laser excitation of the ThF band heads at 17712, 17865 and 18575 cm^{-1}. The spectra have not been corrected for instrumental response sensitivity.

The pulse dye laser excitation spectrum in the range of 18,555 to 18,585 cm^{-1} extracted from the "Stokes 3" horizontal slice of a 2D spectrum recorded using a laser step

size of 0.1 cm^{-1} is presented in the top panel of Figure 5.3. The *P*, *Q* and *R* branches are straightforwardly identified and observed. The lower panel, panel B, presents the 18,575.5 to 18,576.5 cm^{-1} portion of the corresponding band obtained employing both the single frequency cw-dye laser excitation and a skimmed molecular beam. The branch features marked with "•" were recorded in the presence of a static electric field (Stark effect) while those with an "♦" were recorded in the presence of a static magnetic field (Zeeman effect). In this experiment, the fluorescence was recorded off-resonance using a 570 nm ±10 nm bandpass filter and the signals were processed with photon counting. The branch features have a linewidth of approximately 30 MHz. Assisted by the previously determined rotational constant[10] B_0'' (=0.237(5) cm^{-1}) and an estimated value of B_0', the quantum number assignment of the branch features was assigned completely. The observation of the lowest branch features (*R*(3/2), *Q*(3/2) and *P*(5/2), the Ω=3/2 assignment of the excited state and the band is firmly assigned as the [18.6] Ω=3/2 – $X^2\Delta_{3/2}$(v',0) transition. The ^{19}F(I=1/2) hyperfine splitting or Ω-doubling was not observed in the recorded spectra. The rotational states of both the $X^2\Delta_{3/2}$, [18.6]Ω=1.5 exist as pairs of very nearly degenerate levels of opposite parity. The branch assignments were verified by the Zeeman and Stark measurements (see below). The least-square fitting involving 48 precisely measured transition branch features was performed. The frequencies, assignments and residuals are presented in Table 5.1.

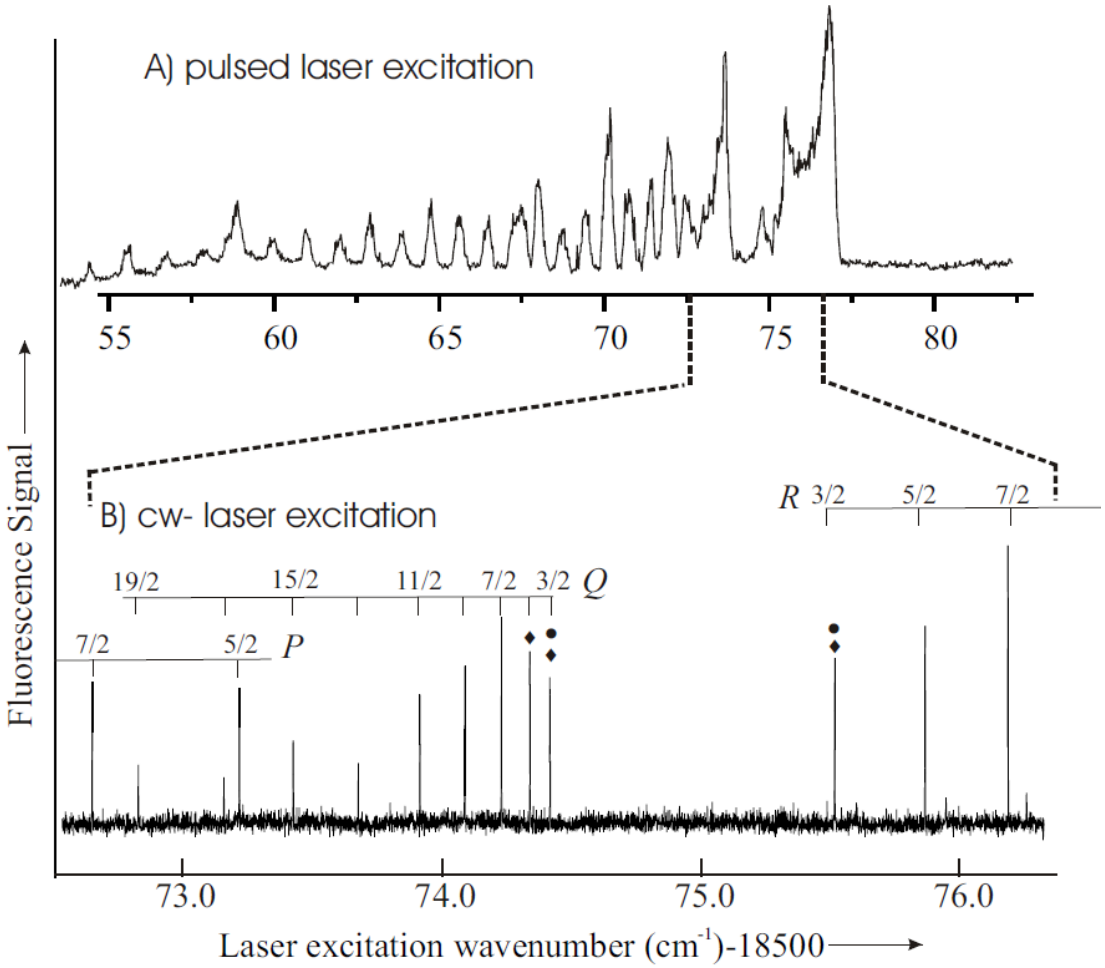

Figure 5.3. Laser excitation spectra of ThF. Upper panel: the laser excitation spectrum of the [18.6] Ω=3/2 – $X\,^2\Delta_{3/2}$(v′,0) transition extracted from the 2D spectrum. Lower panel: a portion of the high-resolution, field-free, spectrum of the [18.6] Ω=3/2 – $X\,^2\Delta_{3/2}$(v′,0) band and associated assignments.

Table 5.1. The observed, calculated field free transition wavenumbers (from the optimized parameters) and the differences between the observed and calculated ones for the [18.6] Ω=3/2 – X $^2\Delta_{3/2}$(v′,0) band of ThF.

J	*R*(*J*)	Obs-Calc	*Q*(*J*)	Obs-Calc	*P*(*J*)	Obs-Calc
1.5	18575.4762	0.0000	18574.3900	-0.0007		
2.5	75.8311	0.0003	74.3117	0.0005	18573.2251	-0.0006
3.5	76.1535	-0.0001	74.2003	0.0005	72.6804	0.0003
4.5	76.4442	-0.0004	74.0569	0.0003	72.1027	0.0000
5.5	76.7037	0.0000	73.8816	0.0001	71.4931	-0.0004
6.5	76.9309	-0.0001	73.6750	0.0003	70.8525	0.0000
7.5	77.1263	-0.0002	73.4363	0.0003	70.1793	-0.0003
8.5	77.2901	-0.0001	73.1657	0.0002		
9.5	77.4221	0.0000	72.8630	-0.0001		
Std. dev. of fit = 0.0003 cm^{-1}						

The *R*(3/2) (at 18575.4762 cm^{-1}) and *Q*(3/2) (at 18575.4900 cm^{-1}) lines were selected for the optical Stark studies. Under the static electric field up to 932 V/cm, the Stark spectra were recorded and measured. The recorded spectra of the *R*(3/2) line, recorded field-free and with the laser polarized parallel (ΔM_J =0) perpendicular (ΔM_J =±1) relatively to the direction of a 759 V/cm electric field, are presented in Figure 5.4. The field-free line splits into four components (= 2J+1) under the parallel polarization due to the interaction of the electric field and near degeneracy of Ω doublets associated with the J = 3/2 level of the [18.6] Ω=3/2 state. The spectrum exhibits a very nearly linear Stark tuning confirming the quantum number assignment and the negligibly small Ω-doubling. Also included in Figure 5.4 are the energy levels obtained using the optimized parameters (*infra vide*) and quantum number assignments. The 40 precisely measured Stark shifts along with quantum number assignments and residuals are presented in Table 5.2.

Table 5.2. The observed and calculated Stark shifts for the [18.6] $\Omega=3/2 - X^2\Delta_{3/2}(v',0)$ band of ThF.

Assignment					Shift (MHz)		
Branch, pol.	J'	$M_{J'}$	J''	$M_{J''}$	Obs.	Obs-Calc.	Field (V/cm)
$Q(3/2)$, ∥	3/2	+3/2	3/2	+3/2	-126	2	506
	3/2	+1/2	3/2	+1/2	-54	-12	
	3/2	-1/2	3/2	-1/2	57	14	
	3/2	-3/2	3/2	-3/2	135	6	
	3/2	+3/2	3/2	+3/2	-189	3	759
	3/2	+1/2	3/2	+1/2	-57	6	
	3/2	-1/2	3/2	-1/2	60	-5	
	3/2	-3/2	3/2	-3/2	189	-5	
$R(3/2)$, ∥	5/2	+3/2	1/2	+3/2	-183	-4	506
	5/2	+1/2	1/2	+1/2	-66	-7	
	5/2	-1/2	1/2	-1/2	9	8	
	5/2	-3/2	1/2	-3/2	183	3	
	5/2	+3/2	1/2	+3/2	-267	2	759
	5/2	+1/2	1/2	+1/2	-90	-1	
	5/2	-1/2	1/2	-1/2	99	7	
	5/2	-3/2	1/2	-3/2	272	20	
	5/2	+3/2	1/2	+3/2	-312	10	911
	5/2	+1/2	1/2	+1/2	-96	10	
	5/2	-1/2	1/2	-1/2	99	-11	
	5/2	-3/2	1/2	-3/2	324	-1	
	5/2	+3/2	1/2	+3/2	-159	-5	506
	5/2	+1/2	1/2	+1/2	-33	1	
	5/2	-1/2	1/2	-1/2	39	4	
	5/2	-3/2	1/2	-3/2	167	12	
$R(3/2)$, ⊥	5/2	+1/2	1/2	+3/2	-312	-5	759
	5/2	+5/2	1/2	+3/2	-237	-6	
	5/2	-1/2	1/2	+1/2	-132	-5	
	5/2	+3/2	1/2	+1/2	-485	2	
	5/2	-3/2	1/2	-1/2	455	-8	
	5/2	+1/2	1/2	-1/2	1205	-10	
	5/2	-5/2	1/2	-3/2	225	-7	
	5/2	-1/2	1/2	-3/2	321	12	
	5/2	+1/2	1/2	+3/2	-366	23	911
	5/2	+5/2	1/2	+3/2	-282	-5	
	5/2	-1/2	1/2	+1/2	-153	-1	
	5/2	+3/2	1/2	+1/2	-72	-12	
	5/2	-3/2	1/2	-1/2	69	5	
	5/2	+1/2	1/2	-1/2	156	0	
	5/2	-5/2	1/2	-3/2	265	-14	
	5/2	-1/2	1/2	-3/2	369	2	
Std. dev. of fit =7.3MHz							

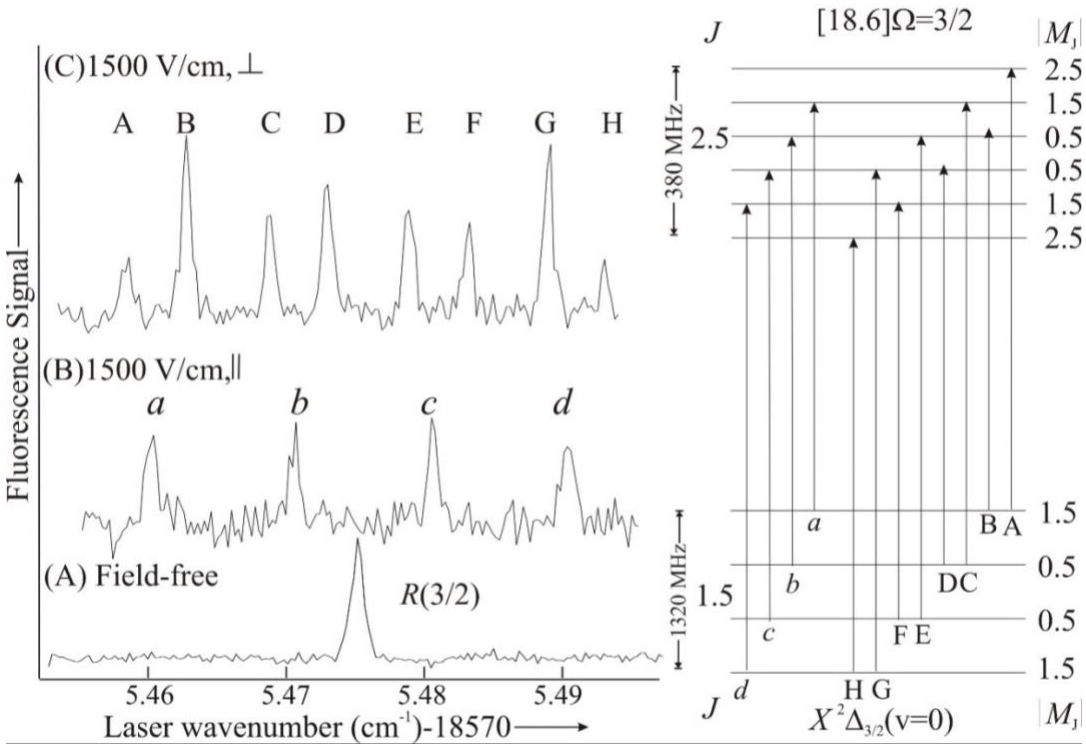

Figure 5.4. The $R(3/2)$ (ν=18575.4762 cm^{-1}) line of the [18.6] $\mathbf{\Omega}$=3/2 – $X^2\Delta_{3/2}(v',0)$ band of ThF recorded field-free and in the presence of a 759 V/cm electric field with parallel (ΔM_J =0) and perpendicular (ΔM_J =±1) polarizations. Also shown are the energy level pattern and assignment

The Zeeman effect in the [18.6] $\mathbf{\Omega}$=3/2 – $X^2\Delta_{3/2}(v',0)$ band system of ThF has been recorded and analyzed. Zeeman spectra for the $R(3/2)$, $Q(3/2)$ and $Q(5/2)$ (ν=18574.3117cm^{-1}) lines were selected and measured at a magnetic field of 876 G because these peak are relatively intense and separated from other spectral features. The recorded spectrum of $R(3/2)$ line recorded field-free, and at 876 G magnetic field oriented parallel (ΔM_J =0) and perpendicular (ΔM_J =±1) polarizations are shown in Figure 5.5. The spacing of the Zeeman shifts are very nearly identical and the peaks shift symmetrically centering the field-free feature, verified that the second-order contributions is negligible. Figure 5.5 also includes the predicted spectra and associated energy levels obtained using the optimized parameters for both the ground and excited state. The 34 precisely measured

Zeeman shifts along with quantum number assignments and residuals are presented in Table 5.3.

Table 5.3. The observed and calculated Zeeman shifts for the [18.6] Ω=3/2 – $X\,^2\Delta_{3/2}$(v′,0) band of ThF.

Assignment					Shift (MHz)		
Branch, pol.	J'	$M_{J'}$	J"	$M_{J"}$	Obs	Obs-Calc	Field (Gauss)
P(5/2), ∥	3/2	-3/2	5/2	-3/2	-519	-2	876
	3/2	-1/2	5/2	-1/2	-188	-7	876
	3/2	+1/2	5/2	+1/2	172	12	876
	3/2	+3/2	5/2	+3/2	500	-6	876
Q(3/2), ∥	3/2	+3/2	3/2	+3/2	63	5	876
	3/2	+1/2	3/2	+1/2	19	1	876
	3/2	-1/2	3/2	-1/2	-19	3	876
	3/2	-3/2	3/2	-3/2	-58	3	876
R(3/2), ∥	5/2	+3/2	3/2	+3/2	-428	-6	876
	5/2	+1/2	3/2	+1/2	-142	-9	876
	5/2	-1/2	3/2	-1/2	153	2	876
	5/2	-3/2	3/2	-3/2	428	-3	876
P(5/2), ⊥	3/2	-3/2	5/2	-1/2	-726	19	876
	3/2	-1/2	5/2	+1/2	-385	22	876
	3/2	-3/2	5/2	-5/2	-275	14	876
	3/2	+1/2	5/2	+3/2	-49	16	876
	3/2	-1/2	5/2	-3/2	61	15	876
	3/2	+3/2	5/2	+5/2	292	9	876
	3/2	+1/2	5/2	-1/2	392	6	876
	3/2	+3/2	5/2	+1/2	734	4	876
Q(3/2), ⊥	3/2	1/2	3/2	+3/2	-586	-1	876
	3/2	-1/2	3/2	+1/2	-544	5	876
	3/2	-3/2	3/2	-1/2	-514	-2	876
	3/2	+3/2	3/2	+1/2	515	12	876
	3/2	+1/2	3/2	-1/2	566	21	876
	3/2	-1/2	3/2	-3/2	608	20	876
R(3/2),⊥	5/2	+1/2	3/2	+3/2	-663	0	876
	5/2	-1/2	3/2	+1/2	-380	-4	876
	5/2	+5/2	3/2	+3/2	-182	1	876
	5/2	-3/2	3/2	-1/2	-92	22	876
	5/2	3/2	3/2	+1/2	100	-8	876
	5/2	-5/2	3/2	-3/2	172	-12	876
	5/2	+1/2	3/2	-1/2	389	-5	876
	5/2	-1/2	3/2	-3/2	665	-11	876

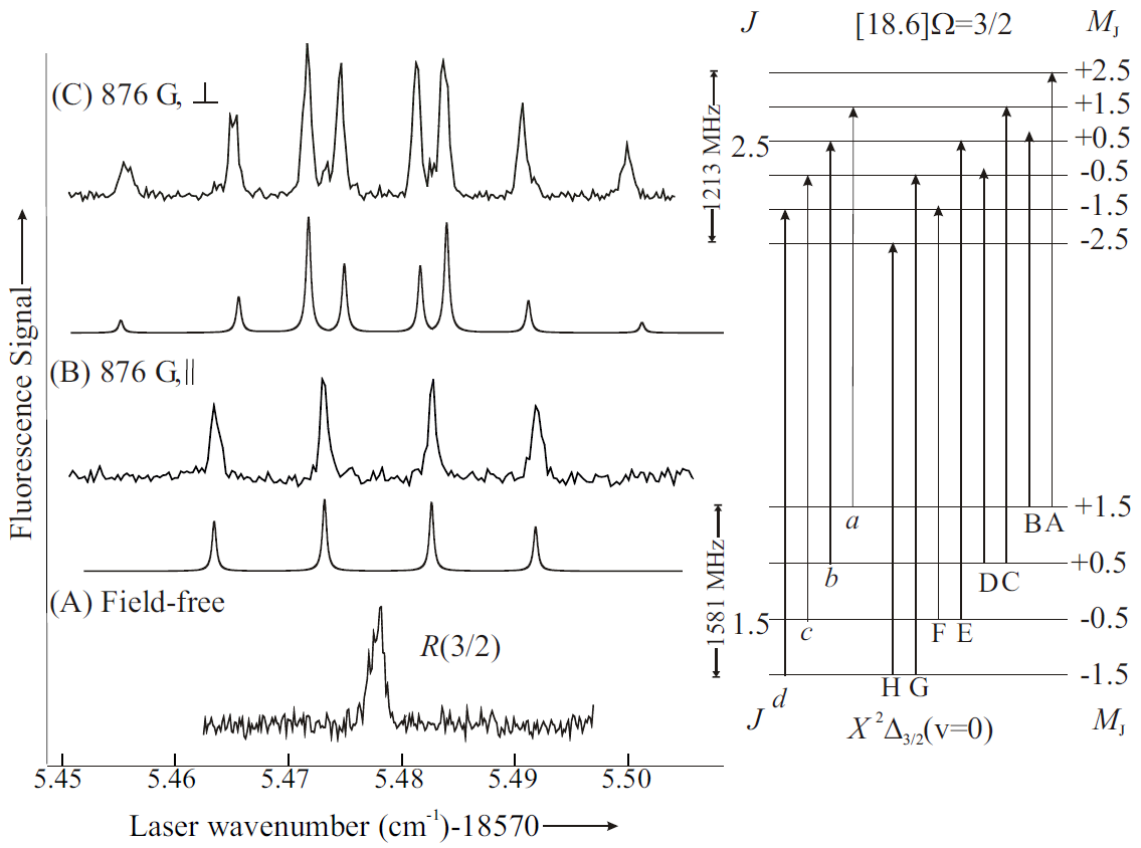

Figure 5.5. The *R*(3/2) (ν=18575.4762 cm^{-1}) line of the [18.6] **Ω**=3/2 – $X\,^2\Delta_{3/2}$(v′,0) band of ThF recorded field-free and in the presence of a 876 G magnetic field with parallel (ΔM_J =0) and perpendicular (ΔM_J =±1) polarizations. Also shown are the energy level pattern and assignment.

Following similar procedure, the pulse dye laser excitation spectrum of the ablated Th/CCl_4 reaction products extracted from the observed 2D spectrum in the range of 18,050 to 18,250 cm^{-1} is presented in the upper panel of Figure 5.6. The upper panel spectrum originated from the 2D spectrum and was obtained by slide horizontally the on-resonance horizontal fluorescence of the spectrum. There is only one band associated with ThCl in the spectral range of 16,400 cm^{-1}-18,800 cm^{-1} range surveyed employing 2D spectroscopy. In comparison with the intensity of [18.6] **Ω**=3/2 – $X^2\Delta_{3/2}$(v′,0) transition of ThF, the signal

is significantly weaker. As being seen in the Figure 5.6. The strong and sharp feature around 18180 cm^{-1} corresponds to the fluorescence from excitation of the $^2P_0$ ($6d^27s^2$,E=2558.1 cm^{-1}) to a J=0 level (E= 20737.3cm^{-1}) of Th atoms. In the lower panel, the branch features marked with "•" were chosen and recorded in the presence of a static electric field (Stark effect) while those with an "♦" were chosen and recorded in the presence of a static magnetic field (Zeeman effect).

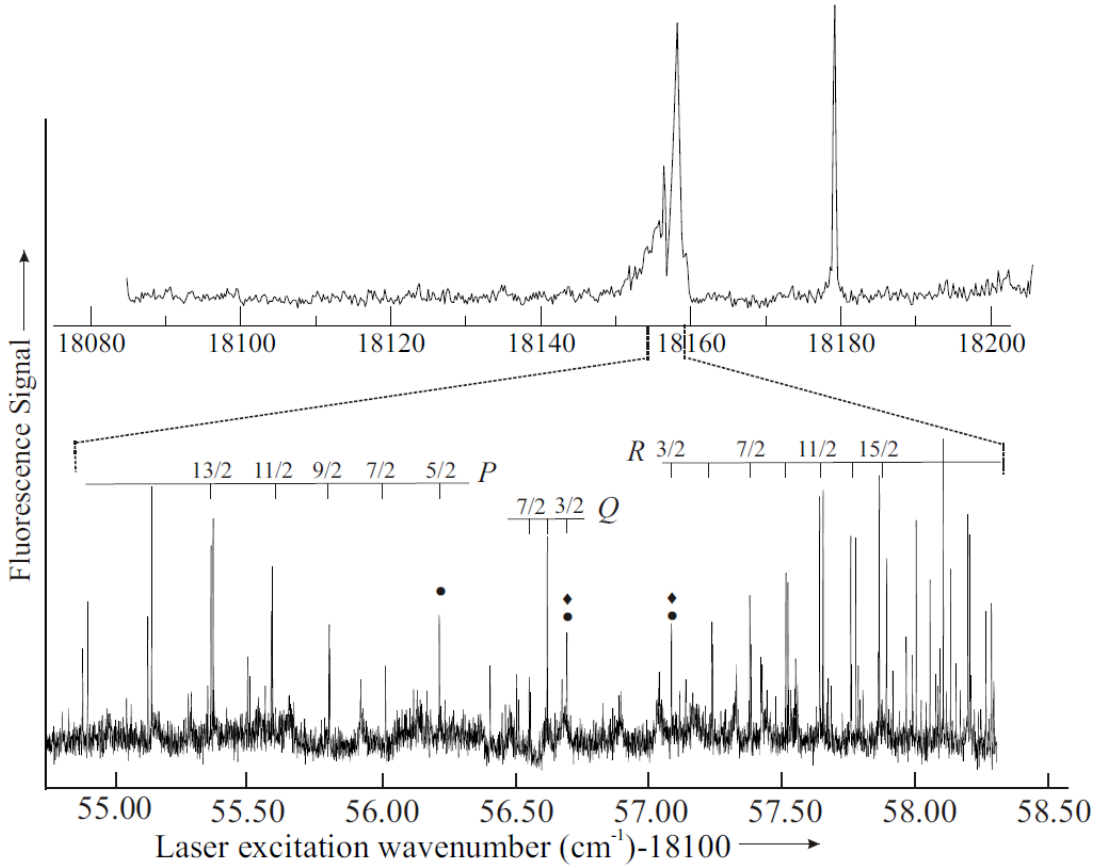

Figure 5.6. Laser excitation spectra of ThCl. Upper panel: the laser excitation spectrum of the [18.2] Ω=3/2 – $X\,^2\Delta_{3/2}$(v′,0) transition extracted from the 2D spectrum. Lower panel: a portion of the high-resolution, field-free, spectrum of the [18.2] Ω=3/2 – $X\,^2\Delta_{3/2}$(v',0) band and associated assignments.

Figure 5.7 shows the DLIF spectrum corresponding to the excitation near the band head at 18158 cm^{-1}. The measured $\Delta G_{1/2}$ and $\Delta G_{3/2}$ spacings gives ω_e = 341(14) cm^{-1}

which agrees with the previously determined values[12]. The high-resolution spectrum ranging from 18,154.8 to 18,558.3 cm^{-1} of this band was recorded using the cw-dye laser excitation. The spectrum is presented in the lower panel of Figure 5.8. The splitting due to the ^{35}Cl(I=3/2) or ^{37}Cl(I=3/2) magnetic and nuclear electric quadrupole hyperfine interactions was not observed. In contrast with ThF, there is significant contribution from the Ω-doubling which has been expected to depend on J^3. The splitting in the $R(J\text{-}1)$, $Q(J)$ and $P(J+1)$ lines gives identical values demonstrates that the Ω- doubling is resulted from the excited state Ω-doubling. The spectra of both isotopologues, $Th^{35}Cl$ and $Th^{37}Cl$ were recorded and analyzed. Then Ω=3/2 is assigned in both ground and excited state based on the observation of the lowest branch features and thus, the band is assigned as the [18.2] $\Omega=3/2 - X\,^2\Delta_{3/2}(v',0)$ transition. The least-square fitting was performed with the input involving the precisely measured transition frequencies of 80 branch features of $Th^{35}Cl$ and 46 of $Th^{37}Cl$. Those peaks along with their assignments and residuals are presented in Table 5.4 and Table 5.5.

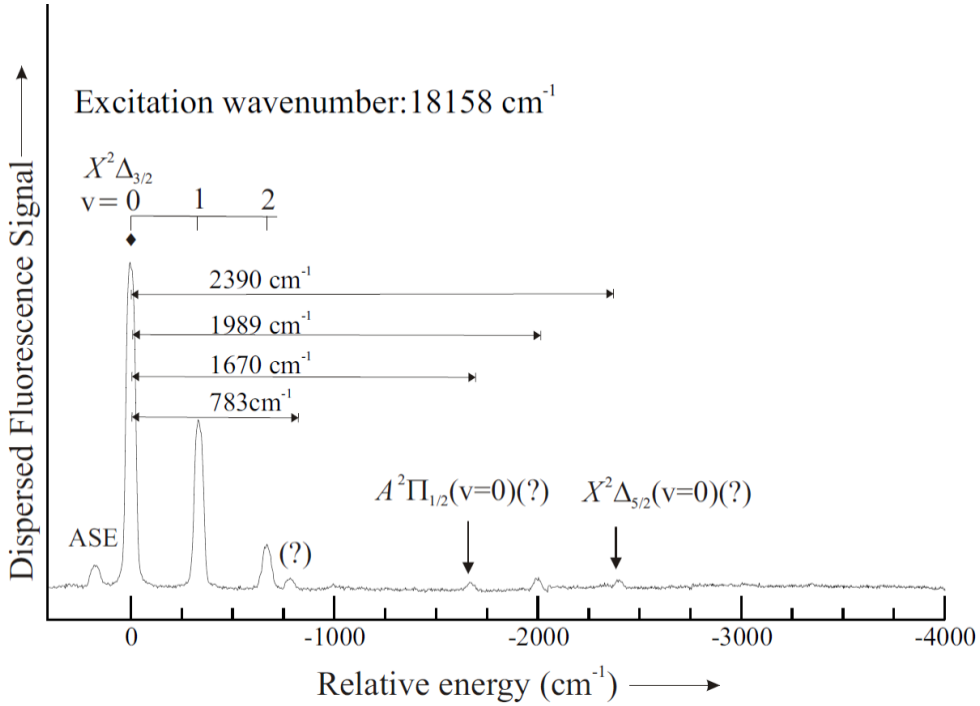

Figure 5.7. High resolution DLIF spectrum resulting from pulsed dye laser excitation of near the *R*-branch head (ν=18158 cm^{-1}) of the [18.2] **Ω**=3/2 – $X^2\Delta_{3/2}$(v′,0) band of ThCl.

Table 5.4. The observed and calculated field-free transition wavenumbers for the [18.2] Ω=3/2 – $X\,^2\Delta_{3/2}$(v′,0) band of $Th^{35}Cl$.

J	R_a		Q_a		P_a	
	Obs.[a]	Dif.[b]	Obs.	Dif.	Obs.	Dif.
3/2	7.1306	0.0004	6.7075	0.0004		
5/2	7.2783	-0.0008	6.6875	0.0006	6.2634	-0.0004
7/2	7.4186	-0.0004	6.6588	0.0004	6.0676	0.0014
9/2	7.5509	-0.0006	6.6218	0.0003	5.8603	-0.0001
11/2	7.6741	-0.0007	6.5762	0.0001	5.6457	-0.0005
13/2	7.7893	-0.0001	6.5224	0.0003	5.4233	-0.0002
15/2	7.8949	-0.0003	6.4598	0.0004	5.1918	-0.0003
17/2	7.9910	-0.0011	6.3869	-0.0010	4.9516	-0.0005
19/2	8.0794	-0.0005	6.3065	-0.0009	4.7025	-0.0007
21/2	8.1580	-0.0006			4.4451	-0.0003
23/2	8.2274	-0.0006			4.1775	-0.0010
25/2	8.2885	0.0005			3.9025	0.0000
27/2	8.3389	0.0004			3.6175	0.0002
29/2	8.3808	0.0013			3.3225	-0.0001

31/2	8.4126	0.0018			3.0187	0.0002
33/2	8.4306	-0.0016				
35/2	8.4437	-0.0001				
	R_b		Q_b		P_b	
	Obs.[a]	Dif.[b]	Obs.	Dif.	Obs.	Dif.
3/2	7.1310	-0.0001	6.7075	0.0002		
5/2	7.2809	-0.0003	6.6883	0.0005	6.2634	-0.0006
7/2	7.4236	-0.0003	6.6610	0.0004	6.0676	0.0005
9/2	7.5583	-0.0008	6.6264	0.0005	5.8622	-0.0004
11/2	7.6872	0.0002	6.5841	0.0003	5.6501	-0.0004
13/2	7.8079	0.0002	6.5351	0.0008	5.4313	0.0002
15/2	7.9215	0.0001	6.4787	0.0010	5.2041	-0.0002
17/2	8.0284	0.0003	6.4135	-0.0005	4.9701	-0.0003
19/2	8.1281	0.0002	6.3432	-0.0002	4.7293	-0.0001
21/2	8.2218	0.0009			4.4811	-0.0003
23/2	8.3078	0.0005			4.2268	0.0003
25/2	8.3882	0.0010			3.9657	0.0008
27/2	8.4614	0.0008			3.6975	0.0009
29/2	8.5287	0.0009			3.4222	0.0004
31/2	8.5891	0.0004			3.1407	0.0001
33/2	8.6427	-0.0008				
35/2	8.6901	-0.0022				
	Std. dev. fit =0.00066 cm^{-1}					

a) Observed transition wavenumber (cm^{-1}) -18150.0.

b) Observed- calculated transition wavenumber (cm^{-1}).

Table 5.5. The observed and calculated field-free transition wavenumbers for the [18.2] $\Omega=3/2 - X^2\Delta_{3/2}(v',0)$ band of $Th^{37}Cl$.

J	R_a		Q_a		P_a	
	Obs.[a]	Dif.[b]	Obs.	Dif.	Obs.	Dif.
3/2	7.1833	0.0001	6.7796	0.0001		
5/2	7.3253	-0.0005	6.7614	0.0007	6.3561	-0.0008
7/2	7.4604	-0.0001	6.7341	-0.0001	6.1688	-0.0003
9/2	7.5875	0.0001			5.9732	-0.0005
11/2	7.7072	0.0009			5.5594	0.0002

13/2	7.8175	0.0004			5.3401	0.0000
15/2	7.9200	0.0003			5.1138	0.0009
17/2	8.0150	0.0010			4.8777	0.0003
19/2	8.1002	0.0003			4.6337	0.0000
21/2	8.1777	0.0003			4.3817	0.0001
23/2	8.2463	0.0000				
25/2						
27/2	8.3565	-0.0014				
	R_b		Q_b		P_b	
	Obs.	Dif.	Obs.	Dif.	Obs.	Dif.
3/2	7.1833	-0.0007	6.7796	-0.0001		
5/2	7.3271	-0.0007	6.7614	-0.0001	6.3561	-0.0010
7/2	7.4647	0.0002	6.7365	0.0003	6.1688	-0.0011
9/2	7.5947	0.0004			5.9756	-0.0001
11/2	7.7177	0.0003			5.5663	0.0001
13/2	7.8343	0.0006			5.3509	-0.0003
15/2	7.9439	0.0004			5.1306	0.0011
17/2	8.0472	0.0005			4.9012	0.0001
19/2	8.1434	-0.0002			4.6666	0.0001
21/2	8.2329	-0.0012			4.4250	-0.0003
	Std. dev. fit =0.00056 cm^{-1}					

a) Observed transition wavenumber (cm^{-1}) -18150.0.

b) Observed- calculated transition wavenumber (cm^{-1}).

The partially resolved R_a(3/2) (ν=18157.1306 cm^{-1}) and R_b(3/2) (ν=18157.1310 cm^{-1}) lines, and the unresolved Q(3/2) (ν=18156.7075 cm^{-1}) lines were selected to perform the optical Stark studies. The applied electric flied is generated up to 1025 V/cm. Figure 5.8 shows the Stark spectra of the Q(3/2) line recorded in the presence of a 405 V/cm electric field. As being seen from the figure, the Stark spectra has a slight asymmetric shift at lower wavenumbers. The associated energy levels and assignment are also presented in Figure 5.8. The 33 precisely measured Stark shifts along with quantum number assignments and residuals inputted in the lease-square fitting are presented in Table 5.6.

Table 5.6. The observed and calculated Stark shifts for the [18.2] $\Omega=3/2 - X^2\Delta_{3/2}(v',0)$ band of $Th^{35}Cl$.

Assignment					Shift (MHz)		
Branch, pol.	J'	$M_{J'}$	J''	$M_{J''}$	Obs	Obs-Calc	Field (V/cm)
$R(3/2)$, ‖	5/2	+3/2	3/2	+3/2	-157	6	759
	5/2	+1/2	3/2	+1/2	-36	11	
	5/2	-1/2	3/2	-1/2	60	-4	
	5/2	-3/2	3/2	-3/2	184	14	
	5/2	+3/2	3/2	+3/2	-219	-3	1013
	5/2	+1/2	3/2	+1/2	-43	15	
	5/2	-1/2	3/2	-1/2	91	8	
	5/2	-3/2	3/2	-3/2	230	2	
$Q(3/2)$, ‖	3/2	+3/2	3/2	+3/2	237	15	759
	3/2	+1/2	3/2	+1/2	65	-2	
	3/2	-1/2	3/2	-1/2	-81	5	
	3/2	-3/2	3/2	-3/2	-249	-14	
$R(3/2)$, ‖	5/2	+3/2	3/2	+3/2	-95.75	14	506
	5/2	+1/2	3/2	+1/2	-37.52	-4	
	5/2	-1/2	3/2	-1/2	56.11	15	
	5/2	-3/2	3/2	-3/2	117	4	
	5/2	+3/2	3/2	+3/2	-109	1	
	5/2	+1/2	3/2	+1/2	-28	5	
	5/2	-1/2	3/2	-1/2	36	-5	
	5/2	-3/2	3/2	-3/2	113	0	405
	5/2	+3/2	3/2	+3/2	-100	-12	
	5/2	+1/2	3/2	+1/2	-33	-6	
	5/2	-1/2	3/2	-1/2	31	-1.13	
	5/2	-3/2	3/2	-3/2	93	3	
$Q(3/2)$, ⊥	3/2	+1/2	3/2	-1/2	275	-11	405
	3/2	-1/2	3/2	-3/2	202	-0.91	
	3/2	+1/2	3/2	+3/2	122	1.15	
	3/2	+3/2	3/2	-1/2	-122	5.68	
	3/2	-3/2	3/2	-1/2	-207	1.38	
$Q(3/2)$, ‖	3/2	+3/2	3/2	+3/2	110	-10.28	405
	3/2	+1/2	3/2	+1/2	36	-1.96	
	3/2	-1/2	3/2	-1/2	-34	9.43	
	3/2	-3/2	3/2	-3/2	-106	17.93	
Std. dev. of fit = 8.8686 MHz							

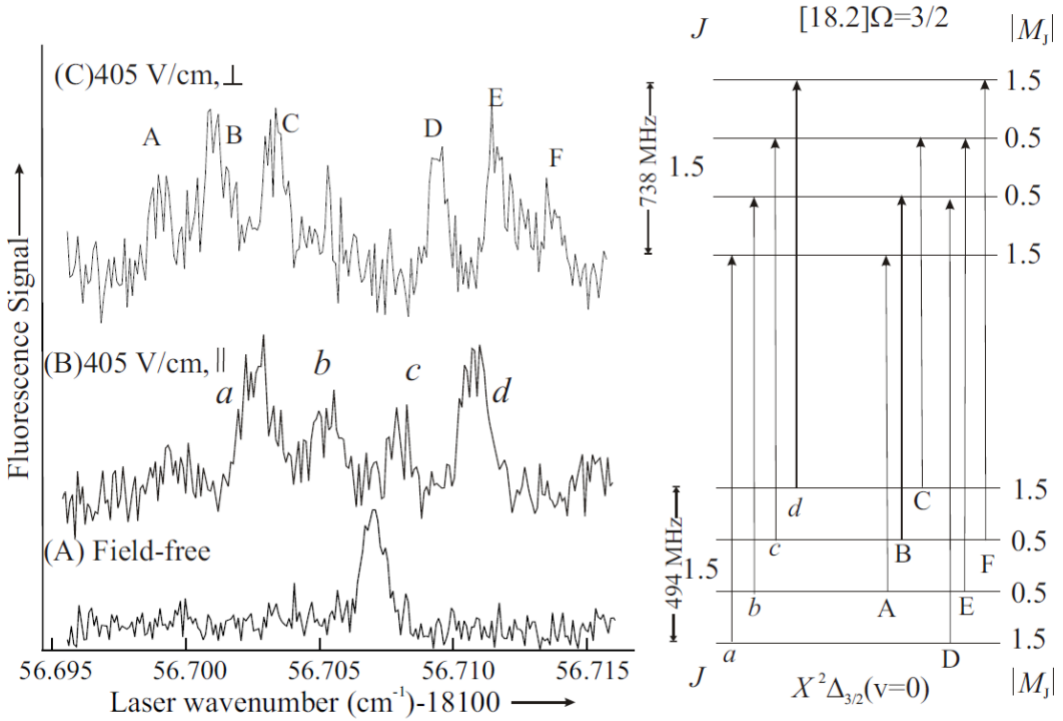

Figure 5.8. Stark spectra of the $Q(3/2)$ line of the ThCl [18.2] Ω=3/2 – $X^2\Delta_{3/2}(v',0)$ band recorded in the presence of a 405 V/cm electric field and associated energy levels and assignment. The energy level spacings were obtained using the optimized set of parameters of Table 5.9.

Four lines $R_a(3/2)$, $R_b(3/2)$, and unresolved $Q(3/2)$ and $P(3/2)$ (ν= 18156.2643 cm^{-1}) lines were selected to perform the optical Zeeman measurements. The spectra for those lines were recorded at fields of 452G and 931G. Figure 5.9 shows the Zeeman spectra of the $P(3/2)$ line involving field-free spectrum along with the spectra under a 931G field with parallel and perpendicular polarization relatively to the cw laser. Similar to the Stark spectra, the Zeeman spectra has a slight asymmetric shift to the low wavenumbers. The fitting involves 55 precisely measured Zeeman shifts was perform and the results along with those lines with their quantum number assignments and residuals are presented in Table 5.7

Table 5.7. The observed and calculated Zeeman shifts for the [18.2] $\Omega=3/2 - X^2\Delta_{3/2}(v',0)$ band of $Th^{35}Cl$.

Assignment					Shift (MHz)		
Branch, pol.	J'	$M_{J'}$	J''	$M_{J''}$	Obs	Obs-Calc	Field (Gauss)
R(3/2), ⊥	5/2	-1/2	3/2	1/2	-208	16	452
	5/2	-3/2	3/2	-1/2	-110	10	
	5/2	5/2	3/2	3/2	-189	-12	
	5/2	-5/2	3/2	-3/2	166	-17	
	5/2	3/2	3/2	1/2	148	19	
	5/2	1/2	3/2	-1/2	230	-8	
Q(3/2), ⊥	3/2	-3/2	3/2	-1/2	-479	4	452
	3/2	-1/2	3/2	1/2	-344	13	
	3/2	1/2	3/2	3/2	-212	17	
	3/2	-1/2	3/2	-3/2	211	1	
	3/2	1/2	3/2	-1/2	347	5	
P(5/2), ⊥	3/2	3/2	5/2	1/2	484	7	452
	3/2	-3/2	5/2	-1/2	-558	12	
	3/2	-3/2	5/2	-5/2	-320	3	
	3/2	-1/2	5/2	1/2	-287	-5	
	3/2	-1/2	5/2	-3/2	-34	3	
	3/2	1/2	5/2	3/2	5.6	-6	
	3/2	1/2	5/2	-1/2	259	5	
	3/2	3/2	5/2	5/2	298	-13	452
P(5/2), ∥	3/2	3/2	5/2	1/2	566	15	931
	3/2	-3/2	5/2	-3/2	-445	2	
	3/2	-1/2	5/2	-1/2	-144	16	
	3/2	1/2	5/2	1/2	116	-16	
R(3/2), ∥	5/2	3/2	3/2	3/2	-166	-9	931
	5/2	1/2	3/2	1/2	-46	0	
	5/2	-1/2	3/2	-1/2	54	-7	
	5/2	-3/2	3/2	-3/2	168	5	
Q(3/2), ∥	3/2	3/2	3/2	3/2	196	6	931
	3/2	-1/2	3/2	-1/2	-75	-3	
	3/2	-3/2	3/2	-3/2	-203	-3	
	3/2	3/2	3/2	3/2	393	13	
	3/2	1/2	3/2	1/2	107	5	
	3/2	-1/2	3/2	-1/2	-162	3	
	3/2	-3/2	3/2	-3/2	-435	-13	
R(3/2), ⊥	5/2	1/2	3/2	3/2	-681	-9	931
	5/2	-1/2	3/2	1/2	-427	19	
	5/2	-3/2	3/2	-1/2	-231	6	
	5/2	3/2	3/2	1/2	276	-3	
	5/2	1/2	3/2	-1/2	513	6	
	5/2	-1/2	3/2	-3/2	731	14	
R(3/2), ∥	5/2	3/2	3/2	3/2	-324	-8	931
	5/2	1/2	3/2	1/2	-66	12	
	5/2	-1/2	3/2	-1/2	156	16	
	5/2	-3/2	3/2	-3/2	352	12	

P(5/2), ∥	3/2	-3/2	5/2	-3/2	-938	0	931
	3/2	-1/2	5/2	-1/2	-348	12	
	3/2	1/2	5/2	1/2	252	11	
	3/2	3/2	5/2	3/2	881	15	
P(5/2), ⊥	3/2	-3/2	5/2	-1/2	-1178	16	931
	3/2	-3/2	5/2	-5/2	-672	6	
	3/2	-1/2	5/2	1/2	-596	15	
	3/2	1/2	5/2	3/2	13	19	
	3/2	-1/2	5/2	-3/2	-96	8	
	3/2	1/2	5/2	-1/2	499	7	
	3/2	3/2	5/2	5/2	641	16	931
Std. dev. of fit = 11.1591 MHz							

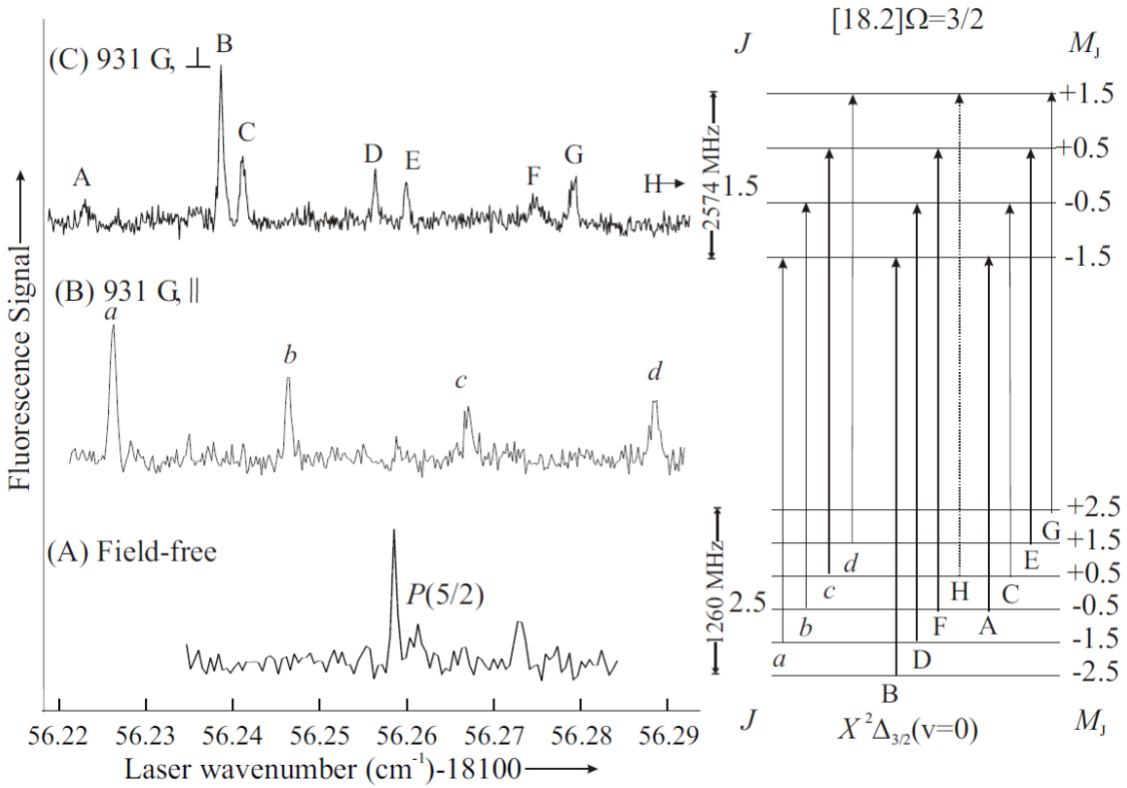

Figure 5.9. The Zeeman spectra of the *P*(3/2) of the ThCl [18.2] **Ω**=3/2 – $X^2\Delta_{3/2}$(v′,0) band recorded field free and in the presence of a 931G field with parallel and perpendicular polarization and the associated assignment. The energy level spacings were obtained using the optimized set of parameters of Table 5.9.

5.3. Analysis

There is not any observed contribution originating from the local perturbation from both the [18.6] Ω=3/2 – $X^2\Delta_{3/2}$ band of ThF and the [18.2] Ω=3/2 – $X^2\Delta_{3/2}$ band of ThCl.

Based on previous studies[10, 12] the $X^2\Delta$ states of both molecules are treated according to the Hund's case(a) coupling limit along with the previously determined spin-orbit splitting[10, 12] to be 2575 cm^{-1} and 3498 cm^{-1} for ThF and ThCl, respectively. For the analysis performed here, the [18.6] Ω=3/2 and [18.2] Ω=3/2 states were treated as components of $^2\Delta$ states with identical spin-orbit splitting to the ground state counterparts. This Hund's case(a) picture assists in making a comparison with the *ab initio* predictions. Since there is not observed hyperfine splitting in the spectra, the effective Hamiltonian operator used to model the energies and wave functions of these $^2\Delta$ states involved spin-orbit, rotational, and Ω-doubling terms[19]. The spin-orbit parameters, A, for the $X^2\Delta$ states, staying the same values for the excited $^2\Delta$ states, were kept fixed to 1287.5 cm^{-1} for ThF and 1749 cm^{-1} for ThCl, as being determined previously measured[10, 12] separation between the $X^2\Delta_{3/2}$ and $X^2\Delta_{5/2}$ states. All precise measured transition wavenumbers were input in a non-linear least square fitting program to obtain optimized set of T_v, B, and $(p_\Delta+4q_\Delta)$ values. The parameter's values and their associated errors for ThF and ThCl are showed in Table 5.8 and 5.9. The final standard deviations of the fits were 0.0003 cm^{-1} and 0.0008 cm^{-1} for ThF and ThCl, respectively. The slightly larger rms for ThCl is noticeable due to the poorer signal to noise of the spectra.

Table 5.8. Spectroscopic parameters for [18.6] **Ω**=3/2 – $X^2\Delta_{3/2}$(v′,0) transition of ThF.

	[18.2] Ω=3/2	$X^2\Delta_{3/2}$(v=0)
Field-free		
B [a]	0.217115(8)	0.233031(9)
T_0 [b]	18574.42255 (12)	
σ [c]	0.00032	
Stark		
$\lvert\mu_{el}\rvert$	0.589(10) D	1.426 (19) D
σ	0.00023	
Zeeman		
g_S	2.0023(fix)	2.0023(fix)
g_L	1.079(4)	1.038(4)
g_e	1.156(4)	1.075(4)
σ	0.00033	
	[18.6] **Ω**=3/2	$X^2\Delta_{3/2}$(v=0)

a) B, T_0 and σ in units of wavenumber (cm^{-1}). $\lvert\mu_{el}\rvert$ in units of Debye (D). The numbers in parentheses represent a 2σ error estimate.

b) The spin-orbit parameters, A, of the $X^2\Delta_{3/2}$(v=0) and [18.2] $^2\Delta_{3/2}$ states constrained to 1749 cm^{-1}.

c) Standard deviation of the fit.

Table 5.9. Spectroscopic parameters for [18.2] Ω=3/2 – X $^2\Delta_{3/2}$(v′,0) transition of ThCl.

	[18.2] Ω=3/2		$X^2\Delta_{3/2}$(v=0)	
Field-free				
	$Th^{35}Cl$	$Th^{37}Cl$	$Th^{35}Cl$	$Th^{37}Cl$
B [a]	0.084690(7)	0.080814(9)	0.088671(7)	0.085100(9)
$(p_\Delta+4q_\Delta)$ $(\times10^{-5})$	-3.6338(10)	-3.3078(30)		
T_0 [b]	18156.71516(17)	18156.78696(20)		
σ [c]	0.00066	0.00058		
Stark				
$\lvert\mu_{el}\rvert$	3.020(6) D		2.022(35) D	
σ	0.00030			
Zeeman				
g_S	2.0023(fix)		2.0023(fix)	
g_L [d]	1.3256(45)		1.0656(45)	
g_e	1.6501(45)		1.1301(45)	
σ	0.00037			

a) B, $(p_\Delta+4q_\Delta)$, T_0 and σ in units of wavenumber (cm^{-1}). $\lvert\mu_{el}\rvert$ in units of Debye (D). The numbers in parentheses represent a 2σ error estimate.

b) The spin-orbit parameters, A, of the $X^2\Delta_{3/2}$(v=0) and [18.2] $^2\Delta_{3/2}$ states constrained to 1749 cm^{-1}.

c) Standard deviation of the fit.

d) Value obtained assuming $^2\Delta$ state designation.

The Stark and Zeeman interactions were modelled using standard effective Hamiltonian operators[20]:

$$\hat{H}^{Stark} = -\hat{\mu}_{el}\cdot\hat{E} \qquad 2)$$

and

$$\hat{H}^{Zee} = \hat{\mu}_m\cdot\hat{B} \approx g_L\mu_B B_z\hat{L}_Z + g_S\mu_B\hat{S}_Z B_z\,. \qquad 3)$$

The observed Stark data only depends on the magnitude of the electric dipole moment, $|\mu_{el}|$. The peaks split and shift nearly linearly with respect to the magnitude of the applied electric field. In analyzing the Zeeman data, the part of the magnetic moment depends on the rotation and nuclear spin were ignored because of the anisotropic corrections to the electron spin Zeeman term[20]. The optical Stark and Zeeman studies of ThF and ThCl presented here, the electronic orbital and spin g-factors denoted g_L and g_S, are left varied and not set fixed to the free-electron values of 1.000 and 2.0023, respectively. Either g_L or g_S can be determined since the data are restricted to limited to one spin-orbit component of the $^2\Delta$ states. The g_L values was allowed to vary from the normal value of 1.0 because of the interaction of the $X^2\Delta_{3/2}$ state with other states, g_s was fixed. Based upon the fact that the interaction amongst the low-lying group of other nearby state should make g_L values are slightly greater than 1.000 and then gives a slight increase upon rotational excitation[21], g_S was set fixed to the free electron value of 2.002 and use g_L as the fitting parameter. It confirmed that there are perturbation resulting from the departure of the states from $^2\Delta$ character.

Initial processing of the observed Stark and Zeeman shifts were performed employing the simple expressions derived from degenerate perturbation theory[20]. The resulting residuals representing small systematic trends were observed and an alternative, the more complete matrix representation approach was employed in the final data processing. The matrix representation of the is diagonalized in M_J, the projection of total angular momentum, for eigen values and eigen vectors. The energies were calculated to the level of accuracy of the experimental measurement (≈30 MHz) by truncating the matrix representation to include J = 0.5 through J = 8.5. The standard deviation of the final fits

for the Stark measurements were 7 and 9 MHz for ThF and ThCl, respectively. For the Zeeman measurement, the standard deviation of the final fit is 10 and 11 MHz. The slightly higher standard deviation for ThCl is due to the poorer signal to noise. The determined $|\mu_{el}|$ and g_L values and associated errors and are presented in Table 5.8 and Table 5.9 for ThF and ThCl, respectively.

5.4. Discussion

Least-square fitting of identified peaks in the DLIF spectra of ThF (in Figure 5.2) at 17712, 17865 and 18575 cm^{-1} gives a better values of ground vibrational parameters (ω_e=600.6±4 cm^{-1}, $\omega_e x_e$ =1.2 ± 1/2 cm^{-1}) and a T_0 (for the $X^2\Delta_{5/2}$ state (=2593 ± 10 cm^{-1} in comparison with the previous determined values[10]. There are features in the ThF DLIF spectra (Figure 5.2) which are shifted by 3158± 10 cm^{-1} and 4130 ± 10 cm^{-1} from the excitation laser. These features are identified as the emission to low-lying excited states. The calculations by Barket et al.[10] employing MRCI + SO-CI at the CCSD(T) level of theory predicted values[10] for the $X^2\Delta_{3/2}$, $X^2\Delta_{5/2}$, $A^2\Pi_{1/2}$ and $A^2\Pi_{3/2}$ states shifting from the $Th^+(7s^26d^1)$ configuration are 0, 1939, 4253, and 6134 cm^{-1}, respectively. Additionally, those energy arising from those states which were predicted using the four-component relativistic calculation prediction[22] gives 0, 2415 3132, and 6099 cm^{-1}, respectively. Based on the values obtaining from the four-component relativistic calculation for $T_0(X^2\Delta_{5/2})$ (2582 ± 10 cm^{-1} vs. 2415 cm^{-1}), the observed energy shift of 3158 cm^{-1} was assigned to the $A^2\Pi_{1/2}$ state. Excitation of the 17865 cm^{-1} band exhibits more emission to the $A^2\Pi_{1/2}$ state than excitation of either the 18 575 or 17 712 band. Consequently, the excited state associated with the 17865 cm^{-1} band should have Ω assigned to be Ω=1/2. With this

approach, the absence of emission to the $X^2\Delta_{5/2}$ state in the 17865 cm^{-1} band DLIF spectrum becomes understandable.

There is no evidence of local perturbation in analyzing the spectra. Both rotational spectra of $Th^{35}Cl$ and $Th^{37}Cl$ were processed and assigned. The ratio of the optimized rotational constants, $B(Th^{35}Cl)/B(Th^{37}Cl)$, is 1.0493 and 1.0487 for the ground state and the excited state, respectively. The ratio of the reduced masses is 1.0493 so the ground state in particular is very well behaved and the ratio for the excited state is close to the theoretical value.

Analysis of the DLIF spectrum of ThCl (Figure 5.7) produces ground vibrational constants was determined as ω_e =342.3± 1.4 cm^{-1} and $\omega_e x_e$ =1.02 cm^{-1}. The combination of the vibrational isotope shifts for T_0 and the ground state vibrational constants gives an ω_e for the [18.2] Ω=3/2 state of approximately 338 cm^{-1}. In Figure 5.7 presenting the DLIF spectrum for ThCl, there are additional features shifted from the laser by 783 ± 15, 1670 ± 15, 1989 ± 15 and 2390 ± 15 cm^{-1}, along with features assigned to vibrational mode of the $X^2\Delta_{3/2}$ state. There are no features shifted from the laser by the value of 3498 cm^{-1}, which was previously assigned to emission to the $X^2\Delta_{5/2}$ state. The theoretical calculations[12] predicts energies corresponding to the $X^2\Delta_{3/2}$, $X^2\Delta_{5/2}$, $A^2\Pi_{1/2}$, and $A^2\Pi_{3/2}$ states associated with the $Th^+(7s^26d^1)$ configuration are 0, 3050, 1820, and 4288 cm^{-1}, respectively. Also, those calculations provide energies for the $^4\Phi_{3/2}$, $^4\Phi_{5/2}$, $^4\Sigma_{1/2}$, and $^4\Sigma_{3/2}$ states originating from the $Th^+(7s^16d^2)$ configuration 3641, 5198, 4107, and 4796 cm^{-1}, respectively. In the observed DLIF spectrum of ThCl, there are three features being observed, features shifted by 1670 ± 15, 1989 ± 15 cm^{-1} and by 2390 ± 15 cm^{-1} from the excitation laser. To assign those feature, ThCl bond is needed to consider, the Th-Cl's distance is much further than

in ThF, consequently, the electrostatic repulsion is weak, there is less number of states originating. It is undoubtful to assign those features shifted by 1670 ± 15 and 1989 ± 15 cm^{-1} relative to the laser emission to the v = 0 and 1 levels of the $A^2\Pi_{1/2}$ state, whereas the feature shifted by 2390 ± 15 cm^{-1} is the emission to the v=0 level of the $X^2\Delta_{5/2}$ state.

Table 5.10. Dipole moments of ThX (X=F, Cl, O, S) and UF.

	ThF ($X\ ^2\Delta_{3/2}$)	ThCl($X\ ^2\Delta_{3/2}$)	ThO ($X\ ^1\Sigma^+$)	ThS($X\ ^1\Sigma^+$)	UF($X(1)4.5$)
$\lvert\mu_{el}\rvert$ (D)	1.426	2.023	2.022	4.58	2.01
R(Å)	2.02937	5/2009	1.84018	2.3436	2.030
$\lvert\mu_{el}\rvert/R$ (D/Å)	0.7026	0.8085	1.0988	1.95	0.99
q(eff) [a]	0.146e	0.168e	0.229e	0.406e	0.206e
Config.	$Th^+(7s^26d^1)$	$Th^+(7s^26d^1)$	$Th^{2+}(7s^2)$	$Th^{2+}(7s^2)$	$U^+(5f^3\,7s^2)$
Δ(Elec. Neg.)[b]	2.68	1.86	2.14	1.28	2.60

a) The effective point charge needed to reproduce the observed $\lvert\mu_{el}\rvert$ for the observed bond distances.
b) Difference in electronegativity between the ligand and the metal.

The experimentally measured dipole moments of ThF and ThCl are compared with those of other thorium containing molecules and UF in Table 5.10. The table includes bond distances, R, the reduced dipole moments, $\mu_{el}^{Red.} \equiv \lvert\mu_{el}\rvert/R$, which emphasizes on the electronic contribution, the effective nuclear charge, q^{eff}, and the difference of the Pauling electro- negativities of F, Cl, O, and S and those of the metal. The effective nuclear charge is calculated as the ratio of the the observed $\lvert\vec{\mu}_{el}\rvert$ values and the corresponding bond

lengths. The bond lengths for ThF and ThCl are from the current study and those for ThO, ThS, and UF from previous studies including Ref.[23], Ref.[24] and Ref[15], respectively. The trending of the reduced dipole moments $\mu_{el}^{Red.}$ and q^{eff} values amongst isovalent molecule is ThF < ThCl and ThO < ThS, which is opposite to the trending order of the electronegativity differences (ThF > ThCl and ThO > ThS). This can be understood by through interfering the dominant configurations and polarization of the Th-metal centered electrons. Each of these four molecules has the 7*s* orbital in those molecules occupied by two electrons. The localization of the electrons will tend to hybridize the orbital and hence shift the electron density away from the electrophilic ligand center. Consequently, the electron distribution is reduced along the nuclei's bond. The induced dipole moment associated with polarization of the Th-metal centered electrons opposes that of the primary moment. The net permanent dipole moment ends up having a small value. This effect reduces with the increase of the molecule's bond distance, and hence smaller hybridization, causes induced dipole moments in ThS and ThCl to be smaller than that for ThF and ThO resulting in $\mu_{el}^{Red.}$ and q^{eff} for ThF and ThO being smaller than those for ThS and ThCl.

In the Hund's case (a) effective Hamiltonian approach used here $g_e = \Lambda g_L + g_S \Sigma$ with g_L and g_S treated as variables to account for mixing of electronic states. The determined g_e values are 1.075(4) and 1.156(4) for the $X^2\Delta_{3/2}$ and [18.6]Ω=3/2 states of ThF and 1.130(4) and 1.638(4) for the $X^2\Delta_{3/2}$and [18.2]Ω=3/2 states of ThCl. For an isolated pure Hund's case (a) $^2\Delta_{3/2}$ state $g_e = 0.9988$ and for a $^2\Pi_{3/2}$ state $g_e = 2.0011$. The observed g_e values can be reproduced by assuming that the $X^2\Delta_{3/2}$ and [18.6]Ω=3/2 states of ThF and the $X\ ^2\Delta_{3/2}$ and [18.2]Ω=3/2 states of ThCl are composed of 7%, 15%, 13%,

and 64% $^2\Pi_{3/2}$ character, respectively. The ground state of ThCl is predicted[12] to be 92% $^2\Delta_{3/2}$ and 7% $^2\Pi_{3/2}$.

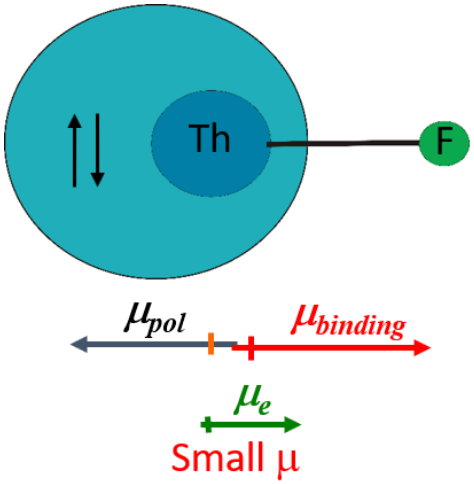

Figure 5.10. The scheme describing the interaction of a pair of electrons on 7s orbital on the ThF bonding

5.5. Conclusion

The most fundamental magneto-static and electrostatic properties of ThF and ThCl have been experimentally determined. Several newly observed bands of ThF were determined. From the Stark 's measurement, the permanent electric dipole moments are unusually small for a metal halide bond because of the polarization of the nonbonding metal-centered valence electrons. Additionally. the demonstrate that the ground state of ThF is nearly a pure $^2\Delta_{3/2}$ as being indicated by the determined g_e values, whereas that for ThCl is more strongly mixed, which is consistent with the weaker electrostatic repulsion due to the longer bond distance. Although diatomic molecules such as ThF and ThCl are the simplest molecules in terms of the number of nuclei involved and geometry, they are also difficult to generate and detect. As in the case of ThF and ThCl, the nonbonding

electrons produce a multitude of low-lying interacting electronic states, which are difficult to model.

5.6. References

1. Huang, P.-W.; Wang, C.-Z.; Wu, Q.-Y.; Lan, J.-H.; Song, G.; Chai, Z.-F.; Shi, W.-Q., Understanding Am3+/Cm3+ separation with H4TPAEN and its hydrophilic derivatives: a quantum chemical study. *Phys. Chem. Chem. Phys.* **2018,** *20* (20), 14031-14039.

2. Kong, X.-H.; Wu, Q.-Y.; Wang, C.-Z.; Lan, J.-H.; Chai, Z.-F.; Nie, C.-M.; Shi, W.-Q., Insight into the Extraction Mechanism of Americium(III) over Europium(III) with Pyridylpyrazole: A Relativistic Quantum Chemistry Study. *J. Phys. Chem. A* **2018,** *122* (18), 4499-4507.

3. Leoncini, A.; Huskens, J.; Verboom, W., Ligands for f-element extraction used in the nuclear fuel cycle. *Chem. Soc. Rev.* **2017,** *46* (23), 7229-7273.

4. Afsar, A.; Distler, P.; Harwood, L. M.; John, J.; Westwood, J., Extraction of minor actinides, lanthanides and other fission products by silica-immobilized BTBP/BTPhen ligands. *Chem. Commun. (Cambridge, U. K.)* **2017,** *53* (28), 4010-4013.

5. Gorden, A. E. V.; DeVore, M. A.; Maynard, B. A., Coordination Chemistry with f-Element Complexes for an Improved Understanding of Factors That Contribute to Extraction Selectivity. *Inorg. Chem.* **2013,** *52* (7), 3445-3458.

6. Heaven, M. C.; Barker, B. J.; Antonov, I. O., Spectroscopy and Structure of the Simplest Actinide Bonds [Erratum to document cited in CA161:686740]. *J. Phys. Chem. A* **2015,** *119* (41), 10440.

7. Heaven, M. C.; Barker, B. J.; Antonov, I. O., Spectroscopy and Structure of the Simplest Actinide Bonds. *J. Phys. Chem. A* **2014,** *118* (46), 10867-10881.

8. Kaledin, L. A.; McCord, J. E.; Heaven, M. C., Laser spectroscopy of UO: characterization and assignment of states in the 0- to 3-eV Range, with a comparison to the electronic structure of ThO. *J. Mol. Spectrosc.* **1994,** *164* (1), 27-65.

9. Field, R. W., Diatomic molecular electronic structure beyond simple molecular constants. *Ber. Bunsenges. Phys. Chem.* **1982,** *86* (9), 771-9.

10. Barker, B. J.; Antonov, I. O.; Heaven, M. C.; Peterson, K. A., Spectroscopic investigations of ThF and ThF+. *J. Chem. Phys.* **2012,** *136* (10), 104305/1-104305/9.

11. Bross, D. H.; Peterson, K. A., Theoretical spectroscopy study of the low-lying electronic states of UX and UX+, X = F and Cl. *J. Chem. Phys.* **2015**, Ahead of Print.

12. Van Gundy, R. A.; Bartlett, J. H.; Heaven, M. C.; Battey, S. R.; Peterson, K. A., Spectroscopic and theoretical studies of ThCl and ThCl+. *J. Chem. Phys.* **2017,** *146* (5), 054307/1-054307/8.

13. Schall, H.; Gray, J. A.; Dulick, M.; Field, R. W., Sub-Doppler Zeeman spectroscopy of the cerium oxide (CeO) molecule. *J. Chem. Phys.* **1986,** *85* (2), 751-62.

14. Heaven, M. C.; Goncharov, V.; Steimle, T. C.; Ma, T.; Linton, C., The permanent electric dipole moments and magnetic g factors of uranium monoxide. *J. Chem. Phys.* **2006,** *125* (20), 204314/1-204314/11.

15. Linton, C.; Adam, A. G.; Steimle, T. C., Stark and Zeeman effect in the [18.6]3.5 - X(1)4.5 transition of uranium monofluoride, UF. *J. Chem. Phys.* **2014,** *140* (21), 214305/1-214305/7.

16. Jung, J.; Atanasov, M.; Neese, F.; Atanasov, M., Ab Initio Ligand-Field Theory Analysis and Covalency Trends in Actinide and Lanthanide Free Ions and Octahedral Complexes. *Inorg Chem* **2017,** *56* (15), 8802-8816.

17. Matthew, D. J.; Morse, M. D., Resonant two-photon ionization spectroscopy of jet-cooled UN: Determination of the ground state. *J. Chem. Phys.* **2013,** *138* (18), 184303/1-184303/7.

18. Edvinsson, G.; Selin, L. E.; Aslund, N., Band spectrum of ThO. *Ark. Fys.* **1965,** *30* (22), 283-319.

19. Brown, J. M.; Cheung, A. S. C.; Merer, A. J., Λ-Type doubling parameters for molecules in Δ electronic states. *J. Mol. Spectrosc.* **1987,** *124* (2), 464-75.

20. Brown, J. M.; Carrington, A., *Rotational Spectroscopy of Diatomic Molecules*. Cambridge University Press: 2003; p 1046 pp.

21. Qin, C.; Linton, C.; Steimle, T. C., Optical Zeeman spectroscopy of the (0,0) B4Γ - X4Φ band systems of titanium monohydride, TiH, and titanium monodeuteride, TiD. *J. Chem. Phys.* **2012,** *137* (7), 074301/1-074301/7.

22. Irikura, K. K., Gas-Phase Energetics of Thorium Fluorides and Their Ions. *J. Phys. Chem. A* **2013,** *117* (6), 1276-1282.

23. Dewberry, C. T.; Etchison, K. C.; Cooke, S. A., The pure rotational spectrum of the actinide-containing compound thorium monoxide. *Phys. Chem. Chem. Phys.* **2007,** *9* (35), 4895-4897.

24. Steimle, T. C.; Zhang, R.; Heaven, M. C., The pure rotational spectrum of thorium monosulfide, ThS. *Chem. Phys. Lett.* **2015,** *639*, 304-306.

CHAPTER 6

FLUORESCENCE BRANCHING RATIOS AND MAGNETIC TUNING OF THE VISIBLE SPECTRUM OF SROH

6.1. Introduction

Production of trapped ultracold (<1mK) samples of polyatomic molecules will significantly impact many diverse areas of physics and chemistry. The additional rotational and vibrational degrees of freedom offered by molecules with three and more atoms will open new frontiers in quantum simulation[1], quantum computation[2], tests of fundamental symmetries of nature[3], and studies of inelastic collisions and chemical reactions[4]. Laser cooling and magneto-optical trapping (MOT) allows for production of ultracold and dense atomic samples[5]. However, the absence of closed transitions in molecules significantly hinders optical cycling and laser cooling in even the simplest diatomic species[6]. Recent successful MOTs of SrF[7-8] and CaF[9-12] have invoked interest in similar isoelectronic triatomic molecules SrOH[13] and CaOH[14]. In the case of SrF the (0,0) $A\,^2\Pi_{1/2}$-$X\,^2\Sigma^+$ transition was employed as the laser cooling transition in order to prevent electronic branching[15]. Additionally, the $B^2\Sigma^+ - X^2\Sigma^+$ transition in CaF was used for laser slowing and longitudinal cooling because of its highly diagonal Franck-Condon factors (FCFs) and small $B\,^2\Sigma^+$ to $A\,^2\Pi$ branching ratio[11].

It has been shown[16] that for these molecules the correct choice of laser polarization critically depends upon the sign and magnitude of the magnetic g-factors and the magnetic hyperfine splitting of the levels associated with the optical transition. In the Hund's case

(*a*) limit a $^2\Pi_{1/2}$ state has a negligibly small g-factor and leads to significantly reduced MOT confining forces in the traditional d.c. or type I trapping configuration[16]. The success of the original SrF d.c. MOT is partly due to non-vanishing magnetic tuning in the $A\,^2\Pi_{1/2}$ state caused by mixing with the nearby $B\,^2\Sigma^+$ state. The success of SrF MOT can also be attributed to the fact that the employed $A^2\Pi_{1/2} - X\,^2\Sigma^+$ transition is essentially a Sr^+-centered atomic transition and the bonding remains nearly unchanged upon excitation. As a consequence the branching ratios, $b_{v',v''}$, are very diagonal (i.e. $b_{v',v''} \approx 1$ for $v' = v''$ and $b_{v',v''} \approx 0$ for $v' \neq v''$) permitting a multitude of optical excitations before the vibrational state changes. The $0_0^0\ \tilde{A}^2\Pi_{1/2} - \tilde{X}\,^2\Sigma^+$ transition of SrOH should have similar characteristics: significant $\tilde{A}^2\Pi_{1/2}$ excited state magnetic tuning due to mixing with $\tilde{B}\,^2\Sigma^+$ state and nearly diagonal fluorescence. In addition, SrOH has an advantage over SrF because the proton magnetic hyperfine splitting in the $\tilde{A}^2\Pi_{1/2}$ and $\tilde{X}\,^2\Sigma^+$ states of SrOH is significantly smaller than the ^{19}F hyperfine splitting in $X^2\Sigma^+$ and $A\,^2\Pi_{1/2}$ states of SrF. In SrF four magnetic hyperfine substates have to be addressed with four distinct laser frequencies, whereas SrOH should only require two frequencies because the hyperfine splitting is less than the natural linewidth, reducing the experimental complexity. The success of the SrF MOT was also due to use of a helium buffer gas source[17] to generate a slow, cold, molecular beam sample. This source can also generate a cold, slow, intense beam of SrOH[18], which was then used to demonstrate optical cycling and radiative force deflection[13], and most recently Sisyphus laser cooling reducing the transverse translational temperature from 50 mK to approximately 750 μK[19] in one dimension. However, based upon the SrF studies[20],

it is expected that scattering in excess of 10^4 photons per molecule is required to slow the cryogenic buffer-gas beam of SrOH to below the MOT capture velocity, necessitating multiple re-pumping lasers for de-populating excited vibrational levels of the $\tilde{X}^2\Sigma^+$ state.

Here we report on the near natural linewidth limit recording and analysis of the 0_0^0 $\tilde{B}^2\Sigma^+ - \tilde{X}^2\Sigma^+$, 0_0^0 $\tilde{A}^2\Pi_{3/2} - \tilde{X}^2\Sigma^+$ and 0_0^0 $\tilde{A}^2\Pi_{1/2} - \tilde{X}^2\Sigma^+$ transitions of SrOH recorded field-free and in the presence of a static magnetic field. These spectra are analyzed to produce an improved determination of the energy levels, magnetic tuning, and associated spectroscopic parameters in support of proposed MOT measurements. Dispersed fluorescence (DF) spectra arising from the excitation of these bands are also recorded and analyzed to determine the branching ratios, $b_{v',v''}$. A multi-dimensional Franck-Condon factor (FCF) prediction, accounting for the Duschinsky effect and anharmonicity, is performed to predict $b_{v',v''}$. In what follows, mode ν_2 is the degenerate bending vibration whereas ν_1 and ν_3 are approximately the O-H and Sr-O stretching vibrations, respectively.

Spectroscopic studies of SrOH are relatively limited compared to those for SrF. The field-free spectroscopic parameters for the $\tilde{X}^2\Sigma^+(0,0,0)$ state are well determined from the analysis of the pure rotational spectrum[21-22]. A summary of previous studies of excited electronic states can be found in the manuscripts by the Bernath group[23-25]. Particularly relevant to the present investigation is the work by Presunka and Coxon[26-28], involving the Doppler limited excitations of numerous bands in the $\tilde{B}^2\Sigma^+ - \tilde{X}^2\Sigma^+$ [26] and $\tilde{A}^2\Pi_r - \tilde{X}^2\Sigma^+$ [27-28]electronic systems. As part of those studies, DF from various vibrational levels of the $\tilde{A}^2\Pi$ and $\tilde{B}^2\Sigma^+$states were recorded and analyzed to produce vibrational spacing for the

$\tilde{X}^2\Sigma^+$ state. The intensities of the DF spectra were not analyzed to determine branching ratios, which are crucial for determining the feasibility of magneto-optical trapping. Those studies employed a flowing reactor cell to produce a hot sample, which precluded the measurements of numerous low-*J* branch features, which are relevant to future SrOH MOT experiments.

The most accurate field-free spectroscopic parameters for the $\tilde{X}^2\Sigma^+(0,0,0)$ and $\tilde{A}^2\Pi(0,0,0)$ states come from the work by Wang et. al[25]. In that study the Doppler limited transition wavenumbers for the $0_0^0\ \tilde{C}^2\Pi_r - \tilde{A}^2\Pi_r$ band were combined with Doppler limited transition wavenumbers for the $0_0^0\ \tilde{A}^2\Pi_r - \tilde{X}^2\Sigma^+$ band[29] and the pure rotational transitions[21-22] in a least squares fit to an effective Hamiltonian model. The spectroscopic parameters for the $B^2\Sigma^+(0,0,0)$ state are far less accurately determined and result from the analysis of the Doppler limited spectrum of a high temperature sample, which was performed some time ago[30]. The only previously reported high-resolution optical spectroscopic study of a cold molecular beam sample was that performed as part of an optical-Stark measurement[31] of the $0_0^0\ \tilde{B}^2\Sigma^+ - \tilde{X}^2\Sigma^+$, $0_0^0\ \tilde{A}^2\Pi_{3/2} - \tilde{X}^2\Sigma^+$ and $0_0^0\tilde{A}^2\Pi_{1/2} - \tilde{X}^2\Sigma^+$ transitions and the pump/probe microwave double resonance study[32]. Extensive analysis of the field-free electronic spectrum was not performed as part of that study.

As part of a reaction dynamics study, Oberlander and Parson[33] simulated $\tilde{X}^2\Sigma^+(v_1,v_2,v_3) \rightarrow \tilde{B}^2\Sigma^+(v_1,v_2,v_3)$ excitation spectrum using a multi-dimensional FCF

prediction following a methodology first presented by Sharp and Rosenstock[34]. In addition to assuming harmonic potentials, that prediction treated the Duschinsky effect (i.e. the transformation for relating the normal coordinates of the initial and final electronic states) by assuming that the same internal coordinates can be adopted for the molecule in the two electronic states involved. Similar assumptions (i.e. harmonic potentials and an approximate Duschinsky effect treatment) were employed to estimate the FCFs for the $\tilde{A}^2\Pi_{1/2}(0,0,0) \rightarrow \tilde{X}^2\Sigma^+(v_1,v_2,v_3)$ emission as part of the optical cycling and radiative force deflection study[13, 35]. In the present study we simulate the $\tilde{B}^2\Sigma^+(0,0,0) \rightarrow \tilde{X}^2\Sigma^+(v_1,v_2,v_3)$ and $\tilde{A}^2\Pi_r(0,0,0) \rightarrow \tilde{X}^2\Sigma^+(v_1,v_2,v_3)$ DF spectra using a more accurate way of handling the Duchinsky effect[36-39] as well as use a numerical integration approach to evaluate the vibrational overlap integrals associated with the bending potentials, which are expected to be anharmonic. Our calculation of the bending mode branching ratios, $b_{v',v''}$, agree with experimental measurements, suggesting that the methodology should be applicable to other linear triatomic alkaline earth molecules.

6.2. Observation

Excitation spectra in the 14802 cm^{-1} to 14808 cm^{-1} spectral range of the $0_0^0\tilde{A}^2\Pi_{3/2} - \tilde{X}^2\Sigma^+$ sub-band, the 14540 cm^{-1} to 14545 cm^{-1} spectral range of the $0_0^0\tilde{A}^2\Pi_{1/2} - \tilde{X}^2\Sigma^+$ sub-band, and the 16373 cm^{-1} to 16381 cm^{-1} spectral range of the $0_0^0\tilde{B}^2\Sigma^+ - \tilde{X}^2\Sigma^+$ were recorded and assigned. The observed transition wavenumbers, quantum number assignments, and the residuals from the subsequent analysis (see below)

for the field-free measurements of the $0_0^0\ \tilde{A}^2\Pi - \tilde{X}^2\Sigma^+$ and $0_0^0\ \tilde{B}^2\Sigma^+ - \tilde{X}^2\Sigma^+$ bands are presented in Table 6.1 and Table 6.2, respectively. The spectral features were easily power broadened and exhibited a full width at half maximum width (FWHM) of approximately 50 MHz using an unfocussed laser of approximately 10 mW. Under these low power conditions, a slight asymmetry of the lowest-*J* branch features, presumably due to $\tilde{B}^2\Sigma^+(0,0,0)$ and $\tilde{A}^2\Pi(0,0,0)$ state proton hyperfine interaction, could be detected. There is no contribution to the asymmetry from the proton hyperfine splitting in the $\tilde{X}^2\Sigma^+$, which is less than 1 MHz[21].

Table 6.1. Observed and calculated transition wavenumbers (cm^{-1}) for the $0_0^0\ \tilde{A}^2\Pi_r \leftarrow \tilde{X}^2\Sigma^+$ band of SrOH.

Branch[a]	Obs.[b]	Obs.-calc.	Branch	Obs.	Obs.-calc	Branch	Obs.	Obs.-calc
$P_2(2.5)$	803.6174	0.0008	$R_2(0.5)$	806.1022	-0.0004	$P_1(1.5)$	542.3366	0.0005
$P_2(3.5)$	802.8955	0.0010	$R_2(1.5)$	806.3749	0.0002	$P_1(2.5)$	542.1730	0.0001
$P_2(4.5)$	802.1824	0.0004	$R_2(2.5)$	806.6574	0.0009	$P_1(3.5)$	542.0186	0.0001
			$R_2(3.5)$	806.9582	-0.0007	$P_1(4.5)$	541.8723	-0.0003
$^QP_{21}(2.5)$	805.1041	-0.0004	$R_2(4.5)$	807.2485	-0.0006	$P_1(5.5)$	541.7355	0.0000
$^QP_{21}(3.5)$	804.8782	-0.0001	$R_2(5.5)$	807.5598	-0.0001	$P_1(6.5)$	541.6074	0.0004
$^QP_{21}(4.5)$	804.6625	0.0007	$R_2(6.5)$	807.8792	-0.0011	$P_1(7.5)$	541.4870	-0.0002
$^QP_{21}(5.5)$	804.4561	0.0012				$P_1(8.5)$	541.3754	-0.0006
$^QP_{21}(6.5)$	804.2573	-0.0005	$Q_1(0.5)$	542.6884	0.0000	$P_1(9.5)$	541.2735	-0.0001
$^QP_{21}(7.5)$	804.0693	-0.0010	$Q_1(1.5)$	542.8771	-0.0004	$P_1(10.5)$	541.1797	-0.0001
$^QP_{21}(10.5)$	803.5660	-0.0001	$Q_1(2.5)$	543.0753	-0.0001	$P_1(11.5)$	541.0946	-0.0001
$^QP_{21}(15.5)$	802.9205	0.0005	$Q_1(3.5)$	543.2817	-0.0001	$P_1(12.5)$	541.0183	0.0001

			$Q_1(4.5)$	543.4968	-0.0002	$P_1(13.5)$	540.9509	0.0003
$Q_2(1.5)$	805.1105	-0.0001	$Q_1(5.5)$	543.7204	-0.0003	$P_1(14.5)$	540.8911	-0.0004
$Q_2(2.5)$	804.8873	0.0005	$Q_1(6.5)$	543.9531	-0.0002			
$Q_2(3.5)$	804.6735	0.0008	$Q_1(7.5)$	544.1945	0.0002	${}^{P}Q_{12}(0.5)$	542.3332	0.0007
$Q_2(4.5)$	804.4686	0.0004	$Q_1(8.5)$	544.4444	0.0003	${}^{P}Q_{12}(1.5)$	542.1670	0.0002
$Q_2(5.5)$	804.2736	0.0001				${}^{P}Q_{12}(2.5)$	542.0098	-0.0001
$Q_2(6.5)$	804.0880	-0.0005	${}^{Q}R_{12}(0.5)$	542.8807	-0.0005	${}^{P}Q_{12}(3.5)$	541.8621	0.0004
$Q_2(9.5)$	803.5920	0.0005	${}^{Q}R_{12}(1.5)$	543.0818	0.0004	${}^{P}Q_{12}(4.5)$	541.7221	0.0000
$Q_2(14.5)$	802.9576	0.0001	${}^{Q}R_{12}(2.5)$	543.2904	0.0000	${}^{P}Q_{12}(5.5)$	541.5917	0.0004
			${}^{Q}R_{12}(3.5)$	543.5079	0.0000	${}^{P}Q_{12}(6.5)$	541.4691	0.0001
${}^{S}R_{21}(0.5)$	806.6025	0.0003	${}^{Q}R_{12}(4.5)$	543.7341	0.0000	${}^{P}Q_{12}(7.5)$	541.3553	-0.0001
${}^{S}R_{21}(1.5)$	807.3724	-0.0003	${}^{Q}R_{12}(5.5)$	543.9692	0.0002	${}^{P}Q_{12}(8.5)$	541.2507	0.0002
${}^{R}Q_{21}(1.5)$	806.1060	-0.0002	${}^{Q}R_{12}(6.5)$	544.2123	-0.0003	${}^{P}Q_{12}(9.5)$	541.1545	0.0001
${}^{R}Q_{21}(2.5)$	806.3802	-0.0006	${}^{Q}R_{12}(7.5)$	544.4649	0.0002	${}^{P}Q_{12}(10.5)$	541.0667	-0.0002
${}^{R}Q_{21}(3.5)$	806.6656	0.0005				${}^{P}Q_{12}(11.5)$	540.9883	0.0002
${}^{R}Q_{21}(4.5)$	806.9471	-0.0009	$R_1(0.5)$	543.6644	-0.0001	${}^{P}Q_{12}(12.5)$	540.9181	0.0002
${}^{R}Q_{21}(5.5)$	807.2615	-0.0010	$R_1(2.5)$	544.5042	-0.0001			
${}^{R}Q_{21}(6.5)$	807.5754	-0.0002				${}^{O}P_{12}(1.5)$	541.1969	0.0000
						${}^{O}P_{12}(2.5)$	540.3912	-0.0004
Std. dev. of fit = 0.00044 cm^{-1}								

[a] A ${}^{\Delta N}\Delta J_{F_i'F_i''}(J'')$ branch designation is used. [b] the transition wavenumber – 14000cm^{-1}.

Table 6.2. Observed and calculated transition wavenumbers (cm^{-1}) for the 0_0^0 $B\ ^2\Sigma^+$-$X^2\Sigma^+$ band system of SrOH.

Branch[a]	Obs.[b]	Obs.-calc.	Branch[a]	Obs.[b]	Obs.-calc.
$R_1(1/2)$	77.9305	-0.0009	${}^{P}Q_{12}(1/2)$	77.0028	0.0005
$R_1(3/2)$	78.3689	-0.0004	${}^{P}Q_{12}(5/2)$	76.4403	0.0004
$R_1(5/2)$	78.8145	0.0013	${}^{P}Q_{12}(2.5)$	75.8827	-0.0007
$R_1(7/2)$	79.2627	-0.0004	${}^{P}Q_{12}(7/2)$	75.3325	-0.0005
$R_1(9/2)$	79.7201	0.0011	${}^{P}Q_{12}(9/2)$	74.7900	0.0014
$R_1(11/2)$	80.1815	0.0006	${}^{P}Q_{12}(11/2)$	74.2503	0.0000
$R_1(13/2)$	80.6481	-0.0007	${}^{P}Q_{12}(13/2)$	73.7171	-0.0009
$R_1(15/2)$	81.1234	0.0007			
$R_2(1/2)$	78.7293	-0.0001	$P_1(3/2)$	76.9983	-0.0003
$R_2(3/2)$	79.3189	0.0005	$P_1(5/2)$	76.4353	0.0016
$R_2(5/2)$	79.9147	0.0014	$P_1(7/2)$	75.8734	-0.0015
$R_2(7/2)$	80.5143	0.0001	$P_1(9/2)$	75.3220	-0.0001
$R_2(9/2)$	81.1203	-0.0008	$P_1(11/2)$	74.7747	-0.0005
			$P_1(13/2)$	74.2342	-0.0004
			$P_1(15/2$	73.6996	-0.0003
${}^{R}Q_{21}(1/2)$	78.1457	0.0004			
${}^{R}Q_{21}(3/2)$	78.7248	-0.0009	$P_2(3/2)$	76.6527	-0.0011
${}^{R}Q_{21}(5/2)$	79.3129	0.0006	$P_2(5/2)$	76.2403	0.0004
${}^{R}Q_{21}(7/2)$	79.9059	0.0011	$P_2(7/2)$	75.8309	-0.0011
			$P_2(9/2)$	75.4305	0.0002
			$P_2(11/2)$	75.0347	0.0002
			$P_2(13/2)$	74.6445	-0.0003
			$P_2(15/2)$	74.2601	-0.0010
			$P_2(17/2)$	73.8831	-0.0005
			$P_2(19/2)$	73.5127	0.0007
Std. dev. of fit = 0.00082 cm^{-1}					

[a] A ${}^{\Delta N}\Delta J_{F_i'F_i''}(J'')$ branch designation is used.

[b] The transition wavenumber -16300 cm^{-1}.

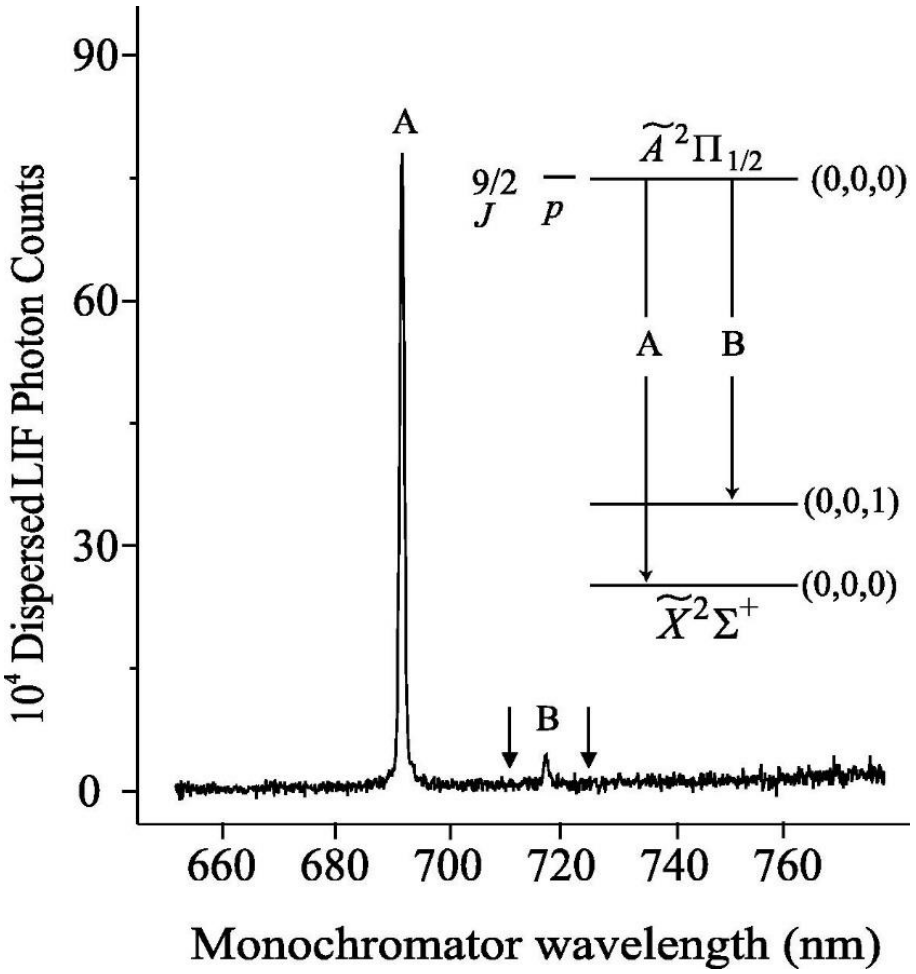

Figure 6.1. The dispersed fluorescence spectrum of the $\tilde{A}^2\Pi_{1/2}(0,0,0)$ state obtained by cw-laser excitation of the $Q_1(9/2)$ (ν = 14453.497 cm^{-1}) line of the 0_0^0 $\tilde{A}^2\Pi_{1/2}$ - $\tilde{X}^2\Sigma^+$ band. The expected locations of the emission to the $\tilde{X}^2\Sigma^+(0,1^1,0)$ and $\tilde{X}^2\Sigma^+(0,2^0,0)$ states are indicated.

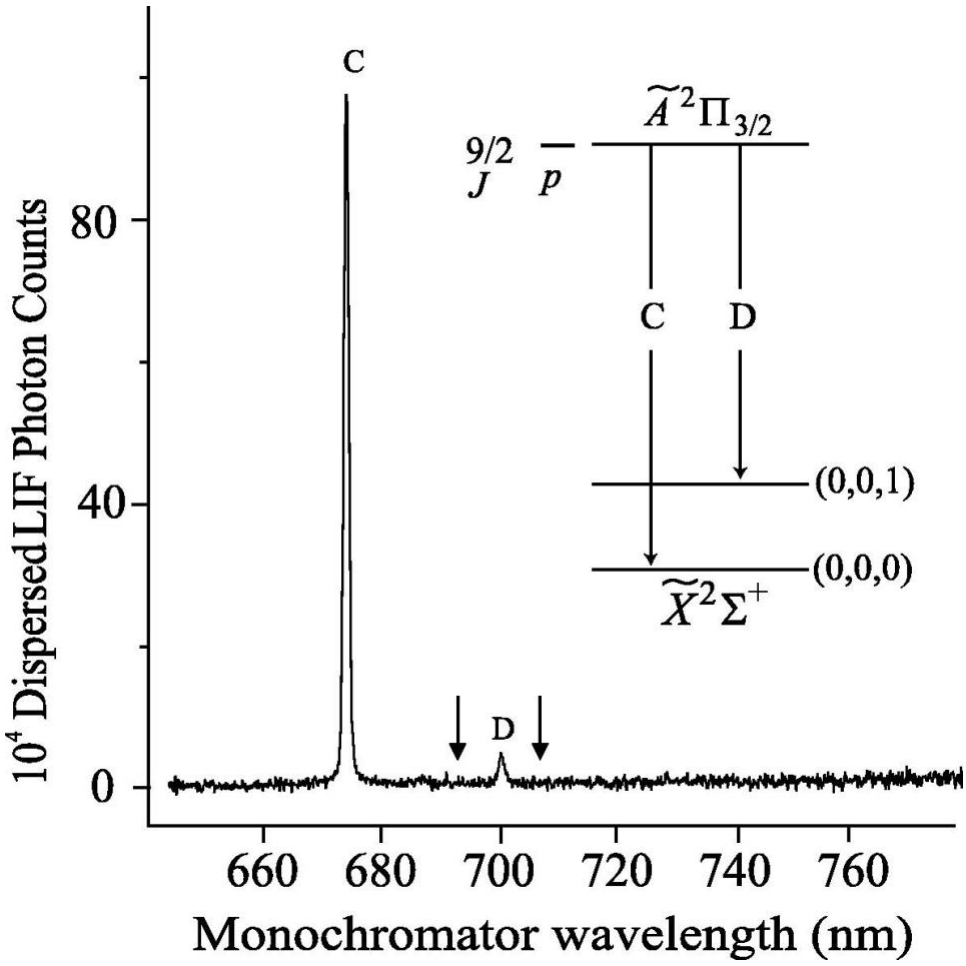

Figure 6.2. The dispersed fluorescence spectrum of the $\tilde{A}^2\Pi_{3/2}(0,0,0)$ states resulting from excitation of the $R_2(7/2)$ (ν = 14806.947 cm^{-1}) line of the $0_0^0\ \tilde{A}^2\Pi_{3/2}$ - $\tilde{X}^2\Sigma^+$ band. The expected locations of the emission to the $\tilde{X}^2\Sigma^+(0,1^1,0)$ and $\tilde{X}^2\Sigma^+(0,2^0,0)$ states are indicated.

The DF spectrum of the $\tilde{A}^2\Pi_{1/2}(0,0,0)$ state was obtained by cw-laser excitation of the $Q_1(9/2)$ line of the $0_0^0\ \tilde{A}^2\Pi_{1/2} - \tilde{X}^2\Sigma^+$ band near 14453.497 cm^{-1} and a typical spectrum is presented in Figure 6.1. The features near 691.8 nm and 718.0 nm are the $0_0^0\ \tilde{A}^2\Pi_{1/2} \rightarrow \tilde{X}^2\Sigma^+$ and $3_1^0\ \tilde{A}^2\Pi_{1/2} \rightarrow \tilde{X}^2\Sigma^+$ transitions, respectively. To account for any

contribution from Sr $^3P_1 \rightarrow {}^1S$ emission (λ_{air} = 689.26 nm) in the observed 691.8 nm feature in Figure 6.1, a background spectrum with the dye laser blocked was recorded and subtracted. To account for any laser scatter, a background spectrum of only the dye laser signal in the absence of a molecular beam was also subtracted. The DF spectrum of the $\tilde{A}^2\Pi_{3/2}(0,0,0)$ states was obtained by cw-laser excitation of the $R_2(7/2)$ line of the 0_0^0 $\tilde{A}^2\Pi_{3/2} - \tilde{X}^2\Sigma^+$ band near 14806.952 cm^{-1} and a typical spectrum is presented in Figure *6.2*. The features near 675.4 nm and 700.2 nm are the $0_0^0\ \tilde{A}^2\Pi_{3/2} \rightarrow \tilde{X}^2\Sigma^+$ and $3_1^0\ \tilde{A}^2\Pi_{3/2} \rightarrow \tilde{X}^2\Sigma^+$ emissions, respectively. As in the case of the $\tilde{A}^2\Pi_{1/2}$ experiments, to account for any contribution from Sr $^3P_1 \rightarrow {}^1S$ emission (λ_{air} = 689.26 nm) in the observed 691.8 nm feature, a background spectrum with the dye laser blocked was recorded and subtracted. Excitation of the $R_1(13/2)$ line of the $0_0^0\ \tilde{B}^2\Sigma^+ - \tilde{X}^2\Sigma^+$ band at 16380.648 cm^{-1} was used for the DF measurement of the $\tilde{B}^2\Sigma^+(0,0,0)$ state, with a typical spectrum presented in Figure *6.3*. In this case the slits of the monochromator were opened slightly to enhance the detection of the non-diagonal peak. The features near 610.5 nm and 630.7 nm are the $0_0^0\ \tilde{B}^2\Sigma^+ \rightarrow \tilde{X}^2\Sigma^+$ and $3_1^0\ \tilde{B}^2\Sigma^+ \rightarrow \tilde{X}^2\Sigma^+$ emissions, respectively. The spectral feature near 690 nm is the Sr $^3P_1 \rightarrow {}^1S$ emission from metastable atoms generated in the laser ablation source. Unlike the DF spectra associated with emission from the $\tilde{A}^2\Pi_{1/2}$ and $\tilde{A}^2\Pi_{3/2}$ levels, subtracting a background spectrum with the dye laser blocked was not performed because the Sr $^3P_1 \rightarrow {}^1S$ emission (λ_{air} = 689.26 nm) does not overlap with SrOH emission features. Also indicated by the arrows in Figure 6.1, Figure *6.2* and Figure *6.3* are

the expected locations of emission to the $\tilde{X}^2\Sigma^+(0,1^1,0)$ and $\tilde{X}^2\Sigma^+(0,2^0,0)$ states. Emission to the $\tilde{X}^2\Sigma^+(1,0,0)$ level, which is expected to be at approximately[40] 3778 cm^{-1} to the red of the excitation, is outside the operating range of the ICCD. The $\tilde{B}^2\Sigma^+(0,0,0) \rightarrow \tilde{X}^2\Sigma^+(1,0,0)$ and $\tilde{A}^2\Pi(0,0,0) \rightarrow \tilde{X}^2\Sigma^+(1,0,0)$ emissions were not detected in the previous flowing reactor DF spectra, indicating a small branching ratio for decays to the excited O-H stretching vibrations, consistent with our calculations (see below).

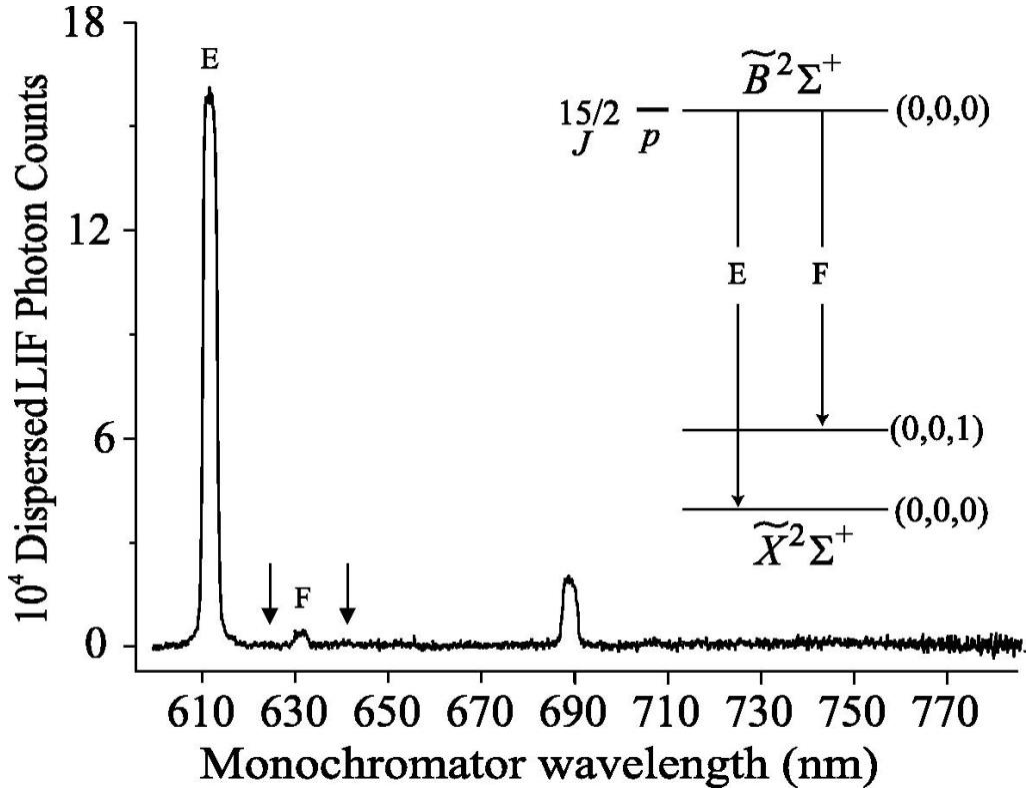

Figure 6.3. The dispersed fluorescence spectrum resulting from excitation of the $R_1(13/2)$ (ν = 16080.648 cm^{-1}) line of the $0_0^0\ \tilde{B}^2\Sigma^+ \leftarrow \tilde{X}^2\Sigma^+$ band and corresponding assignment. The feature near 690 nm is the $^3P_1 \rightarrow {}^1S$ metastable emission (λ_{air} = 689.26 nm) of atomic Sr strontium. The expected locations of the emission to the $\tilde{X}^2\Sigma^+(0,1^1,0)$ and $\tilde{X}^2\Sigma^+(0,2^0,0)$ states are indicated by arrows.

The observed field-free spectrum for the low-J R_{12} and Q_1 branch features of the $0_0^0\ \tilde{A}^2\Pi_{1/2} - \tilde{X}^2\Sigma^+$ band in the 14542.6 cm^{-1} to 14543.1 cm^{-1} spectral range, and the low-J R_2 and ${}^RQ_{21}$ branch features of the $0_0^0\ \tilde{A}^2\Pi_{3/2} - \tilde{X}^2\Sigma^+$ band in the 14805.9 cm^{-1} to 14806.7 cm^{-1} spectral range, are presented in Figure *6.4* and Figure *6.5*, respectively. Also presented are the observed and predicted 477 G Zeeman spectra with parallel (ΔM_J =0) and perpendicular (ΔM_J =±1) orientations relative to linear polarized laser. The $R_{12}(N'')$ and $Q_1(N'')$ branch features and the $R_2(N'')$ and ${}^RQ_{21}(N'')$ branch features are separated by the electron spin-rotation splitting ("ρ-doubling") of the $\tilde{X}^2\Sigma^+(0,0,0)$ state. The observed field-free spectrum for the low-J R_1 and ${}^RQ_{12}$ branch features of the $0_0^0\ \tilde{B}^2\Sigma^+ \rightarrow \tilde{X}^2\Sigma^+$ band in the 16377.9 cm^{-1} to 16378.4 cm^{-1} spectral range along with the observed and predicted 913 G Zeeman spectra are presented in Figure *6.6*. The observed field-free transition wavenumbers, assignments, and observed-calculated residuals are presented in the Table 6.1 and Table 6.2, respectively. The Zeeman induced shifts, spectral assignments and the observed-calculated residuals for the $0_0^0\ \tilde{A}^2\Pi_{1/2} - \tilde{X}^2\Sigma^+$ $0_0^0\ \tilde{A}^2\Pi_{3/2} - \tilde{X}^2\Sigma^+$, and $0_0^0\ \tilde{B}^2\Sigma^+ - \tilde{X}^2\Sigma^+$ bands, respectively, are provided in Table *6.3*, Table 6.4 and Table 6.5.

Table 6.3. The observed and calculated Zeeman shifts of the $0_0^0\ \tilde{A}^2\Pi_{1/2} - \tilde{X}^2\Sigma^+$ band.

Branch, pol.	$\tilde{A}^2\Pi_{1/2}$		$\tilde{X}^2\Sigma^+$				Field-free (cm^{-1})	Shift (MHz)		Field
	J	M_J	J	N	M_S	M_N		Obs.	Obs.-Calc.	G
$Q_1(1/2)$, ll	1/2	-1/2	1/2	0	1/2	0	14542.6884	-1395	-6	913
		1/2	1/2		-1/2	0		1421	33	
$Q_1(3/2)$, ll	3/2	-3/2	3/2	1	1/2	-1	14542.8771	-1333	12	913
		-1/2	3/2		1/2	0		-1283	5	
		1/2	3/2		1/2	1		-1238	-9	
		3/2	3/2		1/2	0		-1069	33	
		-1/2	3/2		-1/2	1		1209	-21	
$R_{12}(1/2)$, ⊥	3/2	1/2	1/2	1	-1/2	-1	14542.8806	1255	1	913
		3/2	1/2		-1/2	0		1379	-2	
$Q_1(5/2)$ ll	5/2	-3/2	5/2	2	1/2	-1	14543.0753	-1241	22	913
		-3/2	5/2		-1/2	2		1166	-19	
$R_{12}(3/2)$, ⊥	5/2	1/2	3/2	2	-1/2	-1	14543.0818	1202	-1	913
	5/2	3/2	3/2		-1/2	0		1312	12	
	5/2	5/2	3/2		-1/2	1		1415	20	
$R_1(1/2)$, ⊥	3/2	-3/2	1/2	0	1/2	0	14543.0753	-1415	0	913
	3/2	1/2	1/2		1/2	0		-1222	9	
	3/2	-1/2	1/2		-1/2	0		1195	-35	
	3/2	3/2	1/2		-1/2	0		1400	-14	
$Q_1(1/2)$, ll	1/2	-1/2	1/2	0	1/2	0	14542.6884	-756	-31	477
	1/2	1/2	1/2		-1/2	0		718	-7	

	3/2	-3/2	3/2	1	1/2	-1	14542.8771	-654	16	477
	3/2	1/2	3/2		1/2	1		-602	41	
	3/2	-3/2	3/2		-1/2	-1		638	-5	
R_{12}(1/2), ⊥	3/2	-1/2	1/2	1	-1/2	1	14542.8806	487	-38	477
	3/2	1/2	1/2		-1/2	-1		628	6	
	3/2	3/2	1/2		-1/2	0		718	12	
Q_1(3/2), ll	3/2	-3/2	3/2	1	1/2	-1	14542.8771	-654	16	477
Q_1(5/2), ⊥	5/2	1/2	5/2	2	1/2	1	14543.0753	-641	-23	477
	5/2	-1/2	5/2		1/2	0		-641	-25	
	5/2	-3/2	5/2		1/2	-1		-641	-29	
	5/2	-3/2	5/2		-1/2	2		587	-32	
R_{12}(3/2), ⊥	5/2	-1/2	3/2	2	-1/2	-2	14542.8771	487	-24	477
		1/2	3/2		-1/2	-1	14543.0818	590	9	
		3/2	3/2		-1/2	0		615	-34	
		5/2	3/2		-1/2	1		705	-9	
Q_1(1/2), ll	1/2	1/2	1/2	0	1/2	0	14542.6884	-617	-8	477
	1/2	-1/2	1/2		-1/2	0		592	-16	
Q_1(3/2) , ll	3/2	3/2	3/2	1	1/2	1	14542.8771	-617	-23	477
	3/2	3/2	3/2		1/2	1		-617	-24	
‖	3/2	-3/2	3/2		-1/2	1		630	36	
R_{12}(3/2) , ⊥‖	5/2	-1/2	3/2	2	-1/2	-1	14543.0818	554	-18	477
		1/2	3/2		-1/2	0		655	-2	
		-3/2	3/2		-1/2	-2		533	55	
		1/2	3/2		-1/2	0		559	-58	
		3/2	3/2	2	-1/2	1	14543.0818	635	-47	
Q_1(5/2) , ll ‖	5/2	3/2	5/2	2	1/2	1	14543.0753	-610	-22	477

		5/2	5/2		1/2	2		-610	-23	
‖		5/2	5/2		1/2	2		-610	-24	
		-5/2	5/2		-1/2	2		597	10	

Table 6.4. The observed and calculated Zeeman shifts of the $0_0^0\ \tilde{A}^2\Pi_{3/2} - \tilde{X}^2\Sigma^+$ band.

Branch, pol.	$\tilde{A}^2\Pi_{3/2}$		$\tilde{X}^2\Sigma^+$				Field-free (cm^{-1})	Shift (MHz)		Field
	J	M_J	J"	*N*	M_S	N		Obs.	Obs.-Calc.	G
$R_2(1/2)$ and $^RQ_{21}(3/2)$, ‖	3/2	1/2	3/2	1	1/2	-1	14806.1022	-910	-41	477
		1/2	3/2	1	1/2	0		-403	-27	
		-3/2	3/2	1	-1/2	-1		-143	-8	
		3/2	3/2	1	1/2	+1		117	-9	
		-1/2	1/2	1	-1/2	+1	14806.1060	325	2	477
		1/2	1/2	1	-1/2	0		910	20	
$R_2(3/2)$ and $^RQ_{21}(5/2)$, ‖	5/2	-3/2	5/2	2	1/2	-2	14806.3749	-928	-61	477
		-1/2	5/2	2	1/2	-1		-724	-47	
		1/2	5/2	2	1/2	0		-521	-34	
		3/2	5/2	2	1/2	1		-317	-22	
		5/2	5/2	2	1/2	2		-114	-12	
		-5/2	5/2	2	-1/2	-2		89	-7	
		-3/2	3/2	2	-1/2	2	14806.3802	216	32	477
		-1/2	3/2	2	-1/2	1		483	32	
		1/2	3/2	2	-1/2	0		737	22	
		3/2	3/2	2	-1/2	-1		991	16	
$^SR_{21}(1/2)$, mixed	3/2	1/2	1/2	0	1/2	0	14806.6025	-422	-13	477
		-1/2	1/2	0	-1/2	0		409	15	

$R_2(5/2)$ and $^{R}Q_{21}(7/2)$, ‖	7/2	-5/2	7/2	3	1/2	-3	14806.6574	-813	-43	477
		-3/2	7/2	3	1/2	-2		-736	-52	
		-1/2	7/2	3	1/2	-1		-654	-49	
		5/2	7/2	3	1/2	3		-349	4	
		7/2	7/2	3	1/2	3		-258	-28	
		-7/2	7/2	3	-1/2	3		181	-44	
		-5/2	5/2	3	-1/2	-3	14806.6656	181	41	477
		-1/2	5/2	3	-1/2	-1		530	59	
		1/2	5/2	3	-1/2	0		685	51	
		3/2	5/2	3	-1/2	1		840	47	
		5/2	5/2	3	-1/2	2		987	38	
$R_2(1/2)$ and $^{R}Q_{21}(3/2)$, ‖	3/2	-1/2	3/2	1	1/2	0	14806.1022	-884	24	477
	3/2	1/2	3/2	1	1/2	-1		-364	-25	
	3/2	-3/2	3/2	1	-1/2	0		-198	8	
	3/2	3/2	1/2	1	1/2	1		143	-15	
	3/2	-1/2	1/2	1	-1/2	0		348	-12	
	3/2	3/2	1/2	1	-1/2	0		1401	-25	
	5/2	-5/2	5/2	2	1/2	-2	14806.1060	-1079	17	477
	5/2	5/2	3/2	2	-1/2	-1		1133	-66	
$^{S}R_{21}(1/2)$, ⊥	3/2	-1/2	1/2	0	1/2	0	14806.6021	-923	17	477
	3/2	-3/2	1/2	0	-1/2	0		-140	-4	
	3/2	3/2	1/2	0	-1/2	0		120	-5	
$R_2(5/2)$ and $^{R}Q_{21}(7/2)$, ‖	7/2	-7/2	7/2	3	1/2	-3	14806.6656	-897	0	477
$R_2(7/2)$ and $^{R}Q_{21}(9/2)$, ‖	9/2	3/2	9/2	4	-1/2	3	14806.9582	1050	59	477

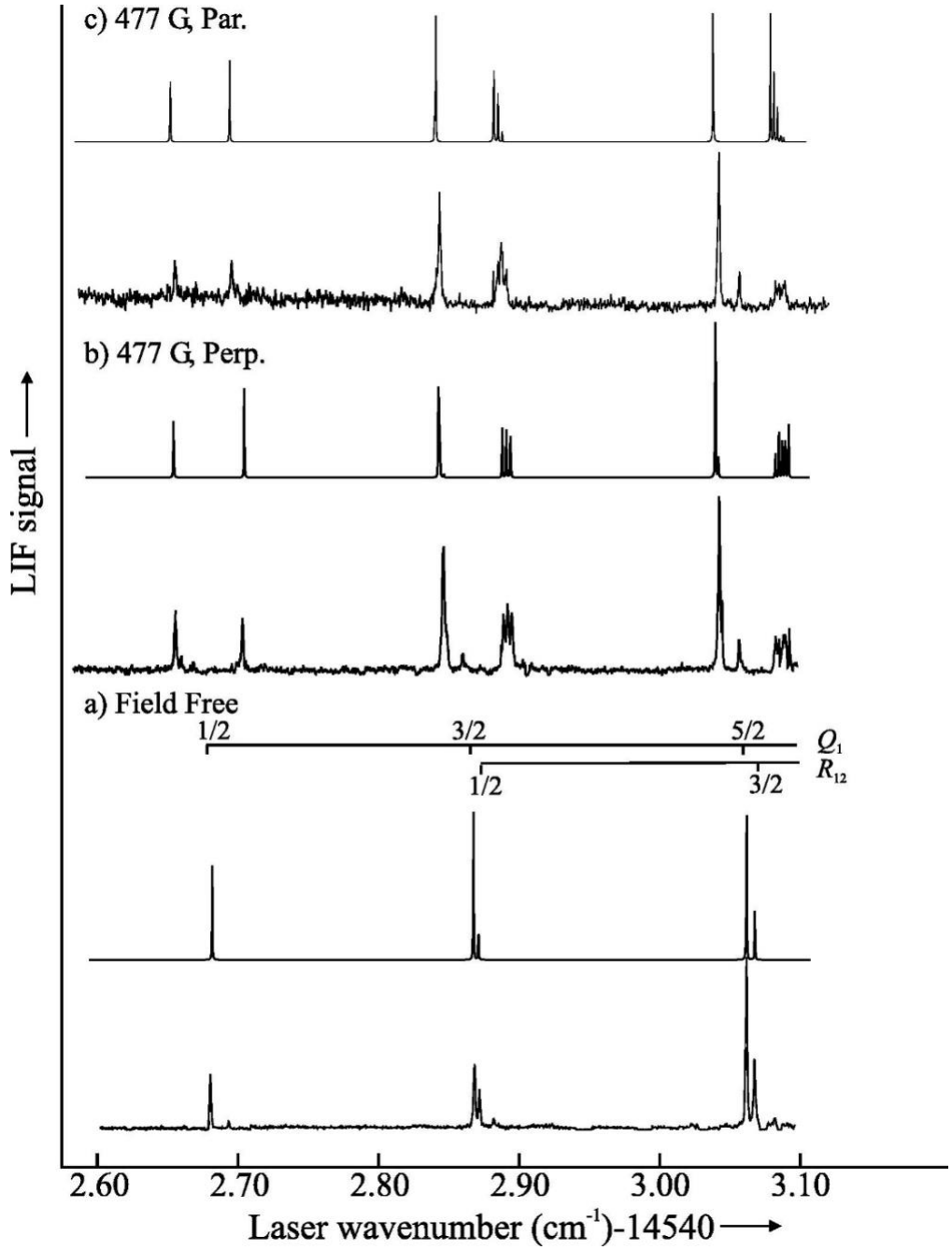

Figure 6.4. The observed and predicted excitation spectra near the origin of the $0_0^0 \tilde{A}^2\Pi_{1/2} - \tilde{X}^2\Sigma^+$ band recorded field-free and in the presence of a 477 G magnetic field oriented perpendicular and parallel to the electric field of the laser radiation.

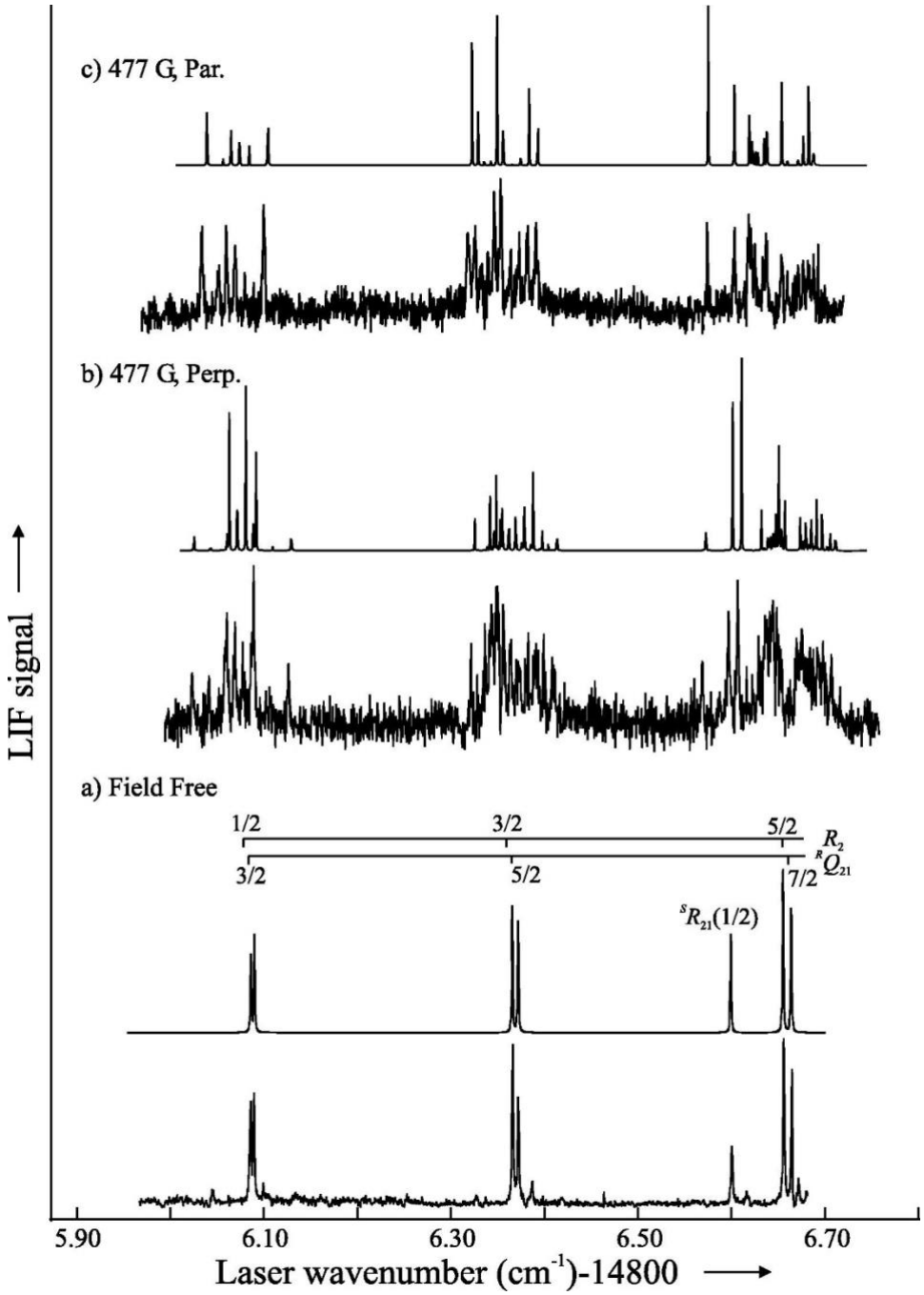

Figure 6.5. The observed and predicted excitation spectra near the origin of the $0_0^0 \tilde{A}^2\Pi_{3/2} - \tilde{X}^2\Sigma^+$ band recorded field-free and in the presence of a 477 G magnetic field orientated perpendicular and parallel to the electric field of the laser radiation.

Table 6.5. The observed and calculated Zeeman shifts of the 0_0^0 $\tilde{B}^2\Sigma^+ - \tilde{X}^2\Sigma^+$ band.

Branch, pol	$\tilde{B}^2\Sigma^+$			$\tilde{X}^2\Sigma^+$				Field-free	Shift (MHz)		Field
	J	N	$M_{J'}$	J	N	M_S	M_N	(cm^{-1})	Obs.	Obs.-Calc.	G
$R_1(3/2)$, ⊥	5/2	2	-3/2	3/2	1	+1/2	-1	16378.3689	-2220	-49	913
			-1/2	3/2		+1/2	1		-1705	-13	
			1/2	3/2		+1/2	1		-1182	-17	
			1/2	3/2		+1/2	-1		-1107	-13	
			3/2	3/2		+1/2	0		-509	1	
			-5/2	1/2		-1/2	+1		-170	0	
			5/2	3/2		+1/2	+1		170	0	
			-3/2	1/2		-1/2	-1		268	27	
			-1/2	1/2		-1/2	0		837	44	
			-1/2	1/2		-1/2	+1		796	-32	
			1/2	1/2		-1/2	-1		1347	28	
			3/2	1/2		-1/2	0		2001	26	
$R_1(3/2)$, ||	5/2	2	-1/2	3/2	1	+1/2	-1	16378.3689	-1643	10	913
			1/2	3/2		+1/2	0		-1100	30	
			3/2	3/2		+1/2	+1		-543	-1	
			-3/2	1/2		-1/2	+1		-326	14	
			-1/2	1/2		-1/2	-1		769	12	
			1/2	1/2		-1/2	0		1373	19	
$P_1(5/2)$ and $^pQ_{12}(3/2)$, ||	3/2	1	-1/2	5/2	2	+1/2	-1	16376.4353	-1916	-47	913
			1/2	5/2		+1/2	0		-1035	-9	
			-3/2	3/2		-1/2	-2	16376.4403	-281	21	

			3/2	5/2		+1/2	+1	16376.4353	152	-41	
			-1/2	3/2		-1/2	-1	16376.4403	458	-15	
			1/2	3/2		-1/2	0		1413	23	
$P_2(3/2)$, ||	1/2	1	+1/2	5/2	2	+1/2	0	16376.6527	-1458	11	913
			-1/2	5/2		+1/2	-1		-409	-15	
			1/2	3/2		-1/2	0		948	0	
			-1/2	3/2		-1/2	-1		1993	44	
$R_1(1/2)$ ⊥	3/2	1	-1/2	1/2	0	+1/2	0	16377.9305	-2026	-51	913
			-3/2	1/2		-1/2	0		-169	-10	
			3/2	1/2		+1/2	0		174	16	
			1/2	1/2		-1/2	0		1494	36	
$R_1(1/2)$, ||	3/2	1	1/2	1/2	0	+1/2	0		-1091	5	
			-1/2	1/2		-1/2	0		577	-1	
${}^{Q}R_{12}(1/2)$, ||	1/2	1	1/2	1/2	0	1/2	0	16378.1457	-511	-11	913
			-1/2	1/2		-1/2	0		1058	41	
${}^{Q}R_{12}(1/2)$, ⊥	1/2	1	-1/2	1/2	0	1/2	0		-1523	14	913
			1/2	1/2		-1/2	0		2071	18	

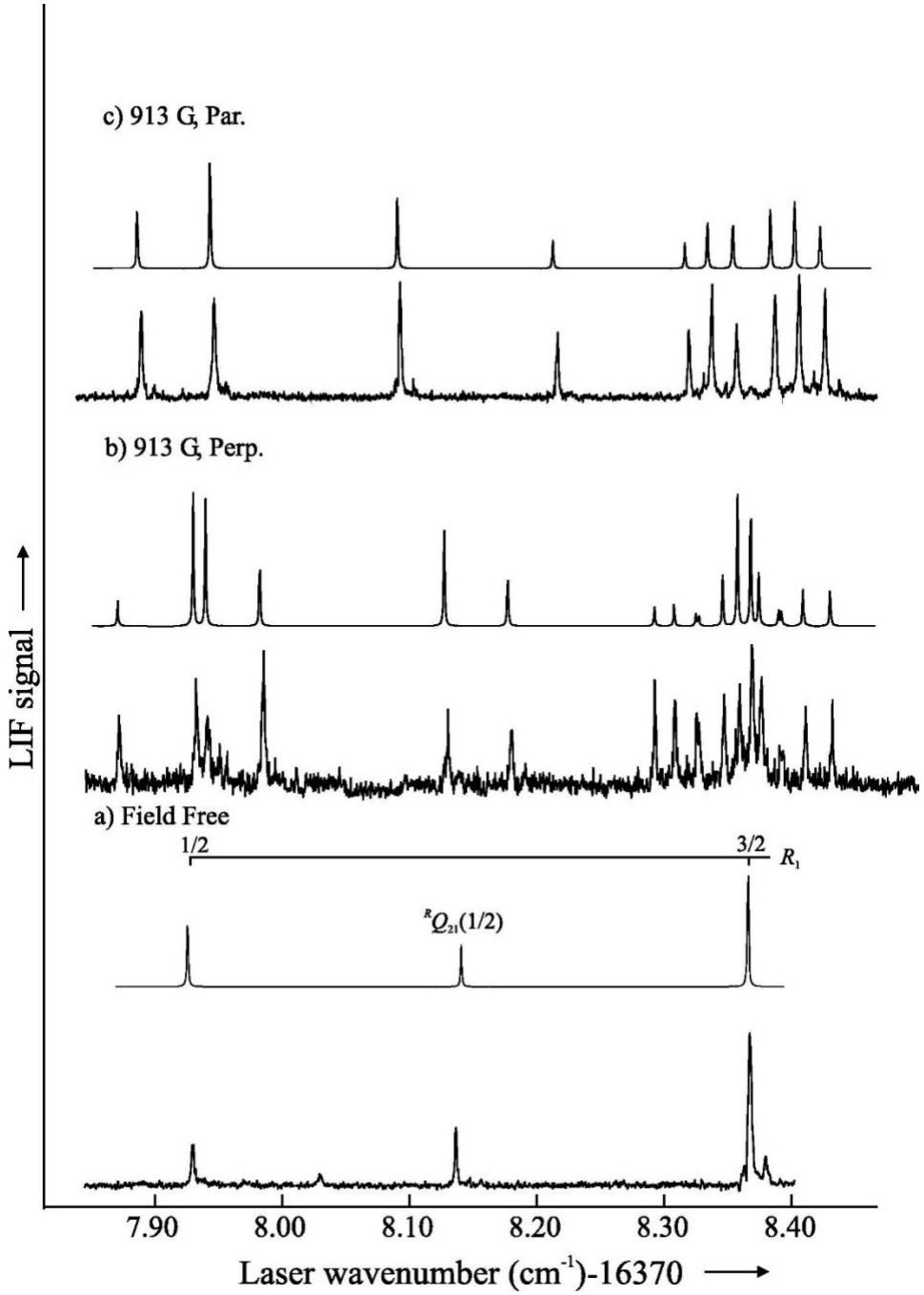

Figure 6.6. The observed and predicted excitation spectra near the origin of the $0_0^0 \tilde{B}^2\Sigma^+ - \tilde{X}^2\Sigma^+$ band recorded field-free and in the presence of a 913 G magnetic field orientated perpendicular and parallel to the electric field of the laser radiation.

6.3. Analysis

6.3.1. Field-free Spectra

A nonlinear least-squares fitting procedure program was written that used as input the observed transition wavenumbers of Table 6.1 and Table 6.2 and optimize the parameters for the $\tilde{A}^2\Pi_r(0,0,0)$ and $\tilde{B}^2\Sigma^+(0,0,0)$ states separately. The rotational, *B* (0.249199914 cm^{-1}), centrifugal distortion correction to rotation, *D* (2.17437×10^{-7} cm^{-1}), spin-rotational, γ (2.4274803×10^{-3} cm^{-1}), parameters for the $\tilde{X}^2\Sigma^+(0,0,0)$ state and the A_D (1.331×10^{-3} cm^{-1}), *D* (2.1685×10^{-7} cm^{-1}), and *q* (-1.528×10^{-4} cm^{-1}) parameters for the $\tilde{A}^2\Pi_r(0,0,0)$ state were held fixed to those determined from the combined analysis of the millimeter wave and optical spectra[25]. For the $\tilde{B}^2\Sigma^+(0,0,0)$ state, *D* (2.15×10^{-7} cm^{-1}) was held fixed to the value that determined from the analysis of the high-temperature excitation spectrum[30]. The determined field-free spectroscopic parameters for the $\tilde{A}^2\Pi_r(0,0,0)$ and $\tilde{B}^2\Sigma^+(0,0,0)$ states are presented in Table *6.6* as are the previously determined values. The standard deviation of the fits for the 82 measured field-free transition wavenumbers of the $0_0^0\ \tilde{A}^2\Pi_r - \tilde{X}^2\Sigma^+$ band (Table 6.1), and the 40 measured field-free transition wavenumbers of the $0_0^0\ \tilde{B}^2\Sigma^+ - \tilde{X}^2\Sigma^+$ band (Table 6.2), are 4.4×10^{-4} cm^{-1} and 8.2×10^{-4} cm^{-1}, respectively, which are commensurate with the estimated measurement error.

Table 6.6. Spectroscopic parameters for the $\tilde{A}^2\Pi_r(0,0,0)$ and $\tilde{B}^2\Sigma^+(0,0,0)$ states of SrOH

	$\tilde{A}^2\Pi_r(0,0,0)$		$\tilde{B}^2\Sigma^+(0,0,0)$		
Parameter[a]	This work [b,c]	Previous[d]	Parameter	This work [b,c]	Previous[e]
A	263.58741(20)	263.58782(61)	*B*	0.2522066(89)	0.25224(2)
B	0.2537833(16)	0.25378477(36)	γ	-0.142583(80)	-0.1447(3)
A_D	1.331×10^{-5}(fix)	1.331×10^{-5}	*D*	2.15×10^{-7}(fix)	2.15×10^{-7}
D	2.16859×10^{-7}(Fix)	2.16859×10^{-7}	$T_0(B\,^2\Sigma^+)$	16377.49826(28)	16377.505(1)
p+2q	-0.143662(37)	-0.143595(14)			
q	-1.528×10^{-4}(fix)	$-1.528(19)\times10^{-4}$			
$T_0(A\,^2\Pi)$	14674.04063(10)	14674.04171(39)			
Std. dev. of field-free fit =0.00046 cm^{-1}			Std. dev. of field-free fit = 0.00090 cm^{-1}		
g_l [f]	-0.269(22)			0.306(18)	
Std. dev. of Zeeman fit = 28 MHz			Std. dev. of Zeeman fit = 31 MHz		

[a] Units for field-free parameters are wavenumbers (cm^{-1}).

[b] Numbers in parentheses represent a 2σ error estimate in the last quoted decimal point.

[c] The $X\,^2\Sigma^+(v=0)$ state parameters were held fixed to those of Ref.[12]: *B*= 0.249199814 cm^{-1}, *D*= 2.17437×10^{-7} cm^{-1}, γ=2.42748×10^{-3} cm^{-1} A_D, *D*, and *q* for the $\tilde{A}^2\Pi_r(0,0,0)$ state are fixed to those of Ref.[23] and for the $\tilde{B}^2\Sigma^+(0,0,0)$ state is fixed to that of Ref. [30].

[d] Ref.[23].

[e] Ref.[30].

[f] g_S and g_L' constrained to 2.0023 and 1.000, respectively and g_l for the $\tilde{X}^2\Sigma^+(0,0,0)$ state constrained to Curl relationship value of $-4.87\text{x}10^{-3}$ (see text) .

6.3.2. Zeeman Spectra

Least squares fits of the magnetic field induced shifts using various combinations of the Zeeman parameters were attempted. In the end, satisfactory fits were obtained by constraining g_S, and g_L' to their nominal values of 2.0023 and unity, and constraining g_l for the $\tilde{X}^2\Sigma^+(0,0,0)$ state to the value of -4.87x10^{-3} predicted by the Curl relationship[41]. The data was insensitive to the parity dependent term, g', and it was constrained to zero. The optimized g_l parameter for the $\tilde{A}^2\Pi_r(0,0,0)$ and $\tilde{B}^2\Sigma^+(0,0,0)$ states and associated errors are presented in Table *6.6*. The standard deviation of the fits for $0_0^0\ \tilde{A}^2\Pi_r - \tilde{X}^2\Sigma^+$ band and the $0_0^0\ \tilde{B}^2\Sigma^+ - \tilde{X}^2\Sigma^+$ band are 28 MHz and 31 MHz, respectively, which are commensurate with the estimated measurement error.

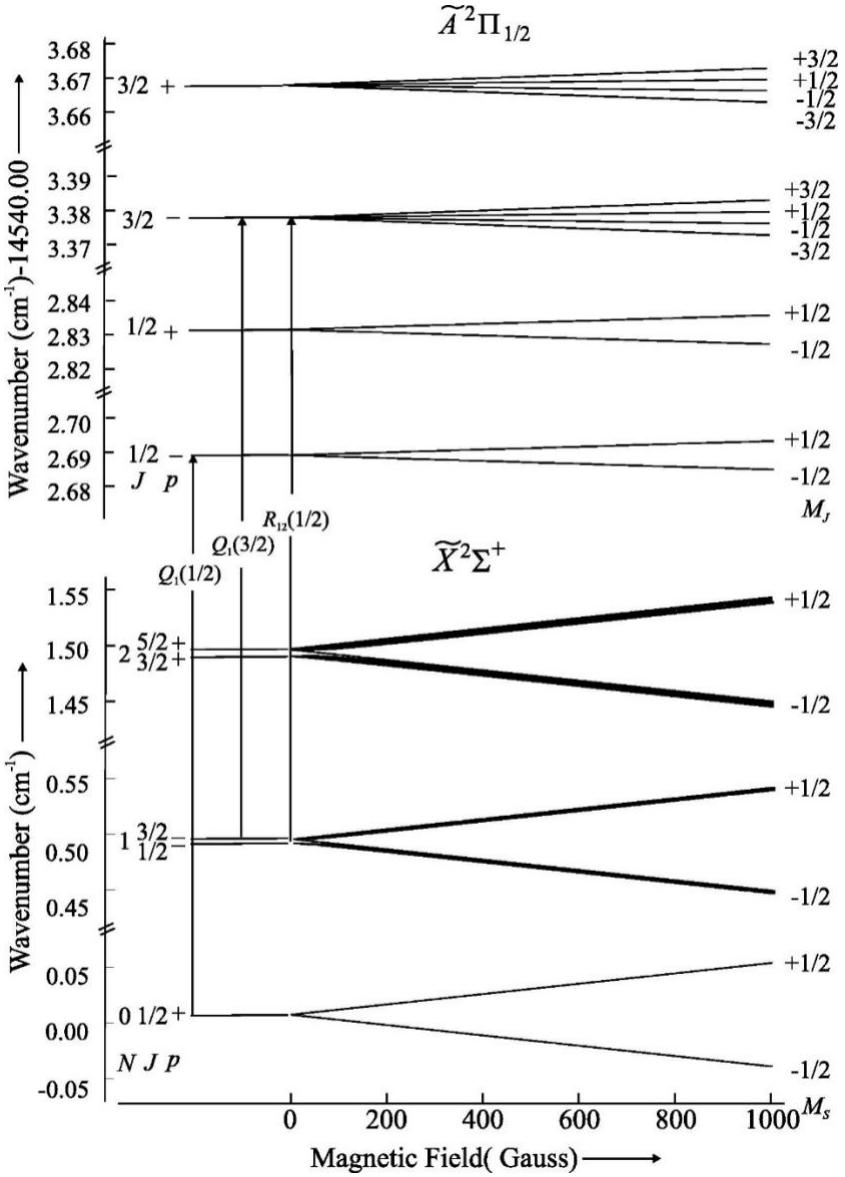

Figure 6.7. The predicted Zeeman tuning of the energy levels associated with low-J branch features of the 0_0^0 $\tilde{A}^2\Pi_{1/2} - \tilde{X}^2\Sigma^+$ band and associated assignment.

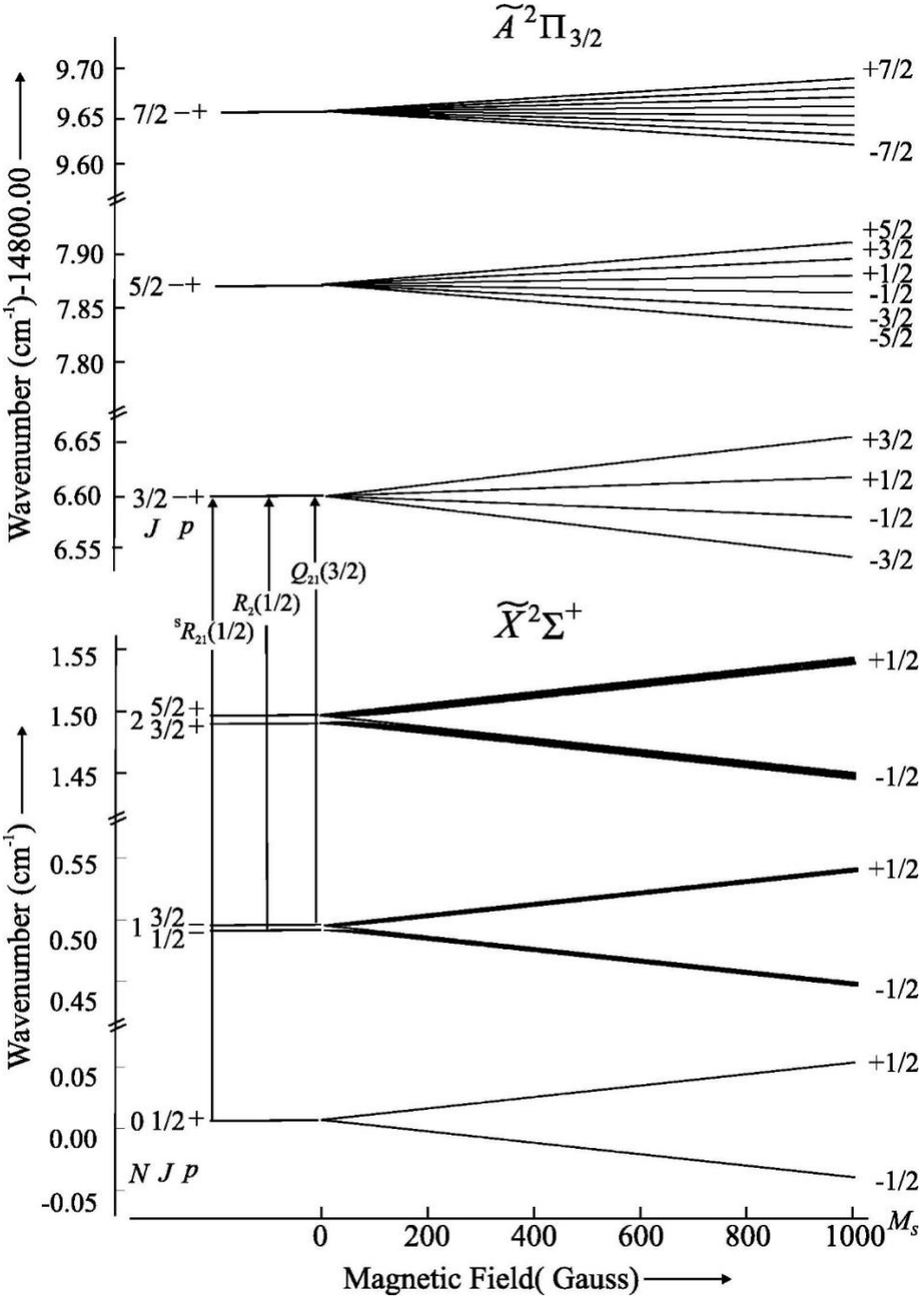

Figure 6.8. The predicted Zeeman tuning of the energy levels associated with low-J branch features of the 0_0^0 $\tilde{A}^2\Pi_{3/2} - \tilde{X}^2\Sigma^+$ band and associated assignment.

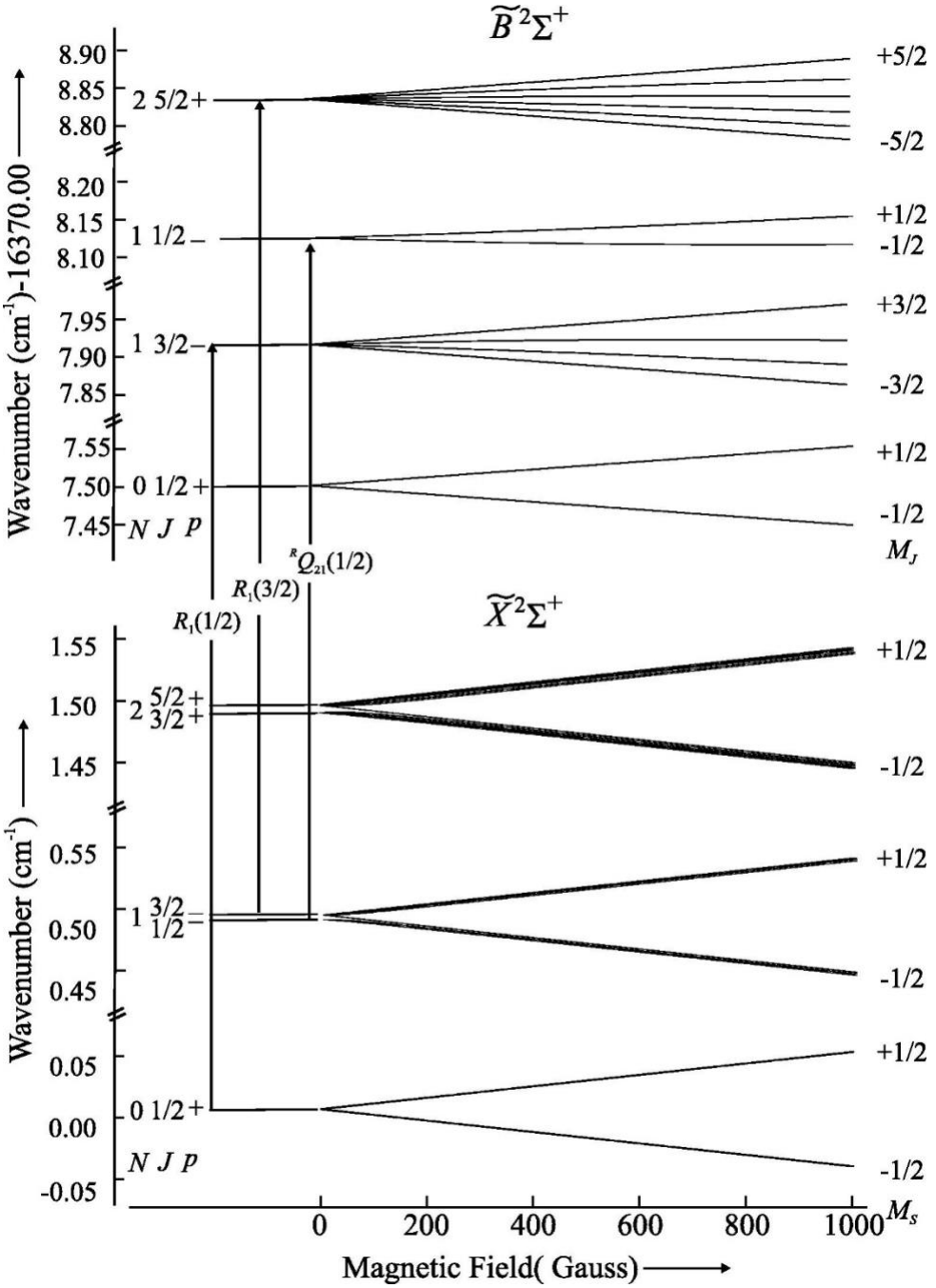

Figure 6.9. The predicted Zeeman tuning of the energy levels associated with low-J branch features of the 0_0^0 $\tilde{B}^2\Sigma^+ - \tilde{X}^2\Sigma^+$ band and associated assignment.

6.3.3. Dispersed Fluorescence Spectra

The relative intensities of the DF spectra were corrected for the wavelength response of the spectrometer. The ratios of the integrated areas of the corrected DF features

were used to determine the branching ratios given in Table *6.7*. The branching ratios were taken as the ratios of the observed integrated intensities, which are assumed to be proportional to the ratio of FCFs and transition frequencies cubed[42]:

$$b_{v',v''} \equiv \frac{I_{iv',fv''}}{\sum_{fv''} I_{iv',fv''}} \approx \frac{\mathrm{FCF}_{iv',fv''} \times \nu^3_{iv',fv''}}{\sum_{fv''} \mathrm{FCF}_{iv',fv''} \times \nu^3_{iv',fv''}} \quad . \qquad 6.1)$$

Also presented in Table *6.7* are the calculated branching ratios from the predicted Franck-Condon factors (see below).

Table 6.7. Franck-Condon factors and branching ratios

Band	$T_{v',v''}$	Calc. FCFs		Branching Ratios	
		Stretch[a]	Bend[b]	Calc.[c]	Obs.
$0^0_0\ \tilde{A}^2\Pi_{1/2} - \tilde{X}^2\Sigma^+$	14546	0.9556	0.9995	0.9552	0.957±0.003
$3^0_1\ \tilde{A}^2\Pi_{1/2} - \tilde{X}^2\Sigma^+$	14024	0.0425	0.9995	0.0425	0.043±0.002
$3^0_2\ \tilde{A}^2\Pi_{1/2} - \tilde{X}^2\Sigma^+$	14182	0.0017	0.9995	0.0017	< 0.005
$1^0_1\ \tilde{A}^2\Pi_{1/2} - \tilde{X}^2\Sigma^+$	(10768) [d]	1.7×10^{-6}	0.9995	1.7×10^{-6}	-
$2^0_2\ \tilde{A}^2\Pi_{1/2} - \tilde{X}^2\Sigma^+$	13818	0.9556	0.0005	0.0004	< 0.005
$0^0_0\ \tilde{A}^2\Pi_{3/2} - \tilde{X}^2\Sigma^+$	14805	0.9556	0.9995	0.9552	0.959±0.003
$3^0_1\ \tilde{A}^2\Pi_{3/2} - \tilde{X}^2\Sigma^+$	14287	0.0425	0.9995	0.0425	0.041±0.004
$3^0_2\ \tilde{A}^2\Pi_{3/2} - \tilde{X}^2\Sigma^+$	14411	0.0017	0.9995	0.0017	< 0.007
$1^0_1\ \tilde{A}^2\Pi_{3/2} - \tilde{X}^2\Sigma^+$	(11027) [d]	1.7×10^{-6}	0.9995	1.7×10^{-6}	-
$2^0_2\ \tilde{A}^2\Pi_{3/2} - \tilde{X}^2\Sigma^+$	14017	0.9556	0.0004	0.0004	< 0.007
$0^0_0\ \tilde{B}^2\Sigma^+ - \tilde{X}^2\Sigma^+$	16380	0.9782	0.9973	0.9756	0.977±0.002
$3^0_1\ \tilde{B}^2\Sigma^+ - \tilde{X}^2\Sigma^+$	15853	0.0212	0.9973	0.0211	0.023±0.003
$3^0_2\ \tilde{B}^2\Sigma^+ - \tilde{X}^2\Sigma^+$	16016	0.0005	0.9973	0.0005	< 0.005

$1_1^0\ \tilde{B}^2\Sigma^+ - \tilde{X}^2\Sigma^+$	(12602) [d]	6.7×10^{-5}	0.9973	6.7×10^{-5}	-
$2_2^0\ \tilde{B}^2\Sigma^+ - \tilde{X}^2\Sigma^+$	15653	0.9782	0.0027	0.0026	< 0.005

a) $\left|\left\langle \tilde{A}^2\Pi, v_1, v_3 \middle| \tilde{X}^2\Sigma^+, v_1, v_3 \right\rangle\right|^2$ and $\left|\left\langle \tilde{B}^2\Sigma^+, v_1, v_3 \middle| \tilde{X}^2\Sigma^+, v_1, v_3 \right\rangle\right|^2$ values obtained using a two-dimensional normal coordinate analysis (see text).

b) $\left|\left\langle \tilde{A}^2\Pi, v_2 \middle| \tilde{X}^2\Sigma^+, v_2 \right\rangle\right|^2$ and $\left|\left\langle \tilde{B}^2\Sigma^+, v_2 \middle| \tilde{X}^2\Sigma^+, v_2 \right\rangle\right|^2$ values obtained using a two-dimensional (2D) DVR method (see text).

c) The product of σ-symmetry stretching FCFs and bending FCFs.

d) Estimated using the 3778 cm^{-1} determined ω_1(O-H stretch) value for the $\tilde{X}^2\Sigma^+$ state of CaOH[44]. The ICCD is insensitive to emission associated with the 1_1^0 bands.

6.3.4. Modeling the spectra

The quantum number assignment of the Zeeman spectra was greatly assisted by spectral intensity simulations. This was achieved by constructing the Hund's case (*a*) transition moment matrices for the $0_0^0\ \tilde{A}^2\Pi_r - \tilde{X}^2\Sigma^+$ and $0_0^0\ \tilde{B}^2\Sigma^+ - \tilde{X}^2\Sigma^+$ bands. The transition moment was obtained by cross multiplication of the transition moment matrix by the Hund's case (*a*) eigenvectors. The transition moment was squared, multiplied by a Boltzmann factor commensurate with a rotational temperature of 10 K and used in conjunction with a Lorentzian linewidth of 30 MHz full width at half maximum to predict each spectral feature. The predicted spectra, such as those given in Figure *6.4*, Figure *6.5* and Figure *6.6*, were obtained by co-adding the individual spectral feature components.

The agreement between the predicted and observed Zeeman spectra is less satisfactory that that of the filed-free spectra because the polarization selection was not perfect (i.e. both parallel ($\Delta M_J = 0$) and perpendicular ($\Delta M_J = \pm 1$) are observed).

6.3.5. DFT calculations

All calculations were performed with the electronic structure program ORCA[43]. Briefly, the method consisted of the following steps:

i. The properties of the $\tilde{X}\,^2\Sigma^+$ state was predicted using DFT /BP86 functional.

ii. The properties of the $\tilde{A}^2\Pi$ and $\tilde{B}^2\Sigma^+$ states were predicted using TD-DFT. Only the first 10 excitations were included.

iii. To determine the potential energy as a function of angle, the angle of the $\tilde{X}\,^2\Sigma^+$ was varied in steps of 1° and the Sr-O and O-H bond lengths optimized. That optimized structure was then employed in the TD-DFT energy predictions of the $\tilde{A}^2\Pi$ and $\tilde{B}^2\Sigma^+$ states. The Sr-O and O-H bond lengths of the $\tilde{A}^2\Pi$ and $\tilde{B}^2\Sigma^+$ states were optimized with the angle constrained.

The numerical thresholds were systematically increased using the "TightOpt", "TightSCF", "Grid5" and "FinalGrid6" options. We carefully studied the accuracy and precise of our calculation by changing the basis set, functional that were all integrated in the ORCA package. In the end the def2-QZVPP[44], and corresponding def2-ECP along with the Weigend's "universal" Coulomb fitting (def2/J)[45] basis sets of the ORCA library were used. ECP parameters for Sr [Def2-ECP][46] have been obtained from TURBOMOLE (7.0.2)[47]. The predicted excitation energies of the $\tilde{A}^2\Pi$ and $\tilde{B}^2\Sigma^+$ states were 1.914 eV and 2.047 eV which compares favorably with the observed values of 1.819 eV and 2.030

eV. The predicted harmonic frequencies also compared favorably with observations (see Table *6.8* below). The optimized energies and bond lengths as a function of bending angle are found in Table *6.9*.

Table 6.8. The predicted harmonic frequencies (cm^{-1})

	$\tilde{X}\,^2\Sigma^+$	$\tilde{A}^2\Pi$	$\tilde{B}\,^2\Sigma^+$
ω_1(O-H stretch)	3813	3818	3807
ω_2(Sr-O-H bend)	315	347	373
ω_3(Sr-O stretch)	533	538	520

Table 6.9. The DFT predicted energies and bond lengths as a function of bending angle.

	$X^2\Sigma^+$			$A^2\Pi_r$			$B^2\Sigma^+$		
Angle (Degrees)	Energy (cm^{-1})	rSr-O (A^0)	rOH (A^0)	Energy (cm^{-1})	rSr-O (A^0)	rOH (A^0)	Energy (cm^{-1})	rSr-O (A^0)	rOH (A^0)
90.00	3375.573	2.18	0.98	18497.234	2.19	0.98	20287.879	2.20	0.98
91.00	3273.129	2.18	0.98	18401.998	2.19	0.98	20178.602	2.20	0.98
92.00	3174.339	2.18	0.98	18310.096	2.19	0.98	20073.625	2.19	0.98
93.00	3079.052	2.18	0.98	18221.536	2.19	0.98	19972.465	2.19	0.98
94.00	2987.151	2.18	0.98	18136.341	2.19	0.98	19874.844	2.19	0.98
95.00	2898.501	2.18	0.98	18054.568	2.19	0.98	19781.422	2.19	0.98
96.00	2812.899	2.18	0.98	17976.067	2.18	0.98	19691.391	2.19	0.98
97.00	2730.084	2.17	0.98	17900.510	2.18	0.98	19604.269	2.18	0.98
98.00	2649.803	2.17	0.98	17827.279	2.18	0.98	19519.631	2.18	0.98
99.00	2571.900	2.17	0.98	17755.840	2.18	0.98	19437.270	2.18	0.98
100.00	2496.339	2.17	0.98	17685.851	2.18	0.98	19357.035	2.18	0.98
101.00	2423.161	2.17	0.98	17617.292	2.18	0.98	19278.396	2.18	0.97
102.00	2352.361	2.17	0.98	17550.268	2.17	0.98	19202.012	2.18	0.97
103.00	2283.846	2.17	0.97	17485.261	2.17	0.98	19127.627	2.18	0.97
104.00	2217.459	2.17	0.97	17422.591	2.17	0.98	19054.768	2.17	0.97

105.00	2152.987	2.17	0.97	17362.542	2.17	0.98	18983.691	2.17	0.97
106.00	2090.212	2.16	0.97	17305.303	2.17	0.98	18913.733	2.17	0.97
107.00	2028.996	2.16	0.97	17250.938	2.17	0.98	18845.687	2.17	0.97
108.00	1969.300	2.16	0.97	17199.131	2.16	0.98	18779.400	2.17	0.97
109.00	1911.163	2.16	0.97	17149.599	2.16	0.98	18714.829	2.17	0.97
110.00	1854.623	2.16	0.97	17101.775	2.16	0.98	18652.614	2.17	0.97
111.00	1799.631	2.16	0.97	17055.257	2.16	0.97	18592.029	2.16	0.97
112.00	1746.042	2.16	0.97	17009.449	2.16	0.97	18533.557	2.16	0.97
113.00	1693.663	2.16	0.97	16964.006	2.15	0.97	18476.323	2.16	0.97
114.00	1642.344	2.15	0.97	16918.690	2.15	0.97	18419.866	2.16	0.97
115.00	1592.027	2.15	0.97	16873.213	2.15	0.97	18364.292	2.16	0.97
116.00	1542.751	2.15	0.97	16828.169	2.15	0.97	18309.483	2.16	0.97
117.00	1494.608	2.15	0.97	16783.666	2.15	0.97	18255.544	2.15	0.97
118.00	1447.658	2.15	0.97	16740.068	2.15	0.97	18201.921	2.15	0.97
119.00	1401.907	2.15	0.97	16657.196	2.15	0.97	18149.546	2.15	0.97
120.00	1357.308	2.15	0.97	16657.195	2.14	0.97	18098.044	2.15	0.97
240.00	1357.308	2.15	0.97	16657.195	2.14	0.97	18098.044	2.15	0.97
241.00	1401.907	2.15	0.97	16657.196	2.15	0.97	18149.546	2.15	0.97
242.00	1447.658	2.15	0.97	16740.068	2.15	0.97	18201.921	2.15	0.97
243.00	1494.608	2.15	0.97	16783.666	2.15	0.97	18255.544	2.15	0.97
244.00	1542.751	2.15	0.97	16828.169	2.15	0.97	18309.483	2.16	0.97
245.00	1592.027	2.15	0.97	16873.213	2.15	0.97	18364.292	2.16	0.97
246.00	1642.344	2.15	0.97	16918.690	2.15	0.97	18419.866	2.16	0.97
247.00	1693.663	2.16	0.97	16964.006	2.15	0.97	18476.323	2.16	0.97
248.00	1746.042	2.16	0.97	17009.449	2.16	0.97	18533.557	2.16	0.97
249.00	1799.631	2.16	0.97	17055.257	2.16	0.97	18592.029	2.16	0.97
250.00	1854.623	2.16	0.97	17101.775	2.16	0.98	18652.614	2.17	0.97
251.00	1911.163	2.16	0.97	17149.599	2.16	0.98	18714.829	2.17	0.97
252.00	1969.300	2.16	0.97	17199.131	2.16	0.98	18779.400	2.17	0.97
253.00	2028.996	2.16	0.97	17250.938	2.17	0.98	18845.687	2.17	0.97
254.00	2090.212	2.16	0.97	17305.303	2.17	0.98	18913.733	2.17	0.97
255.00	2152.987	2.17	0.97	17362.542	2.17	0.98	18983.691	2.17	0.97
256.00	2217.459	2.17	0.97	17422.591	2.17	0.98	19054.768	2.17	0.97

257.00	2283.846	2.17	0.97	17485.261	2.17	0.98	19127.627	2.18	0.97
258.00	2352.361	2.17	0.98	17550.268	2.17	0.98	19202.012	2.18	0.97
259.00	2423.161	2.17	0.98	17617.292	2.18	0.98	19278.396	2.18	0.97
260.00	2496.339	2.17	0.98	17685.851	2.18	0.98	19357.035	2.18	0.98
261.00	2571.900	2.17	0.98	17755.840	2.18	0.98	19437.270	2.18	0.98
262.00	2649.803	2.17	0.98	17827.279	2.18	0.98	19519.631	2.18	0.98
263.00	2730.084	2.17	0.98	17900.510	2.18	0.98	19604.269	2.18	0.98
264.00	2812.899	2.18	0.98	17976.067	2.18	0.98	19691.391	2.19	0.98
265.00	2898.501	2.18	0.98	18054.568	2.19	0.98	19781.422	2.19	0.98
266.00	2987.151	2.18	0.98	18136.341	2.19	0.98	19874.844	2.19	0.98
267.00	3079.052	2.18	0.98	18221.536	2.19	0.98	19972.465	2.19	0.98
268.00	3174.339	2.18	0.98	18310.096	2.19	0.98	20073.625	2.19	0.98
269.00	3273.129	2.18	0.98	18401.998	2.19	0.98	20178.602	2.20	0.98
270.00	3375.573	2.18	0.98	18497.234	2.19	0.98	20287.879	2.20	0.98

6.3.6. The two-dimensional stretching Franck-Condon factors.

Normal coordinate analyses using the **GF** matrix approach is well documented by Wilson Decius & Cross[61]. The 4×4 **GF** matrix is block diagonal consisting of a 2×2 GF matrix associated with σ-symmetry stretching modes and two 1×1 matrices for the two orthogonal π-symmetry bending modes. Selecting the z-axis to coincide with the H-O-Sr bond and following the procedure described in Ref. [61] gives for the **B** matrix:

$$\mathbf{B} = \begin{vmatrix} & x_H & y_H & z_H & x_O & y_O & z_O & x_{Sr} & y_{Sr} & z_{Sr} \\ \Delta r_{OH} & 0 & 0 & 1 & 0 & 0 & -1 & 0 & 0 & 0 \\ \Delta r_{SrO} & 0 & 0 & 0 & 0 & 0 & 1 & 0 & 0 & -1 \\ \Delta\theta^{xz}_{SrOH} & a & 0 & 0 & b & 0 & 0 & c & 0 & 0 \\ \Delta\theta^{yz}_{SrOH} & 0 & a & 0 & 0 & b & 0 & 0 & c & 0 \end{vmatrix}, \qquad (6.2)$$

where $a = -r_{OH}^{-1}$, $b = r_{OH}^{-1} + r_{SrO}^{-1}$, and $c = r_{SrO}^{-1}$. It follows that the **G** matrices are:

$$\mathbf{G} = \begin{vmatrix} & \Delta r_{OH} & \Delta r_{SrO} & \Delta\phi^{xz}_{SrOH} & \Delta\phi^{yz}_{SrOH} \\ \Delta r_{OH} & a & c & 0 & 0 \\ \Delta r_{SrO} & c & b & 0 & 0 \\ \Delta\theta^{xz}_{SrOH} & 0 & 0 & d & 0 \\ \Delta\theta^{yz}_{SrOH} & 0 & 0 & 0 & d \end{vmatrix} \qquad (6.3)$$

Where $a = M_O^{-1} + M_H^{-1}$, $b = M_O^{-1} + M_{Sr}^{-1}$, $c = -M_O^{-1}$, and $d = (M_H r_{OH}^2)^{-1} + (M_{Sr} r_{SrO}^2)^{-1} + (M_O)^{-1}(r_{OH}^{-2} + r_{SrO}^{-2} + 2/(r_{OH} r_{SrO}))$. The required force constants and bond distances for construction of the **GF** matrices are collected in Table *6.10*. The force constants of Table *6.10* were obtained using primarily experimental data with the exception of the stretch-stretch coupling constant, f_{13}, which was set to the value predicted for the $\tilde{X}\,^2\Sigma^+$ state of CaOH[52]. The predictions are least sensitive to this force constant. The O-H and Sr-O stretch force constants, f_{11} and f_{33}, were obtained by non-linear least squares fitting the ω_1(SrOH), ω_3 (SrOH), and ω_3 (SrOD) frequencies given in Table *6.10*. For this purpose, the 2×2 **GF** sub-matrices associated with σ-symmetry stretching modes were constructed using initial guesses for f_{11} and f_{33} and diagonalized to produce predicted harmonic vibrational frequencies. The difference between the observed and predicted frequencies was minimized in non-linear least squares procedure. The statistical errors associated with fitting the three frequencies ω_1(SrOH), ω_3 (SrOH), and ω_3 (SrOD) to the two parameters f_{11} and f_{33} are also given in Table *6.10*. Similarly, the f_{22} force constants for the bending mode were obtained from the 1×1 sub-matrices.

Table 6.10. Force constant and bond lengths used in the normal coordinate analysis.

Property	$\tilde{X}\,^2\Sigma^+$	$\tilde{A}\,^2\Pi$	$\tilde{B}\,^2\Sigma^+$
f_{11}[a]	7.9402±0.0417	7.9398±0.0562	7.9399±0.0438
f_{22}	2.2859±0.0651	2.3943±0.0878	2.3626±0.0684
f_{33}	0.0590	0.0648	0.0711
f_{13}[b]	0.0677	0.0677	0.0677
$r_{\text{Sr-O}}$(Å)[c]	2.111	2.091	2.098
$r_{\text{O-H}}$ (Å)[c]	0.922	0.922	0.921
ω_1(O-H stretch)[d]	3778	3778	3778
ω_2(Sr-O-H bend)	363.7[e]	381.4[f]	399.8[e]
ω_3(Sr-O stretch)	526.9[g] (510.0)[h]	542.6[e] (516.0) [h]	536.3[33](516.0) [h]

a) f_{11}= O-H stretch , f_{33} = Sr-O stretch , f_{22} = Sr-O-H bend, f_{13} = stretch-stretch coupling. Units: f_{11}, f_{33}, and f_{13} in mdyne/Å; f_{22} mdyne/(Å radian).

b) Constrained to the predicted value for CaOH[52] .

c) Ref. [24].

d) Constrained to the experimentally determined value for the $\tilde{X}\,^2\Sigma^+$ state of CaOH[44].

e) Ref.[26]

f) Ref.[27]

g) Ref.[28]

h) Ref.[30]

i) Ref. [33]

The $\mathbf{L}$ matrices that appear above are related to the eigenvectors of the **GF** matrices, $\mathbf{V}$, by a normalization matrix $\mathbf{N}$:

$$\mathbf{L}=\mathbf{V}\cdot\mathbf{N}=\mathbf{V}\cdot\left[\mathbf{V}^{-1}\mathbf{G}(\mathbf{V}^{\mathrm{T}})^{-1}\right]^{1/2}, \tag{6.4}$$

where $\mathbf{N}$ is chosen such that $\mathbf{L}\cdot\mathbf{L}^{T}=\mathbf{G}$ [62]. Using information of Table 1A, the calculated $\mathbf{V}$ and $\mathbf{L}$ matrices are for σ-type stretching modes are:

$$\mathbf{V}(\tilde{X}\,^{2}\Sigma^{+},\tilde{A}^{2}\Pi,\tilde{B}^{2}\Sigma^{+})\approx\begin{vmatrix} & Q_1 & Q_3 \\ \Delta r_{O-H} & 0.9982 & -0.0597,-0.0598,0.0598 \\ \Delta r_{Sr-O} & 0.0087,0.0095,0.0093 & 0.99799 \end{vmatrix} \tag{6.5}$$

$$\mathbf{L}(\tilde{X}\,^{2}\Sigma^{+},\tilde{A}^{2}\Pi,\tilde{B}^{2}\Sigma^{+})\approx\begin{vmatrix} & Q_1 & Q_3 \\ \Delta r_{O-H} & 1.0270 & 0.0023,0.0025,0.0025 \\ \Delta r_{Sr-O} & -0.0615 & 0.2648 \end{vmatrix}. \tag{6.6}$$

As expected $\mathbf{V}$ and $\mathbf{L}$ a nearly identical for the three states. Substitution of $\mathbf{L}$ and $\mathbf{B}$ into Eq. 7 produces a unit **J** rotation matrices, as expected because the normal coordinates Q_1 and Q_3 are parallel for the three states. Substitution of $\mathbf{L}$, $\mathbf{B}$, and the bond lengths of Table *6.10* into Eq. 8 gives:

$$\mathbf{D}(\tilde{X}\,^{2}\Sigma^{+},\tilde{A}^{2}\Pi)\approx\begin{vmatrix}-0.00019\\ 0.07549\end{vmatrix}, \tag{6.7}$$

and

$$\mathbf{D}(\tilde{X}\,^{2}\Sigma^{+},\tilde{B}^{2}\Sigma^{+})\approx\begin{vmatrix}-0.00110\\ 0.05261\end{vmatrix}. \tag{6.8}$$

The FCFs given in Table 4 were obtained solving the analytical equations of Ref.[49] using the vibrational frequencies of Table A1 along with the predicted **J** and **D** matrices.

6.4. Discussion

The determined field-free spectroscopic parameters for the $\tilde{B}^2\Sigma^+(0,0,0)$ state (see Table *6.6*) are significantly improved from the previous values. The determined field-free spectroscopic parameters for the $\tilde{A}^2\Pi_r(0,0,0)$ state is comparable to the previous values because although the current data set is much smaller the measured transition wavenumbers are substantially more precise (0.0001 cm^{-1} *vs* 0.003 cm^{-1}). The improved fine structure constants for the $\tilde{A}^2\Pi_r(0,0,0)$ and $\tilde{B}^2\Sigma^+(0,0,0)$ states can be used to predict the transition wavenumbers associated with planned laser cooling and magneto-optical trapping experiments. The very small standard deviations from the field-free fits of 0.00091 cm^{-1} and 0.00049 cm^{-1} for the $0_0^0\ \tilde{A}^2\Pi_r - \tilde{X}^2\Sigma^+$ and $0_0^0\ \tilde{B}^2\Sigma^+ - \tilde{X}^2\Sigma^+$ bands, respectively, demonstrates that the effective Hamiltonian approach can accurately model the low rotational lines of these bands, and more generally for other linear alkaline earth monovalent triatomic molecules.

The magnetic tuning of the rotational lines associated with magneto-optical trapping of SrOH have been measured and successfully modelled with an effective Hamiltonian approach. The determined g'_l and g_l of -0.269(22) and 0.306(18) for the magnetic g-factors given in Table *6.6* for the $\tilde{A}^2\Pi_r(0,0,0)$ and $\tilde{B}^2\Sigma^+(0,0,0)$ states, respectively, having nearly the same magnitude (within the uncertainty) but opposite sign indicating a high degree of mixing between these two states. The Curl-type relationships[41] $g_l'(\tilde{A}^2\Pi) \approx p/2B$ and $g_l(\tilde{B}^2\Sigma^+) \approx -\gamma/2B$ predict values of -0.2824 and 0.2827, respectively, which is good agreement with the determined values.

The DF spectra resulting from excitation to the $\tilde{A}^2\Pi_r(0,0,0)$ and $\tilde{B}^2\Sigma^+(0,0,0)$ states were modeled by assuming that the relative intensities are proportional to the product of the two-dimensional FCF of the σ-symmetry stretching modes (ν_1 and ν_3) and a FCF for the one-dimensional π-symmetry bending mode (ν_2):

$$\text{FCF} = \left|\langle \nu_1'' \nu_3'' | 0,0 \rangle\right|^2 \left|\langle \nu_2'' \ | 0 \rangle\right|^2 . \qquad 6.9)$$

This assumes that vibronic coupling due to Renner-Teller and spin-orbit interactions[48-49] is negligible and the total wave function can be written as the product of an electronic and vibrational wave function, which is a reasonable assumption for the vibronic states considered here. The previous prediction[13] of FCFs followed the procedure of Sharp and Rosenstock[34] to evaluate the two dimensional integrals of Eq. 5. Here an alternative[50] closed-form formula for the two-dimensional FCFs for the stretching modes is employed. Both formulations assume a harmonic stretching motion. The Sharp and Rosenstock[34] approach also assumes that the same internal coordinates of the ground and excited electronic state can be used for treating the Duschinsky effect (i.e. mode mixing). A more accurate method of handling the Duschinsky effect, which is used here, employs Cartesian coordinates common to both electronic states[36, 38-39]. This approach requires relating the normal coordinates of the $\tilde{X}^2\Sigma^+$ state, $\mathbf{Q}(\tilde{X}^2\Sigma^+)$, to those of the $\tilde{A}^2\Pi$ and $\tilde{B}^2\Sigma^+$ states, $\mathbf{Q}(\tilde{A}^2\Pi, \tilde{B}^2\Sigma^+)$:

$$\mathbf{Q}(\tilde{X}^2\Sigma^+) = \mathbf{J}\mathbf{Q}(\tilde{A}^2\Pi, \tilde{B}^2\Sigma^+) + \mathbf{D} . \qquad 6.10)$$

In Eq. 6, **D** is the vector of geometry displacements given in terms of the normal coordinates of the ground state and J is the Duschinsky rotation matrix which for the $\tilde{A}^2\Pi_r - \tilde{X}^2\Sigma^+$ transition is given by:

$$\mathbf{J}=(\mathbf{L}^{-1}(\tilde{A}^2\Pi_r)\cdot\mathbf{B}(\tilde{A}^2\Pi_r))\cdot\mathbf{M}^{-1}\cdot((\mathbf{L}^{-1}(X^2\Sigma^+)\cdot\mathbf{B}(X^2\Sigma^+))^T \qquad 6.11)$$

and

$$\mathbf{D}=(\mathbf{L}^{-1}(\tilde{A}^2\Pi_r)\cdot\mathbf{B}(\tilde{A}^2\Pi_r))\cdot(\mathbf{R}_{eq}(\tilde{A}^2\Pi_r)-\mathbf{R}_{eq}(\tilde{X}^2\Sigma^+)) \qquad 6.12)$$

In Eqs. 6.11 and 6.12 the **L** matrices relate the internal displacement coordinates to the normal coordinates and $\mathbf{R_{eq}}$ the vectors of equilibrium Cartesian coordinates in a center of mass where the atoms lie along the z-axis. For the linear-to-linear transition studied here the 2×2 rotation matrix associated with the two σ-type stretching modes is a unit matrix. The derivation of the displacement vectors for the σ-type stretching modes from a normal coordinate analyses of the $\tilde{X}^2\Sigma^+$, $\tilde{A}^2\Pi$, and $\tilde{B}^2\Sigma^+$ states is presented in subsection 6.3.6.3.6. Also presented in subsection 6.3.6.3.6 is the derivation of the **G** matrix element for the bending mode, which is required for the one-dimensional overlap integral. The determined two dimensional FCFs $\left|\left\langle \tilde{A}^2\Pi,0,0\middle|\tilde{X}^2\Sigma^+,0,0\right\rangle\right|^2$, $\left|\left\langle \tilde{A}^2\Pi,0,0\middle|\tilde{X}^2\Sigma^+,0,1\right\rangle\right|^2$, $\left|\left\langle \tilde{A}^2\Pi,0,0\middle|\tilde{X}^2\Sigma^+,0,2\right\rangle\right|^2$, $\left|\left\langle \tilde{B}^2\Sigma^+,0,0\middle|\tilde{X}^2\Sigma^+,0,0\right\rangle\right|^2$, $\left|\left\langle \tilde{B}^2\Sigma^+,0,0\middle|\tilde{X}^2\Sigma^+,0,1\right\rangle\right|^2$, and $\left|\left\langle \tilde{B}^2\Sigma^+,0,0\middle|\tilde{X}^2\Sigma^+,0,2\right\rangle\right|^2$ are presented in Table *6.7*. All other two-dimensional FCFs for the stretching modes involving emission from $\tilde{A}^2\Pi_r(0,0,0)$ and $\tilde{B}^2\Sigma^+(0,0,0)$ are less than 1×10^{-4}.

The bending potentials for the $\tilde{X}\,^2\Sigma^+$, $\tilde{A}^2\Pi_r$, and $\tilde{B}^2\Sigma^+$ states of SrOH are expected to be anharmonic, similar to what has been observed for CaOH and MgOH[51-54]. To evaluate the one dimensional bending FCF of Eq. 5 a numerical approach using a two-dimensional (2D) discrete variable representation (DVR) technique[55-58] was employed and is described in our SrOH investigation[59]. The DVR approach is based upon a grid-point representation and replaces the problem of integral evaluation associated with the vibronic Schrödinger equation with a numerical summation of the matrix elements of the kinetic and potential energy operators at the grid points. This approach is particularly useful for the bending FCFs because it does not require an analytic expression for the potential. As applied here the representation for the potential energy operator was obtained from an electronic structure calculation, using the ORCA[43] suite of program. The properties of the $\tilde{X}\,^2\Sigma^+$ state was calculated using Density Functional Theory (DFT) implemented using the BP86 functional and def2-QZVPP basis set, while those for the $\tilde{A}^2\Pi$ and $\tilde{B}^2\Sigma^+$ states were calculated using Time Dependent (TD)-DFT with the same functional and basis set. The potential energies for the $\tilde{X}\,^2\Sigma^+$, $\tilde{A}^2\Pi_r$, and $\tilde{B}^2\Sigma^+$ states as a function of bond angles ranging from 180° to 90° were calculated in 1° steps. The potential is symmetrical about 180° giving a total of 181 energies for each electronic state. At each angle the Sr-O and O-H bond lengths were optimized. The representation for the kinetic energy operator was obtained from analytical expressions of the G-matrix elements[60] for the bending normal coordinate (see the SrOH investigation[59]). The bending FCFs $\left|\left\langle \tilde{A}^2\Pi,0\middle|\tilde{X}\,^2\Sigma^+,0\right\rangle\right|^2$, $\left|\left\langle \tilde{A}^2\Pi,0\middle|\tilde{X}\,^2\Sigma^+,2\right\rangle\right|^2$, $\left|\left\langle \tilde{B}^2\Sigma^+,0\middle|\tilde{X}\,^2\Sigma^+,0\right\rangle\right|^2$, and, $\left|\left\langle \tilde{B}^2\Sigma^+,0\middle|\tilde{X}\,^2\Sigma^+,2\right\rangle\right|^2$, obtained from the 2D-

DVR calculations are presented in Table *6.7*. All other bending FCFs for emission from the $\tilde{A}^2\Pi_r(0,0,0)$ and $\tilde{B}^2\Sigma^+(0,0,0)$ states are less than 1×10^{-4}.

The predicted branching ratios, $b_{v',v''}$, as calculated using Eq. 4, are also presented in Table *6.7* and compared with observations. The predictions are in excellent agreement for the six ($0_0^0, 3_1^0\ \tilde{A}^2\Pi_{1/2,3/2} - \tilde{X}^2\Sigma^+$ and $0_0^0, 3_1^0\ \tilde{B}^2\Sigma^+ - \tilde{X}^2\Sigma^+$ bands) experimentally determined $b_{v',v''}$ values, and reflect the near diagonal nature of the transitions. While the experimental sensitivity of the current measurement allowed us to only observe the dominant off-diagonal $3_1^0\ \tilde{A}^2\Pi_r - \tilde{X}^2\Sigma^+$ and $3_1^0\ \tilde{B}^2\Sigma^+ - \tilde{X}^2\Sigma^+$ transitions, the molecular loss data from the SrOH laser cooling experiment[19] has been used to test the accuracy of our predictions for smaller vibrational $b_{v',v''}$ values. From that analysis the measured 3_2^0 $\tilde{A}^2\Pi_{1/2} - \tilde{X}^2\Sigma^+$ and $2_2^0\ \tilde{A}^2\Pi_{1/2} - \tilde{X}^2\Sigma^+$ branching ratios are $2.2^{+0.9}_{-0.7}\times10^{-3}$ and $4^{+2}_{-1}\times10^{-4}$, respectively, which are in close agreement with the predicted values (see Table *6.7*) of 1.5×10^{-3} and 1.0×10^{-4}, respectively, reaffirming the accuracy of our calculations.

Finally, it is somewhat surprising that the observed (<0.007) and predicted $b_{v',v''}$ (<0.002) values for the symmetry allowed $2_2^0\ \tilde{A}^2\Pi_r - \tilde{X}^2\Sigma^+$ and $2_2^0\ \tilde{B}^2\Sigma^+ - \tilde{X}^2\Sigma^+$ transitions are so small given the expected anharmonic nature of the bending potentials. Although not observed here, both the symmetry allowed $\tilde{A}^2\Pi(0,0,0) \rightarrow \tilde{X}^2\Sigma^+(0,2^0,0)$ emission and symmetry forbidden $\tilde{A}^2\Pi(0,0,0) \rightarrow \tilde{X}^2\Sigma^+(0,1^1,0)$ emission have been seen in the DF spectra [27-29] of a high temperature flowing reactor source. Although no estimates

of the relative intensities of the weak $\tilde{A}^2\Pi(0,0,0) \rightarrow \tilde{X}^2\Sigma^+(0,2^0,0)$ emission to that of intense $\tilde{A}^2\Pi(0,0,0) \rightarrow \tilde{X}^2\Sigma^+(0,0,0)$ emission was given, it was estimated[29] that the nominally symmetry forbidden $\tilde{A}^2\Pi_{1/2}(0,0,0) \rightarrow \tilde{X}^2\Sigma^+(0,1^1,0)$ emission was 1/8 that of the symmetry allowed $\tilde{A}^2\Pi_{1/2}(0,0,0) \rightarrow \tilde{X}^2\Sigma^+(0,2^0,0)$ emission. Similarly, the $\tilde{B}^2\Sigma^+(0,0,0) \rightarrow \tilde{X}^2\Sigma^+(0,1^1,0)$ emission has been seen in the DF spectrum of a rotationally hot sample[30] where it was estimated to be a factor of 1000 less intense than the $\tilde{B}^2\Sigma^+(0,0,0) \rightarrow \tilde{X}^2\Sigma^+(0,0,0)$ emission. The observations here demonstrate these emissions are much weaker for the low rotational levels relevant to the proposed SrOH MOT experiment[35] and suggests that vibration-rotation coupling becomes more important at higher rotational excitation.

Our results are also consistent with the previous *ab initio* calculation for CaOH[14] and provide experimental evidence for the feasibility of direct laser slowing and trapping of SrOH with four distinct laser wavelengths using either $\tilde{A}^2\Pi_r - \tilde{X}^2\Sigma^+$ or $\tilde{B}^2\Sigma^+ - \tilde{X}^2\Sigma^+$ cycling transitions.

6.5. Conclusion

The field-free frequencies, magnetic tuning of the 0_0^0 $\tilde{B}^2\Sigma^+ - \tilde{X}^2\Sigma^+$, 0_0^0 $\tilde{A}^2\Pi_{3/2} - \tilde{X}^2\Sigma^+$ and 0_0^0 $\tilde{A}^2\Pi_{1/2} - \tilde{X}^2\Sigma^+$ transitions, and the fluorescence branching ratios of the $\tilde{A}^2\Pi_r$ (0,0,0), and $\tilde{B}^2\Sigma^+(0,0,0)$ electronic states determined here should be useful for the continuing effort[13, 18-19] towards direct laser slowing and magneto-optical trapping of

SrOH. It is demonstrated that the proton hyperfine splitting of the optical transitions relevant to generation of MOT sample are less than 30 MHz and that like SrF, the low-rotational features of $\tilde{A}^2\Pi_{1/2}$ have a significant magnetic moment due to spin-orbit interaction with the $\tilde{B}^2\Sigma^+$ state, which will enable production of a d.c. MOT of SrOH. The predicted FCFs, are in good agreement with the observed branching ratios. The DVR method for prediction the bending mode eigenvalues and eigenvectors needed for the FCF predictions of linear triatomic molecules has been presented.

Experimental and theoretical results presented here indicate that laser slowing of the cryogenic buffer-gas beam and subsequent loading of a d.c. or r.f. MOT can be achieved with at most four repumping lasers, which is comparable to the number of lasers used in the MOTs of SrF[7-8] and CaF[9-12]. Thus, a technically straightforward path towards direct production of ultracold polyatomic molecules via laser cooling has been confirmed. We anticipate that diagonal FCF arrays should exist for the similar linear triatomic molecules CaOH, BaOH, and YbOH, which we are now investigating. Additionally, other strontium monovalent polyatomic radicals such as strontium monoalkoxides have been considered for laser cooling and trapping[13] and future experimental and theoretical analysis similar to the present work will be necessary in order to specify the optimal conditions for magneto-optical trapping of complex polyatomic species.

6.6. References

1. Wall, M.; Maeda, K.; Carr, L. D., Realizing unconventional quantum magnetism with symmetric top molecules. *New Journal of Physics* **2015,** *17* (2), 025001.

2. Tesch, C. M.; de Vivie-Riedle, R., Quantum computation with vibrationally excited molecules. *Physical review letters* **2002,** *89* (15), 157901.

3. Kozyryev, I.; Hutzler, N. R., Precision measurement of time-reversal symmetry violation with laser-cooled polyatomic molecules. *Physical review letters* **2017,** *119* (13), 133002.

4. Balakrishnan, N., Perspective: Ultracold molecules and the dawn of cold controlled chemistry. *The Journal of chemical physics* **2016,** *145* (15), 150901.

5. Metcalf, H. J.; van der Straten, P., Laser cooling and trapping of atoms. *J. Opt. Soc. Am. B* **2003,** *20* (5), 887-908.

6. Di Rosa, M. D., Laser-cooling molecules. *The European Physical Journal D - Atomic, Molecular, Optical and Plasma Physics* **2004,** *31* (2), 395-402.

7. Barry, J. F.; McCarron, D. J.; Norrgard, E. B.; Steinecker, M. H.; DeMille, D., Magneto-optical trapping of a diatomic molecule. *Nature* **2014,** *512*, 286.

8. McCarron, D.; Norrgard, E.; Steinecker, M.; DeMille, D., Improved magneto–optical trapping of a diatomic molecule. *New Journal of Physics* **2015,** *17* (3), 035014.

9. Anderegg, L.; Augenbraun, B. L.; Chae, E.; Hemmerling, B.; Hutzler, N. R.; Ravi, A.; Collopy, A.; Ye, J.; Ketterle, W.; Doyle, J. M., Radio Frequency Magneto-Optical Trapping of CaF with High Density. *Physical Review Letters* **2017,** *119* (10), 103201.

10. Anderegg, L., L. Anderegg, BL Augenbraun, E. Chae, B. Hemmerling, NR Hutzler, A. Ravi, A. Collopy, J. Ye, W. Ketterle, and JM Doyle, Phys. Rev. Lett. 119, 103201 (2017). *Phys. Rev. Lett.* **2017,** *119*, 103201.

11. Truppe, S., S. Truppe, HJ Williams, M. Hambach, L. Caldwell, NJ Fitch, EA Hinds, BE Sauer, and MR Tarbutt, Nat. Phys. 13, 1173 (2017). *Nat. Phys.* **2017,** *13*, 1173.

12. Williams, H., HJ Williams, S. Truppe, M. Hambach, L. Caldwell, NJ Fitch, EA Hinds, BE Sauer, and MR Tarbutt, New J. Phys. 19, 113035 (2017). *New J. Phys.* **2017,** *19*, 113035.

13. Kozyryev, I.; Baum, L.; Matsuda, K.; Hemmerling, B.; Doyle, J. M., Radiation pressure force from optical cycling on a polyatomic molecule. *Journal of Physics B: Atomic, Molecular and Optical Physics* **2016,** *49* (13), 134002.

14. Isaev, T. A.; Berger, R., Polyatomic candidates for cooling of molecules with lasers from simple theoretical concepts. *Physical review letters* **2016,** *116* (6), 063006.

15. Shuman, E.; Barry, J.; Glenn, D.; DeMille, D., Radiative force from optical cycling on a diatomic molecule. *Physical review letters* **2009,** *103* (22), 223001.

16. Tarbutt, M., Magneto-optical trapping forces for atoms and molecules with complex level structures. *New Journal of Physics* **2015,** *17* (1), 015007.

17. Maxwell, S. E.; Brahms, N.; deCarvalho, R.; Glenn, D. R.; Helton, J. S.; Nguyen, S. V.; Patterson, D.; Petricka, J.; DeMille, D.; Doyle, J. M., High-Flux Beam Source for Cold, Slow Atoms or Molecules. *Physical Review Letters* **2005,** *95* (17), 173201.

18. Kozyryev, I.; Baum, L.; Matsuda, K.; Olson, P.; Hemmerling, B.; Doyle, J. M., Collisional relaxation of vibrational states of SrOH with He at 2 K. *New Journal of Physics* **2015,** *17* (4), 045003.

19. Kozyryev, I.; Baum, L.; Matsuda, K.; Augenbraun, B. L.; Anderegg, L.; Sedlack, A. P.; Doyle, J. M., Sisyphus Laser Cooling of a Polyatomic Molecule. *Physical Review Letters* **2017,** *118* (17), 173201.

20. Barry, J.; Shuman, E.; Norrgard, E.; DeMille, D., Laser radiation pressure slowing of a molecular beam. *Physical review letters* **2012,** *108* (10), 103002.

21. Anderson, M. A.; Barclay, W. L.; Ziurys, L. M., The millimeter-wave spectrum of the SrOH and SrOD radicals. *Chemical Physics Letters* **1992,** *196* (1), 166-172.

22. Ziurys, L. M.; Fletcher, D.; Anderson, M.; Barclay Jr, W., Rest Frequencies for Alkaline Earth Hydroxide Radicals (X 2 Sigma+). *The Astrophysical Journal Supplement Series* **1996,** *102*, 425.

23. Wang, J. G.; Sheridan, P. M.; Dick, M. J.; Bernath, P. F., Optical–optical double-resonance spectroscopy of SrOH: The C˜2Π(000)–A˜2Π(000) transition. *Journal of Molecular Spectroscopy* **2006,** *236* (1), 21-28.

24. Yu, S.; Wang, J.-G.; Sheridan, P. M.; Dick, M. J.; Bernath, P. F., Laser spectroscopy of the A˜2Π–X˜2Σ+000 and C˜2Π–A˜2Π000 transitions of SrOD. *Journal of Molecular Spectroscopy* **2006,** *240* (1), 26-31.

25. Wang, J. G.; Dick, M. J.; Sheridan, P. M.; Yu, S.; Bernath, P. F., Further spectroscopic investigations of the high energy electronic states of SrOH: The B∼′2Σ+(000)–A∼2Π(000) and the D∼2Σ+(000)–A∼2Π(000) transitions. *Journal of Molecular Spectroscopy* **2007,** *245* (1), 26-33.

26. Presunka, P. I.; Coxon, J. A., High-resolution laser spectroscopy of excited bending vibrations ($\upsilon 2 \leq 2$) of the and electronic states of SrOH: analysis of ℓ-type doubling and ℓ-type resonance. *Canadian Journal of Chemistry* **1993,** *71* (10), 1689-1705.

27. Presunka, P. I.; Coxon, J. A., Laser spectroscopy of the $\tilde{A}\ ^2\Pi$–$\tilde{X}\ ^2\Sigma^+$ transition of SrOH: Deperturbation analysis of K-resonance in the v2=1 level of the $\tilde{A}\ ^2\Pi$ state. *The Journal of Chemical Physics* **1994,** *101* (1), 201-222.

28. Presunka, P. I.; Coxon, J. A., Laser excitation and dispersed fluorescence investigations of the $\tilde{A}^2\Pi$–$\tilde{X}^2\Sigma^+$ system of SrOH. *Chemical Physics* **1995,** *190* (1), 97-111.

29. Brazier, C. R.; Bernath, P. F., Laser and fourier transform spectroscopy of the $\tilde{A}$2II-$\tilde{X}^2\Sigma^+$ transition of SrOH. *Journal of Molecular Spectroscopy* **1985,** *114* (1), 163-173.

30. Nakagawa, J.; Wormsbecher, R. F.; Harris, D. O., High-resolution laser excitation spectra of linear triatomic molecules: Analysis of the $B^2\Sigma^+$-$X^2\Sigma^+$ system of SrOH and SrOD. *Journal of Molecular Spectroscopy* **1983,** *97* (1), 37-64.

31. Steimle, T. C.; Fletcher, D. A.; Jung, K. Y.; Scurlock, C. T., A supersonic molecular beam optical Stark study of CaOH and SrOH. *The Journal of Chemical Physics* **1992,** *96* (4), 2556-2564.

32. Fletcher, D. A.; Jung, K. Y.; Scurlock, C. T.; Steimle, T. C., Molecular beam pump/probe microwave-optical double resonance using a laser ablation source. *The Journal of Chemical Physics* **1993,** *98* (3), 1837-1842.

33. Oberlander, M. D.; Parson, J. M., Laser excited fluorescence study of reactions of excited Ca and Sr with water and alcohols: Product selectivity and energy disposal. *The Journal of Chemical Physics* **1996,** *105* (14), 5806-5816.

34. Sharp, T.; Rosenstock, H., Franck—Condon Factors for Polyatomic Molecules. *The Journal of Chemical Physics* **1964,** *41* (11), 3453-3463.

35. Kozyryev, I., Laser cooling and inelastic collisions of the polyatomic radical SrOH. *Harvard University Ph. D. thesis* **2017**.

36. Warshel, A.; Karplus, M., Vibrational structure of electronic transitions in conjugated molecules. *Chemical Physics Letters* **1972,** *17* (1), 7-14.

37. Özkan, İ., Franck-Condon principle for polyatomic molecules: Axis-switching effects and transformation of normal coordinates. *Journal of Molecular Spectroscopy* **1990,** *139* (1), 147-162.

38. Ng, C.-Y.; Baer, T.; Powis, I., *Unimolecular and bimolecular ion-molecule reaction dynamics*. Wiley: 1994; Vol. 3.

39. Chau, F.-t.; Dyke, J. M.; Lee, E. P.-f.; Wang, D.-c., Franck–Condon analysis of photoelectron and electronic spectra of small molecules1Dedicated to Professor Neville Jonathan to mark his retirement1. *Journal of Electron Spectroscopy and Related Phenomena* **1998,** *97* (1), 33-47.

40. Pereira, R.; Levy, D. H., Observation and spectroscopy of high-lying states of the CaOH radical: Evidence for a bent, covalent state. *The Journal of Chemical Physics* **1996,** *105* (22), 9733-9739.

41. Brown, J. M.; Carrington, A., *Rotational spectroscopy of diatomic molecules*. Cambridge University Press: 2003.

42. Lefebvre-Brion, H.; Field, R. W., *The Spectra and Dynamics of Diatomic Molecules: Revised and Enlarged Edition*. Elsevier: 2004.

43. Neese, F., The ORCA program system. *Wiley Interdisciplinary Reviews: Computational Molecular Science* **2012,** *2* (1), 73-78.

44. Weigend, F.; Ahlrichs, R., Balanced basis sets of split valence, triple zeta valence and quadruple zeta valence quality for H to Rn: Design and assessment of accuracy. *Physical Chemistry Chemical Physics* **2005,** *7* (18), 3297-3305.

45. Weigend, F., Accurate Coulomb-fitting basis sets for H to Rn. *Physical chemistry chemical physics* **2006,** *8* (9), 1057-1065.

46. Kaupp, M.; Schleyer, P. v. R.; Stoll, H.; Preuss, H., Pseudopotential approaches to Ca, Sr, and Ba hydrides. Why are some alkaline earth MX2 compounds bent? *The Journal of Chemical Physics* **1991,** *94* (2), 1360-1366.

47. Ahlrichs, R.; Bär, M.; Häser, M.; Horn, H.; Kölmel, C., Electronic structure calculations on workstation computers: The program system turbomole. *Chemical Physics Letters* **1989,** *162* (3), 165-169.

48. Bolman, P. S. H.; Brown, J. M., The Renner—Teller effect and vibronically induced bands in the electronic spectrum of NCO. *Chemical Physics Letters* **1973,** *21* (2), 213-216.

49. Northrup, F. J.; Sears, T. J., Renner-Teller, spin-orbit and Fermi-resonance interactions in X 2Π NCS investigated by LIF spectroscopy. *Molecular Physics* **1990,** *71* (1), 45-64.

50. Chang, J.-L., A new method to calculate Franck–Condon factors of multidimensional harmonic oscillators including the Duschinsky effect. *The Journal of chemical physics* **2008,** *128* (17), 174111.

51. Bauschlicher, C. W.; Langhoff, S. R.; Partridge, H., Ab initio study of the alkali and alkaline-earth monohydroxides. *The Journal of Chemical Physics* **1986,** *84* (2), 901-909.

52. Bunker, P. R.; Kolbuszewski, M.; Jensen, P.; Brumm, m.; Anderson, M. A.; Barclay, W. L.; Ziurys, L. M.; Ni, Y.; Harris, D. O., New rovibrational data for MgOH and MgOD and the internuclear potential function of the ground electronic state. *Chemical Physics Letters* **1995,** *239* (4), 217-222.

53. Koput, J.; Peterson, K. A., Ab Initio Potential Energy Surface and Vibrational−Rotational Energy Levels of X2Σ+ CaOH. *The Journal of Physical Chemistry A* **2002,** *106* (41), 9595-9599.

54. Taylor, C. M.; Chaudhuri, R. K.; Freed, K. F., Electronic structure of the calcium monohydroxide radical. *The Journal of Chemical Physics* **2005,** *122* (4), 044317.

55. Light, J. C.; Hamilton, I. P.; Lill, J. V., Generalized discrete variable approximation in quantum mechanics. *The Journal of Chemical Physics* **1985,** *82* (3), 1400-1409.

56. Lodi, L.; Tennyson, J., Theoretical methods for small-molecule ro-vibrational spectroscopy. *Journal of Physics B: Atomic, Molecular and Optical Physics* **2010,** *43* (13), 133001.

57. Light, J. S., Separate but Equal?: Reasonable Accommodation in the Information Age. *Journal of the American Planning Association* **2001,** *67* (3), 263-278.

58. Harris, D. O.; Engerholm, G. G.; Gwinn, W. D., Calculation of Matrix Elements for One-Dimensional Quantum-Mechanical Problems and the Application to Anharmonic Oscillators. *The Journal of Chemical Physics* **1965,** *43* (5), 1515-1517.

59. Nguyen, D.-T.; Steimle, T. C.; Kozyryev, I.; Huang, M.; McCoy, A. B., Fluorescence branching ratios and magnetic tuning of the visible spectrum of SrOH. *Journal of Molecular Spectroscopy* **2018,** *347*, 7-18.

60. Frederick, J. H.; Woywod, C., General formulation of the vibrational kinetic energy operator in internal bond-angle coordinates. *The Journal of Chemical Physics* **1999,** *111* (16), 7255-7271.

CHAPTER 7

THE VISIBLE SPECTRUM OF YBOH, YTTERBIUM MONOHYDROXIDE

7.1. Introduction

Molecules hold an important role in the physical sciences nowadays. Molecules made of a small number of atoms provide the upper limit of complexity in studying them completely starting from quantum mechanics. Second, studying molecules is a cornerstone from which investigation on more complex structures base on. Thus, molecules then represent a kind of intellectual point around which knowledge of the small system can be leveraged to probe and manipulate increasingly complex ones. Recently, molecules are being used to test fundamental physics in numerous ways[1-3]. One of the purposes is using heavy polar molecules as a probe to measure the electric dipole moment. This fundamental property of electron, which is predicted by the Standard Model, should be very small. Although the value is small, it is proposed to be measured based on heavy polar molecules that enhances the interaction energy between the EDM and an applied electric field. Molecules are also being used as a tests of fundamental symmetries of nature like the influence of parity violation in nuclei[4].

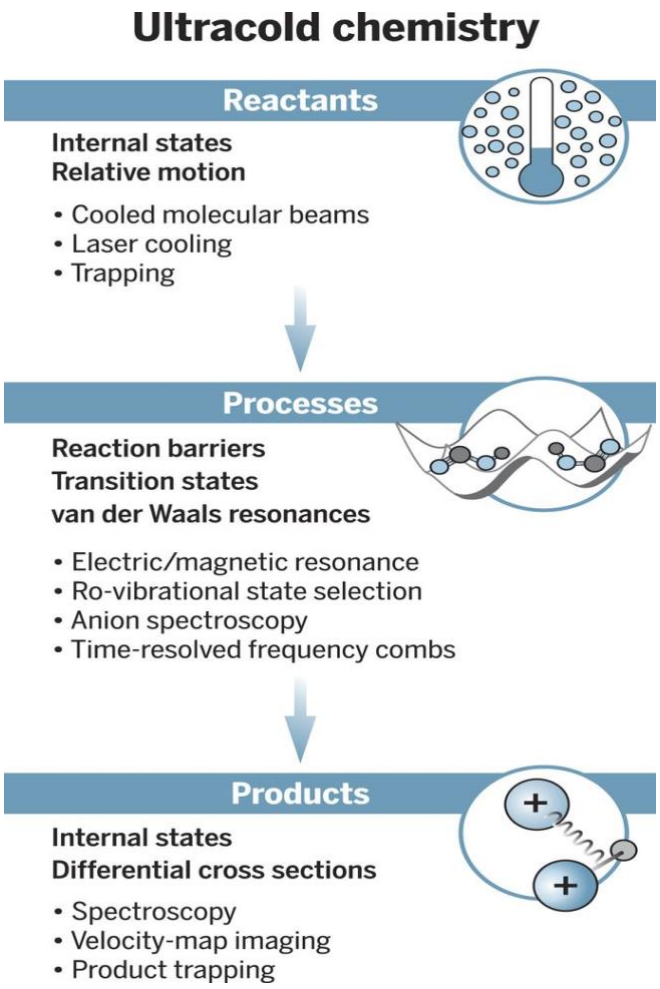

Figure 7.1. A big picture of cold molecule research.[5]

Molecules in a room temperature gas move around at several hundred meters per second. It is difficult to make precise measurements with these molecules, because the high speed limits the observation time, and the wide range of Doppler shifts broadens their spectral lines. Molecules at room temperature also occupy a wide range of rotational and vibrational states, which smears out their quantum-mechanical properties. Regardless of motivations, those measurements require a high level of accuracy and precise. As matter of fact, molecules in a "warm" temperature moves with the speed of couples of hundred meters per second. It makes those desired measurements more difficult because the high

motions shorten the observation time and broaden the spectral lines due to Doppler shifts. Performing those measurements at "warm" temperature also required to involve a lot of rotational and vibrational states which effects greatly the results. Therefore, bringing the temperature of molecules in gas phase to the quantum regime is needed. When molecules' motion is extremely slowly, and their internal degrees of freedom is controlled at the level of individual quantum states, then the observation times will be longer, and the desired values can in principle be measured.

The combination of laser cooling and trapping of neutral atoms and molecules attracts increasing interest and produced new research tools in both physics and chemistry. The basic idea behind laser cooling is the conservation of energy and momentum during the absorption and emission of near- resonant photon. An atom or molecule absorbs a photon from a laser beam travel opposite to its motion and gets excited. The momentum of the absorbed photon is transferred to the atom (or molecule) and reduced its velocity. The exited atom (or molecule) then relax to the ground state through spontaneous emission. Successful laser cooling of a molecular species requires many photon scattering events, and therefore all of the transitions from the hyperfine manifold of the ground state must be addressed. Laser cooling alone can lead to a significant decrease in the molecular motion and a narrow spatial and velocity distributions, but it works even better in conjunction with a trap under the presence of a magnetic field. The magneto-optical trap (MOT), was first demonstrated in 1987[6] and now becomes the basic building block of most experiments involving ultracold samples.

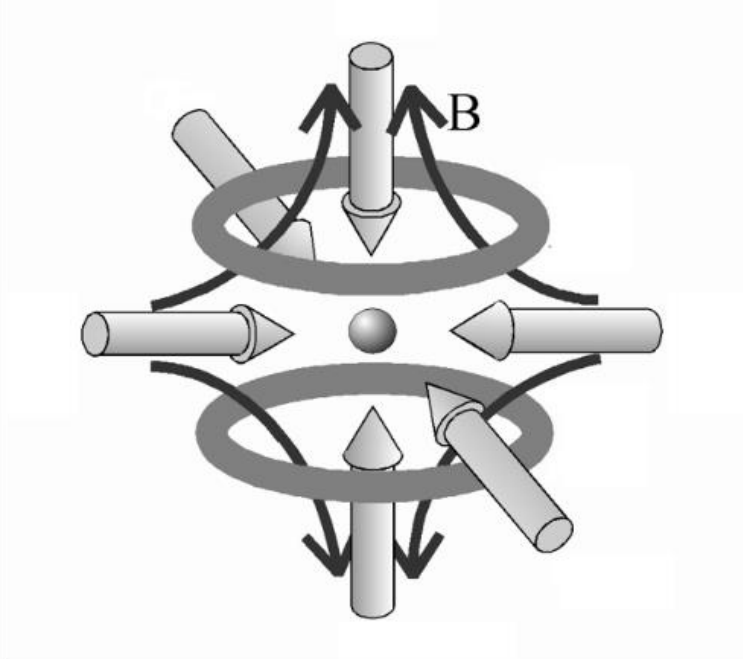

Figure 7.2. Schematic of the typical MOT apparatus used to trap and cool atoms, the draw was based on the work of trapping 40K atoms[7]

The more recent application of cooling and trapping techniques applying to molecules which has been more challenging due to the complexity of molecular structures has now opened the door to precisely controlling molecular interaction processes. As a result, laser cooling techniques, with a precise kinetic energy control, offer a new way to investigate the behavior of atoms and molecules and evolve to enable the understanding of reaction chemistry and the realization of a completely new regime of matter with distinctly quantum mechanical properties such as Bose-Einstein condensation and Fermi degeneracy[8]. However, the absence of closed optical transitions in molecules expressively hampers optical cycling and laser cooling in even the simplest diatomic species[9]. Over the past three decades, many research groups have been successful in preparing many ultracold paramagnetic atomic gas samples by the Magneto-Optical Trapping techniques[10-12].

Recently, YbOH has been proposed as a candidate for the MOT experiment[13] for investigating T-violating physics beyond the standard model (BSM), specifically the electron electric dipole moment (EDM) and nuclear magnetic quadrupole moment (MQM) via the heavy polar Yb- containing molecule. Because YbOH molecule has an electronic structure similar to CaF, SrF and SrOH, those laser cooling molecules, it makes this molecule become a candidate to cool and trap a dense sample of this one. In order to set up the MOT, YbOH's optical transitions are needed. Historically, spectroscopic studies of YbOH were done through both theoretical and experimental approach[14-19]. The most relevant studies to the present investigation is the field-free spectroscopic parameters for the ground state $\tilde{X}^{2}\Sigma^{+}(0,0,0)$ being determined from the analysis of the pure rotational spectrum[19]. The spectrum was recorded using a pump/probe microwave optical double resonance technique with molecules are generated from a cold supersonic molecular beam. A summary of previous studies of excited electronic states of the 000–000 and 000–100 bands of YbOH at high temperature can be found in the manuscripts by the Coxon's group[16]. Thus, their results excluded the measurements of numerous low-J branch features and the needed intensities of the DF spectra were also not determined, which are relevant to the proposed MOT experiments.

Here we report on the two-dimensional and dispersed fluorescence (DF) spectra of YbOH arising from the $\tilde{A}^{2}\Pi_{1/2}(0,0,0) \rightarrow \tilde{X}^{2}\Sigma^{+}(v_1, v_2, v_3)$ transition along with other electronic vibrational bands are recorded and processed to determine the branching ratios, $b_{v',v''}$. The intense transitions near 17323 cm-1 and 16733 cm^{-1} were assigned and studied. The degenerate bending vibration and stretching vibrations associated with Yb-O-H

vibrations are assigned and verified, respectively. Also, the DLIF measurements of the lowest electronic states support the construction of MOT experiments for the laser cooling part.

7.2. Observation

7.2.1. The 2D spectrum of YbOH

The 2D spectrum of products generated through ablation of Yb with the CH_3OH/Å mixture in the spectral range of 17200 $cm^{-1}$to 17400 $cm^{-1}$is presented in Figure *7.3*. The real-time tracking Labview program was used to monitor the monochromator in the way that the excitation puled dye laser is off by 500 cm^{-1} from the center of 75 nm spectral window on the CCD. Various scan over this region suggests that the relative fluorescence intensity of YbOH from the excitation laser depends on the intensity of the pulsed dye laser. The spectral of 200 cm^{-1} is wide enough to cover the fluorescence range of YbOH and able to maintain the stable laser intensity through the scan. There were three distinguishable DLIF fluorescence observed from the 2D spectrum. The bands near 17270 cm^{-1} and 17330 cm^{-1} correspond to Yb- containing species generated through the reaction of ablated Yb and methanol. The second band near 17323 cm^{-1} was assigned as the $\tilde{A}^2\Pi_{1/2} - \tilde{X}^2\Sigma^+$ of YbOH which agrees with Coxon's previous work[16].

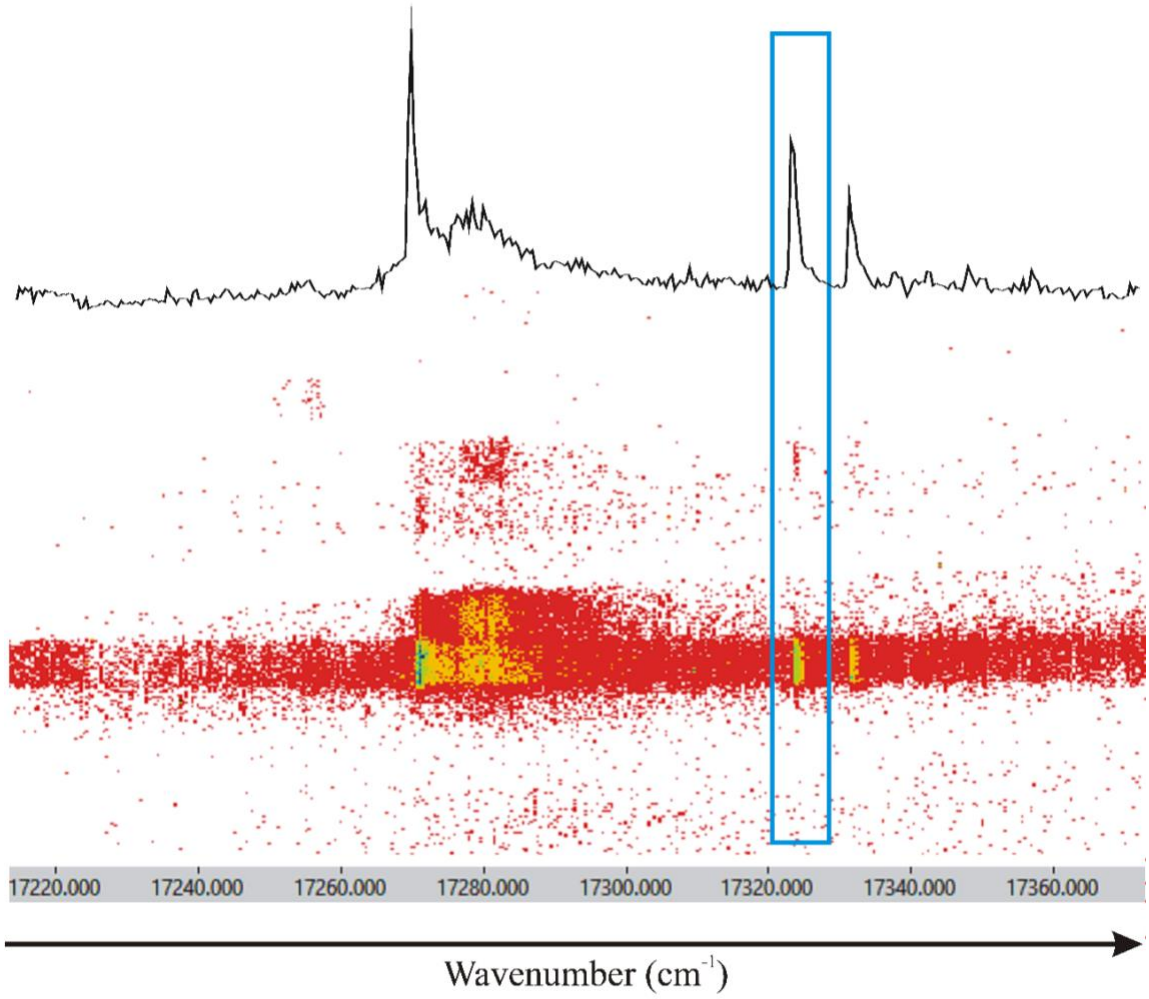

Figure 7.3. The 2D spectrum of molecules generated in the ablation of Yb with Ch_3OH/Ar mixture in the range of 17200 to 17400 cm^{-1}. The horizontal bands of fluorescence are the excitation spectra monitored either on or off resonance. The band near 17323.668 cm^{-1} has the DLIF characteristic of YbOH. The (black) upper panel is the laser excitation spectrum of the fluorescence monitored on resonance of all species generated through the reactions in the nozzle.

7.2.2. The DF spectra of the $\tilde{A}^2\Pi_r - \tilde{X}^2\Sigma^+$ transition of YbOH

The DF spectrum corresponding to the $\tilde{A}^2\Pi_{1/2} - \tilde{X}^2\Sigma^+$ transitions was obtained by pumping specific rotationally resolved lines in the field-free spectrum. The calibrated DF spectrum of the $\tilde{A}^2\Pi_{1/2}(0,0,0)$ state was acquired through the cw-laser excitation of the

$Q_1(3/2)$ line of the corresponding $0_0^0\ \tilde{A}^2\Pi_{1/2} - \tilde{X}^2\Sigma^+$ band near 17323.6723 cm^{-1} and a representative spectrum is showed in Figure 7.4. The features near 16773 cm^{-1} and 16698 cm^{-1} belongs to the $2_1^0\ \tilde{A}^2\Pi_{1/2} \rightarrow \tilde{X}^2\Sigma^+$ (denoted as B) and $3_1^0\ \tilde{A}^2\Pi_{1/2} \rightarrow \tilde{X}^2\Sigma^+$ emissions (denoted as C), respectively. The presence of $2_2^0\ \tilde{A}^2\Pi_{1/2} \rightarrow \tilde{X}^2\Sigma^+$ (denoted as D) belongs to the relaxation to the two quanta of the stretching mode is assigned near.

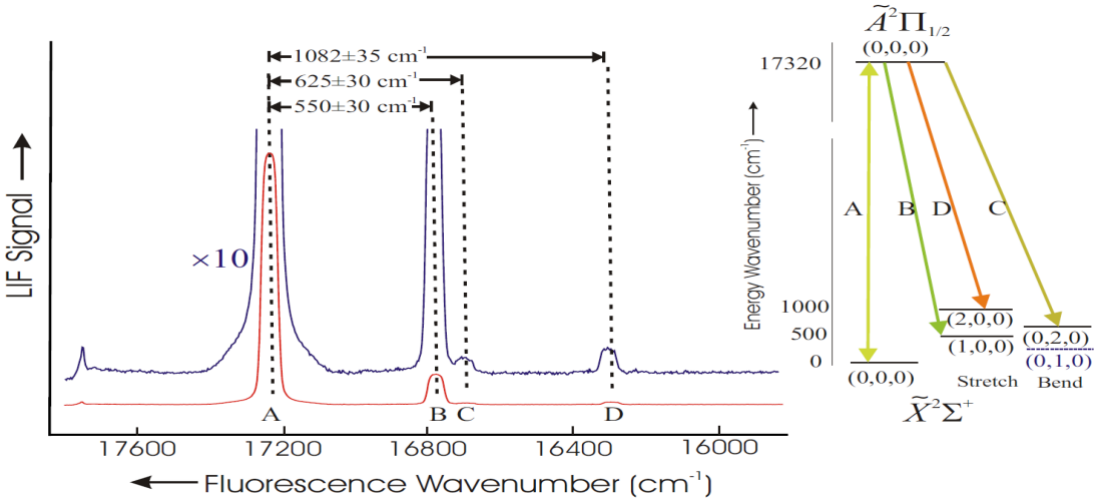

Figure 7.4.The dispersed fluorescence spectrum of the $\tilde{A}^2\Pi_{1/2}(0,0,0)$ state obtained by cw-laser excitation of the $Q_1(3/2)$ (ν = 17323.6723 cm^{-1}) line of the $0_0^0\ \tilde{A}^2\Pi_{1/2} - \tilde{X}^2\Sigma^+$ band. The expected locations of the emission to the $\tilde{X}^2\Sigma^+(0,1^1,0)$, $\tilde{X}^2\Sigma^+(0,1^2,0)$, and $\tilde{X}^2\Sigma^+(0,2^0,0)$ states are indicated

7.3. Analysis

Dispersed Fluorescence Spectra

The relative intensities of the DF spectra were calibrated by using the Argon pen lamp and then corrected for the wavelength response of the spectrometer. The shift of the spectral peaks from the excitation laser were calculated to determine the associated

vibrational modes. The values and assigned vibrational mode of the lowest electronic state of YbOH are given in Table 7.1.

Table 7.1. Franck-Condon factors and branching ratios. The unit is in wavenumber (cm^{-1})

Band	obs $T_{v',v''}$	Rel. Int. (Counts)	Branch Ratio (%)	Vibrational spacing		
				Calc.[b]	Obs.[a]	This study
$\tilde{A}^2\Pi_{1/2}(0,0,0) - \tilde{X}^2\Sigma^+(0,0,0)$	17323.7	7436521	87.49			
$\tilde{A}^2\Pi_{1/2}(0,0,0) - \tilde{X}^2\Sigma^+(1,0,0)$	16974.4	929287	10.93	541	533	550 ± 30
$\tilde{A}^2\Pi_{1/2}(0,0,0) - \tilde{X}^2\Sigma^+(2,0,0)$	16271	71087	0.84	784	678	625 ± 30
$\tilde{A}^2\Pi_{1/2}(0,0,0) - \tilde{X}^2\Sigma^+(3,0,0)$	15748	61199	< 0.1			
$\tilde{A}^2\Pi_{1/2}(0,0,0) - \tilde{X}^2\Sigma^+(0,1,0)$	16988	87277	< 0.1			
$\tilde{A}^2\Pi_{1/2}(0,0,0) - \tilde{X}^2\Sigma^+(0,2,0)$	16649	48491	0.57	1082	1058	1082 ± 35

a. The value were taken from Coxon's work[16]
b. The values are from Brutti's work[17]

7.4. Discussion

The determined vibrational frequencies for the $\tilde{X}^2\Sigma^+(0,0,0)$ state (see Table 7.1) are significantly improved from the previous determined values by Brutti[17] and Coxon[16]. The difference between the current investigation and the previous ones is this one was done at "cold" temperature via supersonic expansion's source. The 2D spectrum has been able to identify the existence of YbOH and the $\tilde{A}^2\Pi_{1/2}(0,0,0) \rightarrow \tilde{X}^2\Sigma^+(v_1,v_2,v_3)$ transition near

17323 cm^{-1} which agrees with previous investigation. The DF spectra collecting from exciting the molecule from the ground state to the $\tilde{A}^2\Pi_r(0,0,0)$ was obtained and used as a tool to verify the associated vibrational modes of YbOH. About studying the branching ratio of the transition, the DF spectrum shows the relative FCF associated with the relaxation to various vibrational mode. The very small fluorescence intensity coming from the fluorescence's to two quanta of the stretching and bending modes of YbOH have been shown in the 2D spectrum and later reconfirmed by the DF spectra. From Figure 7.4, the $\tilde{A}^2\Pi_{1/2}(0,0,0) \rightarrow \tilde{X}^2\Sigma^+(v_1,v_2,v_3)$ transition is very diagonal with less than 1% contributing from relaxation of YbOH to two quanta of the bending and stretching mode.

Lastly, the strong feature in the 2D spectrum at 17271 cm^{-1} may belong to the transition of $YbCH_3$. The structure of the bands in the 2D spectrum suggests it belong to the poly atomic molecule. The strong intensity implies that most species in this investigation have been formed from the reactions with the radicals (either CH_3 or OH) and ablated Yb is very reactive with CH_3 radical. The later switching between H_2O_2 and CH_3OH confirmed the reactivity of ablated Yb with OH radicals.

7.5. Conclusion

In this work, the $\tilde{A}^2\Pi_{1/2}(0,0,0) \rightarrow \tilde{X}^2\Sigma^+(v_1,v_2,v_3)$ emission has been recognized in both the 2S and the DF spectrum from a supersonic molecular beam of YbOH via laser ablation scheme. The 2D spectrum has identifies the transitions belong to YbOH and agrees well with previous work of Coxon. The DF spectrum then verified the determined vibrational frequencies of the round state of YbOH. The observations here confirm that the

emissions of $\tilde{A}^2\Pi_{1/2}(0,0,0) \rightarrow \tilde{X}^2\Sigma^+(0,0,0)$ and $\tilde{A}^2\Pi_{1/2}(0,0,0) \rightarrow \tilde{X}^2\Sigma^+(1,0,0)$ are much stronger and dominate transitions to other vibrational modes. The transitions of this heavy-polar Yb-containing molecule is very diagonal and weaker that may well make them better candidates for the investigation of the eEDM and other CP violating phenomena. High-resolution spectroscopy of this transition was recorded and is processing to understand further details of YbOH's electronic state.

7.6. References

1. DeMille, D.; Doyle, J. M.; Sushkov, A. O., Probing the frontiers of particle physics with tabletop-scale experiments. *Science* **2017,** *357* (6355), 990-994.

2. Safronova, M. S.; Budker, D.; DeMille, D.; Kimball, D. F. J.; Derevianko, A.; Clark, C. W., Search for new physics with atoms and molecules. *Reviews of Modern Physics* **2018,** *90* (2), 025008.

3. Lim, J.; Almond, J.; Trigatzis, M.; Devlin, J.; Fitch, N.; Sauer, B.; Tarbutt, M.; Hinds, E., Ultracold molecules for measuring the electron's electric dipole moment. *arXiv preprint arXiv:1712.02868* **2017**.

4. Altuntaş, E.; Ammon, J.; Cahn, S. B.; DeMille, D., Demonstration of a Sensitive Method to Measure Nuclear-Spin-Dependent Parity Violation. *Physical Review Letters* **2018,** *120* (14), 142501.

5. Bohn, J. L.; Rey, A. M.; Ye, J., Cold molecules: Progress in quantum engineering of chemistry and quantum matter. *Science* **2017,** *357* (6355), 1002-1010.

6. Raab, E., EL Raab, M. Prentiss, A. Cable, S. Chu, and DE Pritchard, Phys. Rev. Lett. 59, 2631 (1987). *Phys. Rev. Lett.* **1987,** *59*, 2631.

7. DeMarco, B.; Jin, D. S., Onset of Fermi Degeneracy in a Trapped Atomic Gas. *Science* **1999,** *285* (5434), 1703-1706.

8. Gerbier, F.; Richard, S.; Thywissen, J.; Hugbart, M.; Bouyer, P.; Aspect, A.; Shvarchuck, I.; Buggle, C.; Petrov, D.; Kemmann, M., B. Bose-Einstein Condensation and Fermi Degeneracy. *Interactions in Ultracold Gases: From Atoms to Molecules* **2003**, 407-443.

9. Di Rosa, M. D., Laser-cooling molecules. *The European Physical Journal D - Atomic, Molecular, Optical and Plasma Physics* **2004,** *31* (2), 395-402.

10. Barry, J. F.; McCarron, D. J.; Norrgard, E. B.; Steinecker, M. H.; DeMille, D., Magneto-optical trapping of a diatomic molecule. *Nature* **2014,** *512*, 286.

11. McCarron, D. J.; Norrgard, E. B.; Steinecker, M. H.; DeMille, D., Improved magneto–optical trapping of a diatomic molecule. *New Journal of Physics* **2015,** *17* (3), 035014.

12. Williams, H. J.; Truppe, S.; Hambach, M.; Caldwell, L.; Fitch, N. J.; Hinds, E. A.; Sauer, B. E.; Tarbutt, M. R., Characteristics of a magneto-optical trap of molecules. *New Journal of Physics* **2017,** *19* (11), 113035.

13. Kozyryev, I.; Baum, L.; Matsuda, K.; Doyle, J. M., Proposal for Laser Cooling of Complex Polyatomic Molecules. *ChemPhysChem* **2016,** *17* (22), 3641-3648.

14. BELYAEV, V.; LEBEDEVA, N.; KRASNOV, K., ELECTRONIC ENERGIES AND IONIZATION POTENTIALS OF YBX (X. *Russian journal of physical chemistry* **1996,** *70* (8), 1328-1333.

15. Belyaev, V.; Lebedeva, N., Dissociation energy of YbOH molecules. *Zhurnal Fizicheskoj Khimii* **1998,** *72* (12), 2176-2181.

16. Melville, T. C.; Coxon, J. A., The visible laser excitation spectrum of YbOH: The Ã 2 Π–X̃ 2 Σ+ transition. *The Journal of Chemical Physics* **2001,** *115* (15), 6974-6978.

17. Brutti, S.; Terai, T.; Yamawaki, M.; Yasumoto, M.; Balducci, G.; Gigli, G.; Ciccioli, A., Mass spectrometric investigation of gaseous YbH, YbO and YbOH molecules. *Rapid Communications in Mass Spectrometry: An International Journal Devoted to the Rapid Dissemination of Up-to-the-Minute Research in Mass Spectrometry* **2005,** *19* (16), 2251-2258.

18. Malika, D.; Ephraim, E.; Anastasia, B., Enhancement factor for the electric dipole moment of the electron in the BaOH and YbOH molecules. *arXiv preprint arXiv:1901.02265* **2019**.

19. Nakhate, S.; Steimle, T. C.; Pilgram, N. H.; Hutzler, N. R., The pure rotational spectrum of YbOH. *Chemical Physics Letters* **2019,** *715*, 105-108.

REFERENCES

CHAPTER 1

1. Brown, J. M.; Carrington, A., *Rotational spectroscopy of diatomic molecules*. Cambridge University Press: 2003.

2. Herzberg, G., Molecular spectra and molecular structure. Vol. 1: Spectra of diatomic molecules. *New York: Van Nostrand Reinhold, 1950, 2nd ed.* **1950**.

3. Kovács, I.; Nemes, L., *Rotational structure in the spectra of diatomic molecules*. Hilger London: 1969.

4. Lefebvre-Brion, H.; Field, R. W., *The Spectra and Dynamics of Diatomic Molecules: Revised and Enlarged Edition*. Elsevier: 2004.

5. Townes, C. H.; Schawlow, A. L., *Microwave spectroscopy*. Courier Corporation: 2013.

6. Steimle, T. C., Permanent electric dipole moments of metal containing molecules. *International Reviews in Physical Chemistry* **2000,** *19* (3), 455-477.

7. Bunker, P. R.; Jensen, P., *Molecular symmetry and spectroscopy*. NRC Research Press: 2006.

8. Hougen, J. T. *The calculation of rotational energy levels and rotational line intensities in diatomic molecules*; NATIONAL STANDARD REFERENCE DATA SYSTEM: 1970.

9. Mills, I.; Cvitas, T.; Homann, K.; Kallay, N.; Kuchitsu, K., Quantities, Units, and Symbols in Physical Chemistry. *Journal of the American Chemical Society* **1994,** *116* (19), 8861.

10. Steimle, T.; Kokkin, D. L.; Muscarella, S.; Ma, T., Detection of the Thorium Dimer via Two-Dimensional Fluorescence Spectroscopy. *The Journal of Physical Chemistry A* **2015,** *119* (35), 9281-9285.

11. Reilly, N. J.; Schmidt, T. W.; Kable, S. H., Two-Dimensional Fluorescence (Excitation/Emission) Spectroscopy as a Probe of Complex Chemical Environments. *The Journal of Physical Chemistry A* **2006,** *110* (45), 12355-12359.

12. Kokkin, D. L.; Steimle, T. C.; DeMille, D., Branching ratios and radiative lifetimes of the U, L, and I states of thorium oxide. *Physical Review A* **2014,** *90* (6), 062503.

13. Barry, J. F.; McCarron, D. J.; Norrgard, E. B.; Steinecker, M. H.; DeMille, D., Magneto-optical trapping of a diatomic molecule. *Nature* **2014,** *512*, 286.

14. McCarron, D. J.; Norrgard, E. B.; Steinecker, M. H.; DeMille, D., Improved magneto–optical trapping of a diatomic molecule. *New Journal of Physics* **2015,** *17* (3), 035014.

15. Julienne, P. S., Quo vadis now, cold molecules? *Nature Physics* **2018,** *14* (9), 873-874.

16. Klos, J.; Li, M.; Petrov, A.; Kotochigova, S., Chemistry of Laser-Coolable Polyatomic Molecules. *Bulletin of the American Physical Society* **2018**.

17. McCarron, D.; Steinecker, M.; Zhu, Y.; DeMille, D., Magnetic Trapping of an Ultracold Gas of Polar Molecules. *Physical review letters* **2018,** *121* (1), 013202.

18. Williams, H. J.; Caldwell, L.; Fitch, N. J.; Truppe, S.; Rodewald, J.; Hinds, E. A.; Sauer, B. E.; Tarbutt, M. R., Magnetic Trapping and Coherent Control of Laser-Cooled Molecules. *Physical Review Letters* **2018,** *120* (16), 163201.

19. Taylor, R., *Reprocessing and recycling of spent nuclear fuel*. Elsevier: 2015.

20. Veliscek-Carolan, J., Separation of actinides from spent nuclear fuel: A review. *Journal of hazardous materials* **2016,** *318*, 266-281.

21. Ewing, R. C., Long-term storage of spent nuclear fuel. *Nature Materials* **2015,** *14* (3), 252.

22. Barker, B. J.; Antonov, I. O.; Heaven, M. C.; Peterson, K. A., Spectroscopic investigations of ThF and ThF+. *The Journal of Chemical Physics* **2012,** *136* (10), 104305.

23. Heaven, M. C.; Barker, B. J.; Antonov, I. O., Spectroscopy and Structure of the Simplest Actinide Bonds. *The Journal of Physical Chemistry A* **2014,** *118* (46), 10867-10881.

24. VanGundy, R. A.; Bartlett, J. H.; Heaven, M. C.; Battey, S. R.; Peterson, K. A., Spectroscopic and theoretical studies of ThCl and ThCl+. *The Journal of Chemical Physics* **2017,** *146* (5), 054307.

CHAPTER 2

1. Kinsey, J. L., Laser-induced fluorescence. *Annual Review of Physical Chemistry* **1977,** *28* (1), 349-372.

2. Kokkin, D. L.; Steimle, T. C.; DeMille, D., Branching ratios and radiative lifetimes of the U, L, and I states of thorium oxide. *Physical Review A* **2014,** *90* (6), 062503.

3. Gascooke, J. R.; Alexander, U. N.; Lawrance, W. D., Two dimensional laser induced fluorescence spectroscopy: A powerful technique for elucidating rovibronic structure in electronic transitions of polyatomic molecules. *The Journal of Chemical Physics* **2011,** *134* (18), 184301.

4. Chen, P. C., High Resolution Coherent 2D Spectroscopy. *The Journal of Physical Chemistry A* **2010,** *114* (43), 11365-11375.

5. Reilly, N. J.; Schmidt, T. W.; Kable, S. H., Two-Dimensional Fluorescence (Excitation/Emission) Spectroscopy as a Probe of Complex Chemical Environments. *The Journal of Physical Chemistry A* **2006,** *110* (45), 12355-12359.

6. Nguyen, D.-T.; Steimle, T. C.; Kozyryev, I.; Huang, M.; McCoy, A. B., Fluorescence branching ratios and magnetic tuning of the visible spectrum of SrOH. *Journal of Molecular Spectroscopy* **2018,** *347*, 7-18.

7. Linton, C.; Adam, A.; Steimle, T., Stark and Zeeman effect in the [18.6] 3.5–X (1) 4.5 transition of uranium monofluoride, UF. *The Journal of chemical physics* **2014,** *140* (21), 214305.

8. Steimle, T.; Kokkin, D. L.; Muscarella, S.; Ma, T., Detection of the Thorium Dimer via Two-Dimensional Fluorescence Spectroscopy. *The Journal of Physical Chemistry A* **2015,** *119* (35), 9281-9285.

9. Wang, H.-W.; Zhu, T. C.; Putt, M. E.; Solonenko, M.; Metz, J.; Dimofte, A.; Miles, J.; Fraker, D. L.; Glatstein, E.; Hahn, S. M.; Yodh, A. G., Broadband reflectance measurements of light penetration, blood oxygenation, hemoglobin concentration, and drug concentration in human intraperitoneal tissues before and after photodynamic therapy. *BIOMEDO* **2005,** *10* (1), 014004-01400413.

10. Nguyen, D.-T.; Steimle, T.; Linton, C.; Cheng, L., Optical Stark and Zeeman Spectroscopy of Thorium Fluoride (ThF) and Thorium Chloride (ThCl). *The Journal of Physical Chemistry A* **2019,** *123* (7), 1423-1433.

CHAPTER 3

1. Herzberg, G., Molecular spectra and molecular structure. Vol. 1: Spectra of diatomic molecules. *New York: Van Nostrand Reinhold, 1950, 2nd ed.* **1950**.

2. Kovács, I.; Nemes, L., *Rotational structure in the spectra of diatomic molecules*. Hilger London: 1969.

3. Brown, J. M.; Carrington, A., *Rotational spectroscopy of diatomic molecules*. Cambridge University Press: 2003.

4. Lefebvre-Brion, H.; Field, R. W., *The Spectra and Dynamics of Diatomic Molecules: Revised and Enlarged Edition*. Elsevier: 2004.

5. Bunker, P. R.; Jensen, P., *Molecular symmetry and spectroscopy*. NRC Research Press: 2006.

6. Townes, C. H.; Schawlow, A. L., *Microwave spectroscopy*. Courier Corporation: 2013.

7. Sauer, B. E.; Cahn, S. B.; Kozlov, M. G.; Redgrave, G. D.; Hinds, E. A., Perturbed hyperfine doubling in the A2Π1/2 and [18.6]0.5 states of YbF. *The Journal of Chemical Physics* **1999,** *110* (17), 8424-8428.

8. Brown, J. M.; Cheung, A. S. C.; Merer, A. J., Λ-Type doubling parameters for molecules in Δ electronic states. *J. Mol. Spectrosc.* **1987,** *124* (2), 464-75.

9. Condon, E. U., Nuclear Motions Associated with Electron Transitions in Diatomic Molecules. *Physical Review* **1928,** *32* (6), 858-872.

10. Franck, J.; Dymond, E. G., Elementary processes of photochemical reactions. *Transactions of the Faraday Society* **1926,** *21* (February), 536-542.

CHAPTER 4

1. Hudson, J. J.; Kara, D. M.; Smallman, I. J.; Sauer, B. E.; Tarbutt, M. R.; Hinds, E. A., Improved measurement of the shape of the electron. *Nature* **2011,** *473*, 493.

2. Kara, D. M.; Smallman, I. J.; Hudson, J. J.; Sauer, B. E.; Tarbutt, M. R.; Hinds, E. A., Measurement of the electron's electric dipole moment using YbF molecules: methods and data analysis. *New Journal of Physics* **2012,** *14* (10), 103051.

3. Shuman, E. S.; Barry, J. F.; DeMille, D., Laser cooling of a diatomic molecule. *Nature* **2010,** *467*, 820.

4. Hummon, M. T.; Yeo, M.; Stuhl, B. K.; Collopy, A. L.; Xia, Y.; Ye, J., 2D magneto-optical trapping of diatomic molecules. *Physical Review Letters* **2013,** *110* (14), 143001.

5. Zhelyazkova, V.; Cournol, A.; Wall, T. E.; Matsushima, A.; Hudson, J. J.; Hinds, E.; Tarbutt, M.; Sauer, B., Laser cooling and slowing of CaF molecules. *Physical Review A* **2014,** *89* (5), 053416.

6. Truppe, S.; Williams, H. J.; Fitch, N. J.; Hambach, M.; Wall, T. E.; Hinds, E. A.; Sauer, B. E.; Tarbutt, M. R., An intense, cold, velocity-controlled molecular beam by frequency-chirped laser slowing. *New Journal of Physics* **2017,** *19* (2), 022001.

7. Kozyryev, I.; Baum, L.; Matsuda, K.; Augenbraun, B. L.; Anderegg, L.; Sedlack, A. P.; Doyle, J. M., Sisyphus Laser Cooling of a Polyatomic Molecule. *Physical Review Letters* **2017,** *118* (17), 173201.

8. Barry, J. F.; McCarron, D. J.; Norrgard, E. B.; Steinecker, M. H.; DeMille, D., Magneto-optical trapping of a diatomic molecule. *Nature* **2014,** *512*, 286.

9. Norrgard, E.; McCarron, D.; Steinecker, M.; Tarbutt, M.; DeMille, D., Submillikelvin dipolar molecules in a radio-frequency magneto-optical trap. *Physical review letters* **2016,** *116* (6), 063004.

10. Truppe, S.; Williams, H.; Hambach, M.; Caldwell, L.; Fitch, N.; Hinds, E.; Sauer, B.; Tarbutt, M., Molecules cooled below the Doppler limit. *Nature Physics* **2017,** *13* (12), 1173.

11. Zhuang, X.; Le, A.; Steimle, T. C.; Bulleid, N. E.; Smallman, I. J.; Hendricks, R. J.; Skoff, S. M.; Hudson, J. J.; Sauer, B. E.; Hinds, E. A.; Tarbutt, M. R., Franck–Condon factors and radiative lifetime of the A2Π1/2–X2Σ+ transition of ytterbium monofluoride, YbF. *Physical Chemistry Chemical Physics* **2011,** *13* (42), 19013-19017.

12. Tarbutt, M.; Sauer, B.; Hudson, J.; Hinds, E., Design for a fountain of YbF molecules to measure the electron's electric dipole moment. *New Journal of Physics* **2013,** *15* (5), 053034.

13. Smallman, I. J.; Wang, F.; Steimle, T. C.; Tarbutt, M. R.; Hinds, E. A., Radiative branching ratios for excited states of 174YbF: Application to laser cooling. *Journal of Molecular Spectroscopy* **2014,** *300*, 3-6.

14. Dunfield, K. L.; Linton, C.; Clarke, T. E.; McBride, J.; Adam, A. G.; Peers, J. R. D., Laser Spectroscopy of the Lanthanide Monofluorides: Analysis of theA2Π–X2Σ+Transition of Ytterbium Monofluoride. *Journal of Molecular Spectroscopy* **1995,** *174* (2), 433-445.

15. Sauer, B. E.; Cahn, S. B.; Kozlov, M. G.; Redgrave, G. D.; Hinds, E. A., Perturbed hyperfine doubling in the A2Π1/2 and [18.6]0.5 states of YbF. *The Journal of Chemical Physics* **1999,** *110* (17), 8424-8428.

16. Ma, T.; Butler, C.; Brown, J. M.; Linton, C.; Steimle, T. C., Optical Zeeman Spectroscopy of Ytterbium Monofluoride, YbF. *The Journal of Physical Chemistry A* **2009,** *113* (28), 8038-8044.

17. Glassman, Z.; Mawhorter, R.; Grabow, J.-U.; Le, A.; Steimle, T. C., The hyperfine interaction in the odd isotope of ytterbium fluoride, 171YbF. *Journal of Molecular Spectroscopy* **2014,** *300*, 7-11.

18. Fukuda, M.; Soga, K.; Senami, M.; Tachibana, A., Local spin dynamics with the electron electric dipole moment. *Physical Review A* **2016,** *93* (1), 012518.

19. Pašteka, L. F.; Mawhorter, R. J.; Schwerdtfeger, P., Relativistic coupled-cluster calculations of the 173Yb nuclear quadrupole coupling constant for the YbF molecule. *Molecular Physics* **2016,** *114* (7-8), 1110-1117.

20. Sunaga, A.; Abe, M.; Hada, M.; Das, B. P., Relativistic coupled-cluster calculation of the electron-nucleus scalar-pseudoscalar interaction constant W s in YbF. *Physical Review A* **2016,** *93* (4), 042507.

21. Sauer, B. E.; Wang, J.; Hinds, E. A., Laser-rf double resonance spectroscopy of 174YbF in the X 2Σ+ state: Spin-rotation, hyperfine interactions, and the electric dipole moment. *The Journal of Chemical Physics* **1996,** *105* (17), 7412-7420.

22. Dickinson, C. S.; Coxon, J. A.; Walker, N. R.; Gerry, M. C. L., Fourier transform microwave spectroscopy of the 2Σ+ ground states of YbX (X=F, Cl, Br): Characterization of hyperfine effects and determination of the molecular geometries. *The Journal of Chemical Physics* **2001,** *115* (15), 6979-6989.

23. Sauer, B. E.; Wang, J.; Hinds, E. A., Anomalous Spin-Rotation Coupling in the ${X}^{2}{\ensuremath{\Sigma}}^{+}$ State of YbF. *Physical Review Letters* **1995,** *74* (9), 1554-1557.

24. Condylis, P.; Hudson, J.; Tarbutt, M.; Sauer, B.; Hinds, E., Stark shift of the A 2 Π 1⁄2 state in YbF 174. AIP: 2005.

25. Steimle, T. C.; Ma, T.; Linton, C., The hyperfine interaction in the A (2) Pi (1/2) and X (2) Sigma (+) states of ytterbium monofluoride (vol 127, art no 234316, 2007). *JOURNAL OF CHEMICAL PHYSICS* **2008,** *128* (20).

26. Brown, J. M.; Carrington, A., *Rotational spectroscopy of diatomic molecules*. Cambridge University Press: 2003.

27. Mawhorter, R. J.; Murphy, B. S.; Baum, A. L.; Sears, T. J.; Yang, T.; Rupasinghe, P.; McRaven, C.; Shafer-Ray, N.; Alphei, L. D.; Grabow, J.-U., Characterization of the ground X 1 state of 204 Pb 19 F, 206 Pb 19 F, 207 Pb 19 F, and 208 Pb 19 F. *Physical Review A* **2011,** *84* (2), 022508.

28. Simard, B.; Watson, J. K. G.; Merer, A. J.; Steimle, T. C., Comment on "Fine and magnetic hyperfine structure in the A2Π and X2Σ+ states of yttrium monoxide" [J. Chem. Phys. 88, 598 (1988)]. *The Journal of Chemical Physics* **1999,** *111* (13), 6148-6149.

29. Linton, C., Private communication. **2017**.

30. Amano, T., Interpretation of magnetic hyperfine coupling constants. *Journal of Molecular Spectroscopy* **1990,** *144* (2), 454-457.

31. Chipman, D. M., The spin polarization model for hyperfine coupling constants. *Theoretica chimica acta* **1992,** *82* (1), 93-115.

32. Munzarová, M.; Kaupp, M., A Critical Validation of Density Functional and Coupled-Cluster Approaches for the Calculation of EPR Hyperfine Coupling Constants in Transition Metal Complexes. *The Journal of Physical Chemistry A* **1999,** *103* (48), 9966-9983.

33. Munzarová, M. L.; Kubáček, P.; Kaupp, M., Mechanisms of EPR Hyperfine Coupling in Transition Metal Complexes. *Journal of the American Chemical Society* **2000,** *122* (48), 11900-11913.

CHAPTER 5

1. Huang, P.-W.; Wang, C.-Z.; Wu, Q.-Y.; Lan, J.-H.; Song, G.; Chai, Z.-F.; Shi, W.-Q., Understanding Am3+/Cm3+ separation with H4TPAEN and its hydrophilic derivatives: a quantum chemical study. *Phys. Chem. Chem. Phys.* **2018,** *20* (20), 14031-14039.

2. Kong, X.-H.; Wu, Q.-Y.; Wang, C.-Z.; Lan, J.-H.; Chai, Z.-F.; Nie, C.-M.; Shi, W.-Q., Insight into the Extraction Mechanism of Americium(III) over Europium(III) with Pyridylpyrazole: A Relativistic Quantum Chemistry Study. *J. Phys. Chem. A* **2018,** *122* (18), 4499-4507.

3. Leoncini, A.; Huskens, J.; Verboom, W., Ligands for f-element extraction used in the nuclear fuel cycle. *Chem. Soc. Rev.* **2017,** *46* (23), 7229-7273.

4. Afsar, A.; Distler, P.; Harwood, L. M.; John, J.; Westwood, J., Extraction of minor actinides, lanthanides and other fission products by silica-immobilized BTBP/BTPhen ligands. *Chem. Commun. (Cambridge, U. K.)* **2017,** *53* (28), 4010-4013.

5. Gorden, A. E. V.; DeVore, M. A.; Maynard, B. A., Coordination Chemistry with f-Element Complexes for an Improved Understanding of Factors That Contribute to Extraction Selectivity. *Inorg. Chem.* **2013,** *52* (7), 3445-3458.

6. Heaven, M. C.; Barker, B. J.; Antonov, I. O., Spectroscopy and Structure of the Simplest Actinide Bonds [Erratum to document cited in CA161:686740]. *J. Phys. Chem. A* **2015,** *119* (41), 10440.

7. Heaven, M. C.; Barker, B. J.; Antonov, I. O., Spectroscopy and Structure of the Simplest Actinide Bonds. *J. Phys. Chem. A* **2014,** *118* (46), 10867-10881.

8. Kaledin, L. A.; McCord, J. E.; Heaven, M. C., Laser spectroscopy of UO: characterization and assignment of states in the 0- to 3-eV Range, with a comparison to the electronic structure of ThO. *J. Mol. Spectrosc.* **1994,** *164* (1), 27-65.

9. Field, R. W., Diatomic molecular electronic structure beyond simple molecular constants. *Ber. Bunsenges. Phys. Chem.* **1982,** *86* (9), 771-9.

10. Barker, B. J.; Antonov, I. O.; Heaven, M. C.; Peterson, K. A., Spectroscopic investigations of ThF and ThF+. *J. Chem. Phys.* **2012,** *136* (10), 104305/1-104305/9.

11. Bross, D. H.; Peterson, K. A., Theoretical spectroscopy study of the low-lying electronic states of UX and UX+, X = F and Cl. *J. Chem. Phys.* **2015**, Ahead of Print.

12. Van Gundy, R. A.; Bartlett, J. H.; Heaven, M. C.; Battey, S. R.; Peterson, K. A., Spectroscopic and theoretical studies of ThCl and ThCl+. *J. Chem. Phys.* **2017,** *146* (5), 054307/1-054307/8.

13. Schall, H.; Gray, J. A.; Dulick, M.; Field, R. W., Sub-Doppler Zeeman spectroscopy of the cerium oxide (CeO) molecule. *J. Chem. Phys.* **1986,** *85* (2), 751-62.

14. Heaven, M. C.; Goncharov, V.; Steimle, T. C.; Ma, T.; Linton, C., The permanent electric dipole moments and magnetic g factors of uranium monoxide. *J. Chem. Phys.* **2006,** *125* (20), 204314/1-204314/11.

15. Linton, C.; Adam, A. G.; Steimle, T. C., Stark and Zeeman effect in the [18.6]3.5 - X(1)4.5 transition of uranium monofluoride, UF. *J. Chem. Phys.* **2014,** *140* (21), 214305/1-214305/7.

16. Jung, J.; Atanasov, M.; Neese, F.; Atanasov, M., Ab Initio Ligand-Field Theory Analysis and Covalency Trends in Actinide and Lanthanide Free Ions and Octahedral Complexes. *Inorg Chem* **2017,** *56* (15), 8802-8816.

17. Matthew, D. J.; Morse, M. D., Resonant two-photon ionization spectroscopy of jet-cooled UN: Determination of the ground state. *J. Chem. Phys.* **2013,** *138* (18), 184303/1-184303/7.

18. Edvinsson, G.; Selin, L. E.; Aslund, N., Band spectrum of ThO. *Ark. Fys.* **1965,** *30* (22), 283-319.

19. Brown, J. M.; Cheung, A. S. C.; Merer, A. J., Λ-Type doubling parameters for molecules in Δ electronic states. *J. Mol. Spectrosc.* **1987,** *124* (2), 464-75.

20. Brown, J. M.; Carrington, A., *Rotational Spectroscopy of Diatomic Molecules*. Cambridge University Press: 2003; p 1046 pp.

21. Qin, C.; Linton, C.; Steimle, T. C., Optical Zeeman spectroscopy of the (0,0) B4Γ - X4Φ band systems of titanium monohydride, TiH, and titanium monodeuteride, TiD. *J. Chem. Phys.* **2012,** *137* (7), 074301/1-074301/7.

22. Irikura, K. K., Gas-Phase Energetics of Thorium Fluorides and Their Ions. *J. Phys. Chem. A* **2013,** *117* (6), 1276-1282.

23. Dewberry, C. T.; Etchison, K. C.; Cooke, S. A., The pure rotational spectrum of the actinide-containing compound thorium monoxide. *Phys. Chem. Chem. Phys.* **2007,** *9* (35), 4895-4897.

24. Steimle, T. C.; Zhang, R.; Heaven, M. C., The pure rotational spectrum of thorium monosulfide, ThS. *Chem. Phys. Lett.* **2015,** *639*, 304-306.

CHAPTER 6

1. Wall, M.; Maeda, K.; Carr, L. D., Realizing unconventional quantum magnetism with symmetric top molecules. *New Journal of Physics* **2015,** *17* (2), 025001.

2. Tesch, C. M.; de Vivie-Riedle, R., Quantum computation with vibrationally excited molecules. *Physical review letters* **2002,** *89* (15), 157901.

3. Kozyryev, I.; Hutzler, N. R., Precision measurement of time-reversal symmetry violation with laser-cooled polyatomic molecules. *Physical review letters* **2017,** *119* (13), 133002.

4. Balakrishnan, N., Perspective: Ultracold molecules and the dawn of cold controlled chemistry. *The Journal of chemical physics* **2016,** *145* (15), 150901.

5. Metcalf, H. J.; van der Straten, P., Laser cooling and trapping of atoms. *J. Opt. Soc. Am. B* **2003,** *20* (5), 887-908.

6. Di Rosa, M. D., Laser-cooling molecules. *The European Physical Journal D - Atomic, Molecular, Optical and Plasma Physics* **2004,** *31* (2), 395-402.

7. Barry, J. F.; McCarron, D. J.; Norrgard, E. B.; Steinecker, M. H.; DeMille, D., Magneto-optical trapping of a diatomic molecule. *Nature* **2014,** *512*, 286.

8. McCarron, D.; Norrgard, E.; Steinecker, M.; DeMille, D., Improved magneto–optical trapping of a diatomic molecule. *New Journal of Physics* **2015,** *17* (3), 035014.

9. Anderegg, L.; Augenbraun, B. L.; Chae, E.; Hemmerling, B.; Hutzler, N. R.; Ravi, A.; Collopy, A.; Ye, J.; Ketterle, W.; Doyle, J. M., Radio Frequency Magneto-Optical Trapping of CaF with High Density. *Physical Review Letters* **2017,** *119* (10), 103201.

10. Anderegg, L., L. Anderegg, BL Augenbraun, E. Chae, B. Hemmerling, NR Hutzler, A. Ravi, A. Collopy, J. Ye, W. Ketterle, and JM Doyle, Phys. Rev. Lett. 119, 103201 (2017). *Phys. Rev. Lett.* **2017,** *119*, 103201.

11. Truppe, S., S. Truppe, HJ Williams, M. Hambach, L. Caldwell, NJ Fitch, EA Hinds, BE Sauer, and MR Tarbutt, Nat. Phys. 13, 1173 (2017). *Nat. Phys.* **2017,** *13*, 1173.

12. Williams, H., HJ Williams, S. Truppe, M. Hambach, L. Caldwell, NJ Fitch, EA Hinds, BE Sauer, and MR Tarbutt, New J. Phys. 19, 113035 (2017). *New J. Phys.* **2017,** *19*, 113035.

13. Kozyryev, I.; Baum, L.; Matsuda, K.; Hemmerling, B.; Doyle, J. M., Radiation pressure force from optical cycling on a polyatomic molecule. *Journal of Physics B: Atomic, Molecular and Optical Physics* **2016,** *49* (13), 134002.

14. Isaev, T. A.; Berger, R., Polyatomic candidates for cooling of molecules with lasers from simple theoretical concepts. *Physical review letters* **2016,** *116* (6), 063006.

15. Shuman, E.; Barry, J.; Glenn, D.; DeMille, D., Radiative force from optical cycling on a diatomic molecule. *Physical review letters* **2009,** *103* (22), 223001.

16. Tarbutt, M., Magneto-optical trapping forces for atoms and molecules with complex level structures. *New Journal of Physics* **2015,** *17* (1), 015007.

17. Maxwell, S. E.; Brahms, N.; deCarvalho, R.; Glenn, D. R.; Helton, J. S.; Nguyen, S. V.; Patterson, D.; Petricka, J.; DeMille, D.; Doyle, J. M., High-Flux Beam Source for Cold, Slow Atoms or Molecules. *Physical Review Letters* **2005,** *95* (17), 173201.

18. Kozyryev, I.; Baum, L.; Matsuda, K.; Olson, P.; Hemmerling, B.; Doyle, J. M., Collisional relaxation of vibrational states of SrOH with He at 2 K. *New Journal of Physics* **2015,** *17* (4), 045003.

19. Kozyryev, I.; Baum, L.; Matsuda, K.; Augenbraun, B. L.; Anderegg, L.; Sedlack, A. P.; Doyle, J. M., Sisyphus Laser Cooling of a Polyatomic Molecule. *Physical Review Letters* **2017,** *118* (17), 173201.

20. Barry, J.; Shuman, E.; Norrgard, E.; DeMille, D., Laser radiation pressure slowing of a molecular beam. *Physical review letters* **2012,** *108* (10), 103002.

21. Anderson, M. A.; Barclay, W. L.; Ziurys, L. M., The millimeter-wave spectrum of the SrOH and SrOD radicals. *Chemical Physics Letters* **1992,** *196* (1), 166-172.

22. Ziurys, L. M.; Fletcher, D.; Anderson, M.; Barclay Jr, W., Rest Frequencies for Alkaline Earth Hydroxide Radicals (X 2 Sigma+). *The Astrophysical Journal Supplement Series* **1996,** *102*, 425.

23. Wang, J. G.; Sheridan, P. M.; Dick, M. J.; Bernath, P. F., Optical–optical double-resonance spectroscopy of SrOH: The C˜2Π(000)–A˜2Π(000) transition. *Journal of Molecular Spectroscopy* **2006,** *236* (1), 21-28.

24. Yu, S.; Wang, J.-G.; Sheridan, P. M.; Dick, M. J.; Bernath, P. F., Laser spectroscopy of the A˜2Π–X˜2Σ+000 and C˜2Π–A˜2Π000 transitions of SrOD. *Journal of Molecular Spectroscopy* **2006,** *240* (1), 26-31.

25. Wang, J. G.; Dick, M. J.; Sheridan, P. M.; Yu, S.; Bernath, P. F., Further spectroscopic investigations of the high energy electronic states of SrOH: The B∼′2Σ+(000)–A∼2Π(000) and the D∼2Σ+(000)–A∼2Π(000) transitions. *Journal of Molecular Spectroscopy* **2007,** *245* (1), 26-33.

26. Presunka, P. I.; Coxon, J. A., High-resolution laser spectroscopy of excited bending vibrations ($\upsilon 2 \leq 2$) of the and electronic states of SrOH: analysis of ℓ-type doubling and ℓ-type resonance. *Canadian Journal of Chemistry* **1993,** *71* (10), 1689-1705.

27. Presunka, P. I.; Coxon, J. A., Laser spectroscopy of the Ã 2Π–X̃ 2Σ+ transition of SrOH: Deperturbation analysis of K-resonance in the v2=1 level of the Ã 2Π state. *The Journal of Chemical Physics* **1994,** *101* (1), 201-222.

28. Presunka, P. I.; Coxon, J. A., Laser excitation and dispersed fluorescence investigations of the Ã2Π−X̃2Σ+ system of SrOH. *Chemical Physics* **1995,** *190* (1), 97-111.

29. Brazier, C. R.; Bernath, P. F., Laser and fourier transform spectroscopy of the Ã2II-X̃2Σ+ transition of SrOH. *Journal of Molecular Spectroscopy* **1985,** *114* (1), 163-173.

30. Nakagawa, J.; Wormsbecher, R. F.; Harris, D. O., High-resolution laser excitation spectra of linear triatomic molecules: Analysis of the B2Σ+-X2Σ+ system of SrOH and SrOD. *Journal of Molecular Spectroscopy* **1983,** *97* (1), 37-64.

31. Steimle, T. C.; Fletcher, D. A.; Jung, K. Y.; Scurlock, C. T., A supersonic molecular beam optical Stark study of CaOH and SrOH. *The Journal of Chemical Physics* **1992,** *96* (4), 2556-2564.

32. Fletcher, D. A.; Jung, K. Y.; Scurlock, C. T.; Steimle, T. C., Molecular beam pump/probe microwave-optical double resonance using a laser ablation source. *The Journal of Chemical Physics* **1993,** *98* (3), 1837-1842.

33. Oberlander, M. D.; Parson, J. M., Laser excited fluorescence study of reactions of excited Ca and Sr with water and alcohols: Product selectivity and energy disposal. *The Journal of Chemical Physics* **1996,** *105* (14), 5806-5816.

34. Sharp, T.; Rosenstock, H., Franck—Condon Factors for Polyatomic Molecules. *The Journal of Chemical Physics* **1964,** *41* (11), 3453-3463.

35. Kozyryev, I., Laser cooling and inelastic collisions of the polyatomic radical SrOH. *Harvard University Ph. D. thesis* **2017**.

36. Warshel, A.; Karplus, M., Vibrational structure of electronic transitions in conjugated molecules. *Chemical Physics Letters* **1972,** *17* (1), 7-14.

37. Özkan, İ., Franck-Condon principle for polyatomic molecules: Axis-switching effects and transformation of normal coordinates. *Journal of Molecular Spectroscopy* **1990,** *139* (1), 147-162.

38. Ng, C.-Y.; Baer, T.; Powis, I., *Unimolecular and bimolecular ion-molecule reaction dynamics*. Wiley: 1994; Vol. 3.

39. Chau, F.-t.; Dyke, J. M.; Lee, E. P.-f.; Wang, D.-c., Franck–Condon analysis of photoelectron and electronic spectra of small molecules1Dedicated to Professor Neville Jonathan to mark his retirement1. *Journal of Electron Spectroscopy and Related Phenomena* **1998,** *97* (1), 33-47.

40. Pereira, R.; Levy, D. H., Observation and spectroscopy of high-lying states of the CaOH radical: Evidence for a bent, covalent state. *The Journal of Chemical Physics* **1996,** *105* (22), 9733-9739.

41. Brown, J. M.; Carrington, A., *Rotational spectroscopy of diatomic molecules*. Cambridge University Press: 2003.

42. Lefebvre-Brion, H.; Field, R. W., *The Spectra and Dynamics of Diatomic Molecules: Revised and Enlarged Edition*. Elsevier: 2004.

43. Neese, F., The ORCA program system. *Wiley Interdisciplinary Reviews: Computational Molecular Science* **2012,** *2* (1), 73-78.

44. Weigend, F.; Ahlrichs, R., Balanced basis sets of split valence, triple zeta valence and quadruple zeta valence quality for H to Rn: Design and assessment of accuracy. *Physical Chemistry Chemical Physics* **2005,** *7* (18), 3297-3305.

45. Weigend, F., Accurate Coulomb-fitting basis sets for H to Rn. *Physical chemistry chemical physics* **2006,** *8* (9), 1057-1065.

46. Kaupp, M.; Schleyer, P. v. R.; Stoll, H.; Preuss, H., Pseudopotential approaches to Ca, Sr, and Ba hydrides. Why are some alkaline earth MX2 compounds bent? *The Journal of Chemical Physics* **1991,** *94* (2), 1360-1366.

47. Ahlrichs, R.; Bär, M.; Häser, M.; Horn, H.; Kölmel, C., Electronic structure calculations on workstation computers: The program system turbomole. *Chemical Physics Letters* **1989,** *162* (3), 165-169.

48. Bolman, P. S. H.; Brown, J. M., The Renner—Teller effect and vibronically induced bands in the electronic spectrum of NCO. *Chemical Physics Letters* **1973,** *21* (2), 213-216.

49. Northrup, F. J.; Sears, T. J., Renner-Teller, spin-orbit and Fermi-resonance interactions in X 2Π NCS investigated by LIF spectroscopy. *Molecular Physics* **1990,** *71* (1), 45-64.

50. Chang, J.-L., A new method to calculate Franck–Condon factors of multidimensional harmonic oscillators including the Duschinsky effect. *The Journal of chemical physics* **2008,** *128* (17), 174111.

51. Bauschlicher, C. W.; Langhoff, S. R.; Partridge, H., Ab initio study of the alkali and alkaline-earth monohydroxides. *The Journal of Chemical Physics* **1986,** *84* (2), 901-909.

52. Bunker, P. R.; Kolbuszewski, M.; Jensen, P.; Brumm, m.; Anderson, M. A.; Barclay, W. L.; Ziurys, L. M.; Ni, Y.; Harris, D. O., New rovibrational data for MgOH and

MgOD and the internuclear potential function of the ground electronic state. *Chemical Physics Letters* **1995,** *239* (4), 217-222.

53. Koput, J.; Peterson, K. A., Ab Initio Potential Energy Surface and Vibrational−Rotational Energy Levels of X2Σ+ CaOH. *The Journal of Physical Chemistry A* **2002,** *106* (41), 9595-9599.

54. Taylor, C. M.; Chaudhuri, R. K.; Freed, K. F., Electronic structure of the calcium monohydroxide radical. *The Journal of Chemical Physics* **2005,** *122* (4), 044317.

55. Light, J. C.; Hamilton, I. P.; Lill, J. V., Generalized discrete variable approximation in quantum mechanics. *The Journal of Chemical Physics* **1985,** *82* (3), 1400-1409.

56. Lodi, L.; Tennyson, J., Theoretical methods for small-molecule ro-vibrational spectroscopy. *Journal of Physics B: Atomic, Molecular and Optical Physics* **2010,** *43* (13), 133001.

57. Light, J. S., Separate but Equal?: Reasonable Accommodation in the Information Age. *Journal of the American Planning Association* **2001,** *67* (3), 263-278.

58. Harris, D. O.; Engerholm, G. G.; Gwinn, W. D., Calculation of Matrix Elements for One-Dimensional Quantum-Mechanical Problems and the Application to Anharmonic Oscillators. *The Journal of Chemical Physics* **1965,** *43* (5), 1515-1517.

59. Nguyen, D.-T.; Steimle, T. C.; Kozyryev, I.; Huang, M.; McCoy, A. B., Fluorescence branching ratios and magnetic tuning of the visible spectrum of SrOH. *Journal of Molecular Spectroscopy* **2018,** *347*, 7-18.

60. Frederick, J. H.; Woywod, C., General formulation of the vibrational kinetic energy operator in internal bond-angle coordinates. *The Journal of Chemical Physics* **1999,** *111* (16), 7255-7271.

CHAPTER 7

1. DeMille, D.; Doyle, J. M.; Sushkov, A. O., Probing the frontiers of particle physics with tabletop-scale experiments. *Science* **2017,** *357* (6355), 990-994.

2. Safronova, M. S.; Budker, D.; DeMille, D.; Kimball, D. F. J.; Derevianko, A.; Clark, C. W., Search for new physics with atoms and molecules. *Reviews of Modern Physics* **2018,** *90* (2), 025008.

3. Lim, J.; Almond, J.; Trigatzis, M.; Devlin, J.; Fitch, N.; Sauer, B.; Tarbutt, M.; Hinds, E., Ultracold molecules for measuring the electron's electric dipole moment. *arXiv preprint arXiv:1712.02868* **2017**.

4. Altuntaş, E.; Ammon, J.; Cahn, S. B.; DeMille, D., Demonstration of a Sensitive Method to Measure Nuclear-Spin-Dependent Parity Violation. *Physical Review Letters* **2018,** *120* (14), 142501.

5. Bohn, J. L.; Rey, A. M.; Ye, J., Cold molecules: Progress in quantum engineering of chemistry and quantum matter. *Science* **2017,** *357* (6355), 1002-1010.

6. Raab, E., EL Raab, M. Prentiss, A. Cable, S. Chu, and DE Pritchard, Phys. Rev. Lett. 59, 2631 (1987). *Phys. Rev. Lett.* **1987,** *59*, 2631.

7. DeMarco, B.; Jin, D. S., Onset of Fermi Degeneracy in a Trapped Atomic Gas. *Science* **1999,** *285* (5434), 1703-1706.

8. Gerbier, F.; Richard, S.; Thywissen, J.; Hugbart, M.; Bouyer, P.; Aspect, A.; Shvarchuck, I.; Buggle, C.; Petrov, D.; Kemmann, M., B. Bose-Einstein Condensation and Fermi Degeneracy. *Interactions in Ultracold Gases: From Atoms to Molecules* **2003**, 407-443.

9. Di Rosa, M. D., Laser-cooling molecules. *The European Physical Journal D - Atomic, Molecular, Optical and Plasma Physics* **2004,** *31* (2), 395-402.

10. Barry, J. F.; McCarron, D. J.; Norrgard, E. B.; Steinecker, M. H.; DeMille, D., Magneto-optical trapping of a diatomic molecule. *Nature* **2014,** *512*, 286.

11. McCarron, D. J.; Norrgard, E. B.; Steinecker, M. H.; DeMille, D., Improved magneto–optical trapping of a diatomic molecule. *New Journal of Physics* **2015,** *17* (3), 035014.

12. Williams, H. J.; Truppe, S.; Hambach, M.; Caldwell, L.; Fitch, N. J.; Hinds, E. A.; Sauer, B. E.; Tarbutt, M. R., Characteristics of a magneto-optical trap of molecules. *New Journal of Physics* **2017,** *19* (11), 113035.

13. Kozyryev, I.; Baum, L.; Matsuda, K.; Doyle, J. M., Proposal for Laser Cooling of Complex Polyatomic Molecules. *ChemPhysChem* **2016,** *17* (22), 3641-3648.

14. BELYAEV, V.; LEBEDEVA, N.; KRASNOV, K., ELECTRONIC ENERGIES AND IONIZATION POTENTIALS OF YBX (X. *Russian journal of physical chemistry* **1996,** *70* (8), 1328-1333.

15. Belyaev, V.; Lebedeva, N., Dissociation energy of YbOH molecules. *Zhurnal Fizicheskoj Khimii* **1998,** *72* (12), 2176-2181.

16. Melville, T. C.; Coxon, J. A., The visible laser excitation spectrum of YbOH: The Ã 2 Π–X̃ 2 Σ+ transition. *The Journal of Chemical Physics* **2001,** *115* (15), 6974-6978.

17. Brutti, S.; Terai, T.; Yamawaki, M.; Yasumoto, M.; Balducci, G.; Gigli, G.; Ciccioli, A., Mass spectrometric investigation of gaseous YbH, YbO and YbOH molecules. *Rapid Communications in Mass Spectrometry: An International Journal Devoted to the Rapid Dissemination of Up-to-the-Minute Research in Mass Spectrometry* **2005,** *19* (16), 2251-2258.

18. Malika, D.; Ephraim, E.; Anastasia, B., Enhancement factor for the electric dipole moment of the electron in the BaOH and YbOH molecules. *arXiv preprint arXiv:1901.02265* **2019**.

19. Nakhate, S.; Steimle, T. C.; Pilgram, N. H.; Hutzler, N. R., The pure rotational spectrum of YbOH. *Chemical Physics Letters* **2019,** *715*, 105-108.